https://ntrs.nasa.gov/search.jsp?R=19940010633 2020-06-16T19:52:55+00:00Z

IN-24
17
109 p

NASA CONTRACTOR REPORT 191522

INELASTIC DEFORMATION OF METAL MATRIX COMPOSITES

C. J. LISSENDEN, C. T. HERAKOVICH, AND M-J. PINDERA
University of Virginia
Charlottesville, VA

Contract NAGI-745
SEPTEMBER 1993

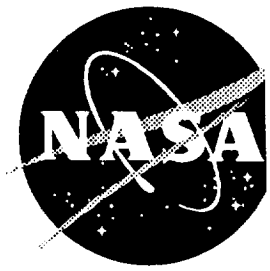

(NASA-CR-191522) INELASTIC DEFORMATION OF METAL MATRIX COMPOSITES Final Report (Virginia Univ.) 109 p

N94-15106

Unclas

G3/24 0189617

National Aeronautics and
Space Administration

LANGLEY RESEARCH CENTER
Hampton, Virginia 23681-0001

ABSTRACT

A theoretical model capable of predicting the thermomechanical response of continuously reinforced metal matrix composite laminates subjected to multiaxial loading has been developed. A micromechanical model is used in conjunction with nonlinear lamination theory to determine inelastic laminate response. Matrix viscoplasticity, residual stresses, and damage to the fiber/matrix interfacial zone are explicitly included in the model.

The representative cell of the micromechanical model is considered to be in a state of generalized plane strain, enabling a quasi two-dimensional analysis to be performed. Constant strain finite elements are formulated with elastic-viscoplastic constitutive equations. Interfacial debonding is incorporated into the model through interface elements based on the interfacial debonding theory originally presented by Needleman (1987), and modified by Tvergaard (1990). Nonlinear interfacial constitutive equations relate interfacial tractions to displacement discontinuities at the interface.

Theoretical predictions are compared with the results of an experimental program conducted on silicon carbide/titanium (SiC/Ti) unidirectional, $[0_4]$, and angle-ply, $[\pm 45]_S$, tubular specimens. Multiaxial loading included increments of axial tension, compression, torque, and internal pressure. Loadings were chosen in an effort to distinguish inelastic deformation due to damage from matrix plasticity and separate time-dependent effects from time-independent effects. Results show that fiber/matrix debonding is nonuniform throughout the composite and is a major factor in the effective response. Also, significant creep behavior occurs at relatively low applied stress levels at room temperature.

ACKNOWLEDGEMENT

This work was supported by the NASA Langley Research Center (NASA Grant NAG-1-745), the National Science Foundation (NSF Grant MSS-9115328), the Center for Light Thermal Structures at the University of Virginia, and the McDonnell Douglas Corporation (supplied composite tubes). The authors are grateful for this financial support, as well as for the technical advice of the NASA grant monitor, Dr. W. Steve Johnson.

Metallography and fractography was conducted on failed specimens by Dr. Bradley A. Lerch of the NASA Lewis Research Center. This work is greatly appreciated and provided additional insight into the damage and failure mechanisms present in the composite tubes.

TABLE OF CONTENTS

LIST OF SYMBOLS

[A]	laminate extensional stiffness matrix
[B]	laminate coupling stiffness matrix
[C]	stiffness matrix
c_f	fiber volume fraction
c_m	matrix volume fraction
[D]	laminate bending stiffness matrix
E	Young's modulus
{M}	moment resultant vector
$\{M^T\}$	equivalent thermal moment vector
$\{M^{NL}\}$	equivalent nonlinear moment vector
{N}	force resultant vector
$\{N^T\}$	equivalent thermal force vector
$\{N^{NL}\}$	equivalent nonlinear force vector
[Q]	reduced stiffness matrix
s_{ij}	deviatoric stress components
$[T_1]$	stress transformation matrix
$[T_2]$	strain transformation matrix
T_n, T_t, T_b	interfacial surface tractions
u_n, u_t, u_b	interfacial displacement discontinuities
Z_o, Z_1, m, n, D_o	viscoplastic material parameters
α	interface property - shear strength property
$\{\alpha\}$	coefficients of thermal expansion
δ	interface property - characteristic length

ε_{ij}	strain components
λ	nondimensional interfacial bonding parameter
ν	Poisson's ratio
μ	interface property - coefficient of friction
σ_o	interface property - normal separation strength
σ_{ij}	stress components

LIST OF FIGURES

LIST OF TABLES

CHAPTER 1

INTRODUCTION

While the range of applications for composite materials is ever increasing, the use of composite materials is anything but new. Reinforced concrete has been widely used as a construction material for years. The Israelites used straw to reinforce mud for making bricks. The Mongols crafted bows from animal tendons, wood and silk bonded together with an adhesive. Many other examples of man-made composites could be given. Composite materials also occur naturally in a wide variety of biological tissues. The recent increase in interest in composite materials is due primarily to the need for materials with high stiffness to weight ratios, and is fueled by advances in computing technology.

Metal matrix composites (MMC) are currently being considered as candidate materials for such structural applications as hypersonic flight vehicles, propulsion systems and missiles. In these types of applications thermomechanical loading is a primary consideration. For the structural applications enumerated above, the material system will be required to maintain significant stiffness and strength at elevated temperatures. A titanium (Ti) matrix reinforced with continuous silicon carbide (SiC) fibers is one type of MMC under consideration and is the model system that will be used in this study.

SiC/Ti composites exhibit many desirable properties, but because the titanium matrix is a viscoplastic material, the composite can respond to thermomechanical loads in a highly nonlinear way. Damage to the fiber/matrix interfacial zone in the form of debonding and radial microcracking can also cause nonlinear composite response.

1.1 Literature Review

MMC have been studied for years but over the last four years a large amount of research has been undertaken in order to obtain a better understanding of the response of MMC to thermomechanical loading. The following literature review summarizes the most important work done in the area of inelastic deformation of MMC; it is not intended to be comprehensive.

1.1.1 Plasticity

Because titanium is an elastic-viscoplastic material, it is necessary to consider creep as well as plasticity when analyzing the thermomechanical response of titanium matrix composites. While creep behavior is not associated with classical plasticity, unified viscoplastic models attempt to describe both time dependent and independent responses through a single model. Thus, related work done in the area of creep response is also included in this section.

Teply (1984) developed the periodic hexagonal array (PHA) model for the plasticity analysis of MMC based on a triangular representative volume element. Piecewise uniform fields were introduced to obtain estimates of local instantaneous fields. Dvorak and Teply (1985) and Teply and Dvorak (1988) exercised the model by subdividing the representative volume element into finite elements. Both displacement and equilibrium approaches were used to obtain upper and lower bounds on instantaneous moduli of elastoplastic composites.

Dvorak, et al. (1988 and 1990) conducted an extensive combined experimental/ theoretical study of the elastoplastic response of a boron/aluminum composite. Experiments were performed on axially reinforced [0] and fiberless tubular specimens by

applying increments of axial load, torque, and internal pressure. Dvorak and co-workers were able to plot the initial yield locus and track the movement of the current yield surface. The experimental program confirmed that the composite yield surface, like the matrix yield surface, must translate in the direction of the applied stress increment. Initial and subsequent yield surfaces were predicted using the periodic hexagonal array (PHA) model (Teply, 1984), bimodal plasticity theory (Dvorak, 1991), and a modified Mori-Tanaka scheme (Mori and Tanaka, 1973 and Benveniste, 1987). These predictions were compared to the experimental results. Dvorak (1991) provides a summary of the state of the art in plasticity theories for fibrous composite materials, extensive references, and summarizes the experimental results discussed above. Only the PHA model, with it's reliance on finite element analysis, was able to quantitatively predict the size and location of the current yield surface under a complex incremental load path. The interfacial bond between boron and aluminum is strong and no damage was observed experimentally until a very large number of load increments had been applied to the tube. Even then, the researchers were unable to conclusively determine that damage had occurred. Damage was not considered in any of the above analyses.

Aboudi (1987a and 1991) has incorporated the viscoplastic theory of Bodner and Partom (1975) and (1987) into the method of cells micromechanical model to predict inelastic composite response due to matrix plasticity. The Bodner-Partom viscoplasticity theory describes the material behavior with five parameters. Either isotropic or anisotropic hardening can be considered. The theory is a unified viscoplasticity theory in that no yield criterion is used. In order to predict initial yield surfaces with the method of cells, Pindera and Aboudi (1988) have included the Mises yield criterion in the model. Aboudi (1991) has demonstrated the versatility and accuracy of the method of cells through correlation with experimental data.

MMC are known to exhibit viscoplastic response, particularly at elevated temperatures (Arnold, et al., 1992). Numerous theories have been developed to describe the viscoplastic response of initially isotropic metallic materials. Freed and Walker (1991) provide a representative bibliography of work done in the field of viscoplasticity of initially isotropic metallic materials prior to presenting their own viscoplastic theory based on thermodynamics. In order to predict the viscoplastic response of MMC it is necessary to use a model that allows the matrix to be described by viscoplastic constitutive equations.

Eggleston and Krempl (1992) observed that creep of [90] SiC/Ti at elevated temperature was generally faster than that of the monolithic titanium alloy. They used the unified viscoplasticity theory based on overstress (VBO) (Majors and Krempl, 1991) to model the matrix response. Both perfect and weak fiber/matrix bonding were considered using a finite element model of a repeating unit cell. They concluded that debonding had occurred during the experiments, and had increased the composite creep rate.

1.1.2 Damage

Long before the current interest in damage to MMC, Adams (1974) considered the transverse tensile loading of a unidirectional composite using a square repeating cell finite element model. The plane strain analysis included matrix plasticity and thermal residual stresses. A finite element scheme was used whereby once an element reached its ultimate strength it was removed from the analysis by setting its material properties equal to zero. A degraded fiber/matrix interface was modelled by reducing the strength of the layer of matrix elements immediately adjacent to the interface. Numerical results indicated that a crack initiates at the interface, propagates partially around the fiber and then across the matrix.

While damage mechanics has been studied for some time, until quite recently imperfections in MMC have commonly been neglected. Benveniste (1985) discussed fundamental concepts in the theory of elasticity of composite materials in the presence of displacement discontinuities at constituent interfaces. Representative volume averages were redefined, and average stress and strain fields were reconsidered under these new definitions. The dual average stress, average strain approach taken yields the result that the effective stiffness tensor is not necessarily the inverse of the effective compliance tensor.

Damage to the fiber/matrix interfacial zone of a MMC has recently been discovered to have significant, deleterious effects on the overall composite response and has been the subject of much current study. Damage, in the form of interfacial debonding, in a titanium alloy matrix reinforced with silicon carbide fibers was first experimentally observed and reported by Johnson, et al. (1990). The experimental study involved applying tensile loading to five different laminates, most containing off-axis plies. Bond failure was observed as a separation between the fiber and matrix in off-axis plies using the edge replica technique. For a $[90_8]$ specimen the initial nonlinearity (knee) in the stress-strain response occurred at the far field stress of 23 ksi; subsequent load cycles produced a knee at the stress of 16 ksi. Edge replicas taken under load revealed that the knee corresponded with fiber/matrix separation, not plasticity. Replicas taken after the removal of the load revealed no separation. The authors postulated that the initial knee corresponded to the actual breaking of the fiber/matrix bond, whereas the knee observed in subsequent cycles was associated with overcoming the thermal residual stresses created in the fabrication process.

In a three part series of papers, Benveniste, et al. (1989, 1991) and Chen, et al. (1990) developed a micromechanical model for predicting stress fields and effective

thermoelastic properties of composites with coated fibers. In the first paper (Benveniste, et al., 1989), the authors use a variant of Benveniste's (1987) restatement of the Mori-Tanaka method to evaluate local fields and overall thermomechanical properties of composites reinforced with coated fibers or particles. Local fields in a coated inclusion are approximated by those found when the coated inclusion is embedded in an unbounded matrix material subjected to the average stresses (or strains) at infinity. This approach allows local fields in the inclusion, coating, and adjacent matrix to be evaluated by using the solution of a single coated inclusion in an infinite matrix. The assumed microstructure in the model is that the matrix phase is continuous. In the application of the model, the fiber and coating constituents are restricted to that of a coating encapsulating a fiber or particle. All constituents are restricted to being isotropic. The second paper (Chen, et al., 1990) extended the model to include cylindrically orthotropic fibers and transversely isotropic coatings and matrices. The third paper (Benveniste, et al., 1991) attempted to provide a framework for computation of the effective thermomechanical moduli of composites reinforced with curvilinearly anisotropic, coated inclusions. It also analytically established the diagonal symmetry of the predicted stiffness tensor.

An aluminum matrix reinforced by unidirectional silicon carbide fibers subjected to transverse tension was studied by Wisnom (1990). The effects of fiber spacing, fiber packing geometry, thermal residual stresses, interfacial strength, and matrix material properties were evaluated with respect to the transverse tensile strength. A generalized plane strain finite element analysis was implemented using a repeating cell model. Rectangular, diamond and single ply microstructures were considered. The Mises yield criterion was used and isotropic hardening assumed for the matrix. Interface elements were formulated to model the fiber/matrix interface as brittle. Perfect bonding was assumed to exist until a state of stress was reached when the interface failed. Compressive

interface failure and frictional slip were not considered. A quadratic interaction equation was used for the case where both tensile and shear stresses were significant.

$$(\sigma/\sigma_f)^2 + (\tau/\tau_f)^2 = 1 \tag{1.1}$$

σ and τ are the normal and shear stresses across the interface, and σ_f and τ_f are the failure stresses for the interface in pure tension and shear, respectively. Of all the parameters studied, the interfacial strengths, σ_f and τ_f, were found to have the largest impact on the transverse composite strength. Also, thermal residual stresses were seen to be beneficial due to the compressive radial stress components at the interface. It was noted that residual circumferential stresses in the matrix were tensile. The aluminum matrix yielded during processing.

The effects of cracking and imperfect bonding in metal matrix composites has been incorporated in the micromechanical method of cells (Aboudi, 1991) by Aboudi (1987b, 1988, and 1989). The effective stress-strain response of MMC containing a doubly periodic array of cracks was predicted by Aboudi (1987b). The effect of cracking was incorporated by adopting a second order expansion of the displacement field which satisfies equilibrium as well as traction and displacement continuity. Imperfect bonding between the fiber and matrix was incorporated into the method of cells (Aboudi, 1988) through the flexible interface model of Jones and Whittier (1967). Interfacial decohesion was modelled by two parameters that represent displacement discontinuity at the interface in the normal and tangential directions. The derived constitutive equations yield closed form expressions for the effective elastic moduli. The equations were readily implemented for determining the thermomechanical response of viscoplastic MMC. The normal and tangential bonding parameters represent a thin elastic film between the fiber and matrix. Parameter values of zero correspond with perfect bonding, while as parameter values

approach infinity the condition of no bond is approached. Herakovich and Hidde (1992) showed that effective elastic moduli are degraded asymptotically, so it is possible to simulate the no bond, or totally debonded condition, using finite bonding parameters.

Aboudi (1989) presented closed form constitutive equations, based on the method of cells, for predicting the response of debonding, continuous fiber composites. An interfacial failure criterion based upon the cohesive strength of the interface was used. Frictional sliding occurs after interfacial shear failure if there is compression present at the interface. The model assumes perfect bonding until a critical shear stress has been reached, above which the fiber and matrix are allowed to slide along the interface. Sliding is governed by the frictional force, which is dependent on the coefficient of friction. The critical interfacial shear stress is a function of the normal interfacial stresses. Compressive normal stresses increase the bond strength, while tensile normal stresses reduce it. The effect of decohesion on effective composite response, initial yield surfaces, and strength envelopes was shown for a SiC/Ti composite.

Effective elastic properties and thermal expansion coefficients of unidirectional composites with imperfect interface conditions were evaluated by Hashin (1990) using the three-phase model (Christensen and Lo, 1979). The imperfect interface was treated as an interphase, and defined in terms of spring type constants relating interface displacement discontinuities (jumps) to tractions.

$$\begin{aligned} \sigma_n^{(f)} &= \sigma_n^{(m)} = D_n [u_n] \\ \tau_{nt}^{(f)} &= \tau_{nt}^{(m)} = D_t [u_t] \\ \tau_{nb}^{(f)} &= \tau_{nb}^{(m)} = D_b [u_b] \end{aligned} \tag{1.2}$$

Where n, t, and b denote a right handed coordinate system with n normal to the interface and b in the direction of the fiber. [ ] denotes a jump discontinuity, and D_n, D_t, D_b are spring constant type material parameters which have units of stress divided by length. An equivalent fiber concept was used to simplify the evaluation of effective axisymmetric elastic properties, axial shear modulus, and thermal coefficients, but a more complex analysis was required for the effective transverse shear modulus.

Achenbach and Zhu (1990) also assumed traction continuity at the fiber/matrix interface and allow for displacement dicontinuity in the interphase region. Again, tractions were assumed to be proportional to the corresponding displacement discontinuities. The transverse response of unidirectional composites was investigated using two different hexagonal arrays of fibers to account for two different fiber packing sequences. Symmetry considerations reduced the region that must be analyzed to a trapezoid and the boundary element method was used to solve the numerical problem. In a later paper Zhu and Achenbach (1991) included the effects of radial matrix cracks and interphase failure on transverse response. Interphase disbonds and radial matrix cracks were assumed to have the same periodicity as the fiber array. The interphase was modelled by radial and circumferential springs. A strain-energy density criterion was used for interphase failure. Here strain energy is given by:

$$U = \frac{\sigma_r^2}{2k_r} + \frac{\tau_{r\theta}^2}{2k_\theta} \tag{1.3}$$

Where U is the strain energy per interface area and k_r, k_θ denote the radial and circumferential interfacial stiffnesses, respectively. Disbond occurs if the strain energy exceeds a critical value. Radial matrix cracks are initiated using a tensile circumferential stress criterion and crack propagation is governed by fracture toughness. For a large critical interphase strain energy or a weak matrix, radial matrix cracking was predicted to

occur before interphase debonding. For a small value of critical interphase strain energy or a strong matrix, interphase failure was predicted to occur before radial matrix cracking took place.

Nimmer (1990) developed a very simple model for unidirectional MMC with weak interfaces based on the presence of thermal residual stresses. A square cell containing a square fiber subcell and two rectangular matrix subcells was used to approximate a square array of fibers reinforcing a metal matrix. For simplicity, the model assumes Poisson's ratio for both fiber and matrix are zero. Thermal residual stresses created in the cool-down process during fabrication arise due to the mismatch in coefficients of thermal expansion between the fiber and matrix constituents. In the MMC under consideration, the coefficient of thermal expansion of the matrix was larger than that of the fiber. Thus, compressive radial residual stresses were present after processing. No chemical bond was considered in the analysis, but a mechanical bond created by the compressive radial residual stresses must be overcome before the interface fails. This is what is frequently referred to in the literature as a weak bond. When sufficient transverse tension had been applied to overcome the residual stresses, a knee in the effective transverse stress-strain response was seen to occur. Results of this simple model were compared with results from a plane stress finite element analysis also conducted using the weak interface. Qualitatively, the same type of behavior was predicted by each approach. The nonlinear finite element analysis was based on a square array of fibers, and contact elements with the capability to represent Coulombic friction were used to model the fiber/ matrix interface. For compressive transverse loading, the matrix yielded before interfacial separation occurred at an interface location 90° away from where separation was observed under transverse tension.

The finite element micromechanical model discussed above was modified by Nimmer, et al. (1991) to represent a rectangular array of fibers by inclusion of an aspect ratio, then compared with experimental results for SiC/Ti-6-4 at three different temperatures. The constituents were assumed to be isotropic and homogeneous. Fiber properties were assumed to be linear elastic and temperature independent. The matrix was assumed to have temperature dependent elastoplastic material properties. The Mises yield criterion with kinematic hardening was used to represent the plastic response of the matrix. Time dependent matrix behavior was considered during the fabrication cool-down process. Large circumferential residual stresses which could lead to radial cracks growing from the interface in the matrix were predicted to occur. Agreement between predicted and experimental response was extremely close except in a few instances. The most notable disagreement occurred during unloading. The model predicted a more distinct knee upon unloading and permanent strains that were not observed experimentally.

The effect of fiber spacing on interfacial damage in SiC/Ti was studied by MacKay (1990). Back-scattered scanning electron microscopy techniques were used to study the condition of the composite in the as-fabricated and heat treated (in argon for 24 hr at 1100 °F) states as well as after 10,000 thermal cycles between 572 and 1022 °F. It was discovered that microscopic radial cracks existed in the fiber/matrix interface in the as-fabricated state. These cracks appeared to be the result of tensile thermal residual circumferential stresses in the matrix at the fiber/matrix interface. The microcracks tended to occur in the direction of the nearest neighboring fiber and were more prevalent for small fiber spacing rather than for large fiber spacing. The heat treatment created no further damage, but thermal cycling did.

The three-phase model (Christensen and Lo, 1979) and a square array generalized

plane strain finite element model were used by Highsmith, et al. (1990) to predict when fiber/matrix separation occurs in laminated SiC/Ti composites. Linear elastic fiber and matrix properties were used in both models. Their procedure was to use micromechanics to predict ply properties, then use lamination theory to determine overall and ply stresses and strains; finally, the ply stresses were input back into the micromechanical model to determine local stress and strain fields. Local matrix stresses at points along the interface as determined from the two models were compared. Thermal residual radial stresses at the interface are compressive. Separation was assumed to occur when the local radial stress at the interface is zero. Reasonably good agreement for the transverse response of unidirectional composites was demonstrated for the two models. The fiber/matrix separation predicted for transverse loading of a unidirectional composite agreed well with the experimental observation of a knee in the transverse response of a unidirectional composite. For laminates however, the predicted overall laminate stresses associated with fiber/matrix separation were extremely low and thermal residual stresses were nearly sufficient to cause separation. The experimentally observed knee occurred at a laminate stress much smaller than the load required to cause local yielding in the absence of fiber/matrix separation. This separation appeared to alter the local stress field and promote local matrix yielding.

Lerch and Saltsman (1991) conducted tension tests on seven different SiC/Ti laminates at room temperature and 1472 °F. Metallography was used to examine specimens prior to loading, after certain predetermined loads were applied, and after failure. Fractography was also conducted after failure. Fiber/matrix interfacial debonding, matrix microcracking, and fiber breakage were all visually observed damage mechanisms. Matrix plasticity was also detected. Fiber/matrix debonding was determined to be the most prevalent damage mechanism for laminates containing off-axis plies. Through comparison

of theoretical predictions with experimental data it was determined that some laminates had sufficiently high tensile thermal residual radial stresses present to cause partial debonding in the as-fabricated condition. Theoretical predictions from the vanishing fiber diameter model (Dvorak and Bahei-El-Din, 1982 and Bahei-El-Din and Dvorak, 1982) were compared with the experimental results. Debonding was simulated in the model by artificially reducing the fiber modulus to 3% of its original value at the stress when the knee in the response was experimentally observed. Reasonably good agreement between theory and experiment was obtained for the longitudinal stress-longitudinal strain response of $[0_8]$, $[90_8]$, and $[0/90]_{2s}$ laminates, but the longitudinal stress-transverse strain predictions did not correlate well with the experimental data.

An attempt to distinguish the inelastic deformation of a SiC/Ti composite due to damage from matrix plasticity was made by Majumdar and Newaz (1991, 1992a, 1992b) and Majumdar, et al. (1992) for tensile loaded unidirectional [0] and [90] specimens. To this end the authors used key experiments conducted at room and elevated temperature as well as exhaustive microstructural examinations. Results showed that the inelastic deformation of a [0] composite was primarily associated with matrix plasticity. The response of [90] composites subjected to tensile loading was separated into three distinct regions. Initially, an elastic response occurred. The slope of the stress-strain curve was then decreased and finally the stress remained constant with increasing strain. The degraded response in the second region was attributed to damage to the fiber/matrix interfacial zone, primarily in the form of debonding, but also due in part to radial cracking. The unloading stiffness was observed to be much reduced from the initial loading stiffness. Only a very small permanent strain was present upon complete unloading. While both matrix plasticity and further damage occurred in the third region, matrix plasticity was the dominant feature. The authors compared their experimental results with

predictions from three micromechanical models. For theoretical predictions of tests conducted at room temperature, zero interfacial strength was used and reasonably good correlation with experimental data was found. The authors suggested, however, that at elevated temperature there may be a bond strength associated with the interface.

The stiffness reduction of a unidirectional composite containing interfacial cracks under longitudinal shear loading was examined by Teng (1992). The composite cylinder assemblage (CCA) model (Hashin and Rosen, 1964 and Hashin, 1972) was employed to predict the shear moduli of a composite weakened by similar cracks along the entire length of the fiber, located symmetrically on either side of the fiber (180° apart). The fiber and matrix were taken to be homogeneous, isotropic, and linearly elastic. Due to the presence of the uniformly distributed interfacial cracks, the composite could no longer be considered transversely isotropic as in the perfectly bonded case. Thus, two effective longitudinal shear moduli exist. The resulting mixed boundary value problems led to systems of dual series equations, which were reduced to Fredholm integral equations of the first kind having a logarithmically singular kernel. The unknown functions were the shear tractions along the uncracked portions of the interface. Nondimensionalized results were presented for various fiber volume fractions and constituent shear modulus ratios.

McGee and Herakovich (1992) incorporated the interfacial constitutive equations developed by Needleman (1987a, 1987b, 1990a, 1990b, 1992) into the method of cells. These interfacial constitutive equations will be presented in Chapter 2 as they are an integral part of the present work. In order to incorporate these interfacial traction-displacement relations which are point-wise in nature into the method of cells, it was necessary to transform them into average quantities. This transformation must also account for fiber geometry differences between a round fiber and the square fiber subcell

used in the method of cells. A linear elastic square repeating cell micromechanics model was implemented using finite element analysis to determine a suitable transformation.

1.2 Problem Definition

Silicon carbide/titanium (SiC/Ti) composites are a type of MMC that is currently under consideration for various high temperature applications. These composites are typically fabricated at high temperatures. Due to the mismatch in coefficient of thermal expansion between SiC and Ti, residual thermal stresses are created during the cool-down process. Many of the SiC fibers currently in use have one or more Carbon/SiC coatings deposited on them before consolidation. This is done in an attempt to keep the reaction zone at the fiber/matrix interface from migrating into the fiber. The presence of these coatings can lead to a very poor bond between the fiber and matrix, thus making the debonding phenomenon very important in determining the inelastic deformation of this type of MMC.

Other damage mechanisms are also known to exist in MMC, namely radial matrix cracking and fiber breakage. While these two damage mechanisms are important, they appear to effect strength more than stiffness, whereas the focus of this study is on stiffness rather than strength. That is not to imply that damage induced strength degradation is not an important consideration in the design of MMC; clearly it is. However, strength degradation is not included in the scope of the current work. Thus, the focus will be on fiber/matrix interfacial debonding.

Metallic matrices are known to be elastic-viscoplastic in nature. In the present context, the term viscoplasticity refers to the path-dependent, time-dependent response associated with the dislocations of a particular alloy. It is noted that the thermomechanical

properties of common metallic matrices are generally temperature dependent as well.

The preceding literature review described many attempts to predict the inelastic response of damaged MMC for tensile loading applied transverse to the fibers, and one attempt to predict the inelastic response for axial shear loading. A few models have been presented that are capable of predicting inelastic response for general loading, but comparisons with experimental data were not made. To date, there is a scarcity of experimental results from any type of tests on MMC other than tension or compression. A relatively simple way to apply a general loading to a material is to use tubular specimens; this allows axial, torsional, internal pressure, and thermal loads to be applied either proportionally or in increments. However, MMC tubes are very difficult to fabricate and are therefore expensive. A limited number of $[0_4]$ and $[\pm 45]_s$ SiC/Ti tubes was available for the present study.

The goal of the current study is to develop an experimentally verified model capable of predicting the thermomechanical response of continuously reinforced metal matrix composites subjected to multiaxial loads in the presence of damage. The model is based on micromechanics and employs nonlinear lamination theory to determine the inelastic deformation of laminates. Constitutive relations for each lamina are determined from a micromechanics analysis that is performed numerically using the finite element method.

The representative cell of the micromechanical model is considered to be in a state of generalized plane strain, enabling a quasi two-dimensional analysis to be performed. Constant strain triangular elements are formulated with elastic-viscoplastic constitutive equations. Interfacial debonding is incorporated into the model through interface elements that use nonlinear interfacial traction-displacement relations. Debonding can occur normal

to the interface and in any tangential direction.

Theoretical predictions are compared with the results of an experimental program conducted on SiC/Ti tubular specimens. Multiaxial loadings included increments of axial tension, compression, torque, and internal pressure. Loadings were chosen in an effort to distinguish inelastic deformation due to damage from matrix plasticity, and separate time dependent effects from time independent effects.

CHAPTER 2

MODEL DEVELOPMENT

A model to predict the inelastic response of unidirectional and laminated MMC to thermomechanical loading is developed in the present chapter. In laminate analysis it is necessary to be able to describe the constitutive behavior of each lamina. This is done using micromechanics. Hence, the ingredients for the micromechanical model are presented first. The laminate analysis procedure is then developed. The implementation of the model is described in Chapter 3.

2.1 Micromechanics

Consider a composite with continuous fiber reinforcement aligned in the x- or 1-direction. The use of micromechanics dictates that constituent properties and geometries are explicitly considered. To do this it is necessary to replace the complex microstructure of the composite with a representative volume element (RVE). The use of an RVE presumes that the fibers are uniformly dispersed (statistically homogeneous) throughout the matrix phase. A sufficient quantity of both material phases must be used such that the response of the RVE is representative of the composite material at large. If the fibers are arranged in a doubly periodic rectangular array as shown in Fig. 2.1 it is sufficient to analyze one unit cell that contains a single fiber embedded in matrix material, provided the appropriate boundary conditions are applied. These boundary conditions will be discussed in Chapter 3. The present model treats the fibers as linear elastic and the matrix as elastic-viscoplastic. Fiber/matrix interfacial constitutive relations are used to model debonding.

2.1.1 Viscoplastic Model

Classical plasticity theory is rate independent. Time dependency is introduced through phenomenologically developed creep models. Thus, plasticity and creep are independent in the classical theory. Viscoplastic constitutive equations attempt to represent the interaction between plasticity and creep. The distinguishing feature between viscoplasticity and plasticity is that viscoplasticity admits states both inside and outside the yield surface, governed by the kinetic equation of state, whereas plasticity admits only states inside and on the yield surface, governed by the consistency equation. Consequently, the plastic strain rate is continuous from the elastic domain across the yield surface and into the inelastic domain of viscoplastic response (Freed, et al., 1993). Unified theories of viscoplasticity are based on the concept of considering both elastic and inelastic deformations to be generally nonzero at all stages of loading; therefore, no yield criterion is required. From a practical standpoint this greatly simplifies the analysis because one does not have to consider different criteria for loading elastically, inelastically, or unloading. Inelastic strains include time independent and time dependent

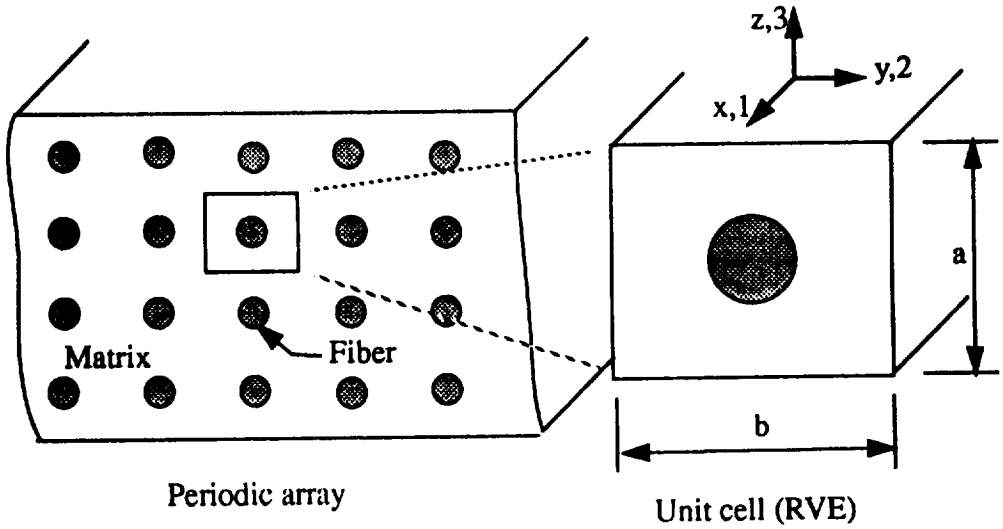

Figure 2.1: Repeating Unit Cell

components.

The elastic-viscoplastic constitutive model of Bodner and Partom (1975, and Bodner, 1987) is used in the current model and will now be presented. The total strain rate is assumed to be separable into elastic and inelastic components

$$\dot{\epsilon}_{ij} = \dot{\epsilon}_{ij}^{el} + \dot{\epsilon}_{ij}^{pl} \tag{2.1}$$

where the dot represents time differentiation. The elastic component is given by the time derivative of Hooke's law and the strain-displacement relationship

$$\dot{\epsilon}_{ij} = \frac{1}{2}\left(\frac{\partial \dot{u}_i}{\partial x_j} + \frac{\partial \dot{u}_j}{\partial x_i}\right) \tag{2.2}$$

The Prandtl-Reuss flow law is assumed to apply to the inelastic strain rate components.

$$\dot{\epsilon}_{ij}^{pl} = \Lambda s_{ij} \tag{2.3}$$

The stress deviators, s_{ij} are given by

$$s_{ij} = \sigma_{ij} - \frac{1}{3}\sigma_{kk}\delta_{ij} \tag{2.4}$$

where δ_{ij} is the Kronecker delta and repeated subscripts imply summation over 1,2, and 3. An expression for Λ can be found by squaring eqn. (2.3)

$$\Lambda^2 = D_2^{pl}/J_2 \tag{2.5}$$

where J_2 is the second invariant of the deviatoric stress

$$J_2 = \frac{1}{2}s_{ij}s_{ij} \tag{2.6}$$

and D_2^{pl} is the second invariant of the plastic strain rate

$$D_2^{pl} = \frac{1}{2}\dot{\epsilon}_{ij}^{pl}\dot{\epsilon}_{ij}^{pl} \tag{2.7}$$

The kinetic equation (*i.e.*, an equation of state) governs the inelastic deformations and is taken to be

$$D_2^{p'} = D_0^2 exp\left[-\left(\frac{Z^2}{3J_2}\right)^n\left(\frac{n+1}{n}\right)\right] \tag{2.8}$$

and Z is assumed to have the form

$$Z = Z_1 + (Z_0 - Z_1)\, exp\,[-m\,(W_p/Z_0)] \tag{2.9}$$

where Z_0 and Z_1 are material parameters and W_p is the plastic work.

Altogether there are five material parameters in the model. The parameter Z_0 is associated with the yield stress of the material in simple tension while Z_1 is proportional to the ultimate stress. The material parameter m determines the work-hardening of the material and the rate sensitivity is controlled by the parameter n. The constant D_0 defines the limiting strain rate for the material. These parameters are often determined from two simple tension tests conducted at different strain rates.

2.1.2 Damage Model

As indicated by the literature review, damage to the fiber/matrix interface has a significant effect on the response of MMC. The current section outlines the interfacial debonding model of Needleman (1987a) and an alternative model developed by Tvergaard (1990).

Debonding of the fiber/matrix interface plays a key role in limiting the ductility of a composite. Needleman (1987a, 1987b, 1990a, 1990b, 1992) has developed a cohesive zone model that describes the process of void nucleation from initial debonding through complete decohesion. The model provides independent constitutive relations for the

interface. With increasing interfacial separation the traction across the interface increases to a maximum, decreases, then vanishes so that complete decohesion occurs. Since the mechanical response of the interface is specified in terms of both a critical strength and the work of separation per unit area, dimensional considerations introduce a characteristic length.

Consider an interface supporting a traction field T which in general has normal and shear components. Two material points, initially on opposite sides of the interface, are considered and the interfacial traction is taken to depend only on the displacement difference Δu across the interface. At each point of the interface

$$u_n = n \cdot \Delta u \qquad u_t = t \cdot \Delta u \qquad u_b = b \cdot \Delta u \tag{2.10}$$

and

$$T_n = n \cdot T \qquad T_t = t \cdot T \qquad T_b = b \cdot T \tag{2.11}$$

where n, t, and b form a right-hand coordinate system as shown in Fig. 2.2. Positive u_n

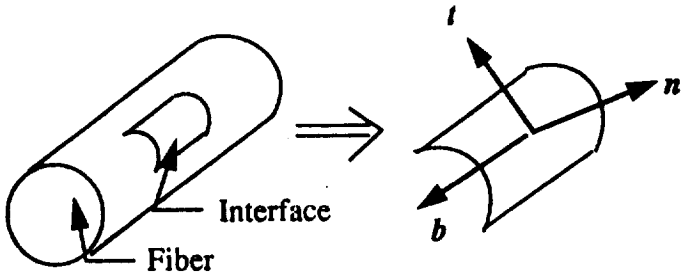

Figure 2.2: Interface Coordinate System

corresponds to increasing interfacial separation, u_t is tangent to the interface, and u_b is parallel to the fiber direction. The mechanical response is described in terms of a potential $\phi(u_n,u_t,u_b)$,

$$\phi(u_n, u_t, u_b) = -\int_0^u (T_n du_n + T_t du_t + T_b du_b) \tag{2.12}$$

A specific form frequently used (Needleman, 1987a, 1987b, 1990a) is

$$\begin{aligned} \phi(u_n, u_t, u_b) &= \frac{27}{4}\sigma_o \delta\Big[\frac{1}{2}u^2\left(1 - \frac{4}{3}u + \frac{1}{2}u\right) \\ &\quad + \frac{1}{2}\alpha(v^2 + w^2)\left(1 - 2u + u^2\right)\Big] \\ u &= \frac{u_n}{\delta} \qquad v = \frac{u_t}{\delta} \qquad w = \frac{u_b}{\delta} \end{aligned} \tag{2.13}$$

for $u_n \leq \delta$. Here σ_o is the tensile strength of an interface undergoing a purely normal separation, δ is a characteristic length, and α specifies the interfacial shear to normal strength ratio. When $u_n > \delta$, $\phi = \phi_{sep}$, where ϕ_{sep} is the work of separation. The work of separation serves to define the characteristic length δ. Thus, even though the characteristic length may not correspond to a physical length, it is a measurable quantity because the work of separation can be determined experimentally. The interfacial tractions are obtained by differentiation of the potential function, eqn. (2.13), to give

$$T_n = -\frac{27}{4}\sigma_o\left[u\left(1 - 2u + u^2\right) + \alpha(v^2 + w^2)(u - 1)\right] \tag{2.14}$$

$$T_t = -\frac{27}{4}\sigma_o \alpha v\left(1 - 2u + u^2\right) \tag{2.15}$$

$$T_b = -\frac{27}{4}\sigma_o \alpha w\left(1 - 2u + u^2\right) \tag{2.16}$$

Relative shearing across the interface leads to shear tractions, but the dependence of these tractions on u_t and u_b is linear. The traction magnitudes increase monotonically for negative u_n.

Other forms of the potential have been presented, including a combined trigonometric-exponential (Needleman, 1990b and 1992) and a double exponential (Needleman, 1992). Little is known about the validity of these specific interfacial

constitutive relations. The most detailed information comes from Rose, et al. (1981 and 1983), which indicates a universal exponential form of the traction-separation relation for coherent atomistically sharp interfaces.

The above model describes debonding by normal separation only. Tvergaard (1990, 1991, and 1993) proposed a model that describes debonding by tangential separation as well as normal separation. The model was implemented in an axisymmetric unit cell analysis, therefore it was only necessary to describe debonding in the normal, ***n*** and tangential, ***b*** directions. For the case of purely normal separation the model reduces to Needleman's (1987a) model. In general no potential exists for Tvergaard's (1990) alternative debonding model. The cohesive zone formulation is viewed as a phenomenological model, which represents the average effect of the debonding mechanisms. Once total debonding has occurred at a point along the interface, tangential tractions are accounted for by Coulombic friction.

The debonding model used in the present study is an extension of the Tvergaard alternative to the Needleman model. Here, interfacial displacements and tractions must also be included in the tangential, ***t*** direction, therefore a three dimensional analysis is required.

The first step in the development of the model is to assume that the condition of the bond can be described by one nondimensionalized parameter, λ.

$$\lambda = \begin{cases} \sqrt{(u_t/\delta_t)^2 + (u_b/\delta_b)^2} & \text{for } u_n \le 0 \\ \sqrt{(u_n/\delta_n)^2 + (u_t/\delta_t)^2 + (u_b/\delta_b)^2} & \text{for } u_n > 0 \end{cases} \tag{2.17}$$

Normal compressive tractions are considered not to be detrimental to the interface. In the most general case there are three characteristic lengths, δ_n, δ_t, and δ_b. Bond failure is represented by λ=1. For λ>1, the interface is only capable of transmitting compressive

normal tractions and frictional tangential tractions. A function F(λ) is chosen as

$$F(\lambda) = \frac{27}{4}\sigma_o(\lambda^2 - 2\lambda + 1) \tag{2.18}$$

For monotonically increasing loads the current value of λ is always the maximum value, λ_{max}. However, for unloading and reloading conditions the current value of λ can be less than the maximum value, λ_{max}, that may have occurred at some previous time in the load history. In order to prevent the interface from being self-repairing, which is physically unrealistic, it is necessary to set the current value of λ equal to the current maximum, $\lambda=\lambda_{max}$, in eqn. (2.18). For $\lambda_{max} < 1$, the interfacial tractions are then given by

$$T_n = \begin{cases} 10^6 (u_n/\delta_n) & \text{for } u_n \le 0 \\ F(\lambda_{max})\,(u_n/\delta_n) & \text{for } u_n > 0 \end{cases} \tag{2.19}$$

$$T_t = \alpha F(\lambda_{max})\,(u_t/\delta_t) \tag{2.20}$$

$$T_b = \alpha F(\lambda_{max})\,(u_b/\delta_b) \tag{2.21}$$

The normal traction, T_n has been made much stiffer than in Tvergaard (1990) for normal compression to minimize interpenetration of the phases.

For $\lambda_{max} \ge 1$, which signifies loading after the interface has failed and is only capable of transmitting compressive and frictional tractions, the interfacial tractions are given by

$$T_n = \begin{cases} 10^6 (u_n/\delta_n) & \text{for } u_n \le 0 \\ 0 & \text{for } u_n > 0 \end{cases} \tag{2.22}$$

$$T_t = \begin{cases} -\text{sgn}\,(du_t)\,\mu T_n & \text{for } |T_t| \ge \mu |T_n| \text{ and } u_n \le 0 \\ -4\mu T_n (u_t/\delta_t) & \text{for } |T_t| < \mu |T_n| \text{ and } u_n \le 0 \\ 0 & \text{for } u_n > 0 \end{cases} \tag{2.23}$$

$$T_b = \begin{cases} -\text{sgn}(du_b)\,\mu T_n & \text{for } |T_b| \geq \mu |T_n| \text{ and } u_n \leq 0 \\ -4\mu T_n (u_b/\delta_b) & \text{for } |T_b| < \mu |T_n| \text{ and } u_n \leq 0 \\ 0 & \text{for } u_n > 0 \end{cases} \tag{2.24}$$

where μ is the coefficient of kinetic friction and du_t, du_b are the current tangential interfacial displacement increments.

To demonstrate the interfacial constitutive relations four interfacial displacement loading cases are shown in Fig. 2.3 and 2.4. The normal and tangential displacement components presented in Table 2.1 are applied to a material point along an interface. Case #1 shown in Fig. 2.3a is first tensile, then compressive normal displacement loading. For increasing normal separation the normal traction, T_n, increases to a maximum then decreases to zero when bond failure occurs at λ=1 (u_n/δ=1 in this case). After bond failure only compressive tractions may be transmitted through the interface. The response to negative (compressive) normal displacements is quite stiff to minimize interpenetration of

Table 2.1: Displacement Loading

Case	Segment	Normal Displacement	Tangential Displacement
1	AB	0→120	0
	BC	120→0	0
	CD	0→-30	0
2	AB	0	0→120
	BC	0	120→0
	CD	0	0→-30
3	AB	0→50	0
	BC	50→0	0
	CD	0→120	0
4	AB	0→50	0→50
	BC	50→0	50
	CD	0→120	50

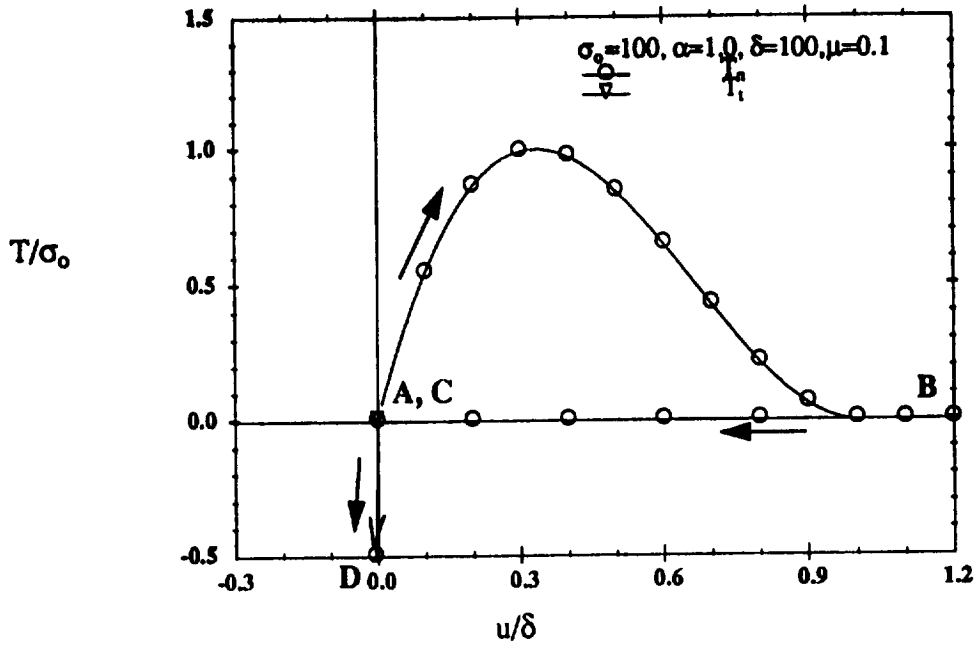

(a) Case #1

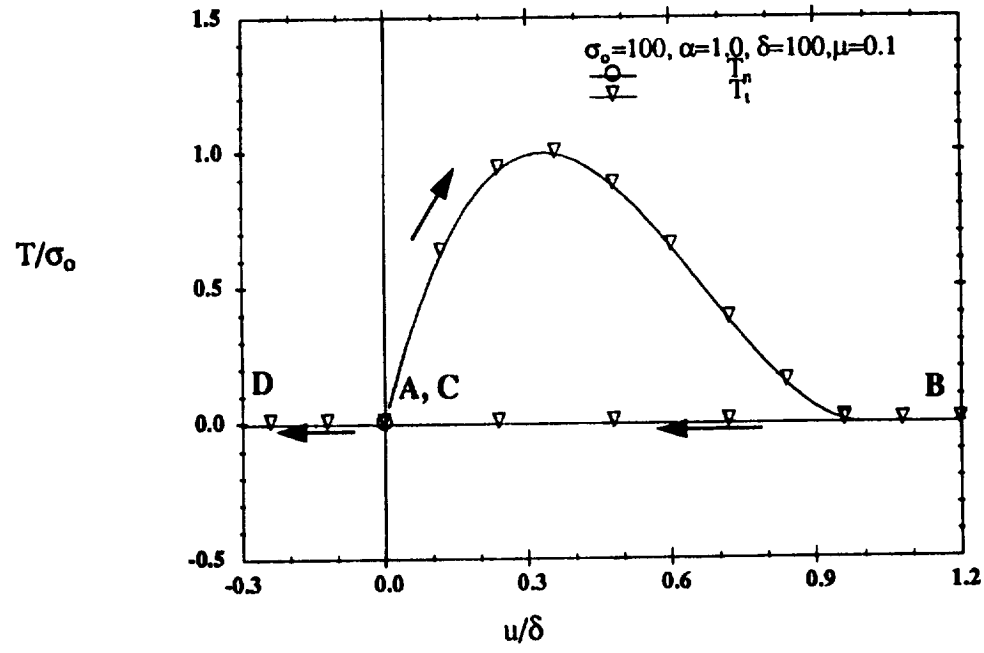

(b) Case #2

Figure 2.3: Interfacial Constitutive Relations

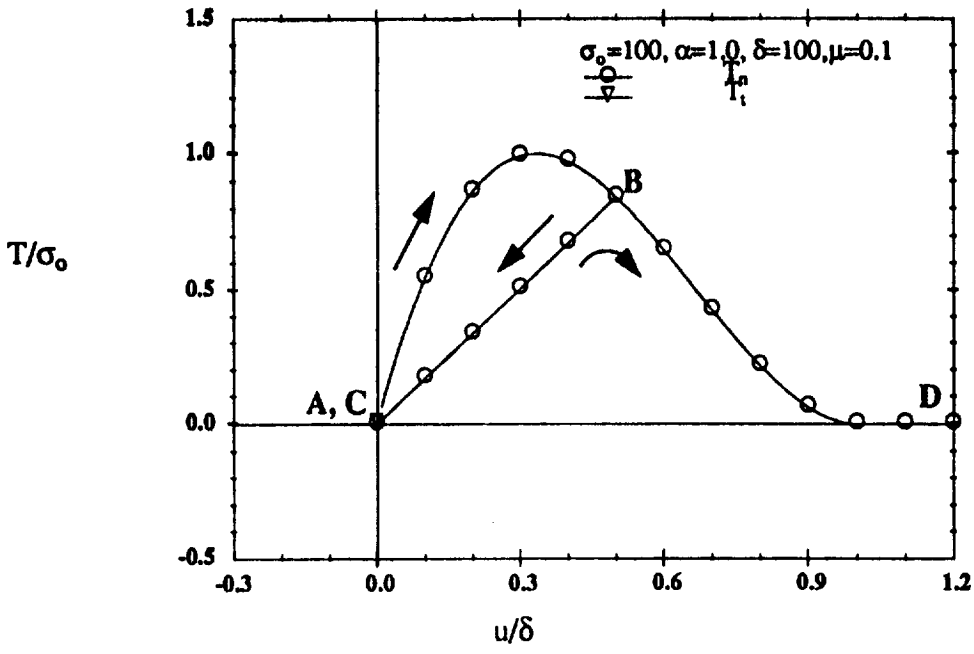

(a) Case #3

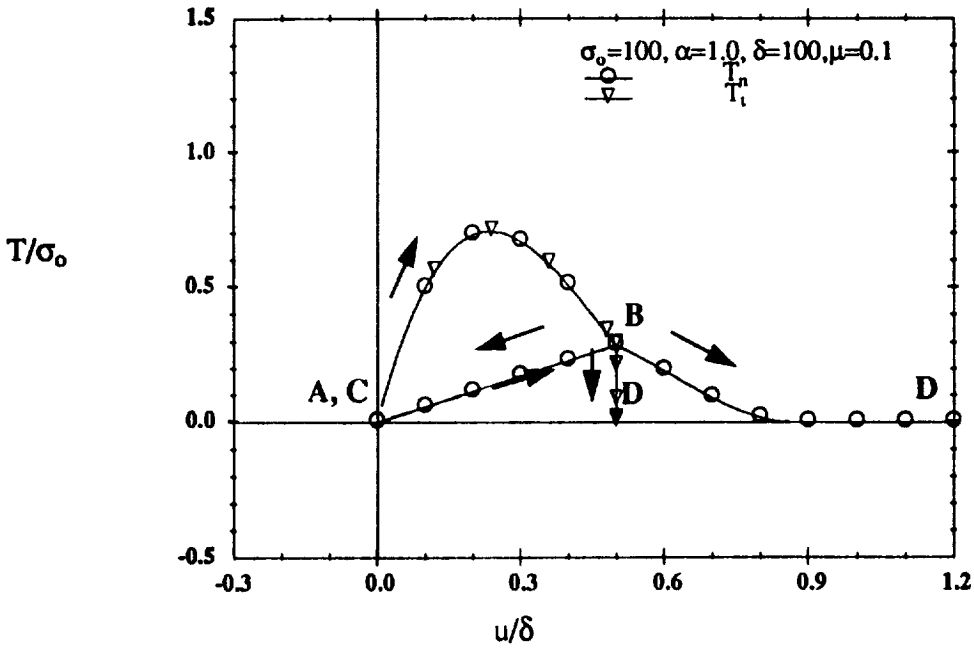

(b) Case #4

Figure 2.4: Interfacial Constitutive Relations

the fiber and matrix. Since no tangential displacements are applied the tangential traction, T_t, remains zero throughout the displacement history. Case #2 (Fig. 2.3b) is tangential displacement loading. The constitutive relations are similar for positive and negative tangential displacements. Once bond failure occurs, at $u_t/\delta=1$ in this case, no tangential tractions are present because there are no normal compressive tractions present. Case #3 (Fig. 2.4a) is tensile loading, unloading then reloading. Both unloading and reloading (below the previous maximum displacement) responses are linear, which demonstrates the use of λ_{max} in eqn. (2.21). Case #4 (Fig. 2.4b) is similar to Case #3 except tangential displacements are also applied. The maximum normal traction is reduced due to the interaction with tangential loading. Once the tangential displacement is held constant at point B the tangential traction remains constant for loading segment BC then decreases to zero in loading segment CD as the bond fails due to normal separation.

2.2 Laminate Analysis

Elastic as well as inelastic behavior of laminated composites can be predicted using nonlinear lamination theory (Hidde and Herakovich, 1992). The assumptions required for the nonlinear theory are the same as those for classical lamination theory (CLT):

(1) The laminae are assumed to be thin such that each lamina is in a state of plane stress (*ie*, $\sigma_{zz} = \tau_{xz} = \tau_{yz} = 0$).

(2) The Kirchhoff plate assumptions apply to the laminate. In particular,

(a) a line originally straight and perpendicular to the midplane of the laminate remains straight and perpendicular (*ie*, $\gamma_{xz} = \gamma_{yz} = 0$),

(b) normals to the midplane do not change length (*ie*, $\varepsilon_{zz} = 0$).

(3) Laminae are perfectly bonded.

The development of CLT is found in many composite mechanics textbooks (such as Jones, 1975) thus only the necessary ingredients will be presented here.

The stresses in the k^{th} ply can be expressed as

$$\begin{bmatrix}\sigma_{xx}\\ \sigma_{yy}\\ \tau_{xy}\end{bmatrix}^k = \begin{bmatrix}\bar{Q}_{11} & \bar{Q}_{12} & \bar{Q}_{16}\\ \bar{Q}_{12} & \bar{Q}_{22} & \bar{Q}_{22}\\ \bar{Q}_{16} & \bar{Q}_{26} & \bar{Q}_{66}\end{bmatrix}^k \left(\begin{bmatrix}\varepsilon_{xx}\\ \varepsilon_{yy}\\ \gamma_{xy}\end{bmatrix} - \begin{bmatrix}\varepsilon^T_{xx}\\ \varepsilon^T_{yy}\\ \gamma^T_{xy}\end{bmatrix} - \begin{bmatrix}\varepsilon^{NL}_{xx}\\ \varepsilon^{NL}_{yy}\\ \gamma^{NL}_{xy}\end{bmatrix} \right)^k \tag{2.25}$$

or simply

$$\{\sigma\}^k = [\bar{Q}]^k (\{\varepsilon\} - \{\varepsilon^T\} - \{\varepsilon^{NL}\})^k \tag{2.26}$$

where $\{\varepsilon\}$ denotes the total strains, $\{\varepsilon^T\}$ denotes the free thermal strains, and $\{\varepsilon^{NL}\}$ represents any nonlinear strains associated with plastic deformation or damage. For any ply the transformed reduced stiffness is defined:

$$\bar{Q}_{ij} = \bar{C}_{ij} - \frac{\bar{C}_{i3}\bar{C}_{j3}}{\bar{C}_{33}} \tag{2.27}$$

The transformed stiffness for any ply is determined to be:

$$[\bar{C}] = [T_1]^{-1}[C][T_2] \tag{2.28}$$

$$[T_1] = \begin{bmatrix} c^2 & s^2 & 2cs \\ s^2 & c^2 & -2cs \\ -cs & cs & c^2 - s^2 \end{bmatrix} \qquad [T_2] = \begin{bmatrix} c^2 & s^2 & cs \\ s^2 & c^2 & -cs \\ -2cs & 2cs & c^2 - s^2 \end{bmatrix} \qquad \begin{matrix}(c = \cos\theta)\\ (s = \sin\theta)\end{matrix} \tag{2.29}$$

where θ is the angle measured from the x-axis to the 1-axis as shown in Fig. 2.5. In general $[C]$ is the stiffness matrix for an orthotropic material. $[T_1]$ and $[T_2]$ are the stress and strain transformation matrices, respectively, associated with transforming quantities in material principal coordinates (1,2,3) to global coordinates (x,y,z). The notation used for the laminate and lamina is shown in Fig. 2.5. The global free thermal strains are determined from

$$\{\varepsilon^T\}^k_x = \{\alpha\}^k_x \Delta T = (|T_2|^{-1}\{\alpha\}_1)^k \Delta T \tag{2.30}$$

where $\{\alpha\}_1$ is the thermal expansion of the k^{th} ply in the material principal coordinate system and ΔT is a uniform temperature change.

The nonlinear strains are found from

$$\{\varepsilon^{NL}\}_x^k = (|T_2|^{-1}\{\varepsilon^{NL}\}_1)^k \tag{2.31}$$

and include nonlinear effects due to both damage and plasticity. The nonlinear strains in material principal coordinates, $\{\varepsilon^{NL}\}_1$, are determined from a micromechanics analysis as described in Section 2.1.

The total strains in each ply can be related to laminate quantities by

$$\{\varepsilon\}_x^k = \{\varepsilon^\circ\} + z^k\{\kappa\} \tag{2.32}$$

where $\{\varepsilon^\circ\}$ is the global midplane strain and $\{\kappa\}$ is the midplane curvature. At this point it is convenient to define several quantities. The resultant mechanical forces and moments acting on a laminate are

$$\{N, M\} = \int_{-H}^{H} \sigma_{xx}(1, z)\, dz \tag{2.33}$$

The equivalent thermal force and moment resultants are defined as

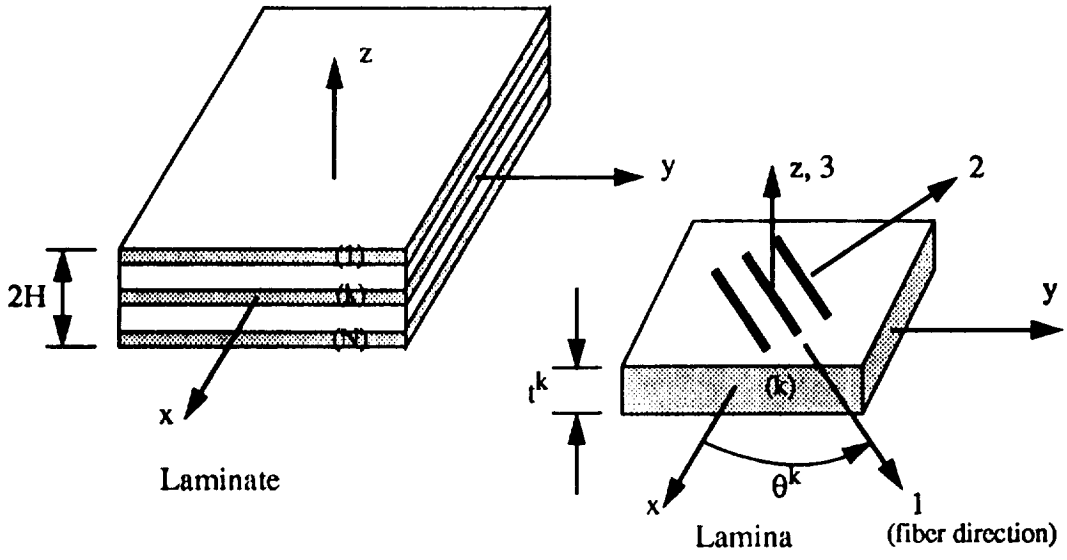

Figure 2.5: Laminate/Lamina Geometry

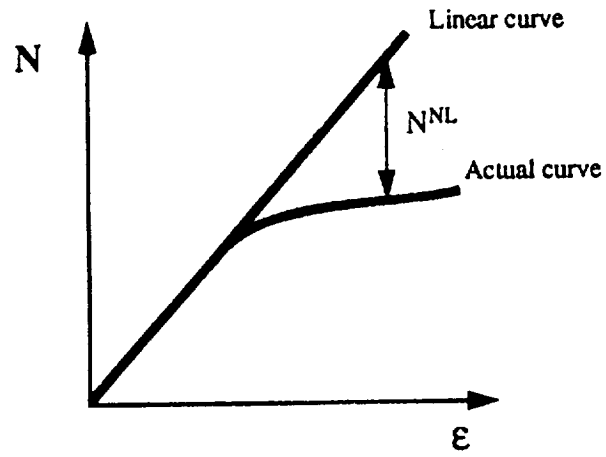

Figure 2.6: Nonlinear pseudo-force

$$\{N^T, M^T\} = \int_{-h}^{h} [\bar{Q}] \{\varepsilon^T\}_x (1, z)\, dz \tag{2.34}$$

Nonlinear pseudo-force and moment resultants represent the effects of plasticity and damage at any given time and are defined to be

$$\{N^{NL}, M^{NL}\} = \int_{-h}^{h} [\bar{Q}] \{\varepsilon^{NL}\}_x (1, z)\, dz \tag{2.35}$$

The term $\{N^{NL}\}$ is not a physical quantity, it is the difference between the actual resultant force-strain (N-ε) curve and the linear N-ε curve as depicted schematically in Fig. 2.6. A similar explanation applies to the pseudo-moment resultant. The laminate extensional, coupling, and bending stiffnesses, respectively, are defined:

$$[A, B, D] = \int_{-h}^{h} [\bar{Q}] (1, z, z^2)\, dz \tag{2.36}$$

Substituting the ply stresses, eqn. (2.26), into the resultant force and moment definitions, eqn. (2.33) and integrating through the thickness of the laminate yields

$$\begin{aligned} \{N\} &= [A] \{\varepsilon^\circ\} + [B] \{\kappa\} - \{N^T\} - \{N^{NL}\} \\ \{M\} &= [B] \{\varepsilon^\circ\} + [D] \{\kappa\} - \{M^T\} - \{M^{NL}\} \end{aligned} \tag{2.37}$$

where eqn. (2.32) has also been used to relate ply strains to laminate strains. Equation (2.37) can be written in the familiar compact form:

$$\begin{bmatrix} \bar{N} \\ \bar{M} \end{bmatrix} = \begin{bmatrix} A & B \\ B & D \end{bmatrix} \begin{bmatrix} \varepsilon^{\circ} \\ \kappa \end{bmatrix} \tag{2.38}$$

where

$$\begin{aligned} \bar{N} &= N + N^{T} + N^{NL} \\ \bar{M} &= M + M^{T} + M^{NL} \end{aligned} \tag{2.39}$$

For strain loading, solution of eqn. (2.38) yields the resultant forces and moments. If resultant forces and moments are applied the *ABD* matrix must be inverted. The effective laminate stresses are determined by dividing the resultant forces by the laminate cross-sectional area.

CHAPTER 3

MODEL IMPLEMENTATION

The viscoplastic and debonding models discussed in Chapter 2 are implemented numerically using the finite element method. The analysis of unidirectional composites is presented first. The method is then extended to laminated composites by employing nonlinear lamination theory.

Effective stress and strain fields in the unit cell under consideration are determined in accordance with Benveniste (1985), namely

$$\bar{\varepsilon}_{ij} = c_f \bar{\varepsilon}^f_{ij} + c_m \bar{\varepsilon}^m_{ij} - \frac{1}{2V}\int_S \left([u_i]\, n_j + [u_j]\, n_i \right) dS$$
$$\bar{\sigma}_{ij} = c_f \bar{\sigma}^f_{ij} + c_m \bar{\sigma}^m_{ij} \tag{3.1}$$

where the sub- and superscripts f and m refer to the fiber and matrix, respectively. Barred quantities are averages. The lower case c is the constituent volume fraction, V is the total volume, and S is the fiber/matrix interface. The outward normal to S is denoted by n_i. The jump in displacement across the interface, S is defined to be

$$[u_i] = u_i^f\big|_S - u_i^m\big|_S \tag{3.2}$$

The surface integral in eqn. (3.1) is evaluated numerically using Simpson's rule and displacement data from the nodes located along the interface.

3.1 Generalized Plane Strain

Consider a unidirectional composite material with continuous fiber reinforcement. If the fibers are arranged in a doubly periodic rectangular array as shown in Fig. 2.1 a single unit cell may be used as the representative volume element. Assume that the

composite is very long in the x (fiber) direction. Away from the ends, a state of generalized plane strain (Lekhnitskii, 1981) exists. The stress and strain fields are independent of the x coordinate. Displacements are allowed in all three coordinate directions. Each displacement is dependent on y and z coordinates and the displacement in the x direction is also linearly dependent on the x coordinate. Including the y and z dependence of the x displacement allows axial shear deformation to occur. In mathematical terms, the strain components are taken to be (Renieri and Herakovich, 1976):

$$\begin{aligned}
\varepsilon_{xx} &= \frac{\partial u}{\partial x} = f_1(y,z) \\
\varepsilon_{yy} &= \frac{\partial v}{\partial y} = f_2(y,z) \\
\varepsilon_{zz} &= \frac{\partial w}{\partial z} = f_3(y,z) \\
\gamma_{yz} &= \frac{\partial v}{\partial z} + \frac{\partial w}{\partial y} = f_4(y,z) \\
\gamma_{xz} &= \frac{\partial u}{\partial z} + \frac{\partial w}{\partial x} = f_5(y,z) \\
\gamma_{xy} &= \frac{\partial u}{\partial y} + \frac{\partial v}{\partial x} = f_6(y,z)
\end{aligned} \tag{3.1}$$

where u, v, w are displacement components in the 1-, 2-, 3-directions, respectively. Integration of the strain field yields the following displacement field:

$$\begin{aligned}
u(x,y,z) &= x(C_1 y + C_2 z + C_3) + U(y,z) \\
v(x,y,z) &= x(C_4 z + C_6) - C_1 \frac{x^2}{2} + V(y,z) \\
w(x,y,z) &= x(-C_4 y + C_5) - C_2 \frac{x^2}{2} + W(y,z)
\end{aligned} \tag{3.2}$$

where C_1 through C_6 are unknown constants and U, V, and W are unknown functions of y and z. A similar formulation was used by Adams and Crane (1984) to predict the response of unidirectional glass/epoxy and graphite/epoxy composites to combined loading.

3.2 Finite Element Formulation

The representative volume element (RVE) shown in Fig. 2.1 is analyzed using the finite element method. Due to material symmetry it is sufficient to model a quarter of the RVE. Considering the RVE to be in a state of generalized plane strain permits the use of a two dimensional model while retaining three dimensional stress and strain fields. Thus, very general combined thermomechanical loading may be applied.

The finite element analysis is conducted using the commercially available general purpose ABAQUS finite element code (Hibbitt, Karlsson, and Sorensen, Inc.,1989) which uses the Newton method to solve a nonlinear system of equations. Both material and geometric nonlinearities may be considered. User elements may also be defined through user subroutines, as is done in the current analysis.

The quarter of the RVE to be analyzed is discretized as shown in Fig. 3.1. Of course any discretization is permissible and the finer the mesh is made, the better the results will be. The trade-off is that as the mesh is made finer, the run time increases. The mesh used in this analysis was chosen because it was fairly coarse, with 68 solid elements and 8 interface elements, and yet still gave reasonably accurate predictions for the effective elastic properties. The dimensions a and b were determined from the packing sequence of the composite under consideration and thus represent the fiber volume fraction.

Boundary conditions for thermal, axial, transverse, and axial shear loadings are also shown in Fig. 3.1. Symmetry dictates that there is no y-displacement along the line y=0 and that there is no z-displacement along the line z=0. Rigid body motion is prevented in the x-direction by restraining the origin. Compatibility with the surrounding material

requires the *y*- and *z*-displacements to be constant along the lines $y=b$ and $z=a$, respectively. Loads are applied to the RVE through displacement loading. Axial load is applied by displacing the common node, which will be discussed in the following section, in the *x*-direction. Transverse load is applied by displacing the line $y=b$ in the y-direction. Axial shear loading is simulated by displacing the line $y=b$ in the x-direction and constraining the x-displacement of the line $y=0$. Thermal loading is applied by subjecting the entire mesh to a uniform temperature change.

Transverse shear loading can be applied to the quarter fiber model, but different boundary conditions are required. Antisymmetric boundary conditions must be used along the lines $y=0$ and $z=0$ in place of the symmetric boundary conditions previously discussed. Compatibility with the surrounding material requires that the edges located at

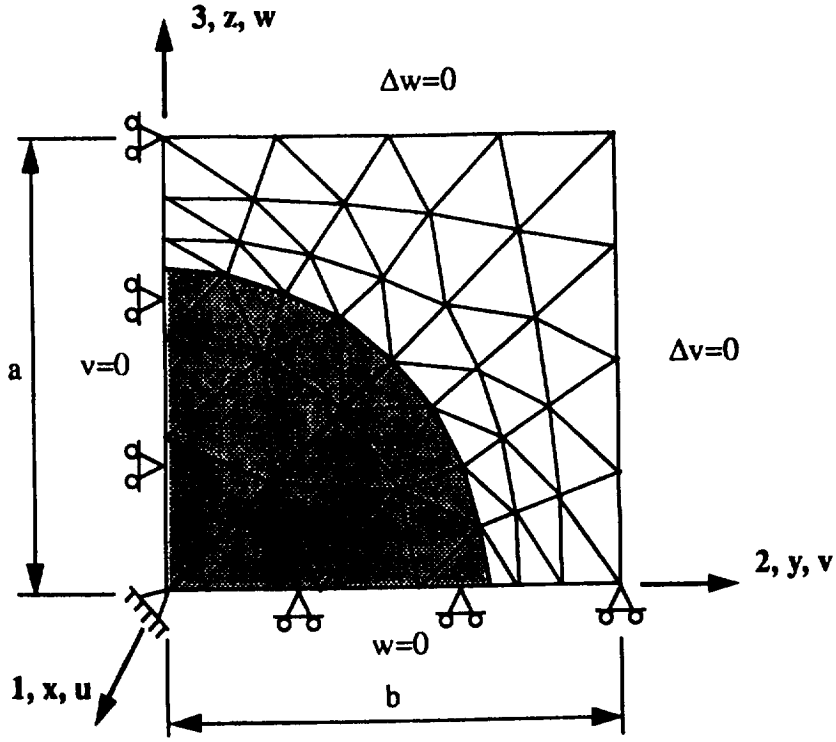

Figure 3.1: Finite Element Mesh

$y=b$ and $z=a$ remain straight. Transverse shear loading is simulated by displacing the edge $z=a$ in the y-direction. Due to the different boundary conditions required for transverse shear loading it can not be combined with the other types of loading discussed. Transverse shear loading is not required for the analysis of laminates due to the assumption of plane stress used in lamination theory. Thus transverse shear loading will not be considered in the remainder of this work.

3.2.1 Solid Elements

Constant strain triangular solid elements are formulated in Appendix A for the condition of generalized plane strain. Both the fiber and matrix are assumed to be isotropic. The elastic-viscoplastic constitutive relations of Bodner-Partom presented in Chapter 2 are used to describe the material behavior. The three corner nodes of each element have three degrees of freedom. The novelty of these elements is that each element has an additional node. Elements in the mesh must be numbered such that the last node specified for each element is the 'common node' located at the centroid of the RVE. The only degree of freedom associated with the common node is in the x-direction, therefore each element is constrained to a constant axial strain.

3.2.2 Interface Elements

Smelser and Becker (1989) developed a user subroutine for interface elements to be used with the ABAQUS program. The user subroutine is for either plane strain or axisymmetric problems and uses the interfacial constitutive relations of Needleman presented in Chapter 2. The interface elements have four nodes, two nodes connect to material points on either side of the interface. The element stiffness matrix is defined

$$K^{NM} = \frac{\partial F^N}{\partial u^M} \tag{3.3}$$

where F^N is the force contributed by the element to degree of freedom N and u^M is the displacement at degree of freedom M. The formulation is currently extended to account for debonding in the normal as well as both tangential directions. The modifed Tvergaard alternative debonding model presented in Chapter 2 was implemented in lieu of the Needleman model. The derivation is summarized in Appendix B.

3.4 Laminate Analysis

For the present purposes the current laminate analysis is restricted to thermal and in-plane mechanical loading of flat symmetric laminates. Therefore no curvatures, $\{\kappa\}$, are present and the coupling stiffness, $[B]$, is zero. Thermal loads are applied by specifying a uniform temperature change over the entire laminate. Any combination of laminate midplane strains, ε_{xx}, ε_{yy}, γ_{xy} may be applied as the mechanical loading.

The analysis of a laminate is initiated by using the micromechanical model presented in Sections 2.1, 3.1, and 3.2 to determine the thermomechanical properties of the laminae. These properties, along with the loading specifications, are used as input to the nonlinear lamination theory (NLLT) to determine both laminate and laminae stresses and strains. The midplane strains and effective laminate stresses are the desired output. The strains in each lamina are input back into the micromechanical model to determine the nonlinear strains. Because the strains in the material principal coordinate system are, in general, different for each lamina and because the interfacial constitutive relations are history dependent each lamina in the laminate has its own unit cell associated with it. The nonlinear strains for the first increment are zero. In all subsequent increments the nonlinear strains from the previous increment are used. Figure 3.2 presents a simplified schematic of the incremental laminate analysis procedure.

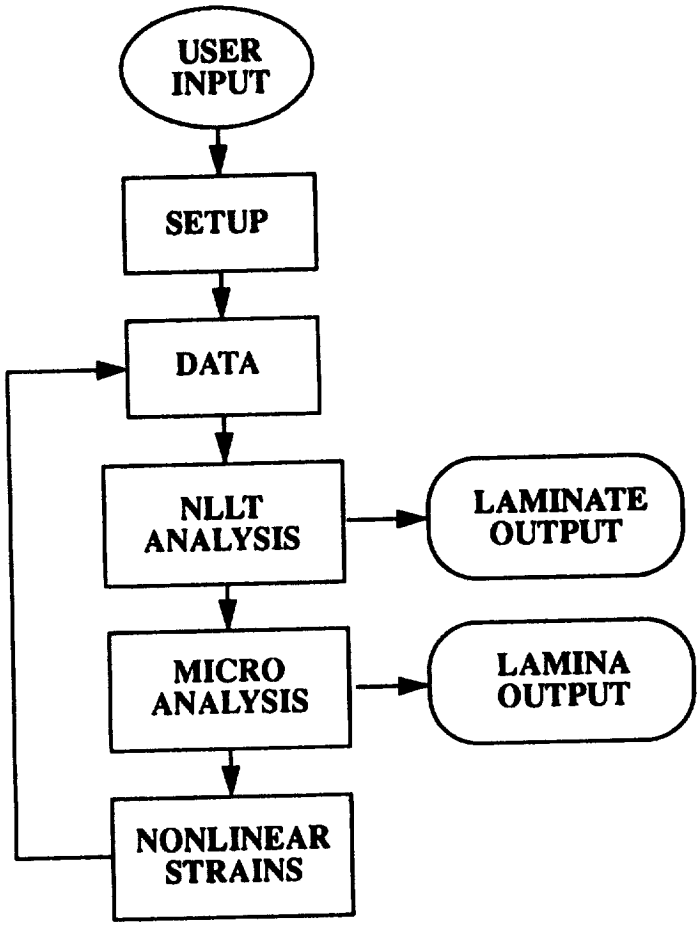

Figure 3.2: Laminate Analysis Schematic

CHAPTER 4

MODEL PREDICTIONS

In this chapter predictions from the model discussed in Chapters 2 and 3 are presented first for unidirectional composites and then for angle-ply laminates. In some instances predictions based on the method of cells (Aboudi, 1991) are also presented for comparison. All predictions are for a titanium matrix reinforced with 40% silicon carbide fibers by volume. The thermomechanical constituent properties used here and for the remainder of this work are listed in Table 4.1.

Table 4.1: Constituent Properties

Matl	Thermo-elastic			Bodner-Partom				
	E	ν	α	D_0	Z_0	Z_1	m	n
	(Msi)		μ(1/°F)	(1/sec)	(ksi)	(ksi)		
SiC	58	0.25	2.77	0	-	-	-	-
Ti	13.2	0.36	5.14	10000	140	170	1700	7

4.1 Unidirectional Composites

To illustrate the capability of the generalized plane strain model and provide a baseline for comparisons consider first the case of perfect bonding between fiber and matrix. Consider also the case of no interfacial bonding. Using the perfect bond and no bond assumptions provides limiting conditions on the effective response of the composite. Perfect bonding is achieved by requiring a continuous displacement field across the fiber/ matrix interface. The condition of no interfacial bond is simulated by setting the interfacial strength, σ_0, equal to zero and the parameter, λ, which describes the condition of the bond, equal to unity.

The method of cells predictions for no interfacial bond are based on imperfect bonding using the flexible interface model (Aboudi, 1988). The no bond condition was approximated by making both normal and tangential bonding parameters quite large (R_n = R_t = 1), this effectively created a cavity in the matrix rather than a debonded inclusion.

4.1.1 Combined Loading

One of the primary goals of this work is to describe the response of MMC subjected to general loading. Therefore combined loadings as well as uniaxial loads will be applied to the unit cell model as designated below:

-x: uniaxial loading in the fiber direction
-y: uniaxial loading transverse to the fiber
-xy: axial shear loading
-x-y: combined axial and transverse loading
-x-xy: combined axial and axial shear loading
-y-xy: combined transverse and axial shear loading
-x-y-xy: combined axial, transverse, and axial shear loading

The reader is reminded that the material principal coordinate system (1, 2, 3) for the unidirectional composite considered here corresponds directly with the global coordinate system (x, y, z), where the 1- and x- directions are in the fiber direction.

Predictions from the unit cell model as well as from the method of cells (Aboudi, 1991) are shown in Figs. 4.1-4.4, where FE denotes the current finite element unit cell model and MC denotes the method of cells. The stiffness tensor obtained from the method of cells has not been transformed to that of a transversely isotropic material because the unit cell model is not transversely isotropic.

The axial response to the four loading conditions that include axial loads is shown in Fig. 4.1a for perfect bonding and Fig. 4.1b for no interfacial bond. Excellent agreement is observed between the two models for both the perfect and no bond cases. The only

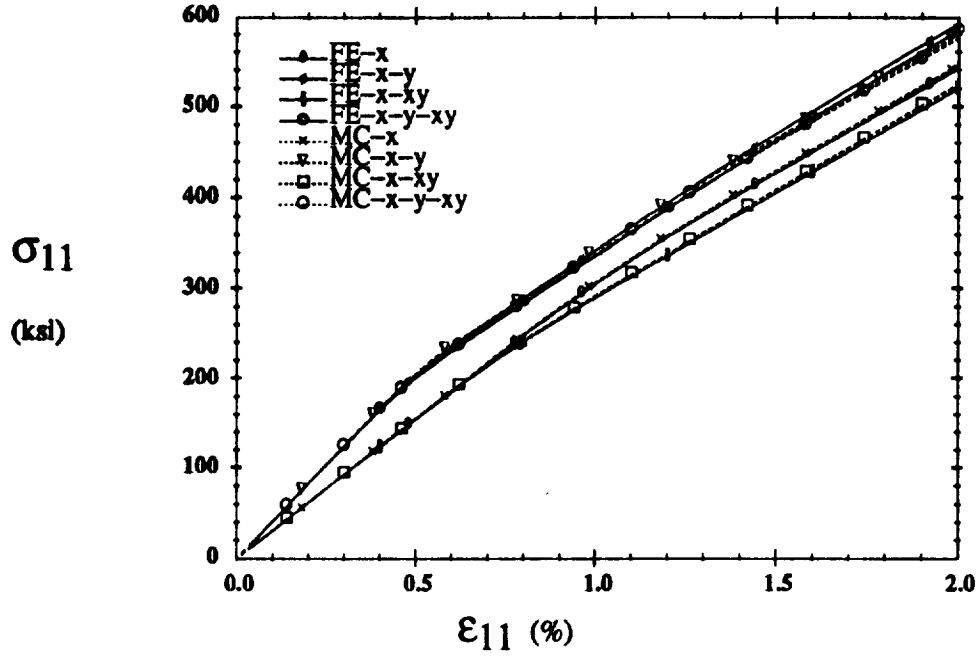

(a)Perfect Bond

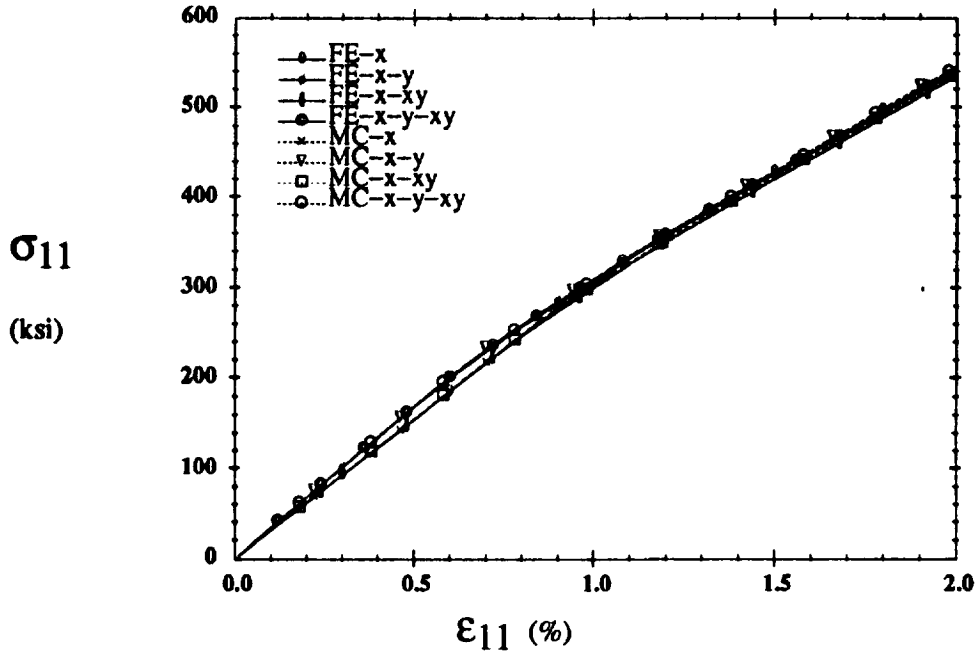

(b)No Bond

Figure 4.1: [0] Predicted Axial Response

variation between the models occurs for load cases that include transverse loading. The only significant difference between the axial response of unidirectional composites with a perfect fiber/matrix bond and those with no bond is when transverse loads are applied. It is noted that the axial stiffness of the composite, defined by the loading ($\sigma_{11} \neq 0$, $\sigma_{ij} = 0$ for all others) is not represented by the initial slope of the response for load combinations that include transverse loads due to the presence of the transverse stress σ_{22}.

The transverse tensile response is shown in Fig. 4.2 for the load cases that include transverse tension. The response of a composite with no bond is very different from that of a perfectly bonded composite, and in fact, is so large that a different vertical scale is used. The two models agree quite well for perfect bonding with only relatively small differences observed in the plastic region. However, for no bond the traction continuity requirements imposed by the method of cells force the transverse stresses in one matrix subcell to be equal to those in the fiber subcell, which are zero in this case. Hence, a lower stiffness is predicted.

Figure 4.3 presents the transverse compressive response for those load cases that include transverse compression. Again, the two models agree well for perfect bonding. On the other hand, poor agreement is observed for transverse stiffness for the case of no interfacial bond. In addition to what was just discussed for transverse tensile loading, the bonding assumptions used here for the method of cells predictions effectively remove the fiber from the composite, such that it can support no tractions. The unit cell model allows the fiber to behave like a debonded inclusion and support compressive tractions.

For perfect bonding the unit cell model predicts a slightly stiffer axial shear response in the elastic region than the method of cells (Fig. 4.4a). In the inelastic region this difference is magnified. Similar to the transverse tensile response, the method of cells

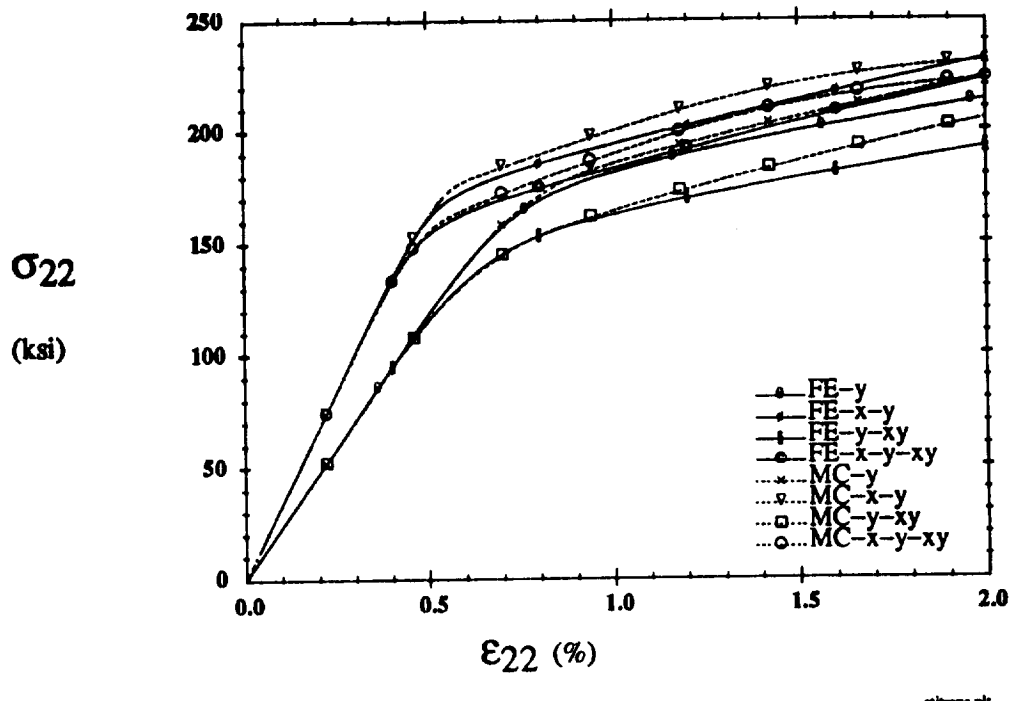

(a)Perfect Bond

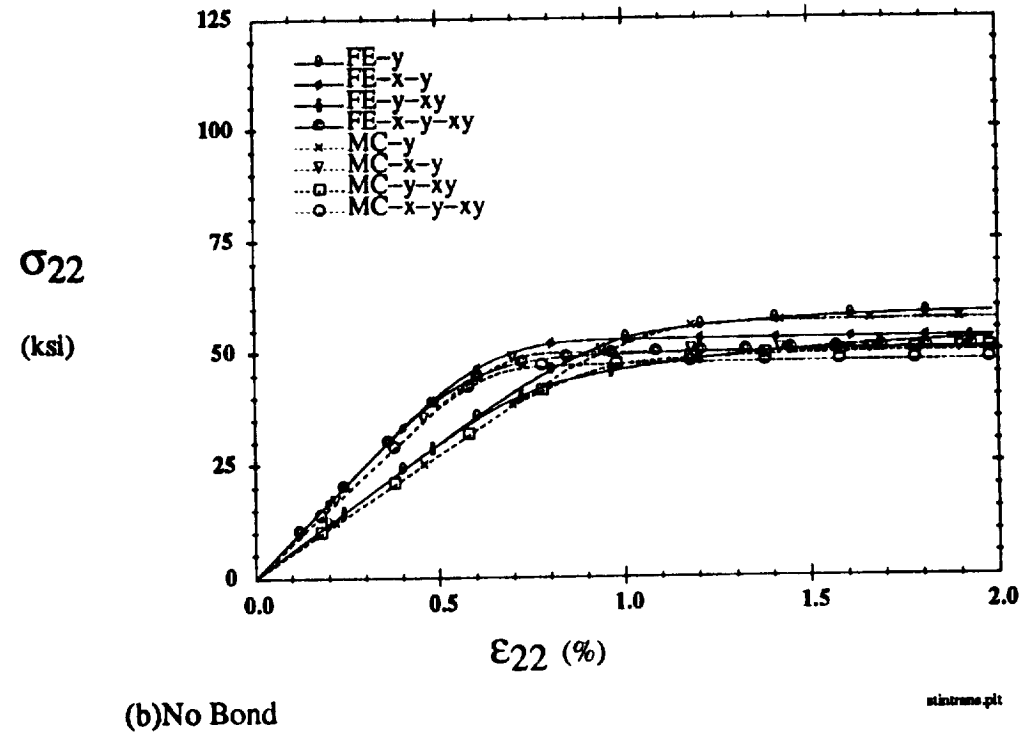

(b)No Bond

Figure 4.2: [0] Predicted Transverse Tensile Response

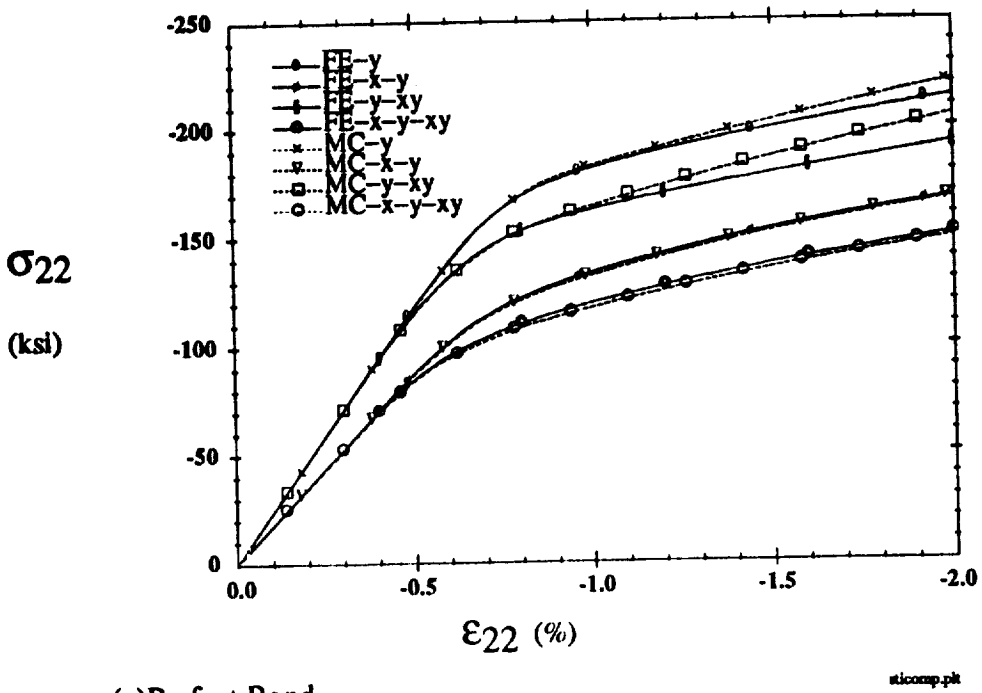

(a)Perfect Bond

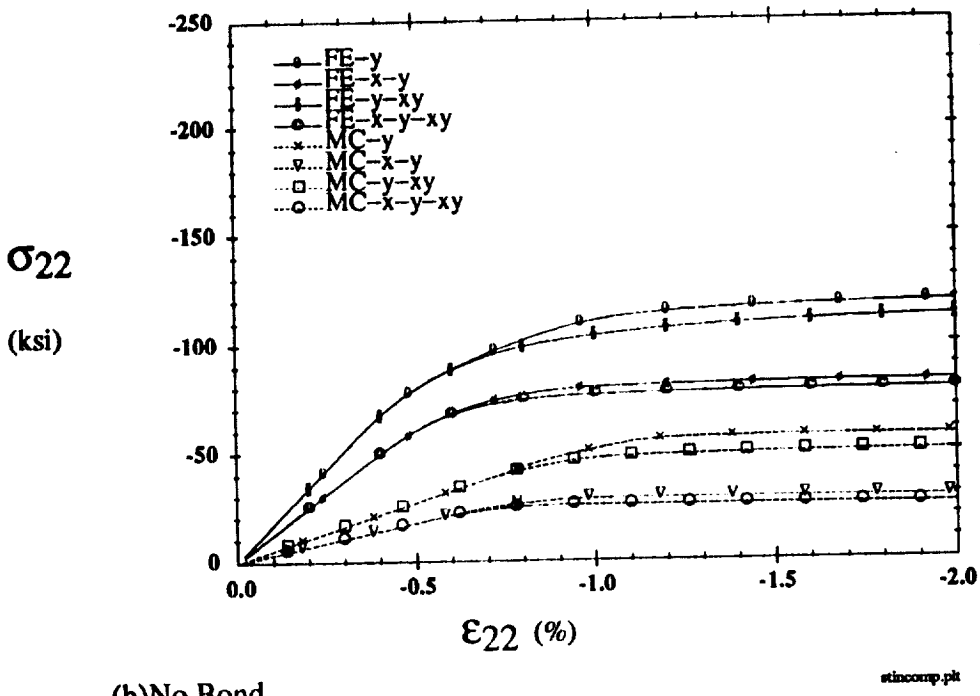

(b)No Bond

Figure 4.3: [0] Predicted Transverse Compressive Response

predicts a more compliant response than the unit cell model for no bond between the fiber and matrix (Fig. 4.4b.). In fact, the agreement for simple axial shear loading (-xy) is not very good for the no bond condition.

4.1.2 Interfacial Parameter Study

The interfacial properties used in the current debonding model (Sect. 2.1) are related to physical quantities that can, in theory at least, be measured. σ_0 is the maximum tensile stress that the interface can sustain under simple tension. The shear-to-normal strength ratio, α, can be found by determining the shear strength of the interface. The characteristic length, δ, can be calculated from the work of separation, which is the area under the interfacial stress-strain curve up to complete bond failure. A small value of δ represents a brittle interface, while a large value represents a ductile interface. μ is simply the coefficient of friction between the two surfaces of a failed interface.

Actually determining these interfacial properties for real fiber/matrix interfaces could be quite difficult due to the small size of the fibers. For example, the SCS-6 fiber is considered to be relatively large and it has a diameter of 0.0057 in. Of course, fiber coatings and how they are applied to the fiber are extremely important in determining the interfacial properties. In light of this, the interfacial properties are treated as parameters that describe mechanical response of the interface. The characteristic lengths are assumed to be equal, $\delta_n = \delta_t = \delta_b = \delta$.

Figures 4.5 through 4.8 present the results of a parametric study undertaken to determine the effects of the interfacial properties on the response of a unidirectional composite. Axial, transverse tensile, transverse compressive, and axial shear loadings are considered individually for this parametric study. As previously mentioned, the perfect

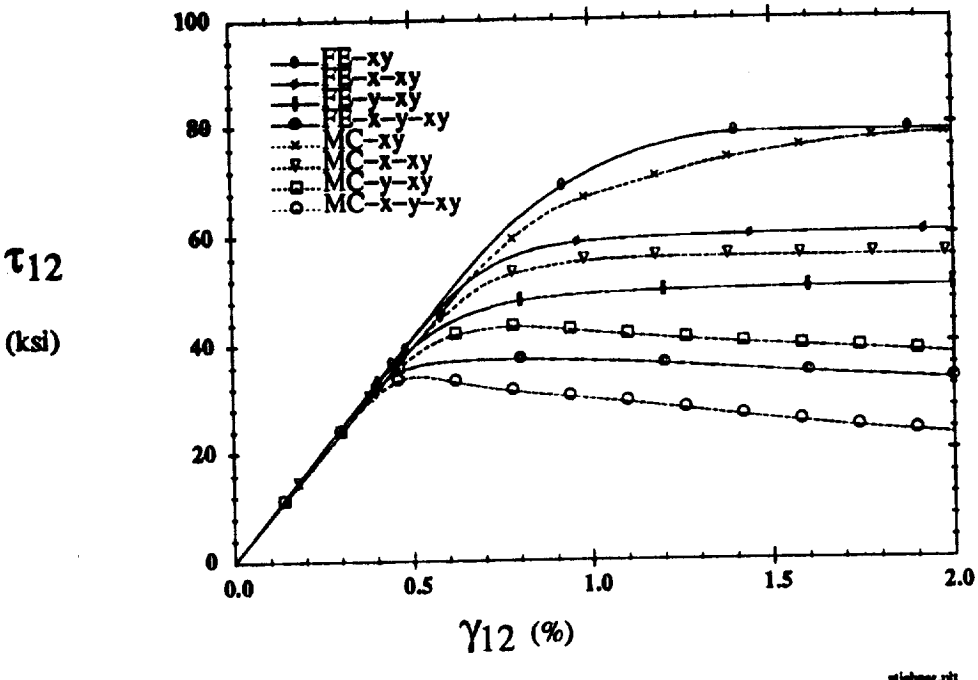

(a)Perfect Bond

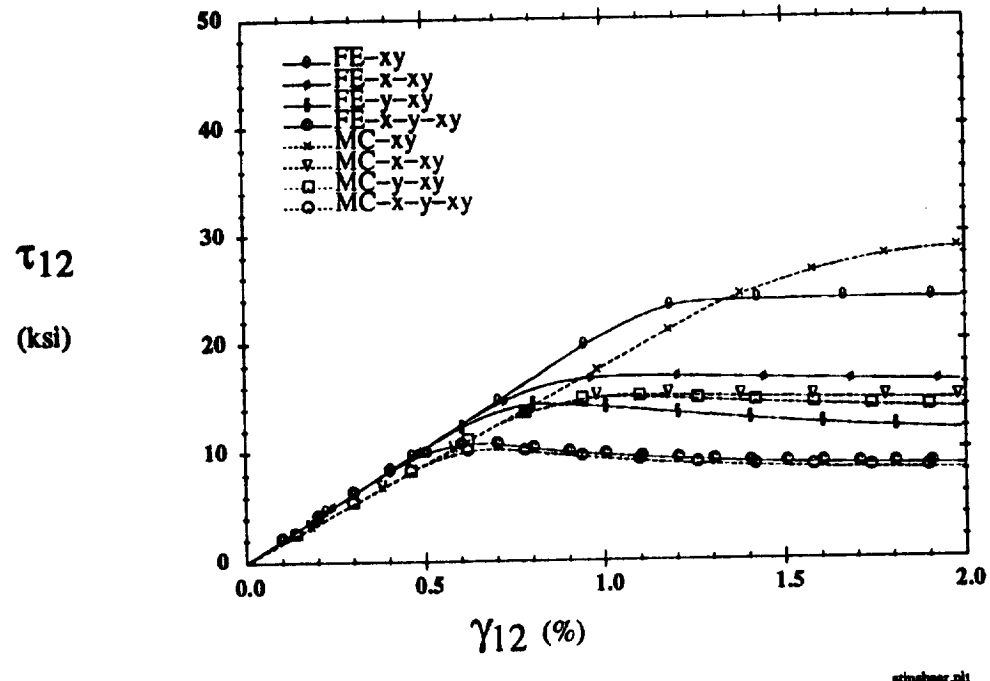

(b)No Bond

Figure 4.4: [0] Predicted Axial Shear Response

bond and no bond conditions serve as extreme conditions for a composite with a debonding interface.

The axial response is shown to be unaffected by the condition of the fiber/matrix interface in Fig. 4.5a. Thus, the effect of interfacial properties on the axial response need not be considered further.

The effect that the interfacial properties have on the transverse compressive response is shown in Fig. 4.5b. While compression normal to an interface is not detrimental to the condition of the bond, the transverse compressive loading considered here creates significant tangential interfacial displacements that do cause debonding. The effective response of a unidirectional composite subjected to transverse compressive loading is quite similar to that for loading which is discussed at length in the following paragraph.

The effect of the interfacial strength, σ_0, on both the transverse tensile and axial shear responses is shown in Fig. 4.6. As expected, the larger the interfacial strength parameter, the closer the initial debonding response is to that of a composite with perfect bonding. After the interface completely debonds the response must be the same as that of a composite with no interfacial bond, and it is. The interesting feature displayed for both transverse tensile and axial shear responses is the unstable response, or falling stress-strain curve, that occurs for the larger bond. The beginning of the unstable response corresponds to the interfacial displacement where the maximum interfacial traction occurs ($u/\delta = 0.33$ in Fig. 2.3a). From this point continued strain increments result in less traction required for additional interfacial displacements. The required traction per unit strain increment continues to decrease as the separation zone increases until final separation is attained.

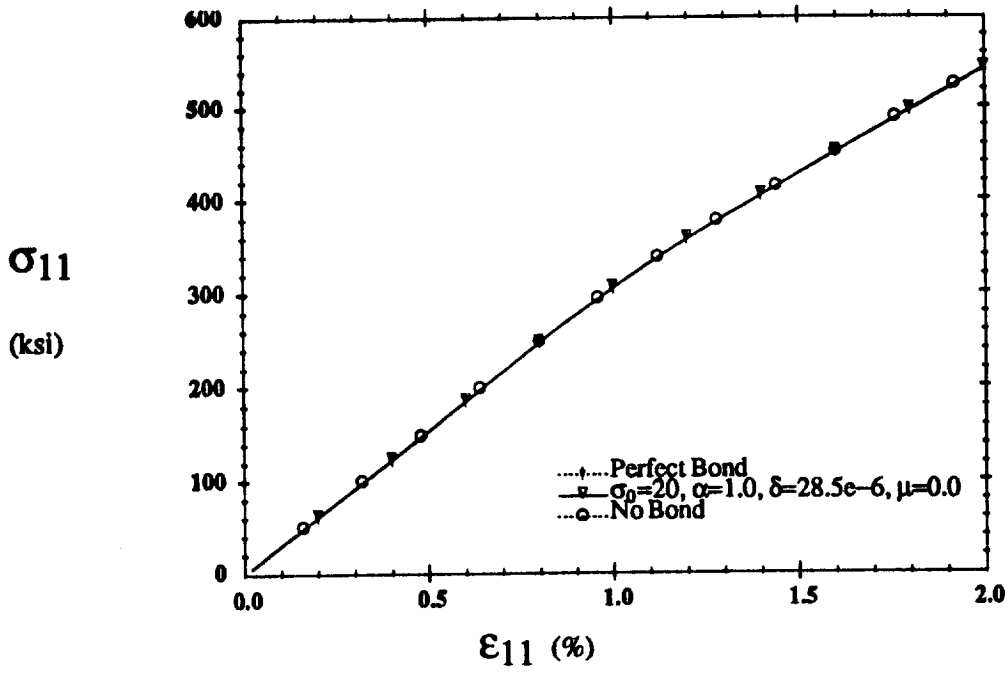

(a)Axial Response

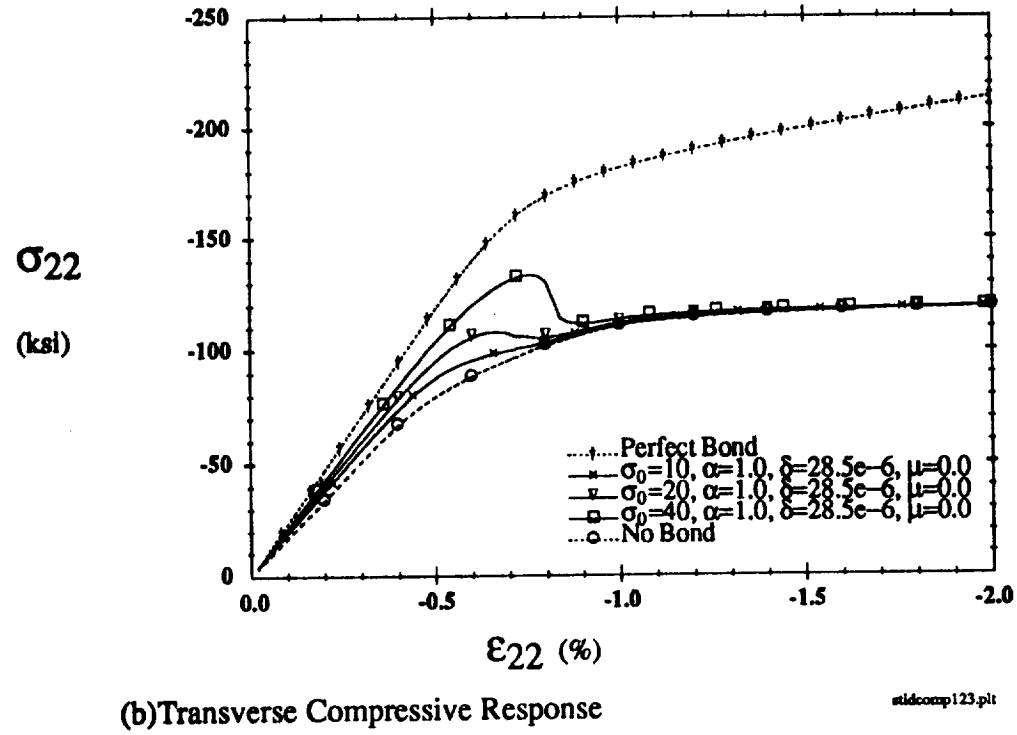

(b)Transverse Compressive Response

Figure 4.5: Effects of Debonding on Axial and Transverse Responses

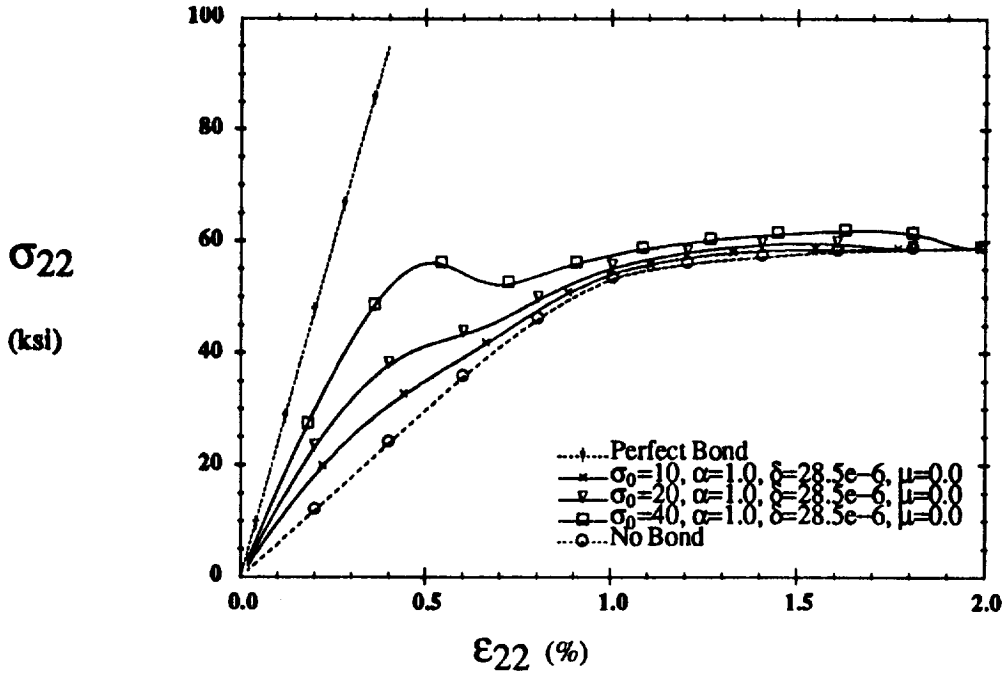

(a)Transverse Tensile Response

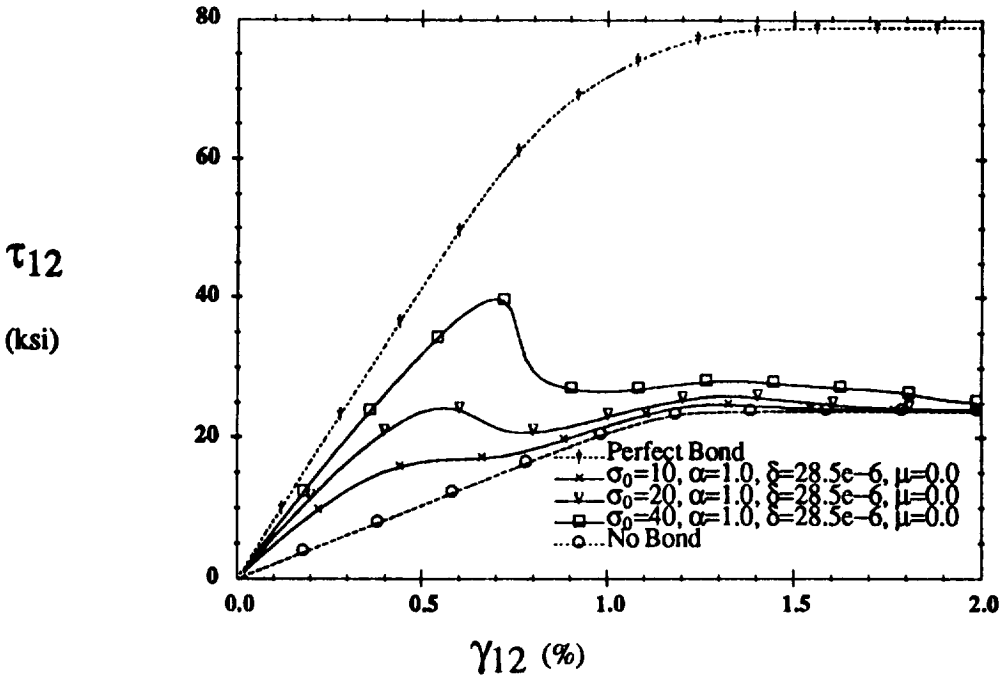

(b)Axial Shear Response

Figure 4.6: Effect of Interfacial Strength, σ_0

The interfacial strength ratio, α, is used to define the interfacial shear strength in terms of the interfacial strength, σ_o. As shown in Fig. 4.7, the interfacial strength ratio has a similar effect on the effective response of unidirectional composites as the interfacial strength. The effective response to axial shear loading is identical for cases #1 and #2 in Table 4.2 because these two sets of properties are equivalent for tangential interfacial

Table 4.2: Interfacial Properties

Case #	σ_o (ksi)	α	δ (in.)	μ
1	40.0	1.0	28.5×10^{-6}	0.0
2	20.0	2.0	28.5×10^{-6}	0.0

displacements and axial shear loading creates tangential interfacial displacements exclusively. The same is not true for transverse tensile loading because debonding is initiated by normal interfacial displacements.

The ductility of an interface is determined by the characteristic length, δ. As shown in Fig. 4.8, a large characteristic length corresponds to a ductile interface while a small characteristic length corresponds to a brittle interface. As seen for $\delta = 5.7\times10^{-6}$ in., a very brittle interface has a very unstable response.

In this study, and in Tvergaard (1990), the coefficient of friction was found to have very little, if any, influence on the effective response of the composite. This is in part because frictional sliding does not occur until after bond failure has taken place; and even then only when compressive normal tractions are present. For the remainder of this study the coefficient of friction is assumed to be zero.

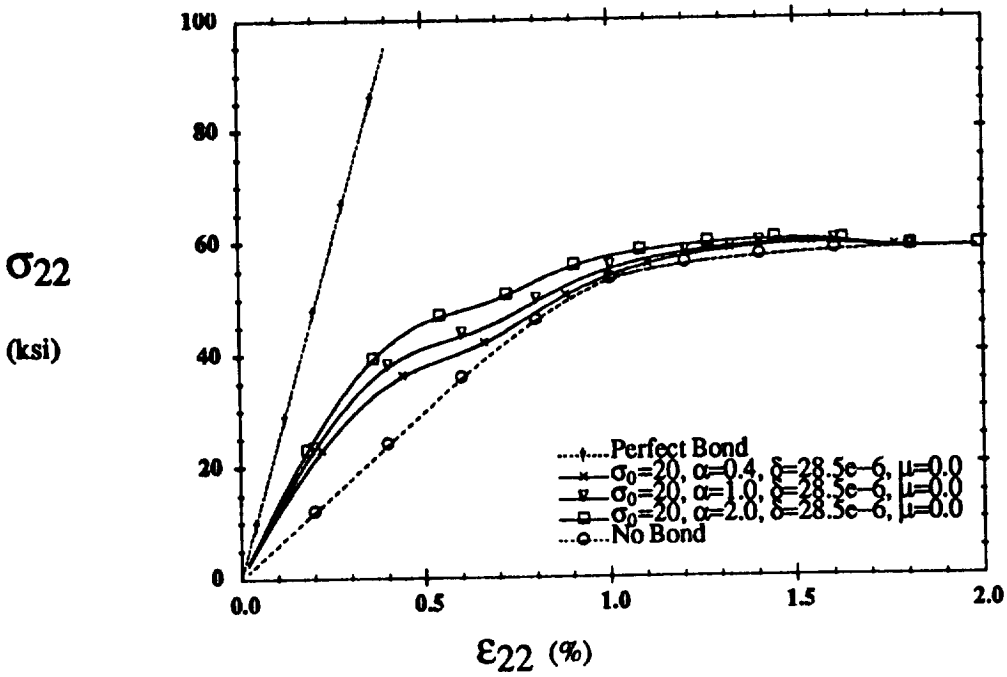

(a)Transverse Tensile Response

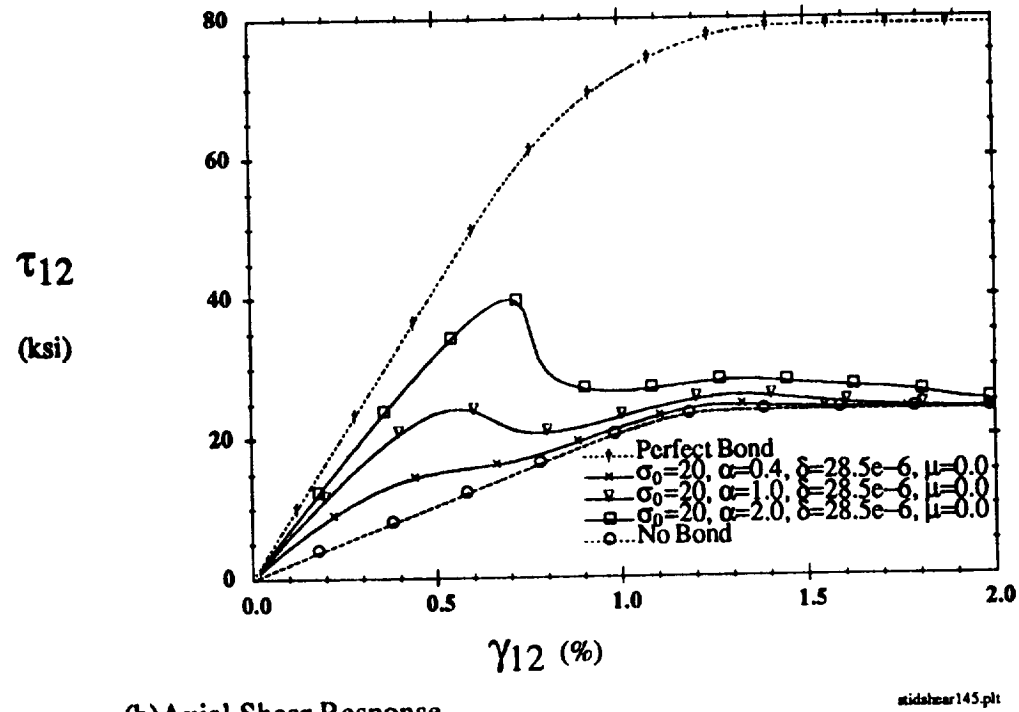

(b)Axial Shear Response

Figure 4.7: Effect of Interfacial Strength Ratio, α

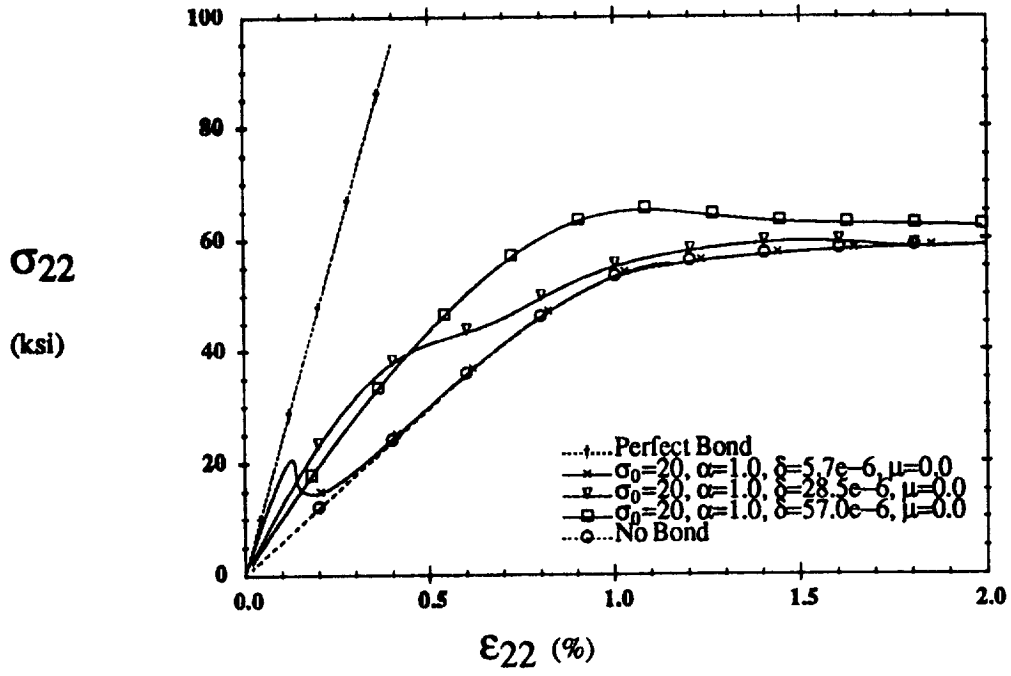

(a)Transverse Tensile Response

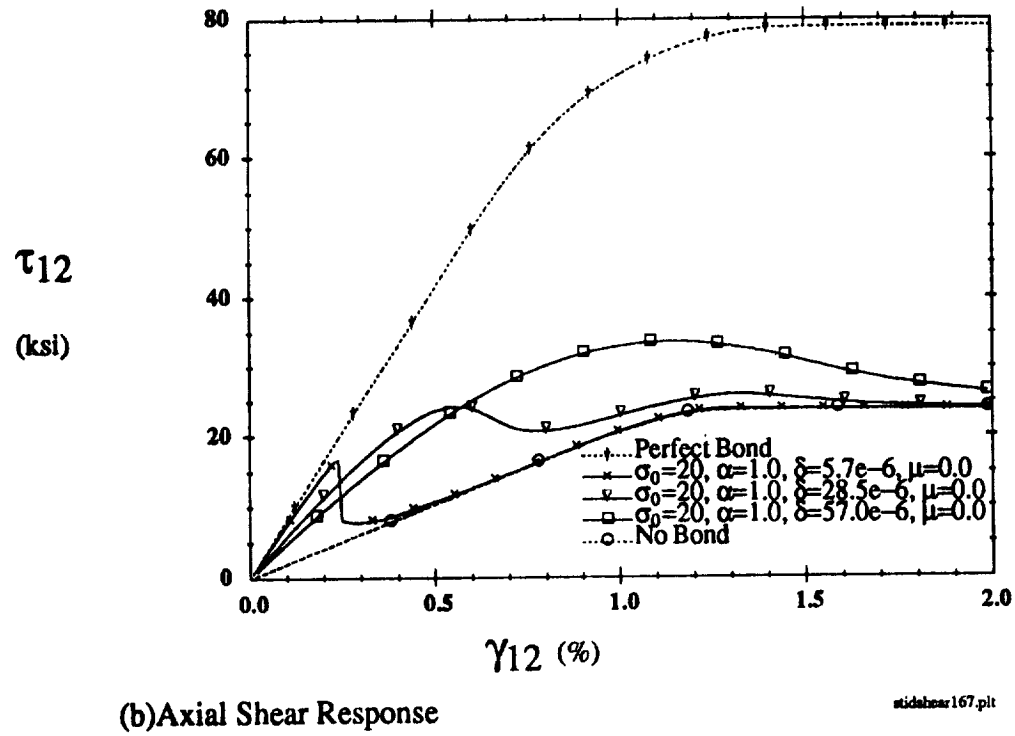

(b)Axial Shear Response

Figure 4.8: Effect of the Characteristic Length, δ

4.1.3 Array Geometry Effects

The geometry of the repeating unit cell is dictated by the fiber packing sequence of the composite that is being modelled. For rectangular array models, the only variable dimensions are the height, a and the width b (Fig. 3.1). Since the fiber diameter is known these two dimensions represent not only the packing sequence, but also the fiber volume fraction. The packing sequence can be defined by the aspect ratio, $R = a/b$. Often MMC are fabricated with uneven fiber spacings. This is frequently caused by uneven layups as well as by fiber swimming during fabrication. The result is that the analyst is faced with having to decide what aspect ratio is most appropriate. Thus, it is critical to understand how the aspect ratio affects the effective composite response. To this end, the response of composites with a fiber volume fraction of 0.4 and aspect ratios of 0.8, 1.0, and 1.2 are presented in Fig. 4.9 and 4.10.

The transverse tensile responses of composites with aspect ratios of 0.8, 1.0 (a square unit cell), and 1.2 are depicted in Fig. 4.9 for both the perfect bond and no interfacial bond conditions. The transverse responses for perfect bonding are the same for aspect ratios of 0.8 and 1.2, with the response for an aspect ratio of 1.0 being slightly more compliant in the plastic region. For the no bond condition shown in Fig. 4.9b there is a large variation in both initial stiffnesses and the onset of plasticity for varying aspect ratios. This is not surprising in view of the fact that the matrix must carry all of the load. The throat of the matrix (distance along the z-axis from the top of the fiber to the top of the repeating cell) increases as the aspect ratio increases. Thus, for imperfect bonding, as the aspect ratio and the throat of the matrix increase the matrix material is more efficiently used for transverse loading in the 2-direction. Conversely, as the aspect ratio increases the effective response is more compliant for transverse loading in the 3-direction.

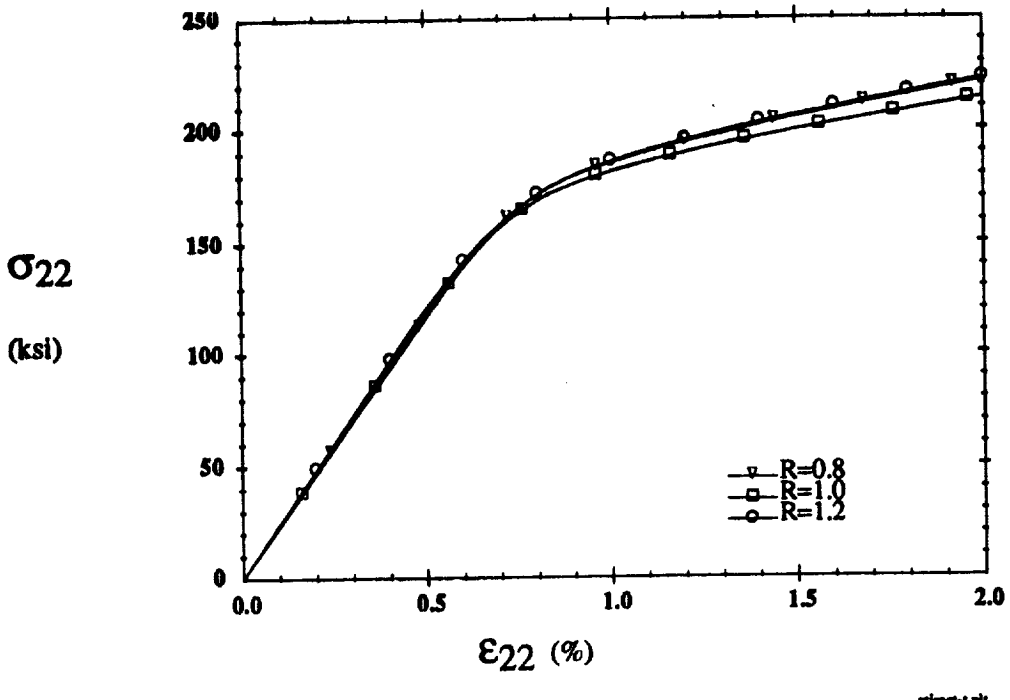

(a)Perfect Bond

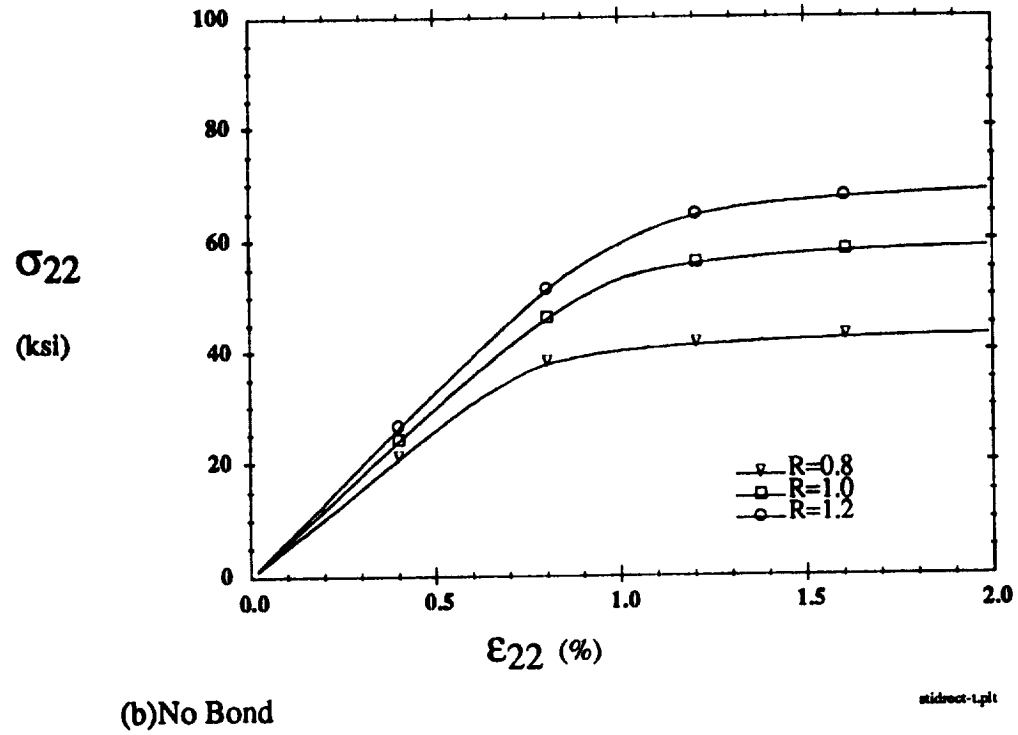

(b)No Bond

Figure 4.9: Effect of Aspect Ratio on Transverse Response

The axial shear responses for aspect ratios of 0.8, 1.0, and 1.2 are shown in Fig. 4.10. For perfect bonding the responses are almost identical. But for no interfacial bond, large differences in stiffness as well as plastic response are observed. The same arguments apply to the axial shear response as to the transverse response.

The obvious conclusion is that while the aspect ratio has a very minimal affect on the response of perfectly bonded composites, it has a very significant affect on the response of imperfectly bonded composites. Therefore one must be very careful when applying a rectangular unit cell to composites with imperfect interfaces. The composites modelled in the present work had a nominal aspect ratio of 1.0, although there were many unevenly spaced fibers (Fig. 5.1). For the remainder of this work the aspect ratio will be taken to be 1.0.

4.2 Angle-ply Composites

The current laminate analysis model is capable of predicting the nonlinear response of a symmetric laminate subjected to thermomechanical loading. To illustrate the nonlinear effects of plasticity and damage the predicted response of a $[\pm 45]_S$ SiC/Ti laminate subjected to axial, shear, and combined axial/shear loading will be presented in this section. The constituent properties are given in Table 4.1 and the thickness of each ply is taken to be 0.008 in. All mechanical loads are applied through strain loading. Perfect bonding between the fiber and matrix is considered as well as a debonding fiber/matrix interface and an interface with no bond.

The response of a $[\pm 45]_S$ laminate to uniaxial loading is shown in Fig. 4.11. Predictions from the current unit cell finite element model are identified by FE. Predictions from the method of cells (Aboudi, 1991) are also presented and are identified

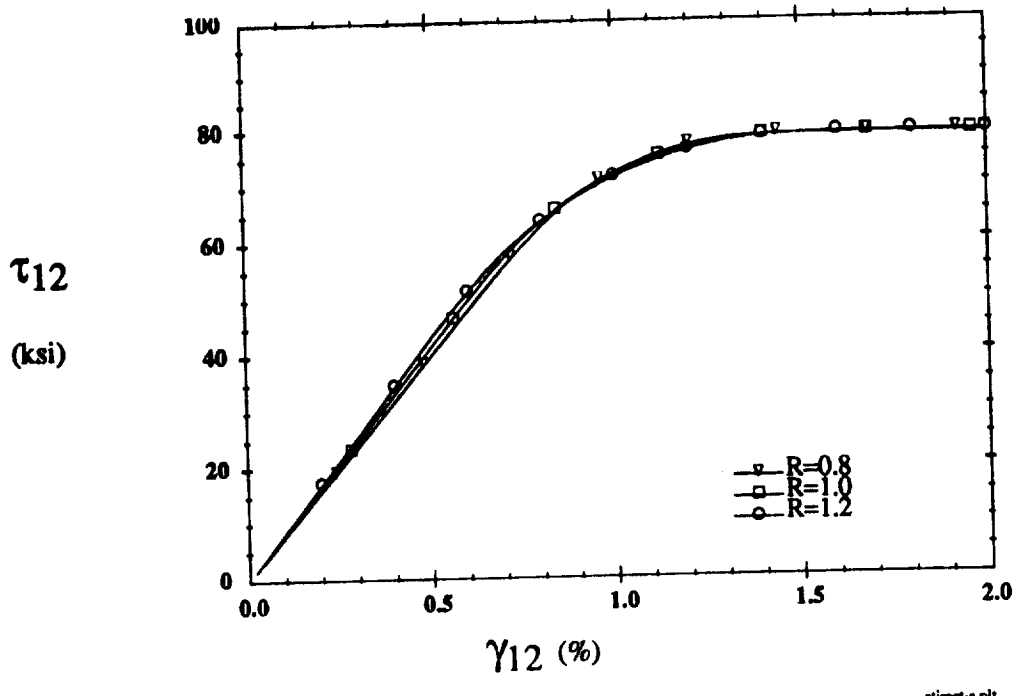

(a)Perfect Bond

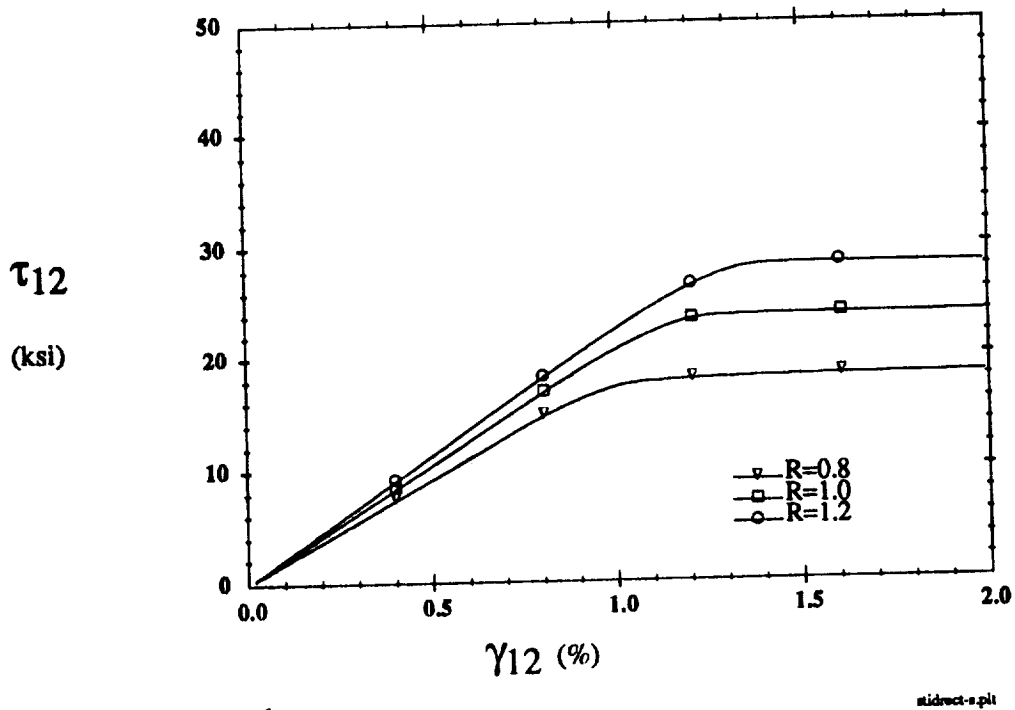

(b)No Bond

Figure 4.10: Effect of Aspect Ratio on Axial Shear Response

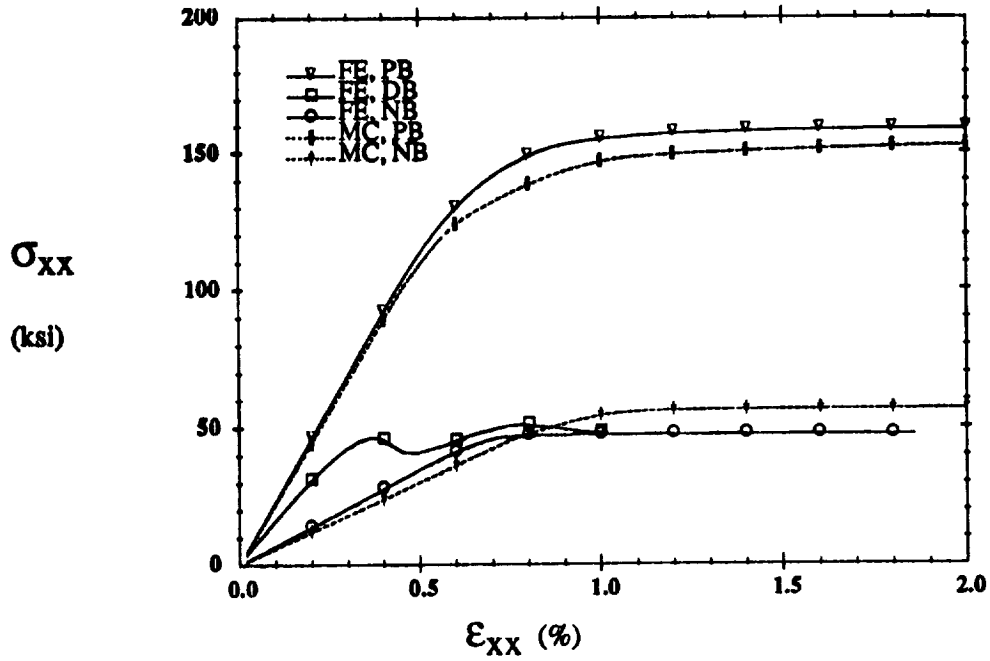

(a)Axial Response

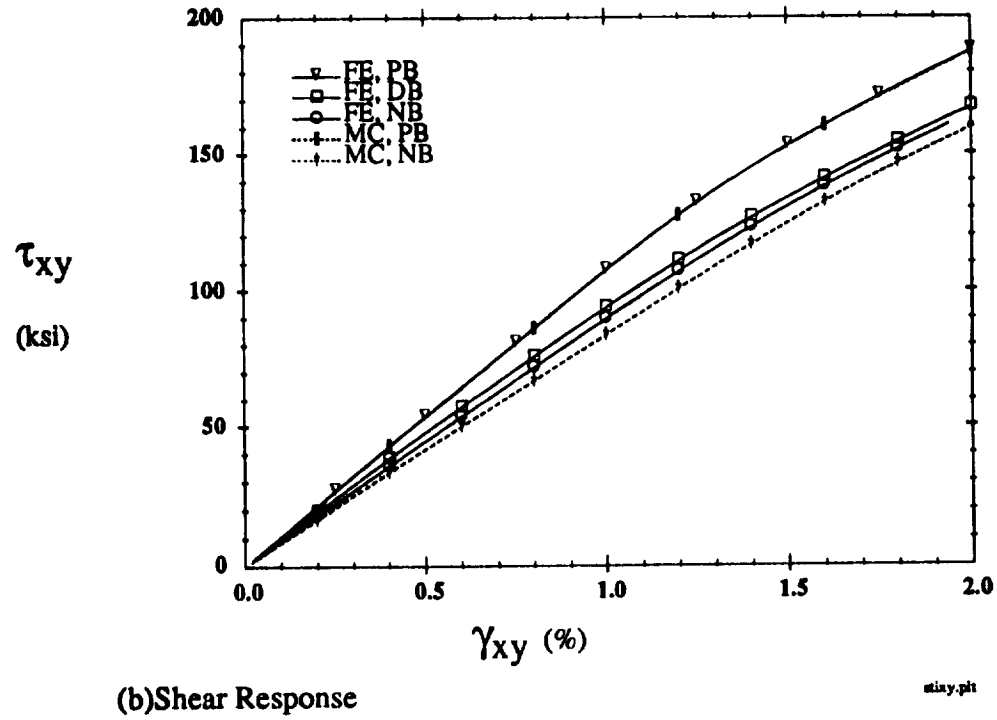

(b)Shear Response

Figure 4.11: $[\pm 45]_s$ Axial and Shear Response

by MC. As for the method of cells predictions for unidirectional composites, the stiffness tensor for each ply has not been transformed to that of a transversely isotropic material. Predictions from both models for perfect bonding and the no bond condition are labelled PB and NB, respectively. The no bond condition is approximated in the method of cells model (Aboudi, 1988) by making both the normal and tangential bonding parameters quite large ($R_n = R_t$ =1 in./ksi). The predictions from the unit cell model for a debonding interface, labelled DB, are based on the following interfacial properties: σ_o=20 ksi, α=1, δ=28.5×10^{-6} in., μ=0. This set of interfacial properties does not necessarily represent a real interface. These interfacial properties were chosen simply because predictions were presented for a unidirectional composite with this set of interfacial properties in Fig. 4.5-4.8.

The predictied axial response (Fig. 4.11a) from the two models agrees reasonably well for both perfect bonding and no bond. The initial axial stiffness predicted by the method of cells for the no bond condition is more compliant because of the imposed traction continuity between subcells and the simplified geometry. For no bond between the fiber and matrix the stresses in the fiber subcell are zero. Traction continuity dictates that some stress components in adjacent matrix subcells are also zero, which may be over-restrictive.

The initial response of a composite with a debonding interface is initially that of a perfectly bonded composite but is quickly degraded. As for unidirectional composites an unstable response, or falling effective stress-strain curve, is exhibited once the peak in the interfacial traction-displacement relation is reached. As the interface becomes completely debonded the prediction for no bond is approached.

The shear response predicted by both models (Fig. 4.11b) is essentially the same

for perfect bonding, but once again the method of cells predicts a more compliant response for the no bond condition. The same reasoning applies here as above for the axial response. The prediction for a composite with a debonding interface falls between the predicted responses for perfect and no bond.

The response of a $[\pm 45]_s$ laminate subjected to combined axial and shear loading is shown in Fig. 4.12. Both axial (Fig. 4.12a) and shear (Fig. 4.12b) responses are quite similar to their uniaxial loading counterparts, the main difference being that nonlinear response occurs at a lower stress level. It is interesting to note that the shear response for combined loading of a $[\pm 45]_s$ laminate with a debonding interface is the same as that for a laminate with no interfacial bonding.

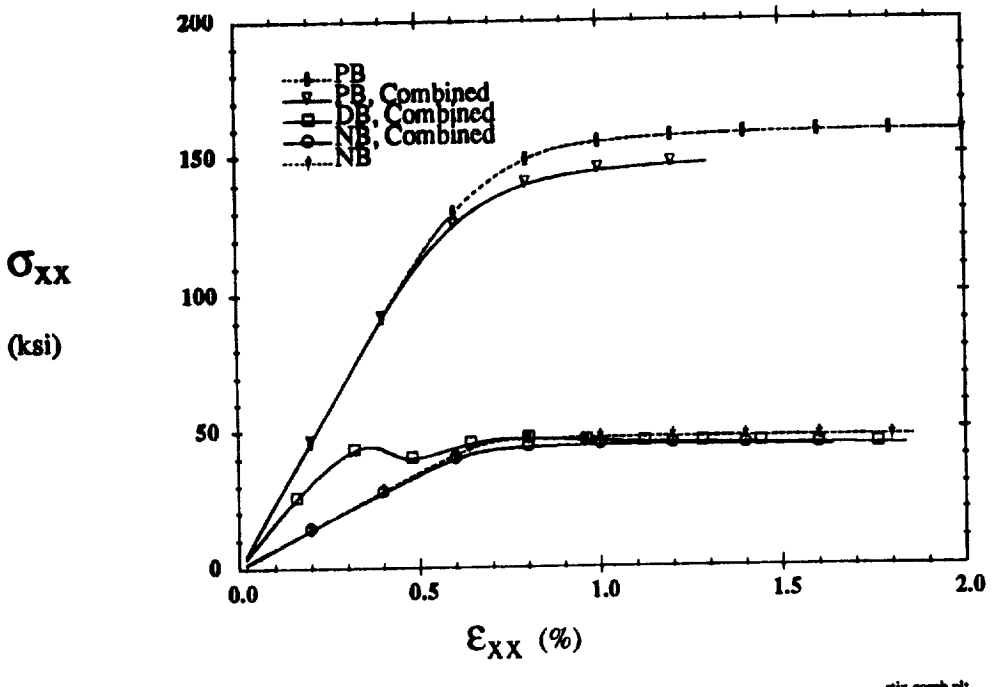

(a)Axial Response

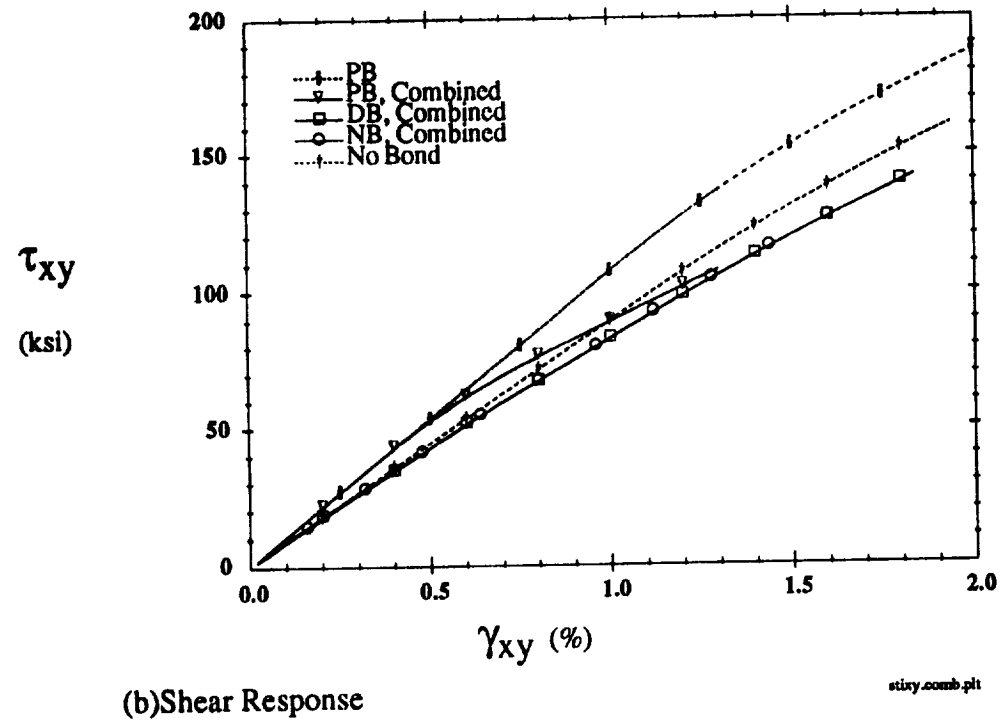

(b)Shear Response

Figure 4.12: $[\pm 45]_s$ Axial and Shear Response, Combined Loading

CHAPTER 5

EXPERIMENTAL PROCEDURES

The experimental program consisted of two phases. The first phase entailed development of a test method most appropriate for the given MMC to be tested. The test matrix was first determined, then other factors such as what data was to be collected, how to measure strains, where to measure strains, how to apply the loads, what type of fixtures are required, etc. were determined. The actual testing was performed in the second phase of the program. This chapter discusses the materials and procedures used in the experimental program. Chapter 6 presents the results of the experimental program.

5.1 Materials

The McDonnell Douglas Corporation originally supplied ten SiC/Ti tubular specimens for testing at the University of Virginia Composite Mechanics Laboratory, six were $[\pm 45]_s$ and four were $[0_4]$. Five more $[\pm 45]_s$ tubes were delivered at a later date. The tubes were manufactured by Textron using a proprietary hot isostatic pressing (HIP) technique. Molybdenum wires were woven together with the fibers to form a cloth and help keep the fibers in the proper alignment during fabrication. Alternating layers of fiber cloth and matrix foil are consolidated at high temperature and pressure to form the composite. Each tube consists of four plies that are nominally 0.008 in. thick.

5.1.1 Constituents

The following sections briefly describe the constituents that make up the composite. Nominally, the composite is comprised of 60.4% Ti matrix, 39.4% SiC fiber, and 0.2% molybdenum wire weave.

5.1.1.1 Matrix

The metal matrix used in the tubes is consolidated from thin foils of the metastable titanium alloy Ti-15V-3Cr-3Sn-3Al, commonly designated Ti-15-3. Lerch, et al. (1988) provide an in-depth discussion of the microstructure of Ti-15-3, suffice it to note here that the microstructure contains orthorhombic grains, and that these grains become finer and more equiaxed near the fiber/matrix interfaces.

5.1.1.2 Fiber

The SCS-6 fiber manufactured by Textron is a SiC fiber designed specifically for use with titanium matrices. These fibers are produced using the chemical vapor deposition (CVD) process. The fiber is a complex, multilayered structure which is built up from a 13×10^{-4} in. (33 μm) diameter carbon monofilament. A pyrolytic carbon coating is deposited on the carbon core up to a thickness of 0.59×10^{-4} in. (1.5 μm). Silicon carbide is then deposited on this substrate to a diameter of 56×10^{-4} in. (142 μm) (Lerch, et al., 1988). Two four-layer coatings (described below) totalling 1.2×10^{-4} in. (3 μm) are applied using the CVD process to control the fiber/matrix reaction zone and improve the strength of the fiber. The first layer consists of small SiC crystallites in a carbon matrix, the second layer is predominantly carbon, the third layer consists of laminar carbon, and the fourth layer is characterized by a more randomly oriented carbon microstructure (Nutt and Wawner, 1985). A disadvantage associated with using these coatings is that the bond between the coatings is quite poor. As described previously, there is an abundance of evidence showing that fiber/matrix debonding in laminates with off-axis plies is a prominent source of degraded response. Figure 5.1 shows the microstructure of both $[0_4]$ and $[\pm45]_s$ composites.

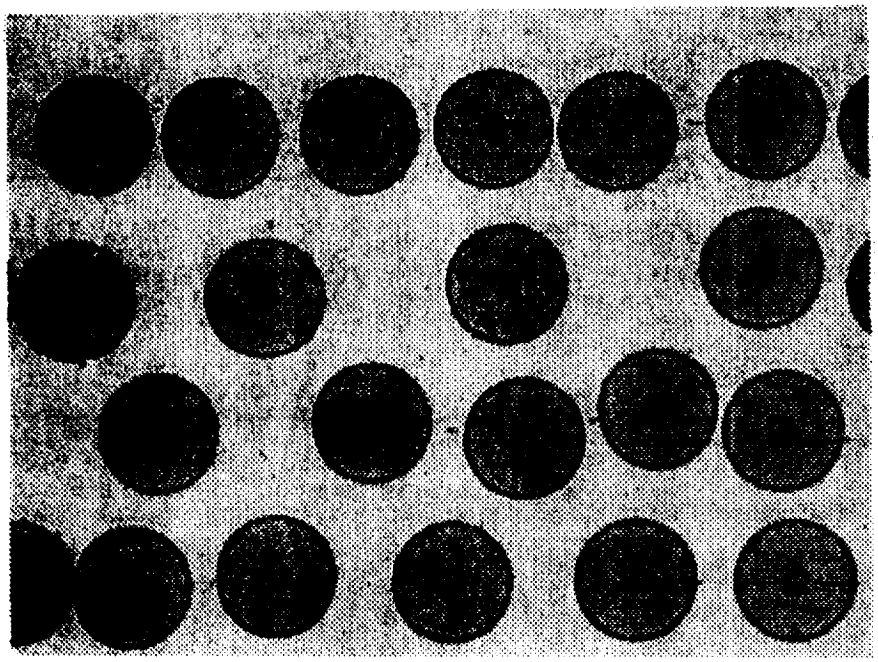

(a) $[0_4]$

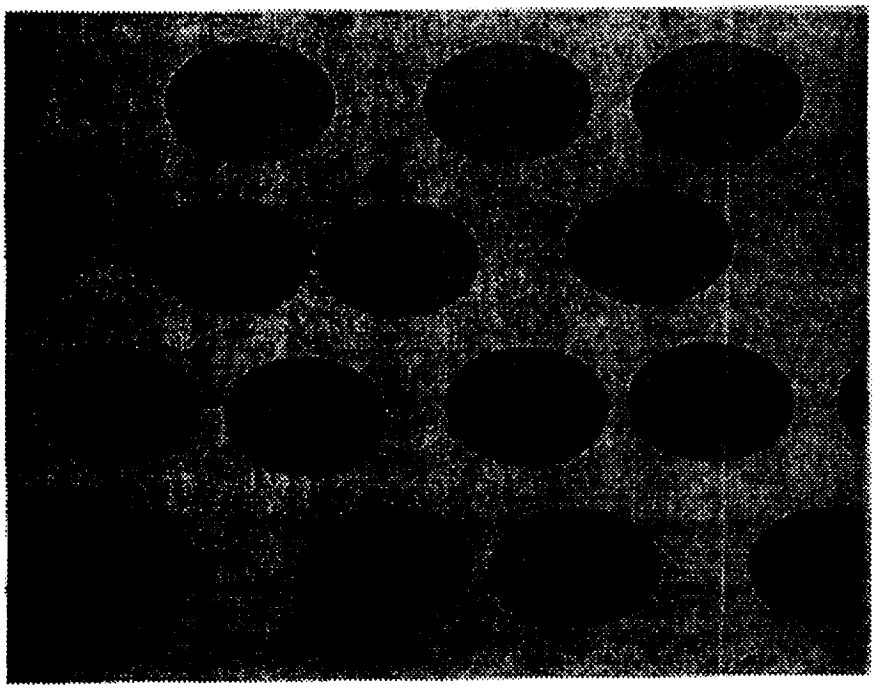

(b) $[\pm 45]_s$

Photos courtesy of Brad Lerch, NASA Lewis Research Center (Lerch, 1993)

Figure 5.1: SiC/Ti Composite Microstructure

5.1.1.3 Wire Weave

The molybdenum wires used to weave the SiC fibers into a cloth are often called 'moly wires'. These wires are 0.002 in. in diameter, run perpendicular to the SiC fibers, and are spaced approximately 0.2 in. apart.

5.1.2 Geometry

The geometry of the $[0_4]$ and $[\pm 45]_s$ tubes are quite different, enough so that even the way they are gripped by the testing apparatus is different. Specimen geometry and the fixtures used to grip the tubes are described below.

5.1.2.1 $[0_4]$ Tubes

The $[0_4]$ tubes are nominally 7 in. long and have an outer diameter of 1.5 in. (Fig. 5.2). The tubes were received with steel plugs 2 in. long bonded to the inner surface of the ends of the tubes to facilitate the introduction of a uniform load into the composite during testing. Thus, the gage length was 3 inches. A half-inch diameter hole was drilled through the tube and steel plug at each end for load introduction. Previous experience with testing of composite materials demonstrated that loading a [0] composite through a bolt could cause failure at the bolt hole. Therefore, a fixture was designed to bond to the outside of the tube, as well as be pinned to the tube. The pin was still required, because the adhesive by itself was not capable of providing adequate strength. Hysol 934NA adhesive mixed in a 100 part A to 33 part B ratio was used, with 1% glass beads added to improve the crack resistance and help control the bond line. Nylon thread, 0.01 in. in diameter, was also used to control the bond line. Surface preparation for bonding was performed on both the outside of the tube and the inside of the fixture. The procedure used is as follows.

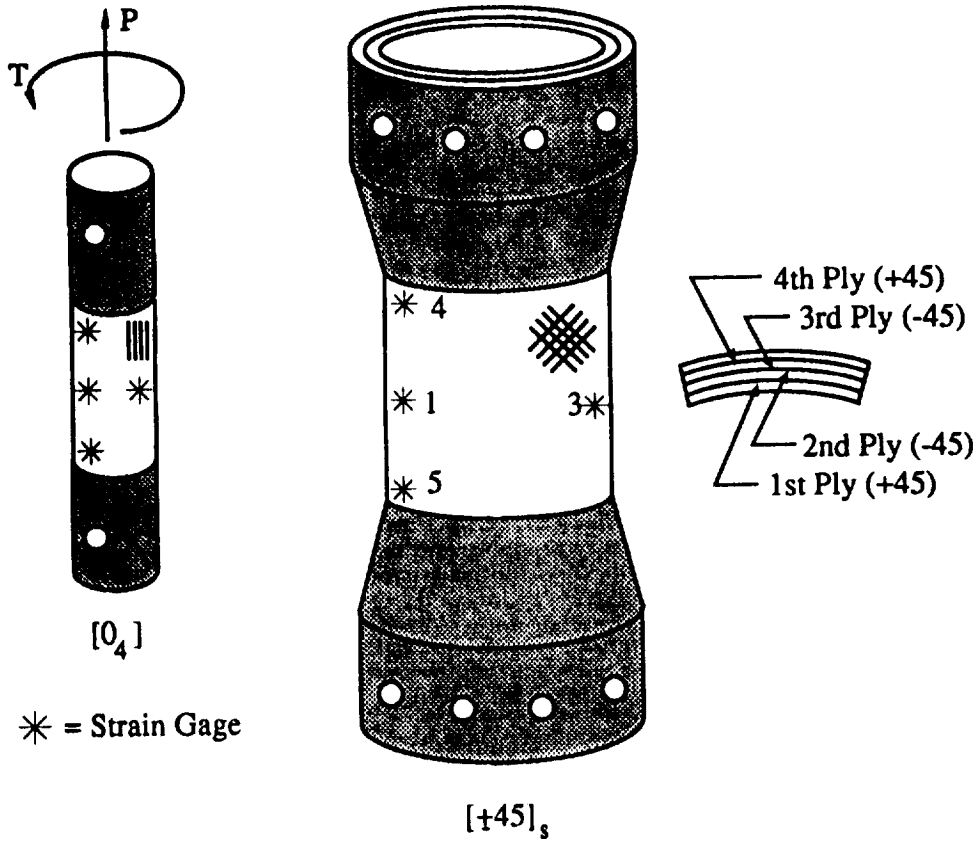

Figure 5.2: Tube Geometry

1. Roughen surface with medium grit emery paper.
2. Thoroughly degrease surface with a mild degreaser.
3. Dip in acid bath (1 part concentrated HCl/1 part distilled water) for 10 minutes.
4. Rinse with cold distilled water.
5. Dry in oven at 150°F for 10 minutes.
6. Apply Hysol adhesive to inside of fixture only.
7. Bond fixture to tube, then insert and bond pin in place.
8. Align in MTS for 2 hours, remove, and cure at room temperature for 20 hours, then cure at 120°F for 12 hours.

With one exception, $[0_4]$ tubes were instrumented with five rectangular strain gage rosettes. Micro-Measurements type EP-08-062RB-120 (Tube #2) and TML type FRA-2-11 (Tube #4) both were used, with the individual gages oriented at angles of -45, 0, and 45 degrees measured from the longitudinal axis of the tube. Three rosettes were spaced at 120° around the mid-length of the tube. The other two rosettes were located at the top and

bottom of the gage length. Figure 5.3a shows a $[0_4]$ tube with fixtures and strain gages bonded to it. Four Micro-Measurements type CEA-06-125UR-350 rectangular strain gages oriented at angles of 0, -45 and 90 degrees were bonded around the mid-length (spaced at 90°) of Tube #1.

5.1.2.2 $[\pm 45]_s$ Tubes

The $[\pm 45]_s$ tubes are nominally 12 in. long and have an outer diameter of 4 in. (Fig. 5.2). Note that plies are numbered from the inside of the tube, and a positive ply orientation angle is defined by a counterclockwise rotation from the longitudinal axis of the tube, as viewed from inside the tube. The tubes were received with tapered steel collars 4 in. long, bonded to both inside and outside of the ends, leaving a gage length of 4 in. Eight half-inch bolt holes were drilled at an even spacing around the circumference of each end of the tube. These holes accommodate eight bolts that transfer load from the fixture to the tube. The fixture itself is comprised of three components (Fig. 5.4), an outer ring, a solid inner core, and the end piece that is actually held by the collet grips of the load frame. The specimen is attached to the fixture by bolts through the outer ring, specimen, and inner core. Figure 5.5 shows a $[\pm 45]_s$ in the load frame. Two $[\pm 45]_s$ tubes were instrumented with five rectangular strain gage rosettes located in the same manner as described for the $[0_4]$ tubes. One tube had four rosettes located 90° apart, bonded around the mid-length of the tube. The axial strain to failure of the $[\pm 45]_s$ tube was expected to be approximately 10%, hence high elongation Micro-Measurements type EP-08-062RB-120 strain gages were used. Figure 5.3b shows a fully instrumented $[\pm 45]_s$ tube.

Visual inspection of the tubes revealed that some fibers, at least in the outermost ply had not remained in the proper alignment during fabrication. It was also apparent that seams existed in the tubes where the ends of the fiber cloth abutted, resulting in fiber-rich

ORIGINAL PAGE
BLACK AND WHITE PHOTOGRAPH

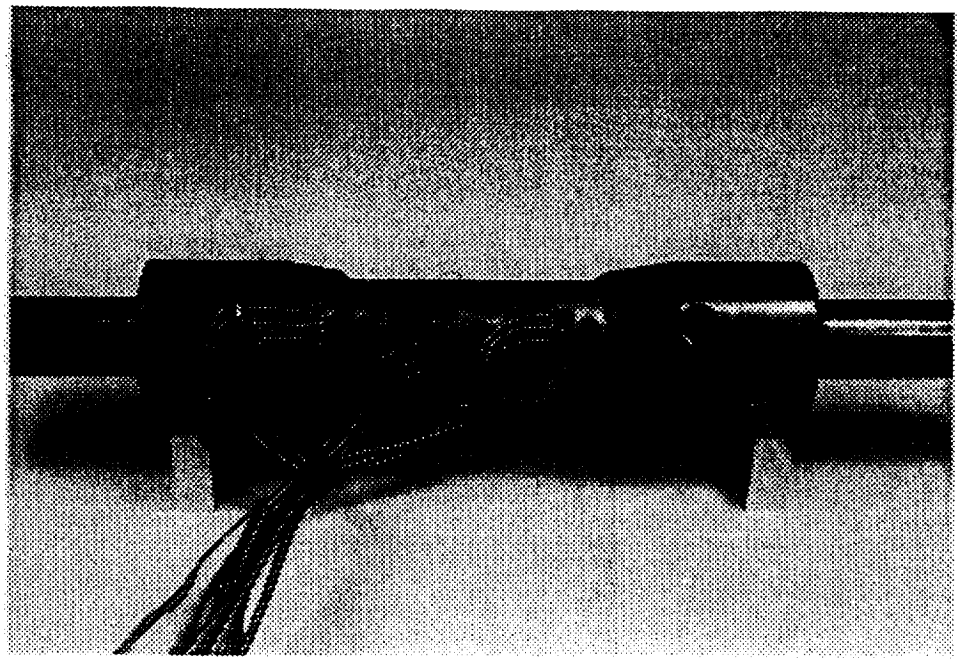

(a) $[0_4]$ Tube

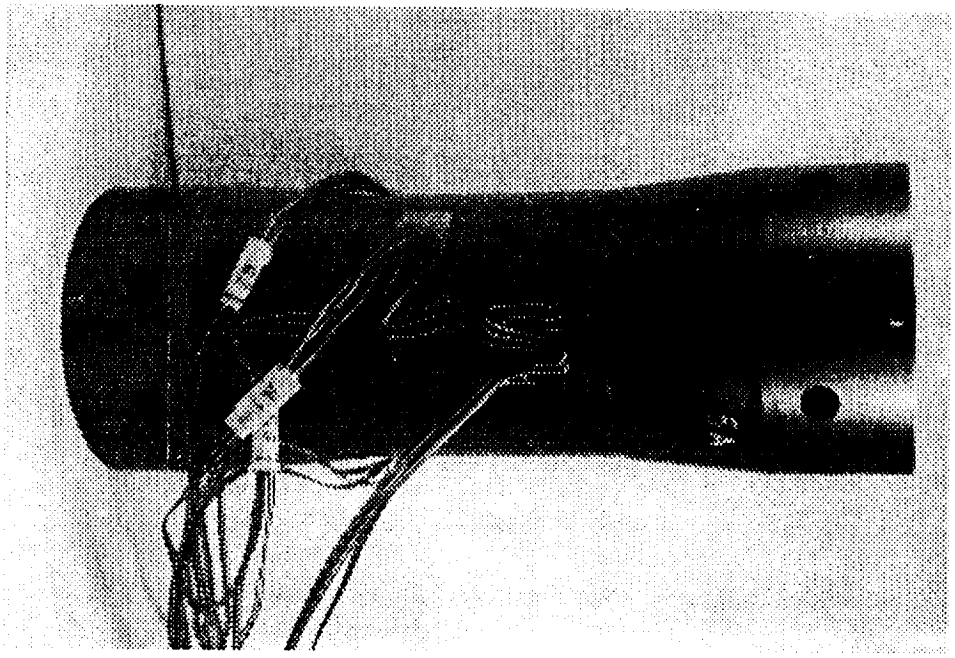

(b) $[\pm 45]_s$ Tube

Figure 5.3: SCS-6/Ti-15-3 Specimens

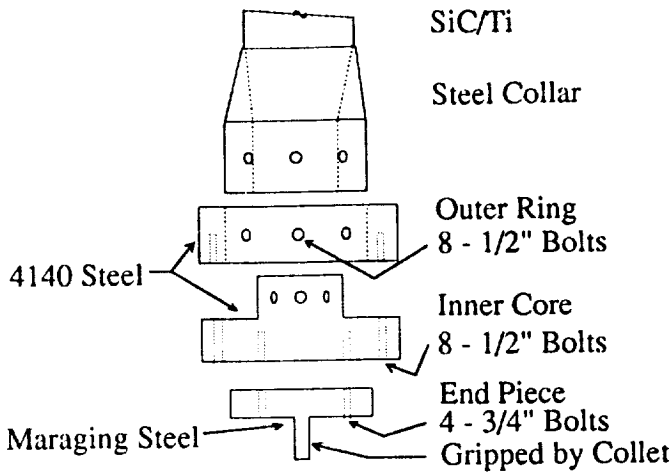

Figure 5.4: $[\pm 45]_s$ Fixture

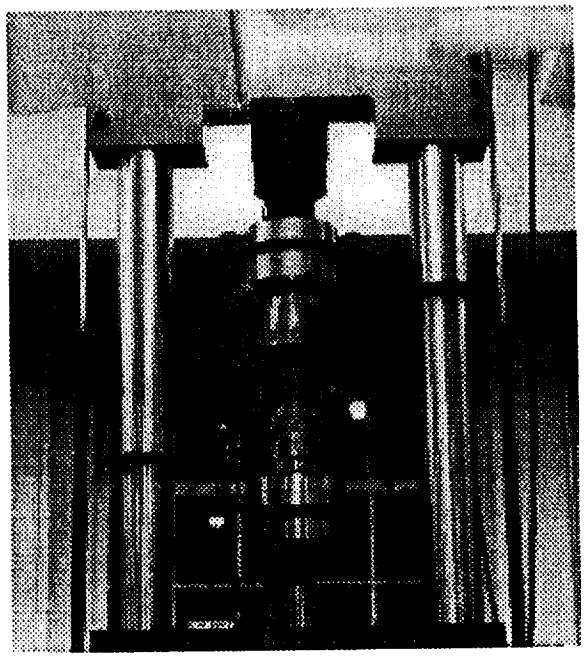

Figure 5.5: $[\pm 45]_s$ tube in load stand

and fiber-depleted regions. Like the fibers, these seams are located at a 45° angle to the tube axis. Strain gage rosettes were located as far as possible from anomalies, while still holding to the pattern described above.

5.2 Procedures

The experimental program consisted of tests conducted on an axial/torsional load frame. The following subsections describe the types of loads applied to the test specimens, the test matrix, equipment, and instrumentation.

5.2.1 Loadings

Uniaxial tension and compression tests were first conducted on both $[0_4]$ and $[\pm 45]_s$ tubes to determine initial axial elastic properties. Torsion tests were then conducted to determine the initial axial shear modulus. Both positive and negative shear were applied to the $[\pm 45]_s$ tubes. Internal pressure was applied to a $[0_4]$ tube to determine the initial transverse modulus. All of these tests were conducted at very low stress levels so that no, or at worst, minimal damage would be done to the specimen.

Three types of multiaxial loadings, designated Type I, Type II, and Type III were then applied to the tubes. After the initial tests to determine elastic properties, only one type of loading was applied to any particular tube. The loadings are represented schematically in Fig. 5.6, and are described below. Type I tests are a series of axial tensile tests to sequentially higher load levels, where at the peak of each individual cycle, a biaxial stress state is introduced by applying an increment of torque. Both axial and shear stiffnesses are measured during the biaxial portion of the test. The torque is unloaded while the tensile load is still held constant, then the tensile load is removed.

Type II tests are a series of torsional tests to sequentially higher load levels, where at the peak of each individual cycle, a biaxial stress state is introduced by applying an increment of axial tension. Again, both axial and shear stiffnesses are measured during the biaxial portion of the test. The tension is unloaded while the torsional load is still held

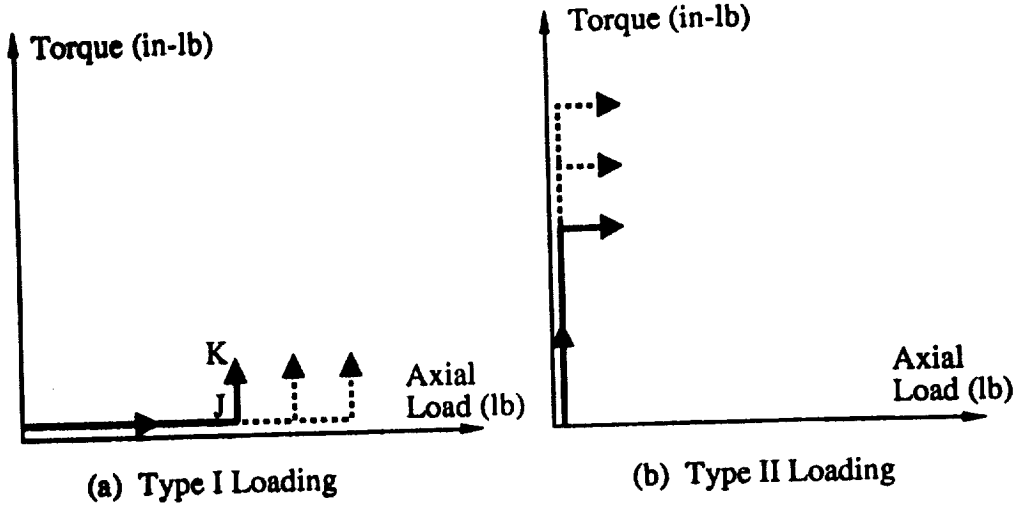

(a) Type I Loading

(b) Type II Loading

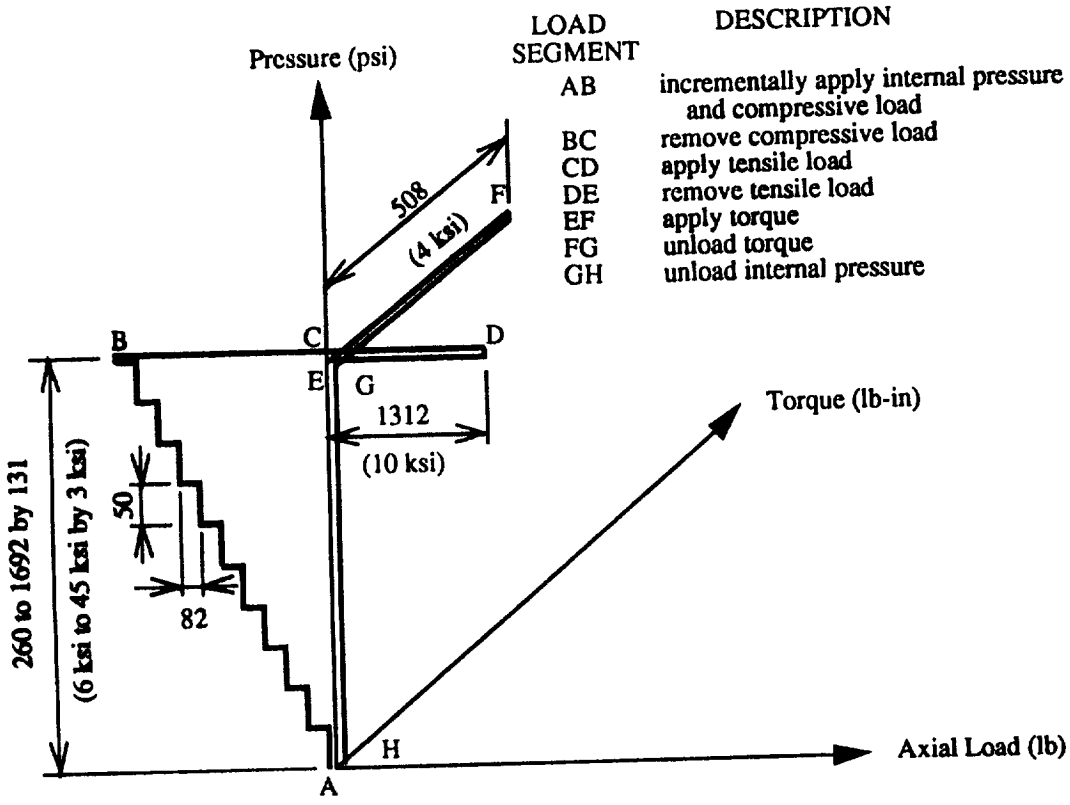

(c) Type III Loading

Figure 5.6: Multiaxial Loading Schematics

Table 5.1: Test Matrix

	Type I	Type IA	Type II	Type III
$[0_4]$	Tube #2	-	Tube #4	Tube #1
$[\pm 45]_s$	Tube #5	Tube #9	Tube #10	-

constant, then the torsional load is removed.

Type III tests were quite complicated to conduct, because it was desirable to have only one stress component, the circumferential (transverse for a [0] tube) stress present. This required that the longitudinal stress component due to internal pressure be eliminated by the application of an axial compression. Due to the type of hydraulic system used to apply the internal pressure, it was impossible to apply axial compression at a rate proportional to the internal pressure, thus the internal pressure and compression were applied incrementally for each cycle. At the peak internal pressure, an increment of axial tension was applied and removed, then an increment of torque was applied and removed. Finally, the internal pressure was unloaded.

Type I tests were modified to study time dependent inelastic effects by the inclusion of hold times where the applied stresses were held constant for a finite time period immediately before the application of torque and at the maximum torque (points J and K in Fig. 5.6). This modified loading is designated Type IA, and has been applied only to $[\pm 45]_s$ tubes.

5.2.2 Test Matrix

The test matrix for biaxial loadings is given in Table 5.1. The tube identification number is given for each sequence of biaxial loading. Table 5.2 presents the test matrix for Type I loadings. These tests were conducted in load and torque control. Table 5.3 displays

Table 5.2: Type I Loading

	$[0_4]$		$[\pm 45]_s$		
Cycle	$\sigma_{11}\|^{max}$ (ksi)	τ_{12} (ksi)	$\sigma_{xx}\|^{max}$ (ksi)	τ_{xy} (ksi)	Hold (sec)
1	13.4	2	8	2.1	355
2	26	4.5	12.3	2.1	109
3	39	4.5	18.4	1.9	103
4	52	4.5	18.4	1.9	91
5	65	4.5	22	2	141
6	78	4.5	27	1.1	44
7	84.5	4.5	29.9	2.1	88
8	91	4.5	33.2	2.1	194
9	97.5	4.5	40	4.8	106
10	104	4.5	44	4.8	104
11	110.5	4.5	47.5	4.8	100
12	119[a]	0	55	4.8	104
13	108[b]	0	60	4.8	104
14	-	-	65	4.8	102
15	-	-	68.2[c]	0	0

a. adhesive failure
b. failure
c. failure

the test matrix for Type IA loading. Recall that the first hold takes place under uniaxial tension, while the second hold occurs at the peak biaxial load. The total hold time is defined to be the amount of time that the axial tension is held constant. The test matrix for Type II tests is shown in Table 5.4. These tests were conducted in rotation and load control. Finally, Table 5.5 gives the test matrix for Type III loading. In Type III tests the peak internal pressure is held constant while axial tension is applied and then removed

using load control. Torque is then applied and unloaded using torque control. The final step is unloading the internal pressure.

5.2.3 Test Equipment and Instrumentation

Testing was performed at room temperature on a servo-hydraulic MTS Axial/ Torsional load stand with an axial capacity of 55,000 pounds and a torsional capacity of 20,000 inch-pounds. The load stand is currently outfitted with hydraulic, one-inch diameter collet grips. The test equipment is shown in Fig. 5.7. Axial and torsional loads were applied independently using a function generator for axial loads and a Micro-Profiler for torsional loads or vise versa. MTS 458 DC and AC Controllers on the MTS Micro-

Table 5.3: Type IA Loading

Cycle	$\sigma_{xx}\|^{max}$ (ksi)	Hold #1 (sec)	τ_{xy} (ksi)	Hold #2 (sec)	Total Hold (sec)
1	17[a]	266	5	0	358
2	18	246	5	297	640
3	24	297	5	284	694
4	30	137[b]	0	0	137
5	30	182	10	301	675
6	36	300	10	301	791
7	41	300	10	266	760
8	48	304	10	299	793
9	54	419	10	285	894
10	60	422	11	0[c]	525
11	64	422	10	361	971
12	68	421	3[d]	0	444

a. τ applied at σ = 12 ksi
b. cycle stopped prematurely
c. cycle stopped prematurely
d. failure

Table 5.4: Type II Loading

	$[0_4]$		$[\pm 45]_s$	
Cycle	$\tau_{12}{}^{max}$ (ksi)	σ_{11} (ksi)	$\tau_{xy}{}^{max}$ (ksi)	σ_{xx} (ksi)
1	5	10	9.7	10
2	10	10	12.4	10
3	15	10	15.2	10
4	18	10	16.5	10
5	20	10	18.0	10
6	22	10	18.3[a]	10
7	25	10	-	-
8	28	10	-	-
9	30	10	-	-
10	32	10	-	-
11	34	10	-	-
12	38.5	10	-	-
13	40	10	-	-
14	42[b]	0	-	-

a. machine capacity reached
b. failure

Console were used to control displacement, rotation, load, or torque. Internal pressure was applied by pumping hydraulic oil into the tube through a hole drilled in the steel end-plug with the pump from a second MTS load stand. A 3500 psi capacity pressure transducer was used to measure the static pressure applied to the tube. The internal pressure test setup is shown in Fig. 5.8. A plexiglass shield and containment pan were used for protection in the event failure occurred.

Transducer and strain gage wires are connected to the connection box, which

Table 5.5: Type III Loading

Cycle	σ_{22}^{max} (ksi)	σ_{11} (ksi)	τ_{12} (ksi)
1	6	10	4
2	9	10	4
3	12	10	4
4	15	10	4
5	18	10	4
6	21	10	4
7	24	10	4
8	27	10	4
9	30	10	4
10	33	10	4
11	36	10	4
12	39	10	4
13	42	10	4
14	45	10	4
15	46.2[a]	0	0

a. failure

provides a quarter bridge for strain gages. The connection box, in turn, is linked to an Orion datalogger, which samples all the data. The datalogger is controlled by an RS-232 link to a 386 class PC. The MATPAC data acquisition software (Hidde, et al., 1988) on the PC provides real time stress-strain (or load-deflection) curves throughout the test. MATPAC also has post-processing capabilities including plotting and correction of strain readings for misalignment, transverse sensitivity, and Wheatstone bridge nonlinearity. All data was sampled at a rate of one sweep per second. This was the fastest data could be transferred from the datalogger to the PC when five strain gage rosettes and four

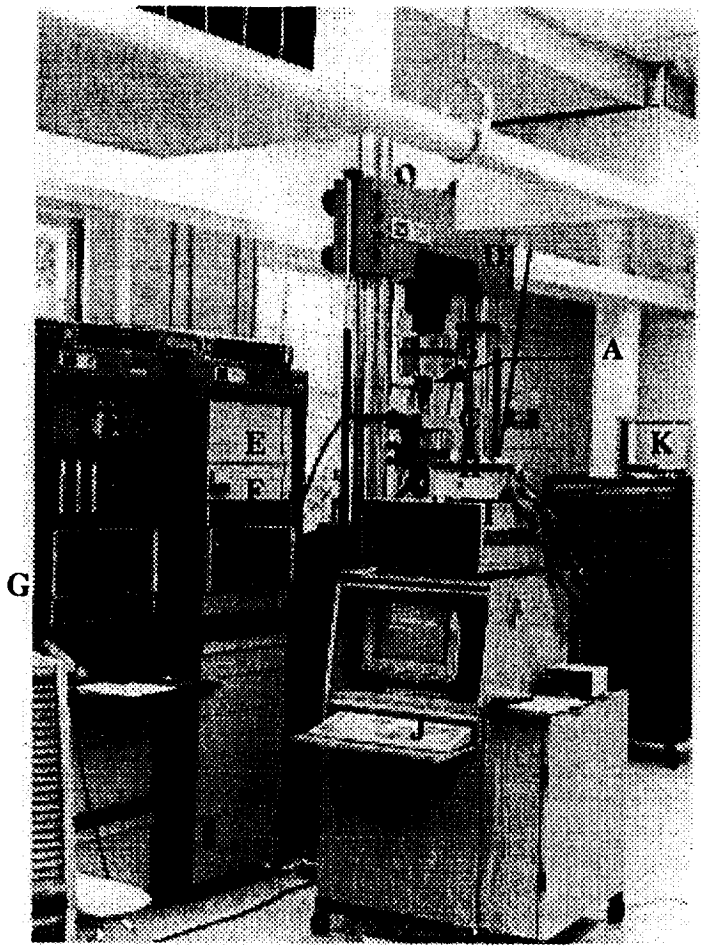

ITEM	DESCRIPTION	ITEM	DESCRIPTION
A	Specimen	G	Function Generator
B	Top Collet Grip	H	Connection Box
C	Bottom Collet Grip	I	Data Logger
D	MTS A/T Load Stand	J	386 PC
E	MTS Console	K	VCR
F	Micro-Profiler		

Figure 5.7: Test Equipment

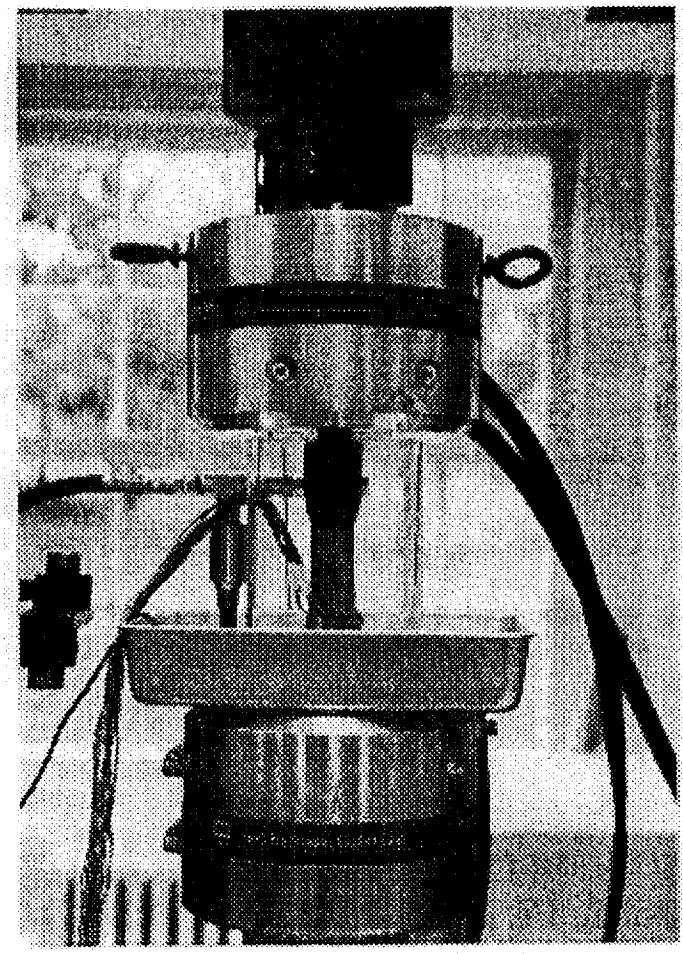

Figure 5.8: [0_4] Tube under internal pressure

transducers were used. Acoustic emissions (AE) were monitored during testing by mounting a microphone to the outer surface of the specimen and recording on a VCR tape. During the Type IA tests a specialized AE data acquisition system was used, this system is described in the following section.

5.2.4 Acoustic Emission Monitoring

Elastic wave energy propagating through a specimen can be converted into a decipherable voltage-time signature through high fidelity piezoelectric sensing of boundary motion. A point contact piezoelectric sensor was used to convert displacement into a voltage-time signature which was then sent to a storage oscilloscope for further

analysis and manipulation. The energy associated with an acoustic emission (AE) event is approximated by computing the RMS voltage of the signature.

AE energy for events in Type IA tests was obtained in the following fashion. Leads from the piezoelectric sensor were directed through charge amplifiers. High pass and low pass filters then eliminated environmental noise. Each channel was then split into four and connected to a LeCroy 7200 precision digital oscilloscope. A custom LeCroy RCL program triggered from incoming signals, used a waveform represented by 20,000 data points to compute the RMS voltage. The effective bandwidth was 20 kHz to 2 MHz. The program then stored the RMS voltage and the time of the event to a file. In this way, AE data could be corresponded with mechanical stress-strain data, as well as with AE recorded on tape.

CHAPTER 6

EXPERIMENTAL RESULTS

This chapter presents experimental results and discusses the features observed in tests conducted on the tubular specimens. The specimens are identified by numbers ranging from one to ten. Tubes #1-4 are $[0_4]$ composites, and tubes #5-10 are $[\pm 45]_s$ composites. Tubes #3, 6, 7, and 8 were not tested in the present study.

6.1 Initial Elastic Response

Before multiaxial loadings were applied to a specimen, simple tension, compression, torsion, and, in one case, internal pressure tests were conducted to determine the initial elastic properties of each specimen. The maximum stress in each of these tests was kept very small so as to minimize the possibility of causing damage or yielding in the specimen.

6.1.1 $[0_4]$ Tubes

The stress-axial strain and transverse-axial strain diagrams for axial tensile and compressive loading of Tube #1 are shown in Fig. 6.1. The stress-strain diagram (Fig. 6.1a) shows very little scatter in the data collected from the four strain gage rosettes located around its mid-length. Slightly less consistent data is obtained for the transverse-axial strain diagram (Fig. 6.1b); however, the data is generally considered good in light of the very small transverse strains obtained. The shear response to positive and negative torsion is shown in Fig. 6.2. Again, very uniform data were collected from the four rosettes, and as one would expect, no difference was observed in the response to positive or negative torsion. The results for internal pressure loading are presented in Fig. 6.3. No

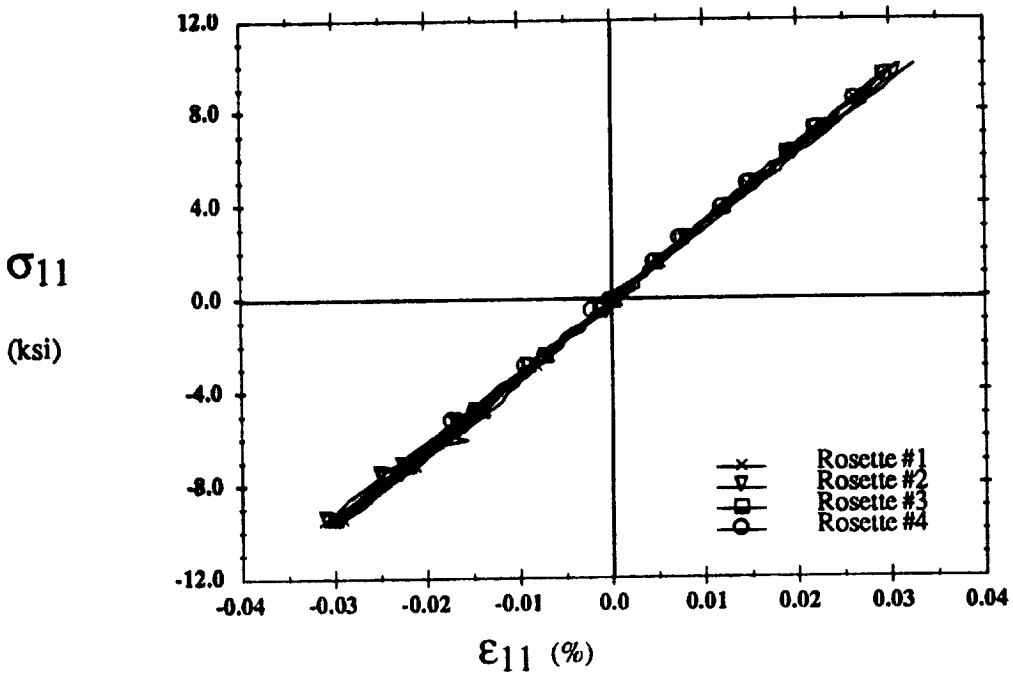

(a) Axial Stress-Strain

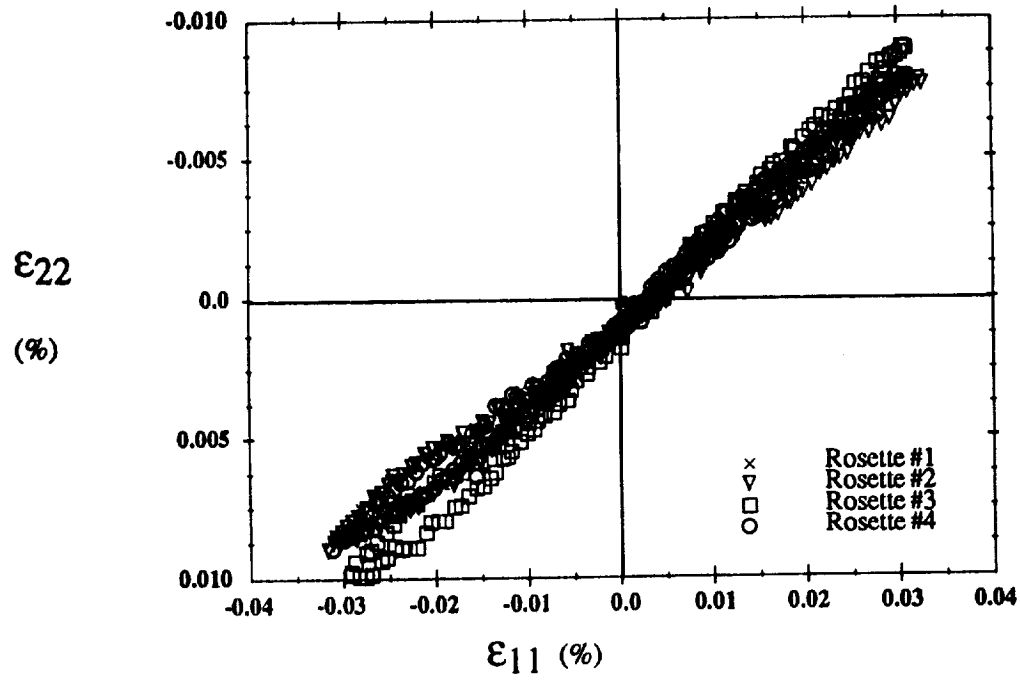

(b) Transverse-Axial Strains

Figure 6.1: [0_4] Axial Loading - Tube #1

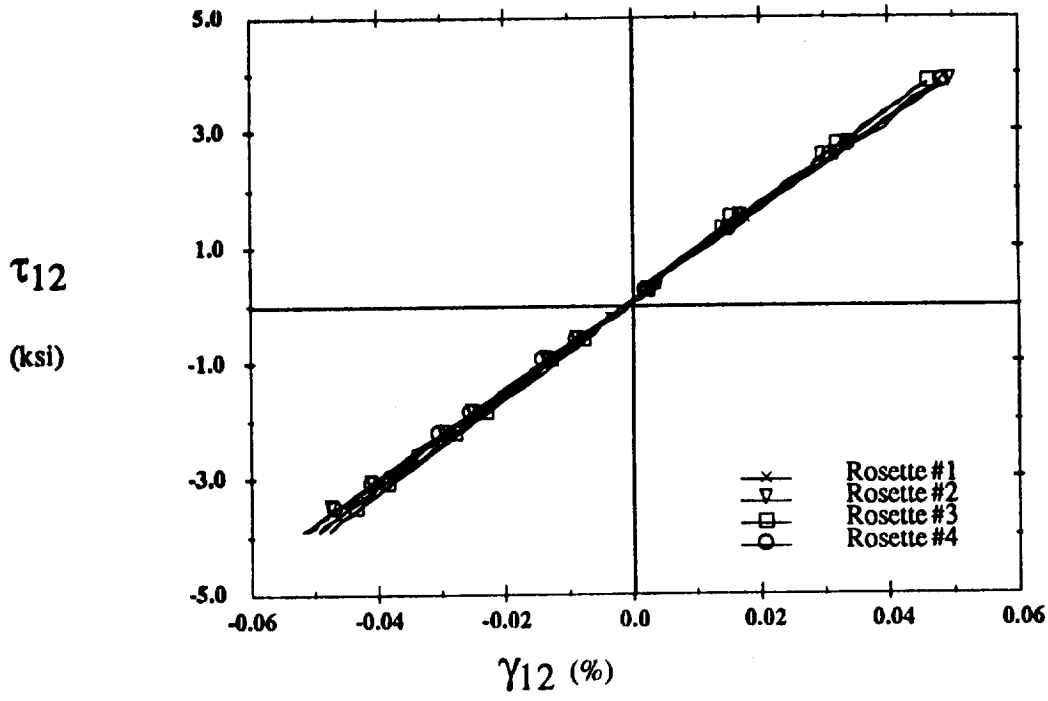

Figure 6.2: [0_4] Shear Loading - Tube #1

axial compression was applied, thus the slope of the stress-strain curve (Fig. 6.3a) does not represent the transverse stiffness of the tube. However, it can be observed that the response is very uniform for three of the four rosettes. Rosette #3 yields a substantially different transverse response that is also evident from Fig. 6.3b which presents the resulting axial strain versus transverse strain diagram. The inconsistent transverse response obtained by Rosette #3 could be due to material nonuniformity, which will be discussed later, and will otherwise be neglected for the remainder of this work.

The response to tensile loading from five strain gage rosettes bonded to Tube #2 is shown in Fig. 6.4. Uniform results are obtained from rosettes #1, 2, and 3, which are located around the mid-length of the tube. The rosettes mounted at either end of the gage length indicate a stiffer response due to stress concentrations created by the fixtures. These stress concentrations will be considered in more detail in Section 7.1. The shear response of the tube subjected to torsional loading is shown in Fig. 6.5, The results from all five

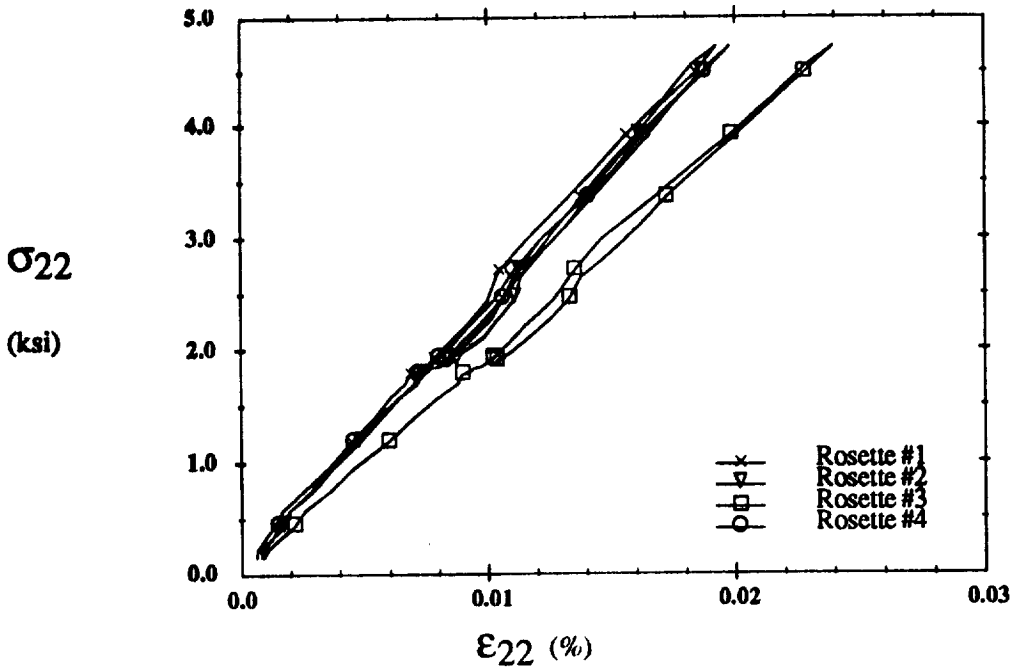

(a) Transverse Stress-Strain

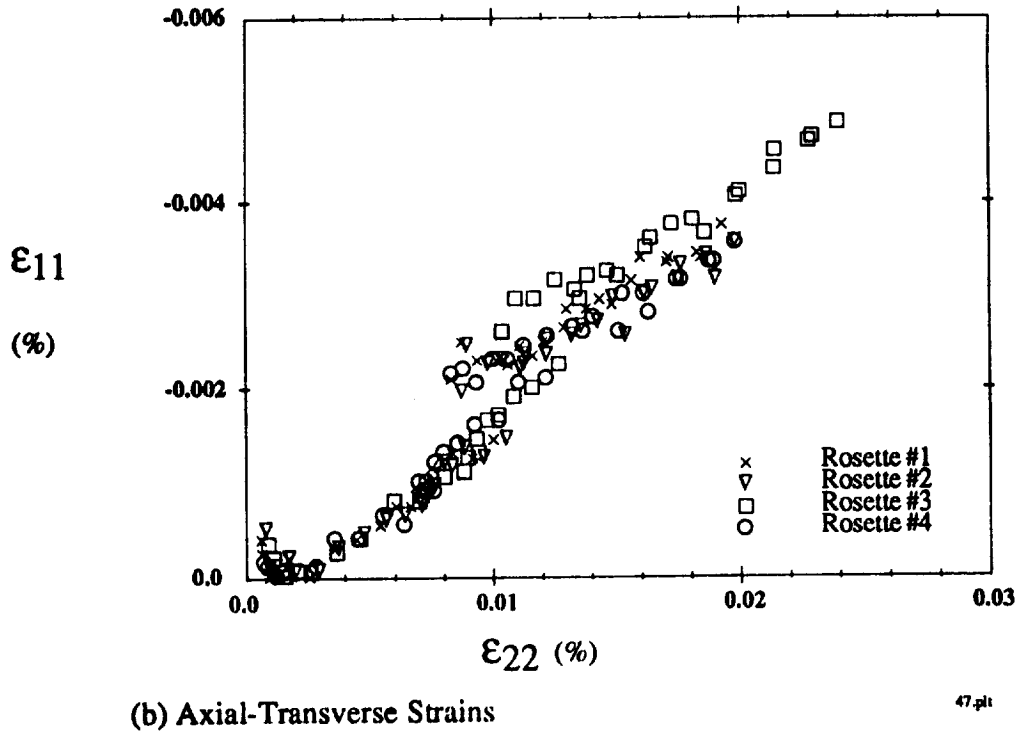

(b) Axial-Transverse Strains

Figure 6.3: [0_4] Transverse Loading - Tube #1

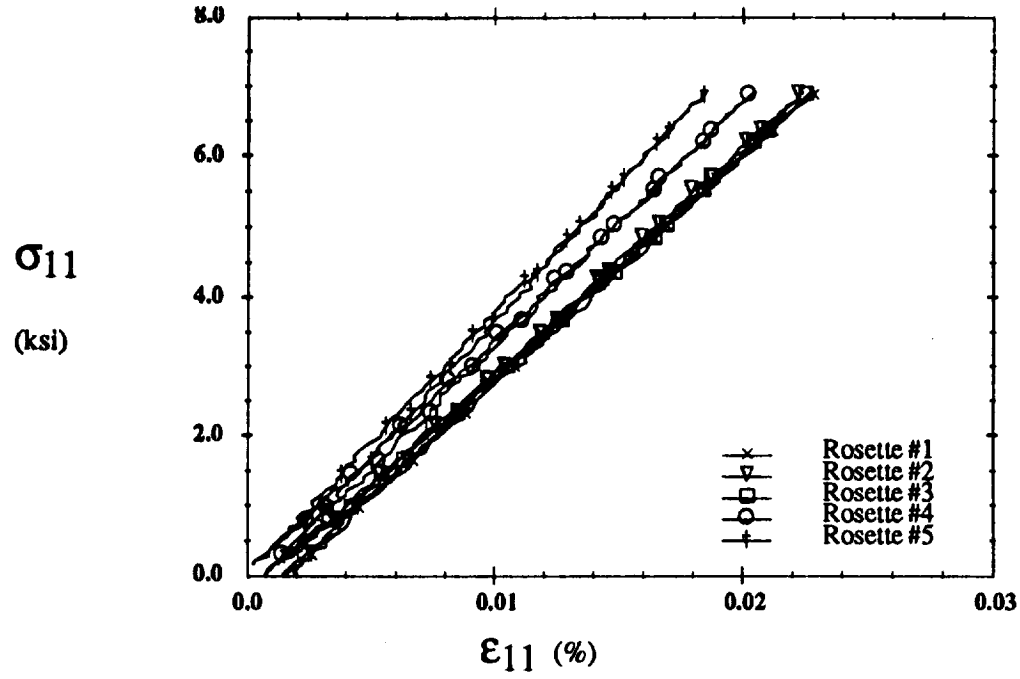

(a) Axial Stress-Strain

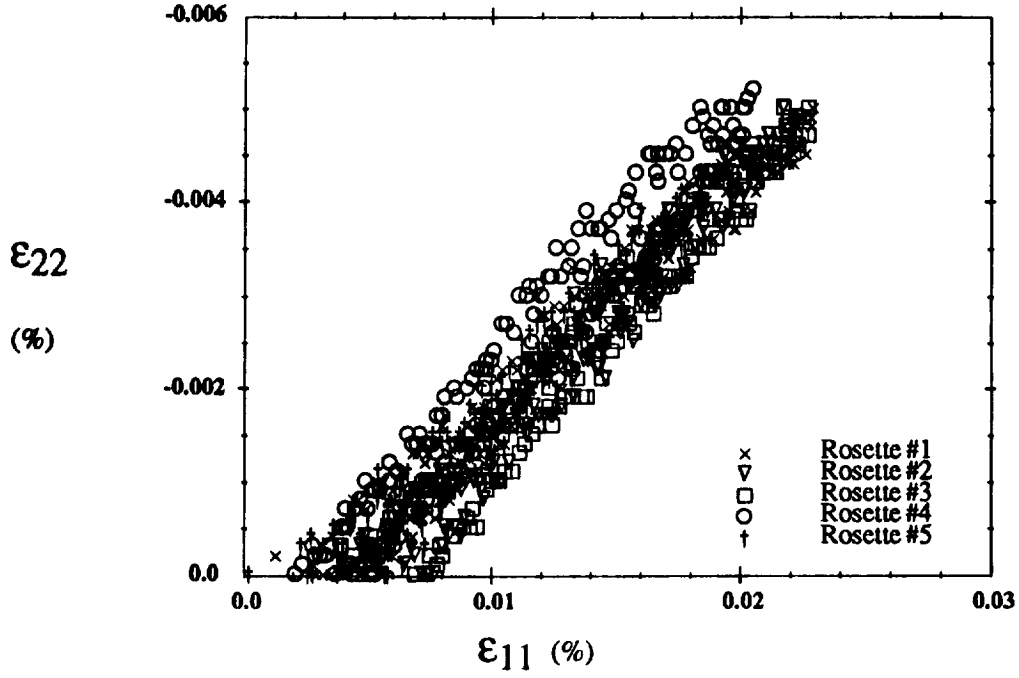

(b) Transverse-Axial Strains

Figure 6.4: [0_4] Axial Loading - Tube #2

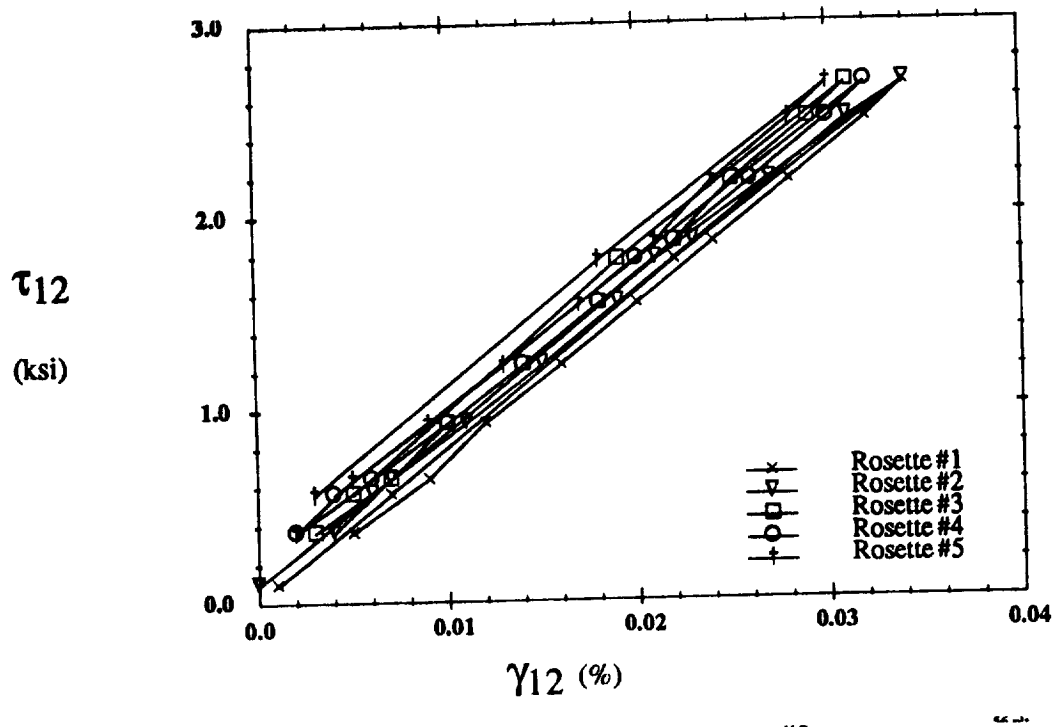

Figure 6.5: [0_4] Shear Loading - Tube #2

rosettes are relatively uniform, indicating that the fixtures do not create large shear stress concentrations under torsional loading.

Figure 6.6 displays the response of Tube #4 to tensile and compressive loadings. In these tests and many subsequent tests, data acquisition was initiated before closing the top grip because a small misalignment in the load train was suspected, even though the alignment of the load frame was within the manufacturer's tolerances. A small misalignment causes measurable bending strains upon gripping the specimen, these strains are responsible for the data from some rosettes not passing through the origin. Aside from the offset associated with these gripping strains, the three rosettes around the mid-length of the tube provide reasonably consistent results. The rosettes at the ends of the gage length yield a stiffer response, and inexplicably, one gives a higher, and one a lower Poisson's ratio than the mid-length rosettes. The shear response to positive and negative torsion is shown in Fig. 6.7; again the mid-length rosettes provide consistent results, aside

C-2

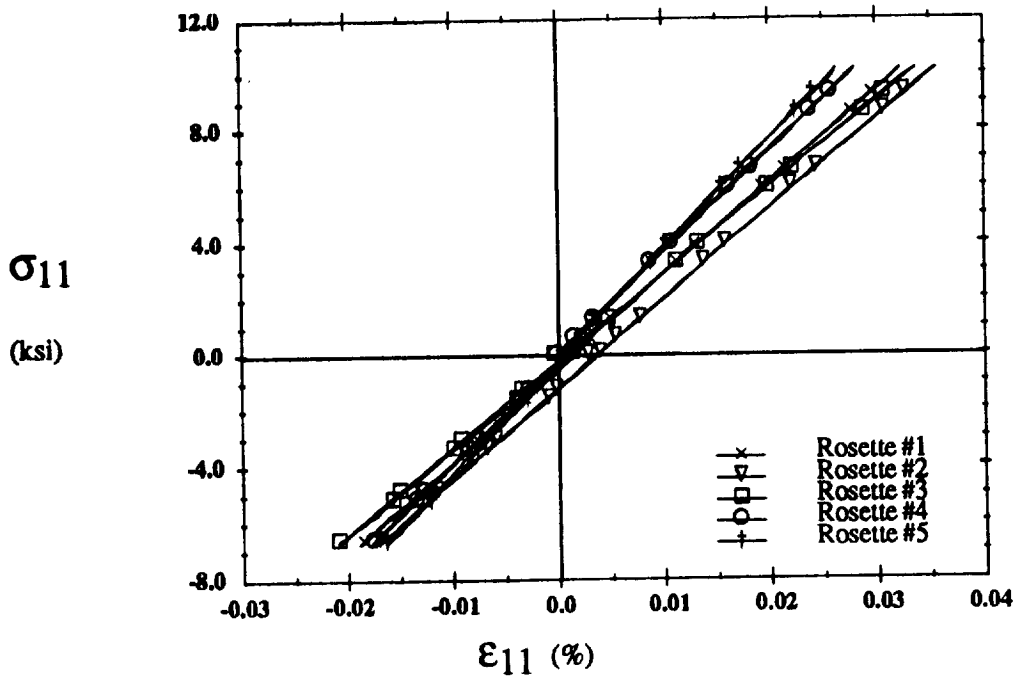

(a) Axial Stress-Strain

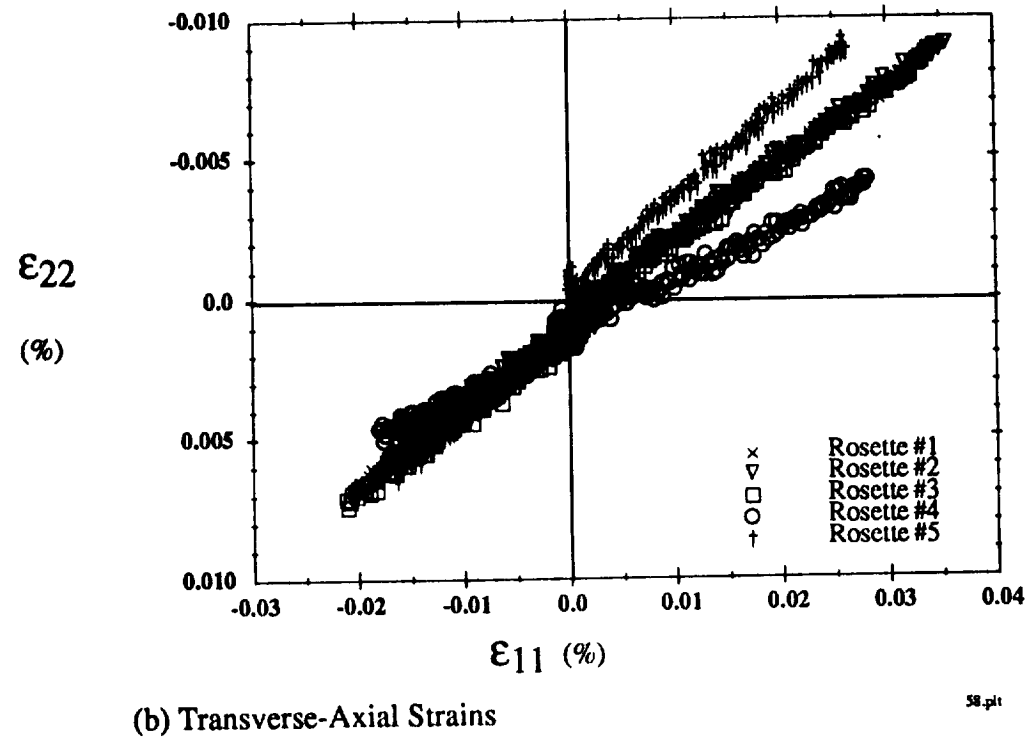

(b) Transverse-Axial Strains

Figure 6.6: [0_4] Axial Loading - Tube #4

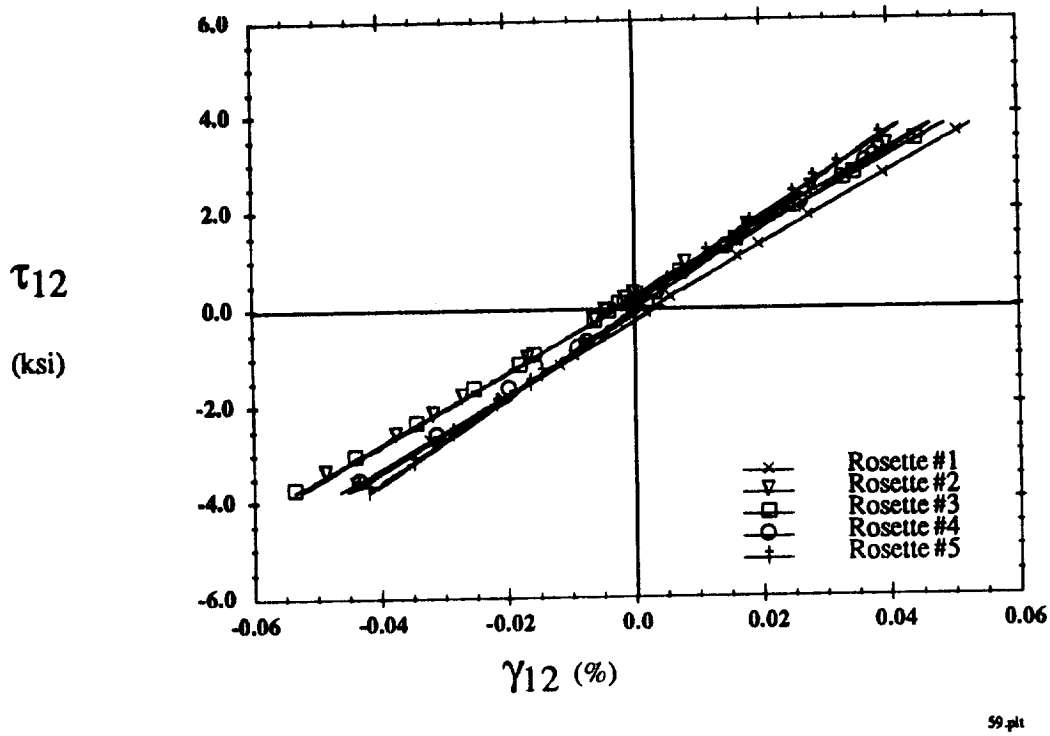

Figure 6.7: [0_4] Shear Loading - Tube #4

from the initial strain offset due to gripping.

The initial elastic properties for [0_4] tubes determined from all strain gages are summarized in Table 6.1. Predictions from the theoretical model discussed in Chapters 2 and 3 are also presented for both perfect bonding and no bond between the fiber and matrix. Comparisons between these predictions and experimental data are presented in Section 7.1.

6.1.2 $[\pm 45]_s$ Tubes

The axial stress-strain diagram and transverse-axial strain diagram are shown in Fig. 6.8 for tensile loading applied to Tube #5. Unlike all other tests no unloading data was recorded. The stress-strain response (Fig. 6.8a) is not as uniform as it was for the [0_4] tubes. There is a range of stiffnesses (16.4 to 17.8 Msi) measured from the three strain gage rosettes located at the mid-length of the tube. The scatter observed in the transverse-

Table 6.1: [0_4] Initial Elastic Properties

		E_{11} (Msi)	ν_{12}	E_{22} (Msi)	ν_{21}	G_{12} (Msi)
Theory	Perfect Bond	31.0	0.312	23.8	0.240	8.29
	No Bond	31.0	0.312	5.97	0.0703	2.10
Experiment	Tube #1 R1	32.4	0.282	21.6	0.187	7.69
	R2	30.7	0.263	21.2	0.207	7.49
	R3	32.3	0.333	17.1	0.140	7.84
	R4	32.1	0.289	21.0	0.193	7.63
	Tube #2 R1	31.9	0.251	-	-	7.85
	R2	32.2	0.293	-	-	8.00
	R3	31.7	0.290	-	-	8.11
	R4	33.6	0.298	-	-	7.69
	R5	37.6	0.275	-	-	8.20
	Tube #4 R1	32.4	0.263	-	-	7.48
	R2	31.7	0.270	-	-	7.56
	R3	30.8	0.274	-	-	7.35
	R4	36.2	0.188	-	-	8.06
	R5	38.5	0.338	-	-	8.82

axial strain data (Fig. 6.8b) is most probably due to numerical inaccuracies (too few significant figures and round-off) in the strain transformation calculations, or possibly to background electronic noise. Figure 6.9 presents the shear response of the tube to positive and negative torsional loading. The data is very uniform with Rosette #2 displaying a slightly stiffer response than the other four rosettes. No shear stress concentrations from the fixtures are notable. Likewise, no significant difference in stiffness is evident between positive and negative torsion.

The response obtained from four rosettes located around the mid-length of Tube

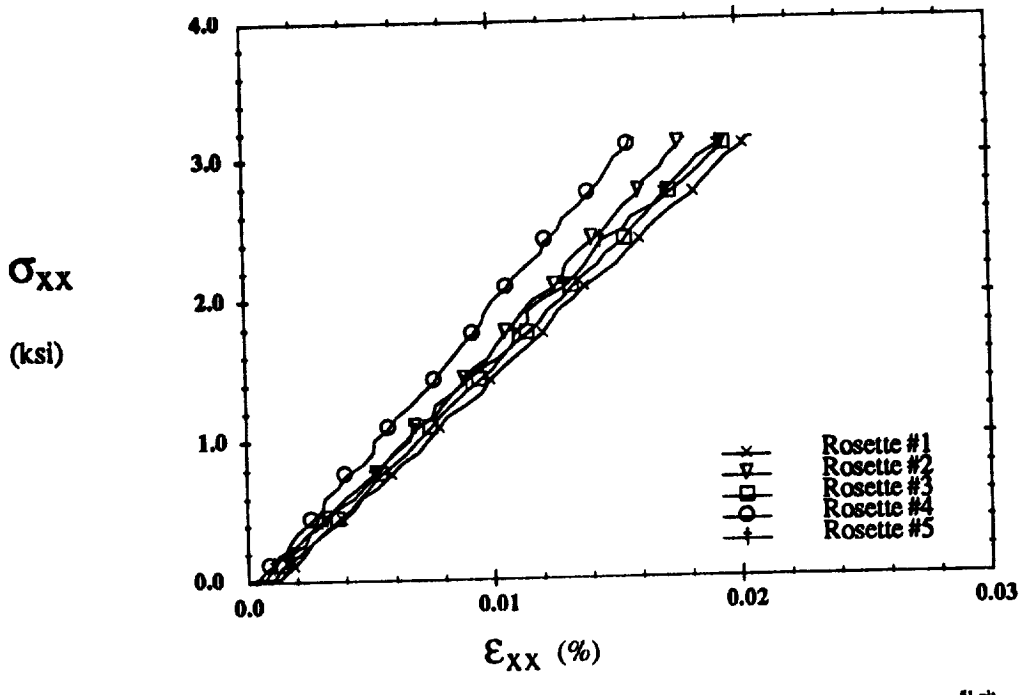

(a) Axial Stress-Strain

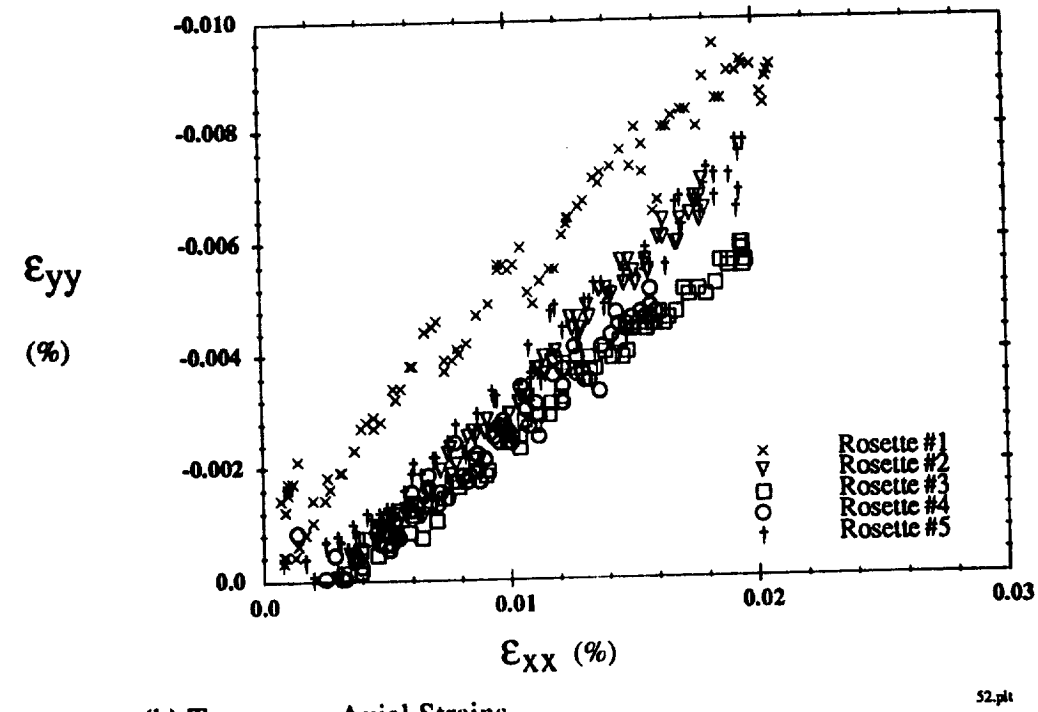

(b) Transverse-Axial Strains

Figure 6.8: $[\pm 45]_s$ Axial Loading - Tube #5

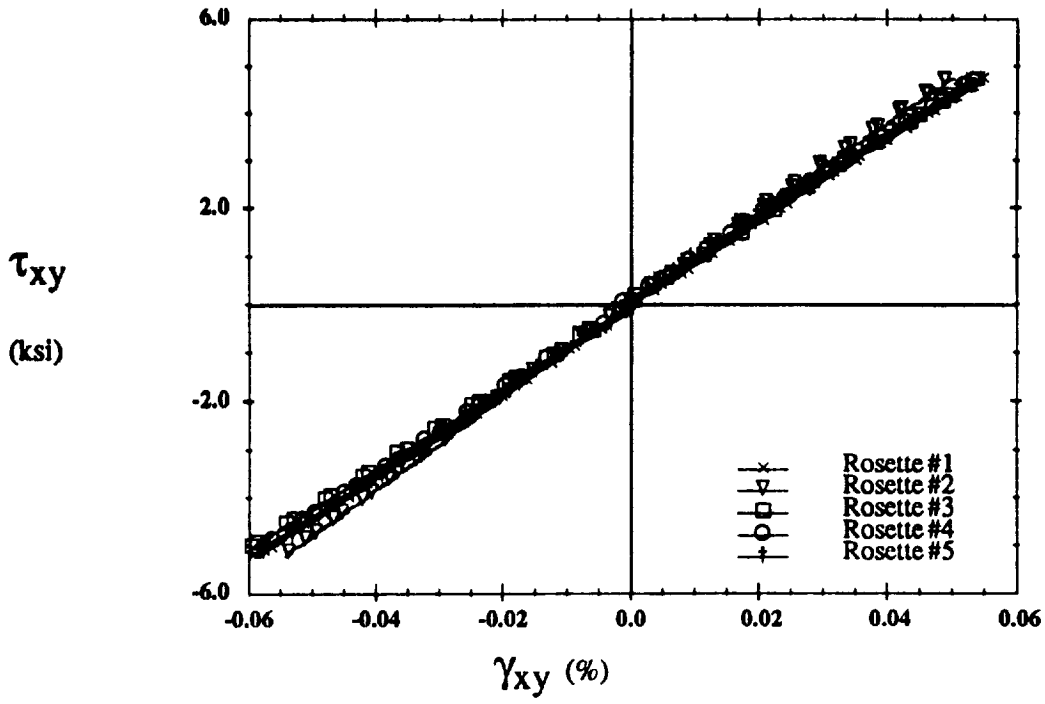

Figure 6.9: $[\pm 45]_s$ Shear Loading - Tube #5

#9, to tensile loading is shown in Fig. 6.10. As for Tube #5, there is a relatively wide range of stiffnesses (17.2 to 21.0 Msi) indicated in Fig. 6.10a. The transverse-axial strain diagram (Fig. 6.10b) is plotted for only two rosettes because data was not collected from all gages in two of the rosettes; hence transverse and shear strain data were not available. The shear response to torsional loading shown in Fig. 6.11 is reasonably consistent for the two rosettes used.

The range of axial stiffnesses measured from different strain gages located around the mid-length of Tubes #5 and 9 suggest that the $[\pm 45]_s$ tubes are nonuniform. Four additional longitudinal TML FLA-2-11 strain gages were bonded at strategic locations around the mid-length of Tube #10. Figure 6.12a shows the response to tensile loading obtained from seven strain gages, located around the mid-length of the tube. The figure clearly shows a wide range of stiffnesses (15.1 to 21.1 Msi). Gages #3, 6, and 7 are the 0° gages of the original rosettes mounted on the tube. While Gages #6 and 7 were far

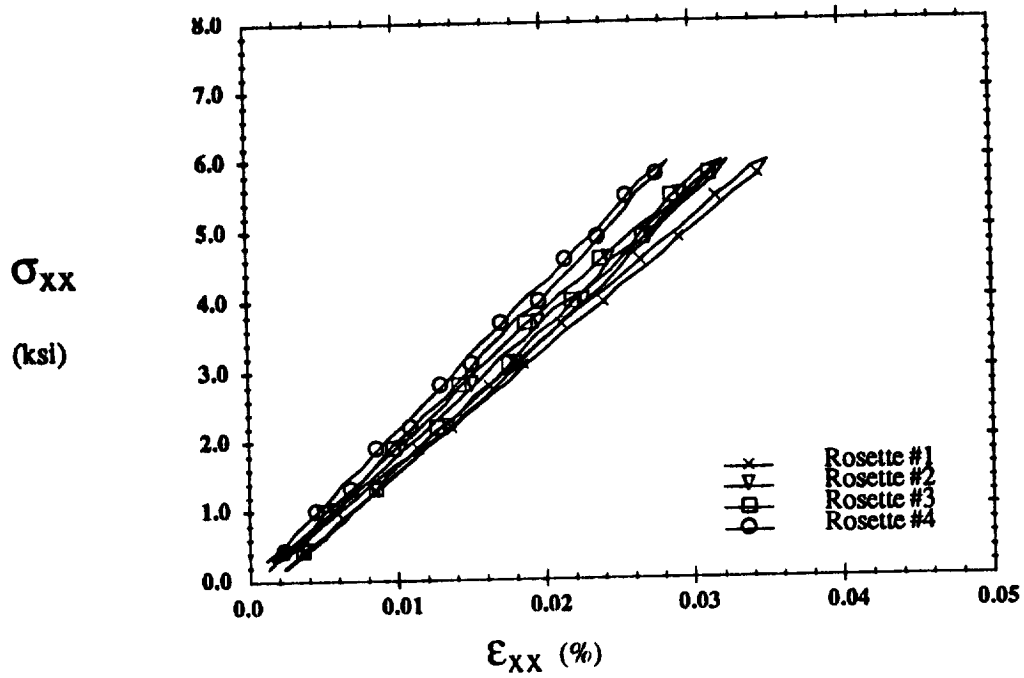

(a) Axial Stress-Strain

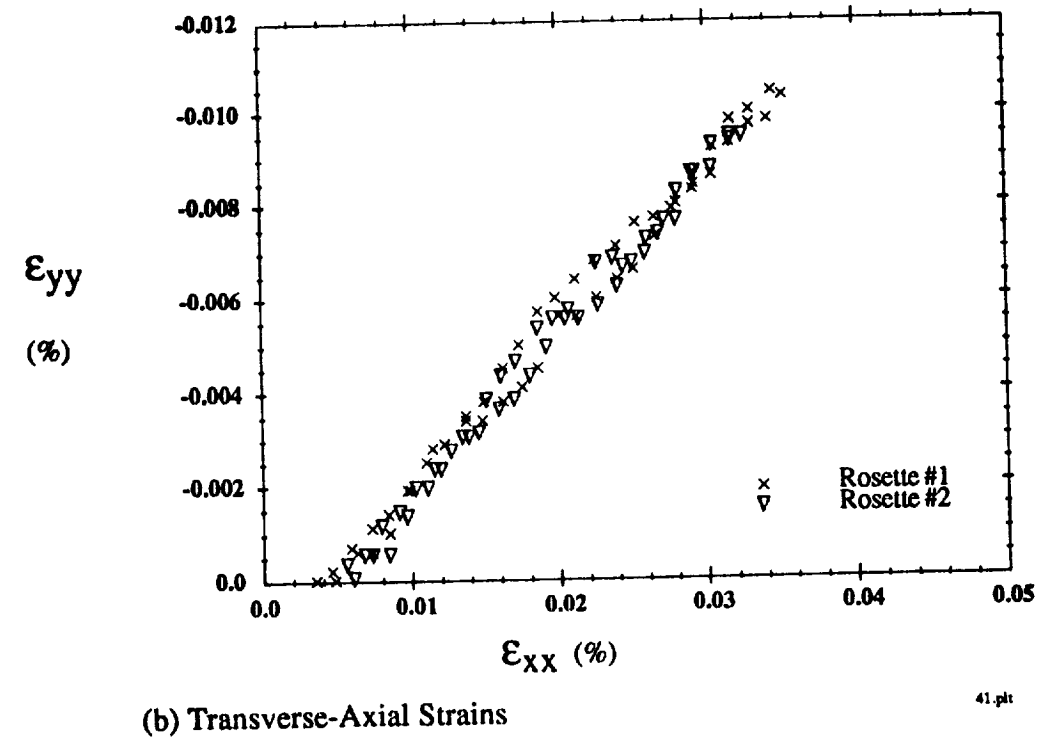

(b) Transverse-Axial Strains

Figure 6.10: $[\pm 45]_s$ Axial Loading - Tube #9

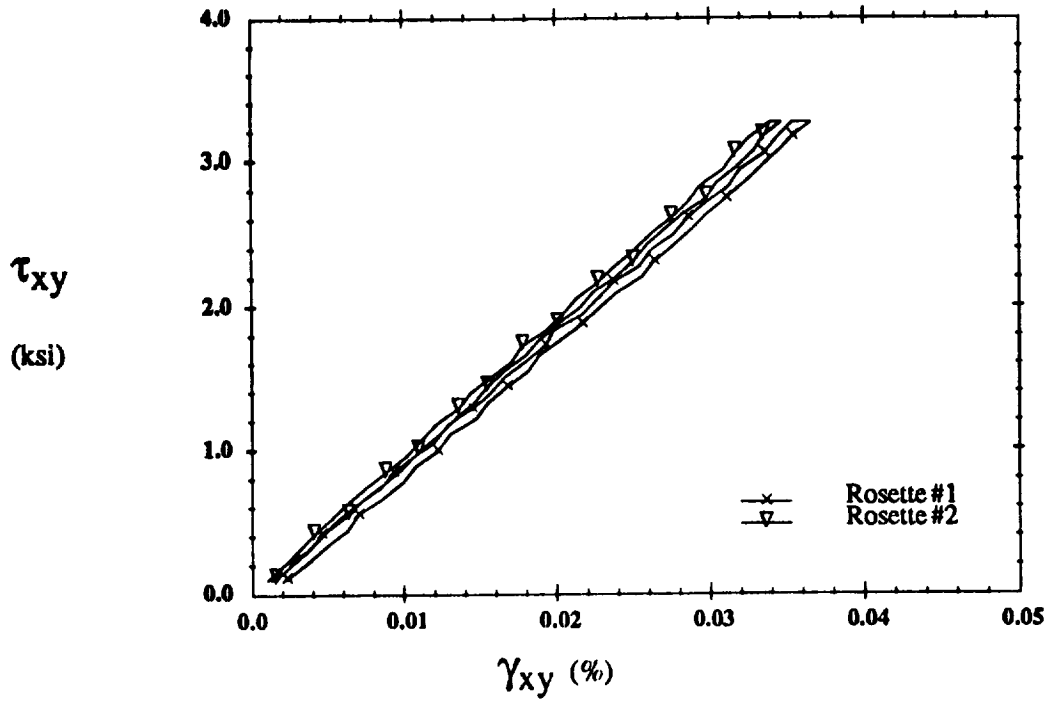

Figure 6.11: $[\pm 45]_s$ Shear Loading - Tube #9

removed from any visible anomalies, Gage #3 was relatively close to a seam in the outermost ply. Gages #1 and 2 were mounted in a region that appeared to be rich in fibers, adjacent to a visible seam in the outermost ply. Gage #5 was mounted in the seam, a region that appeared to have few, if any, fibers in the outermost ply. The gages in the fiber-rich region display a much stiffer response, while the gage in the fiber-depleted region displays a much more compliant response, than do the gages where no surface irregularities are present. It is noted that possible seams and other irregularities in the inner three plies are hidden from view, but would also effect the local stiffness of the composite, although their effect on strain gages mounted on the outer surface would be less pronounced. The transverse-axial strain diagram (Fig. 6.12b) for the original rosettes suggests that the anomalies have little, or no, effect on Poisson ratio.

Figure 6.13 shows the shear response of the tube (#10) to positive and negative torsional loading. Rosette #3, contains Gage #3 discussed above, and is located in the

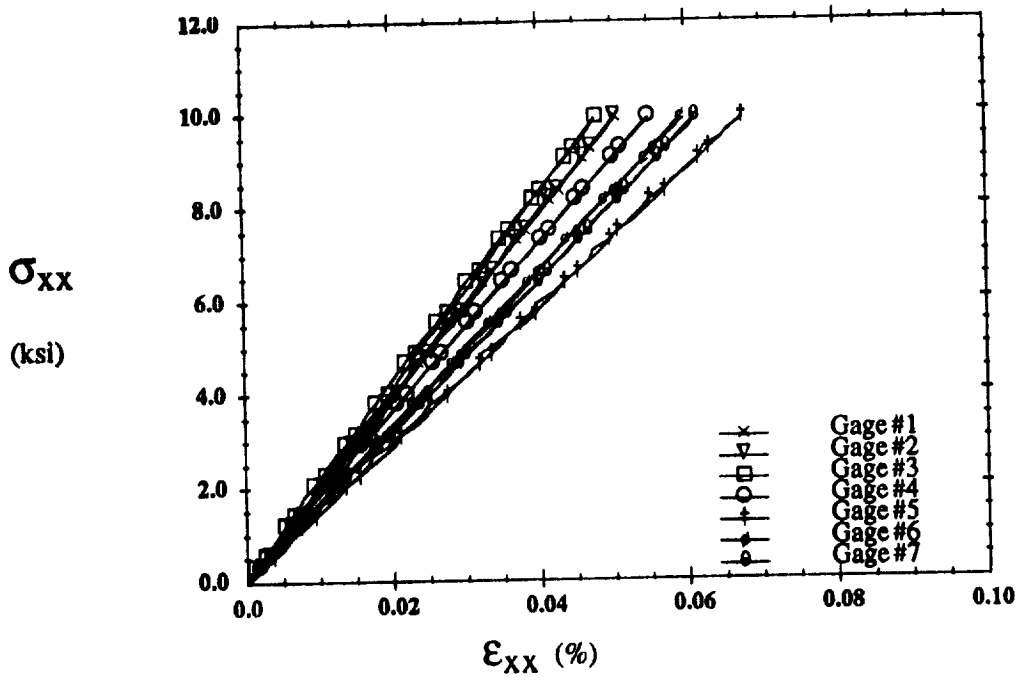

(a) Axial Stress-Strain

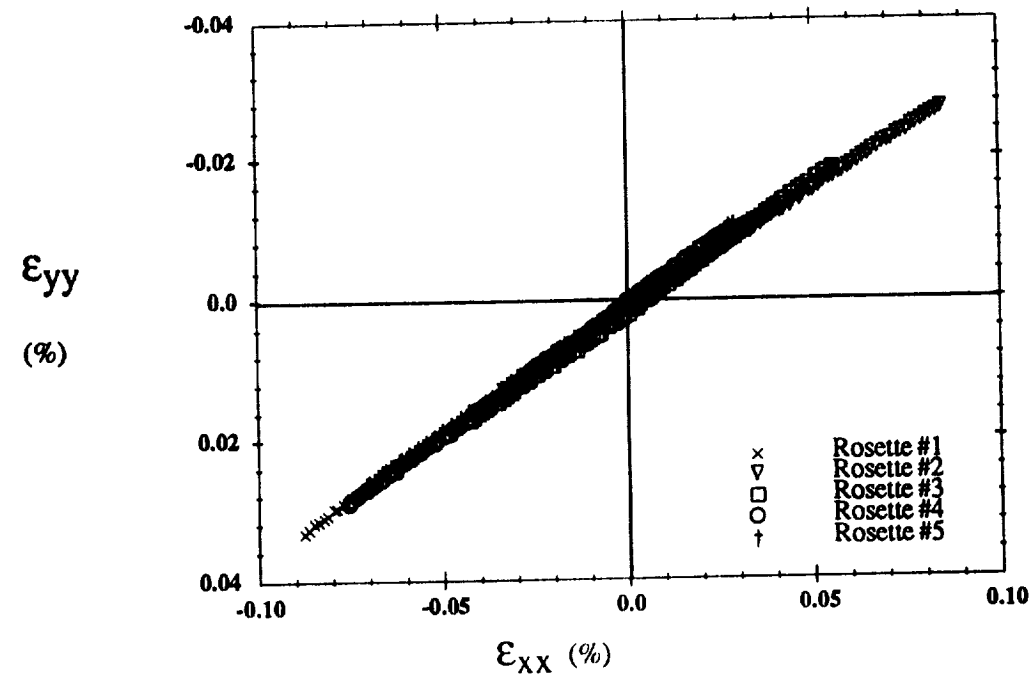

(b) Transverse-Axial Strains

Figure 6.12: $[\pm 45]_s$ Axial Loading - Tube #10

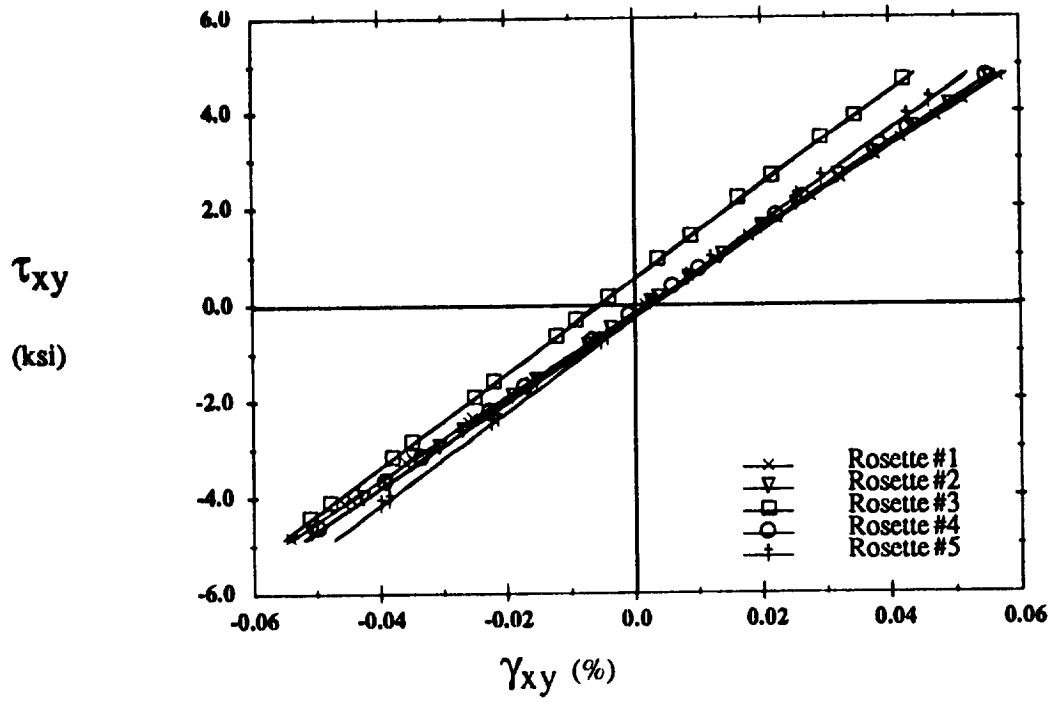

Figure 6.13: $[\pm 45]_s$ Shear Loading - Tube #10

proximity of a seam in a fiber-rich region. Its shear response is stiffer than that of the other rosettes located around the mid-length of the tube, indicating that this type of anomaly can affect both axial and shear stiffness.

The initial elastic properties for $[\pm 45]_s$ tubes determined from all strain gages are summarized in Table 6.2. Predictions based on lamination theory, as presented in Chapters 2 and 3, are also given for both perfect bonding and no bond between the fiber and matrix. Comparisons between these predictions and experimental data are presented in Section 7.2.

6.2 Multiaxial Loading Results

In this section the results of the multiaxial loadings previously described in Section 5.2 and shown schematically in Fig. 5.6 are presented and discussed. These types of loading cycles made it feasible to collect a large amount of unloading data as well as

Table 6.2: $[\pm 45]_s$ Initial Elastic Properties

		E_{xx} (Msi)	ν_{xy}	E_{yy} (Msi)	ν_{yx}	G_{xy} (Msi)
Theory	Perfect Bond	23.0	0.388	23.0	0.388	10.8
	No Bond	6.98	0.664	6.98	0.664	8.47
Experiment	Tube #5 R1	16.4	0.433	-	-	8.69
	R2	17.8	0.459	-	-	9.45
	R3	16.7	0.351	-	-	8.62
	R4	19.8	0.370	-	-	8.60
	R5	16.5	0.418	-	-	8.71
	Tube #9 R1	17.2	0.331	-	-	9.57
	R2	18.6	0.352	-	-	9.13
	R3	19.1	-	-	-	-
	R4	21.0	-	-	-	-
	Tube #10 (G7) R1	16.1	0.360	-	-	8.59
	(G6) R2	16.7	0.332	-	-	8.85
	(G3) R3	21.1	0.362	-	-	9.75
	R4	18.5	0.360	-	-	8.93
	R5	20.3	0.369	-	-	9.70
	(G1)	19.8	-	-	-	-
	(G2)	19.8	-	-	-	-
	(G4)	18.1	-	-	-	-
	(G5)	15.1	-	-	-	-

loading data. Having both loading and unloading data makes it possible to delineate inelastic deformation due to damage from that due to matrix plasticity.

6.2.1 $[0_4]$ Tubes

In the previous section it was shown that the response of a $[0_4]$ tube is very uniform around the mid-length of the tube. Results will now be presented from one strain gage rosette representative of the specimen response at the mid-length of the tube.

6.2.1.1 Type I Loading

The axial and shear responses of a $[0_4]$ tube subjected to Type I loading are shown in Fig. 6.14 and 6.15, respectively. The maximum axial stress is increased with each successive cycle and a small increment of shear stress is applied at this maximum axial stress. The axial load cycles shown in Fig. 6.14 have been offset for clarity. The shear response shown in Fig. 6.15 displays an elastic coupling phenomenon during the axial loading and unloading portions of the tests. During axial loading shear strains are accumulated, then upon axial unloading the accumulated shear strains are released. This coupling had no apparent effect on the shear stiffness, or the inelastic response, possibly because shear stresses were kept very low. While the exact cause of the coupling is uncertain, it seems plausible that the small misalignment in the load train could be the cause. Finally, it is noted that some degree of coupling was observed in virtually all multiaxial loading tests.

Both axial and shear responses were generally linear elastic until failure occurred. The maximum axial stress in cycle #12 was 119 ksi, this load cycle was terminated prior to application of shear stresses because a very loud acoustic emission was heard. Inspection of the specimen revealed that the adhesive bonding the tube to the top fixture had failed, however the bolt was still bonded in place. The tube failed in the top grip during cycle #13 at an axial stress of 108 ksi. As shown in Fig. 6.16, the failure surface ran

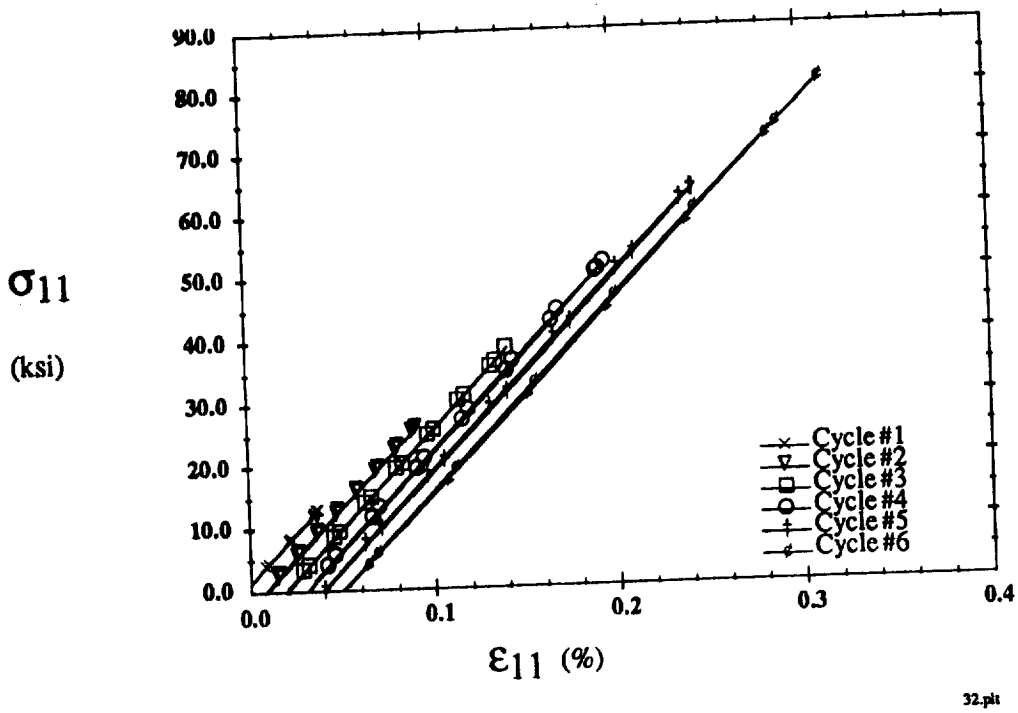

(a) Cycles #1-6

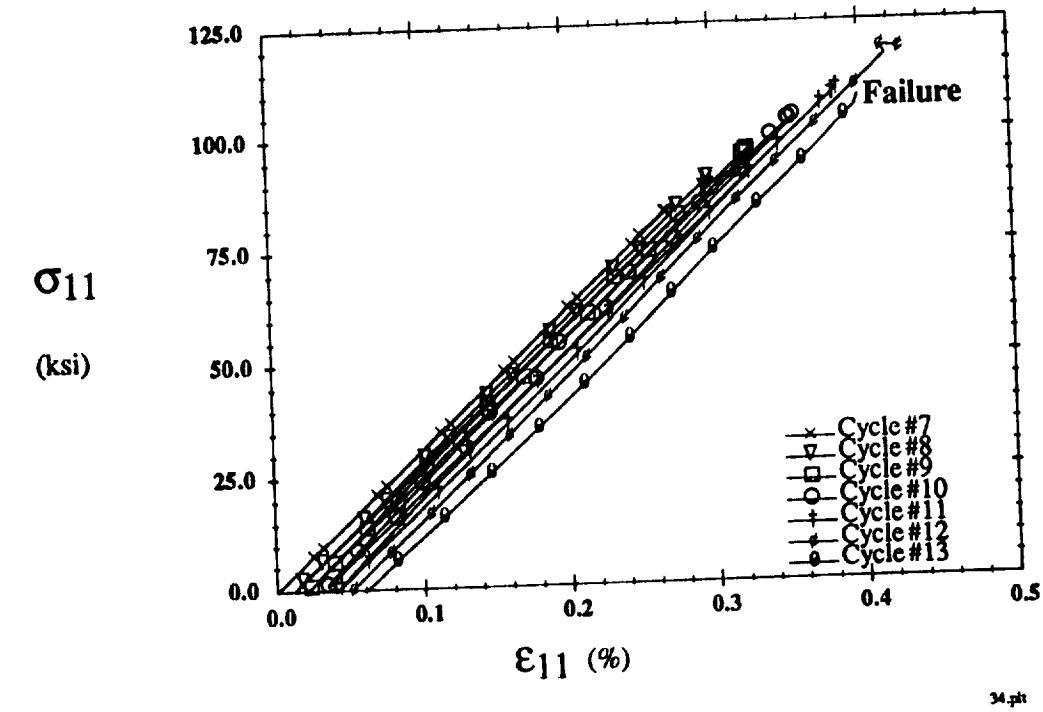

(b) Cycles #7-13

Figure 6.14: [0_4] Type I Loading - Axial Response

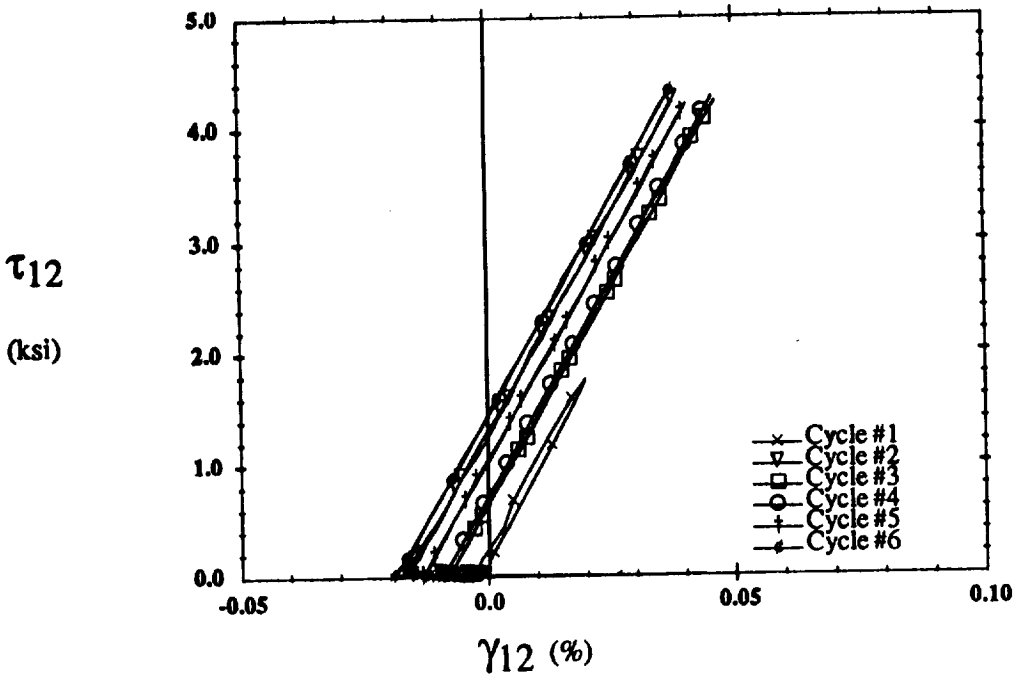

(a) Cycles #1-6

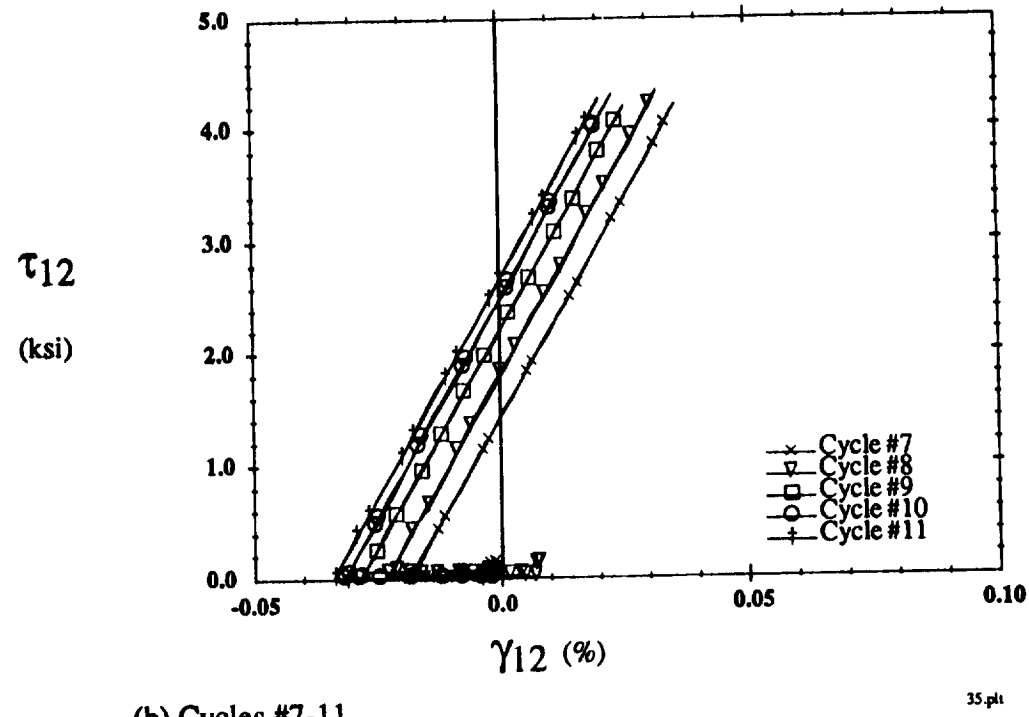

(b) Cycles #7-11

Figure 6.15: [0_4] Type I Loading - Shear Response

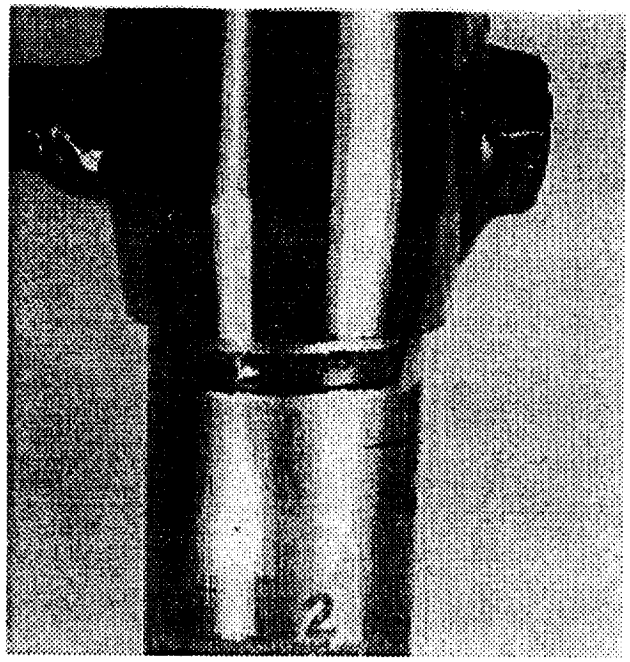

Figure 6.16: [0_4] Type I loading fracture surface

across the tube near the bottom of the steel plug bonded to the top of the tube, and connected to the bolt holes on either side of the specimen. Visual microscopy revealed that the fracture surface transverse to the fibers occurred at the closest moly wire to the end of the steel plug. A finite element analysis of the tube was performed to better understand this failure, the results are discussed in Section 7.1. As indicated by data in Fig. 6.17, no stiffness degradation was observed.

6.2.1.2 Type II Loading

The shear and axial responses for Type II loading on a [0_4] tube are shown in Fig. 6.18 and 6.19, respectively. In Type II tests the shear stress is increased with each cycle, and a small increment of tensile stress is applied at the peak shear stress. The shear responses in Fig. 6.18 are artificially offset for clarity. The axial responses (Fig. 6.19) display the elastic coupling discussed for Type I loading. Both shear and axial responses are linear elastic until cycle #13. Low level acoustic emissions (AE) initiated at a shear

stress of 35 ksi in cycle #12. The intensity of these emissions increased with increasing shear stress. In the subsequent cycle (#13), AE began at the shear stress of 37 ksi. When the shear stress of 39.5 ksi was attained a distinct knee was observed in the shear response. After this knee, the response resembled that of a nearly perfectly plastic material. The unloading response was nonlinear with an initial stiffness of 6.5 Msi, which is less than the initial loading stiffness of 7.4 Msi. The final cycle (#14) displayed a nonlinear response beginning at approximately 10 ksi, with AE starting at 38 ksi. The initial shear stiffness was degraded by 10%, and again a distinct knee developed, followed by a linear hardening type response.

The inelastic response obtained from the three rosettes located around the mid-length of the tube was substantially different, so data from all three rosettes is presented

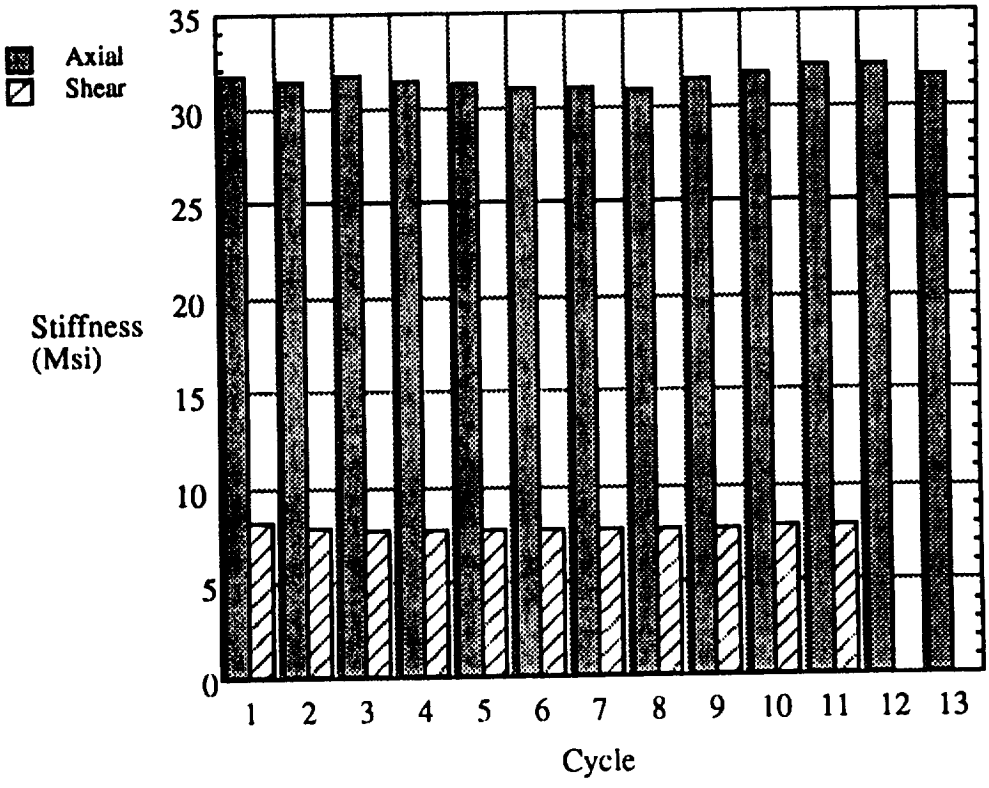

Figure 6.17: [0_4] Type I Loading Stiffnesses

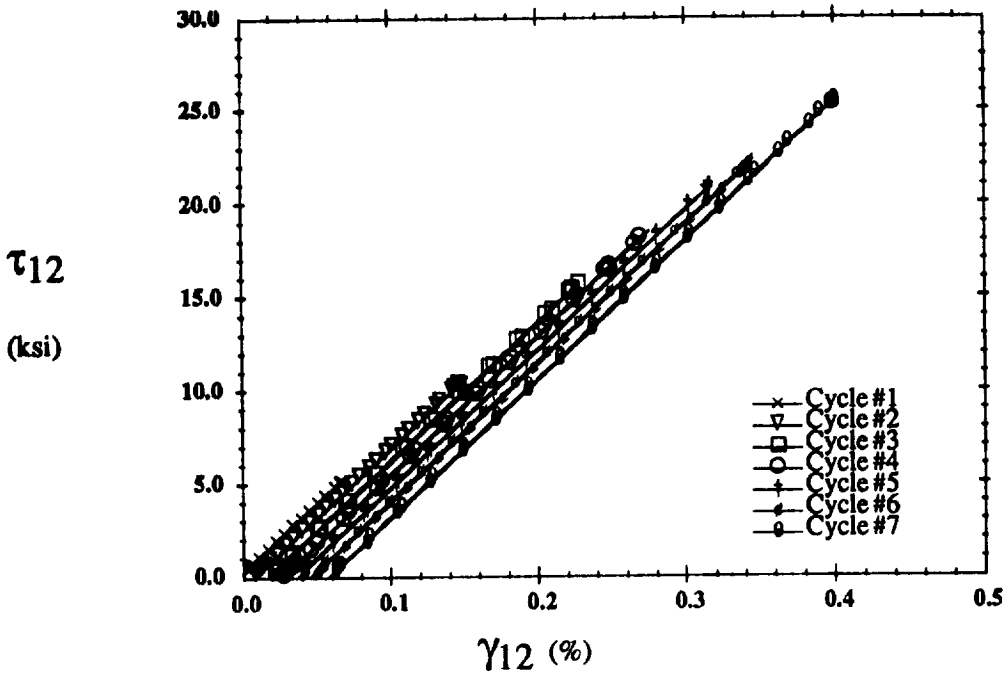

(a) Cycles #1-7

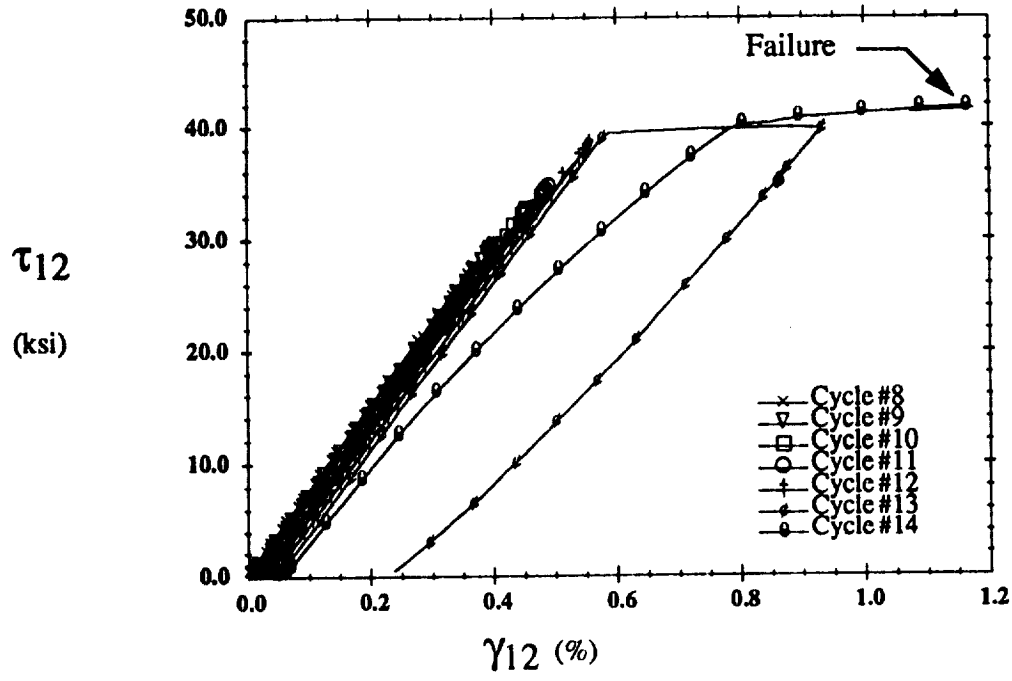

(b) Cycles #8-14

Figure 6.18: [0_4] Type II Loading - Shear Response

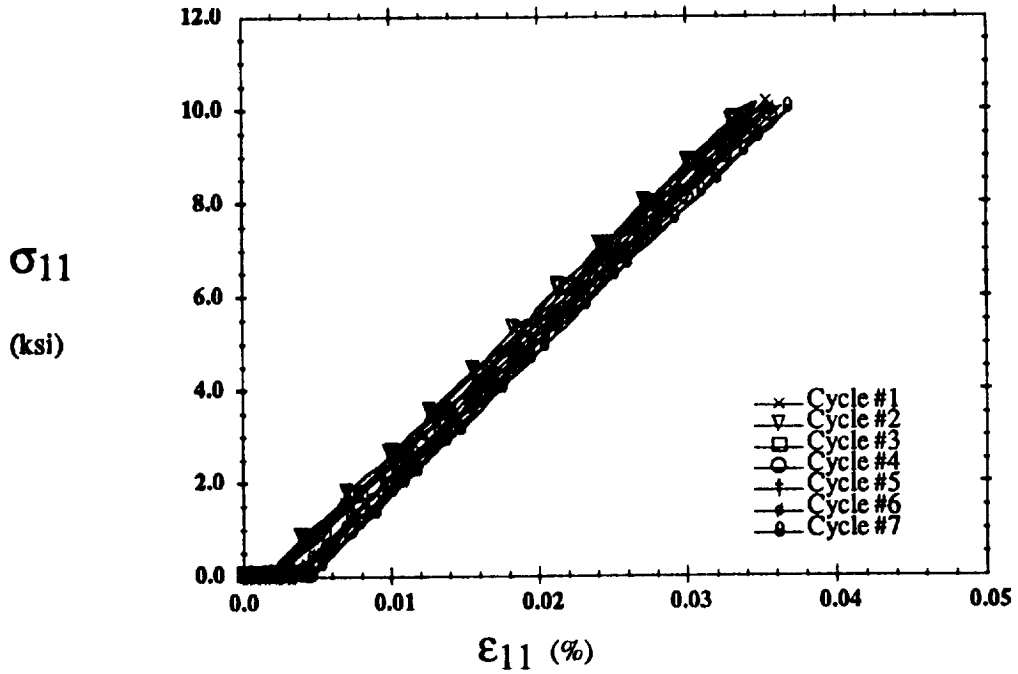

(a) Cycles #1-7

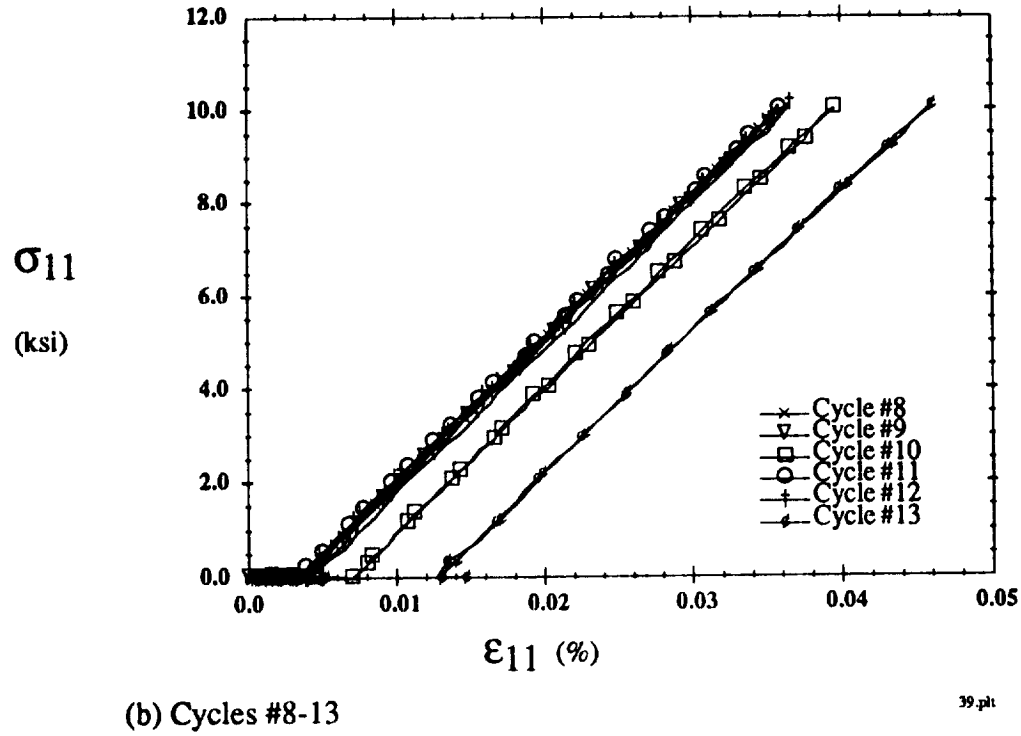

(b) Cycles #8-13

Figure 6.19: $[0_4]$ Type II Loading - Axial Response

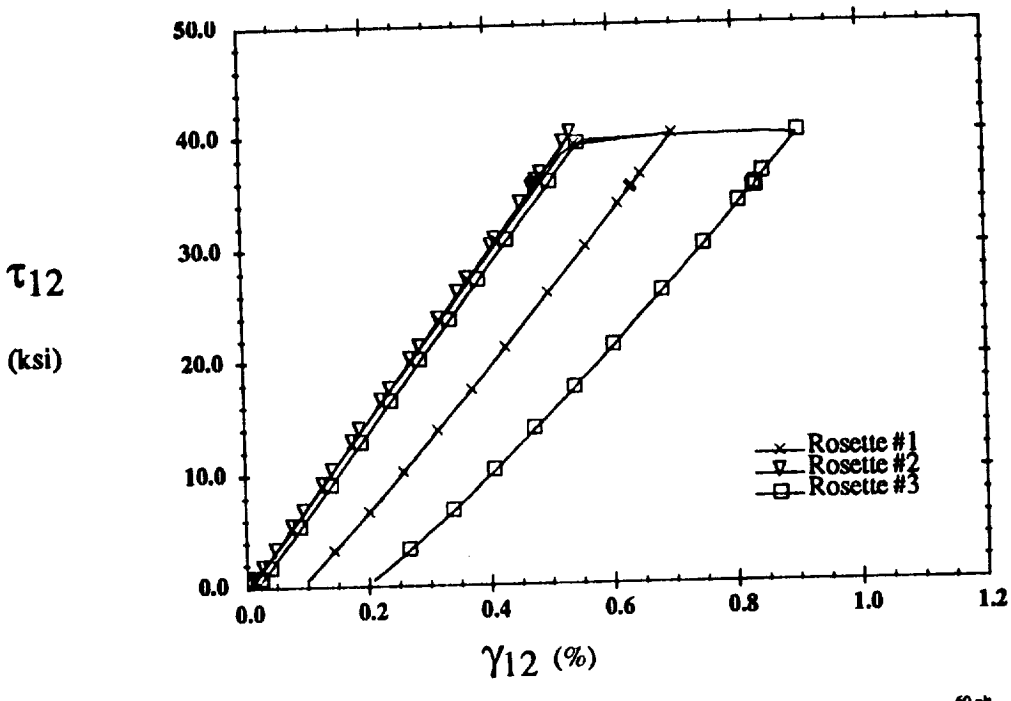

(a) Cycle #13

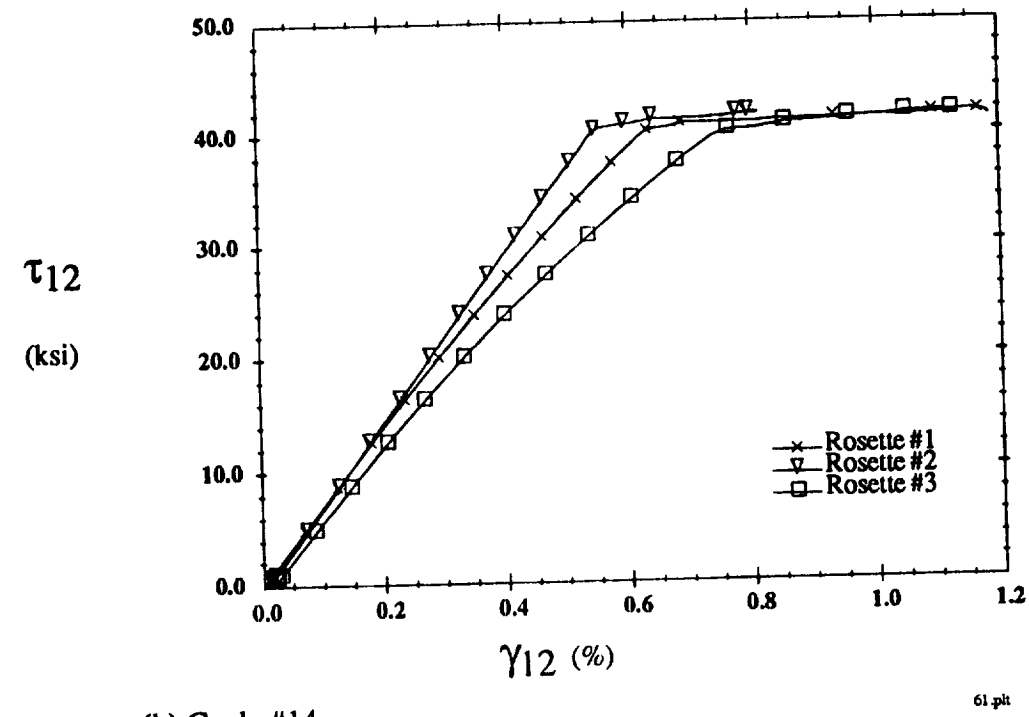

(b) Cycle #14

Figure 6.20: [0_4] Type II Loading - Shear Response

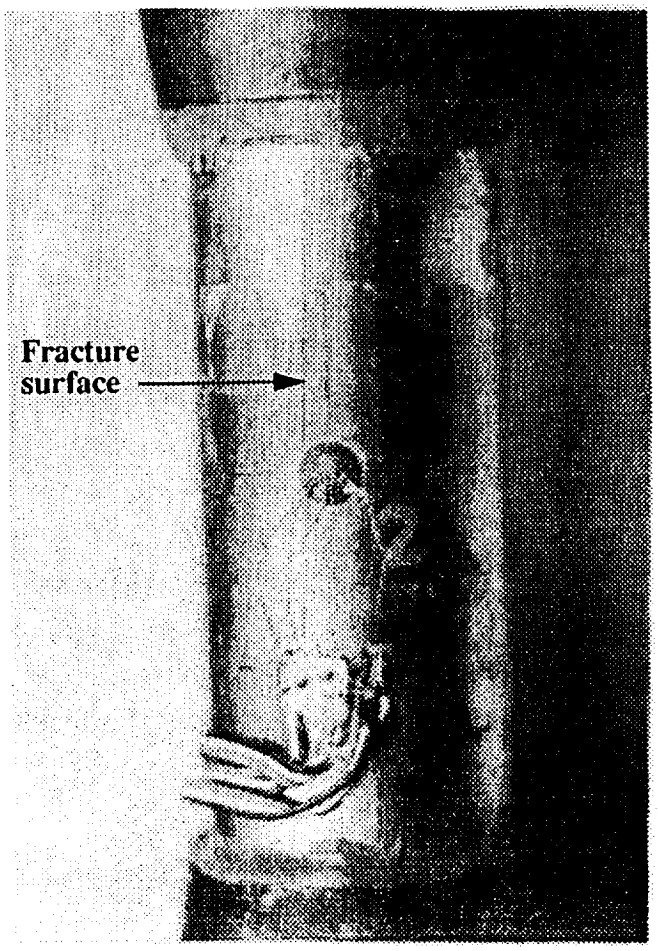

Figure 6.21: [04] Type II loading fracture surface

for cycles #13 and 14 in Fig. 6.20. Failure, in the form of a fine longitudinal crack running the length of the tube (Fig. 6.21), occurred at the shear stress of 42 ksi. The AE followed the Kaiser effect (Kaiser, 1950), which to summarize, simply states that AE will increase as the applied stress increases, and upon unloading/reloading, will not be heard until the previous maximum stress has been surpassed. Figure 6.22 presents a histogram that plots axial and shear stiffness versus cycle for Type II loading. No degradation is observed with the exception of the final cycle, where the shear stiffness was degraded 10% as discussed above.

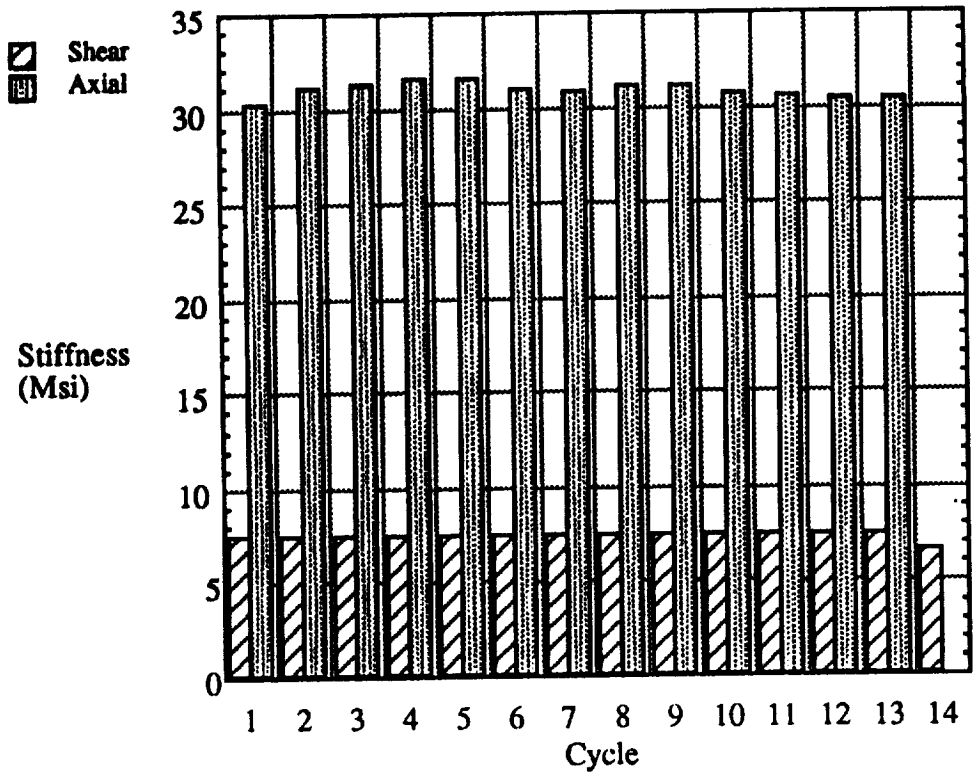

Figure 6.22: [0_4] Type II Loading Stiffnesses

6.2.1.3 Type III Loading

Type III tests were developed such that multiaxial loads would be applied with the primary stresses being transverse to the fibers. Internal pressure was used to apply transverse stresses and axial compression was applied to eliminate the axial stress due to the internal pressure. At the peak transverse stress, increments of axial tensile and shear stresses were applied sequentially. The transverse response obtained when the net axial stress equals zero is plotted in Fig. 6.23. The unloading response is not shown and the data was adjusted such that each cycle starts at the origin. The transverse stress, σ_{22} is calculated using the well known equation:

$$\sigma_{22} = \frac{pr}{t} \tag{6.1}$$

where p is the internal pressure, t is the wall thickness, and r is the radius of the cylinder to

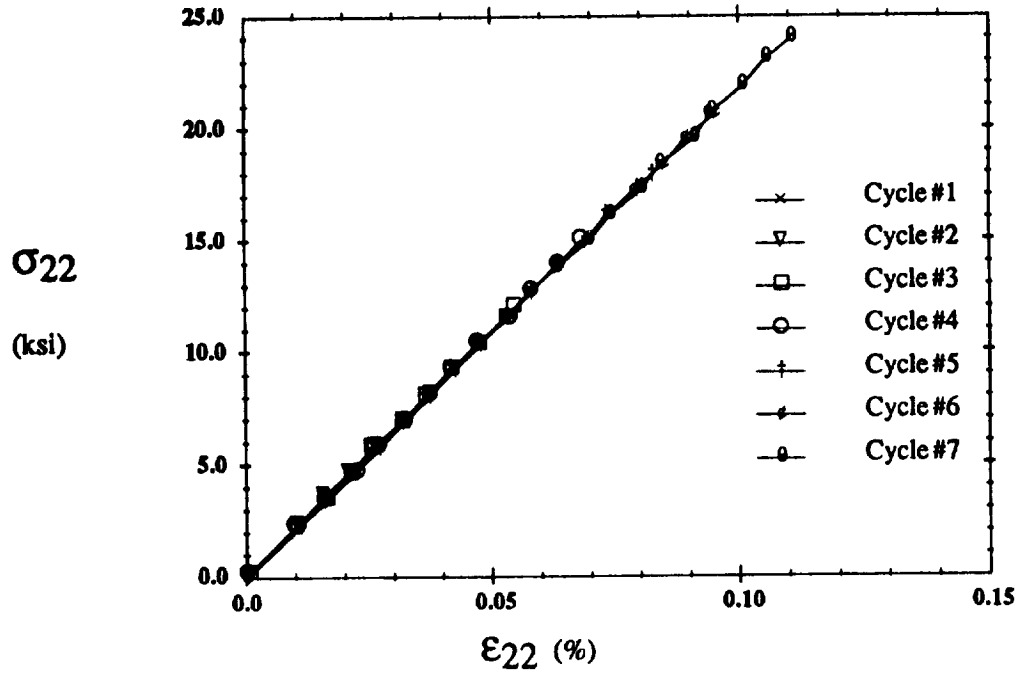

(a) Cycles #1-7

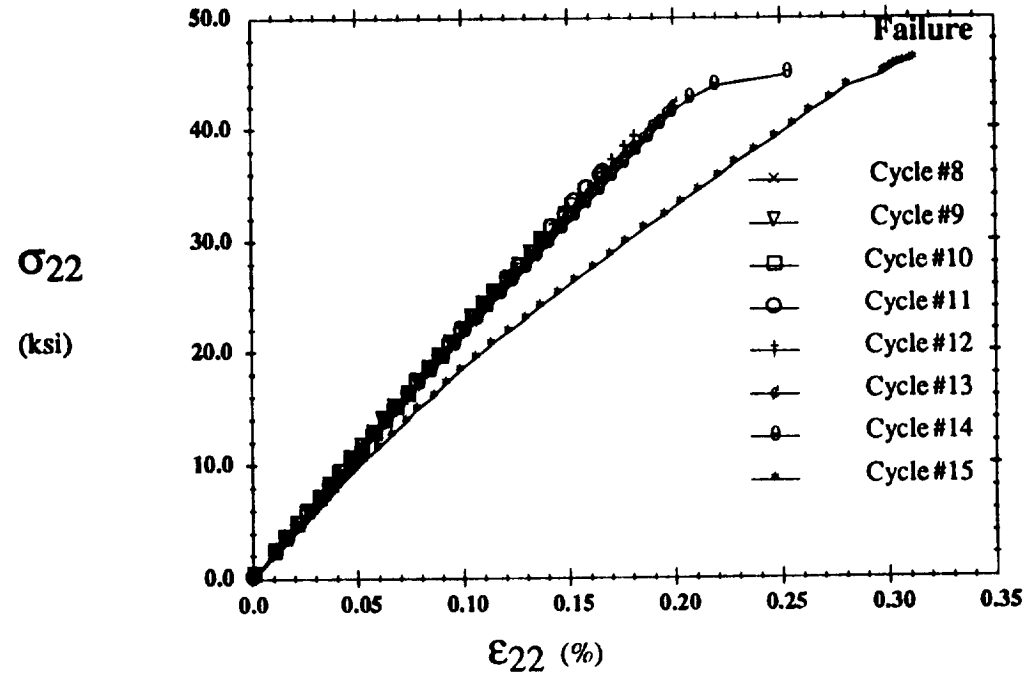

(b) Cycles #8-15

Figure 6.23: [0_4] Type III Loading - Transverse Response

the center of the wall, which is assumed to be thin. The transverse response of the first twelve cycles is linear elastic, with low level AE first heard at the transverse stress of 37 ksi in cycle #12. The initial nonlinear response, or knee, occurred at σ_{22}=40 ksi in cycle #13. The intensity of acoustic activity increased as the transverse stress increased and followed the previously discussed Kaiser effect. A knee in the transverse response also occurred at 25 ksi in cycle #14, and 21 ksi in cycle #15. The initial transverse modulus remained unchanged for all Type III tests. The axial and shear responses of a few typical cycles are shown in Fig. 6.24. The axial response was linear elastic and displayed the elastic coupling characteristic of these multiaxial loadings. Initially, the shear response was also linear elastic, but in cycle #14 an inelastic response was exhibited.

Cycle #14 was the only complete cycle in which inelastic deformation occurred. Fig. 6.25 provides a detailed view of the transverse and axial strains as a function of the applied transverse stress in cycle #14. The letters A-H designate points in the load history shown in Fig. 5.6c. It is noted that no data was collected during the removal of axial compression, between points B and C. The figure shows the nonlinear transverse response as well as the permanent transverse and axial strains present upon unloading. It also shows an accumulation of transverse strain during shear loading (E-F) and unloading (F-G). Figure 6.26 shows the nonlinear response obtained from all four rosettes located around the mid-length of the tube and indicates that the inelastic deformation is nonuniform around the tube. The most likely explanation for this is uneven fiber spacing. It seems reasonable that the local transverse response would be affected by uneven fiber spacing, while the axial response would not.

Figures 6.27-6.29 present the transverse response, shear response, and raw strain data from Rosettes #1 and 2 during cycle #14. Figure 6.27 accentuates the nonuniform

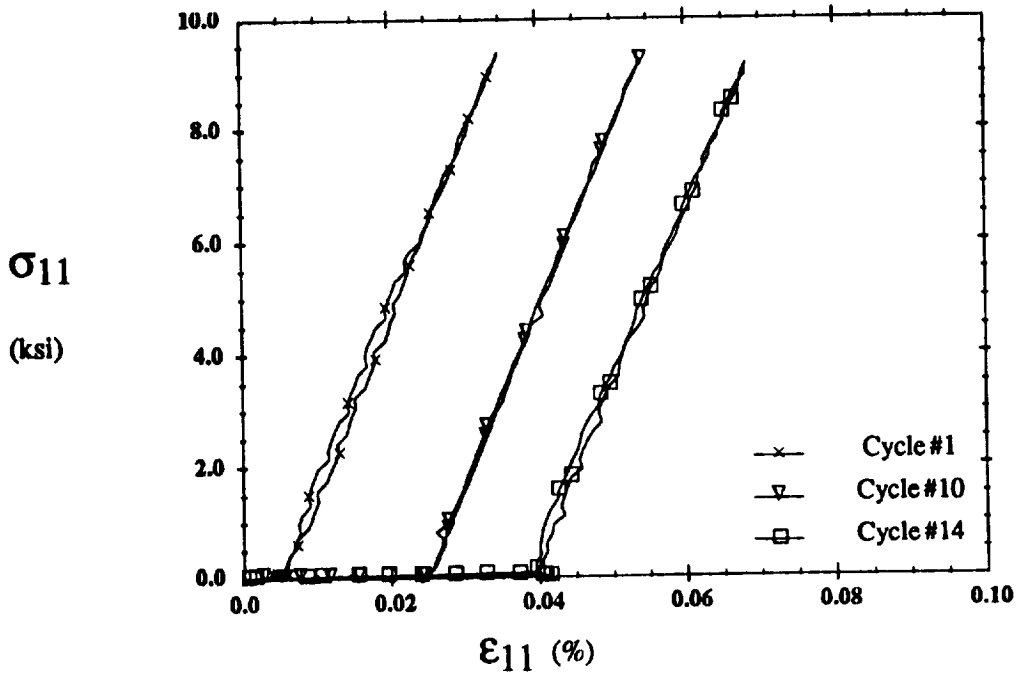

(a) Axial Response

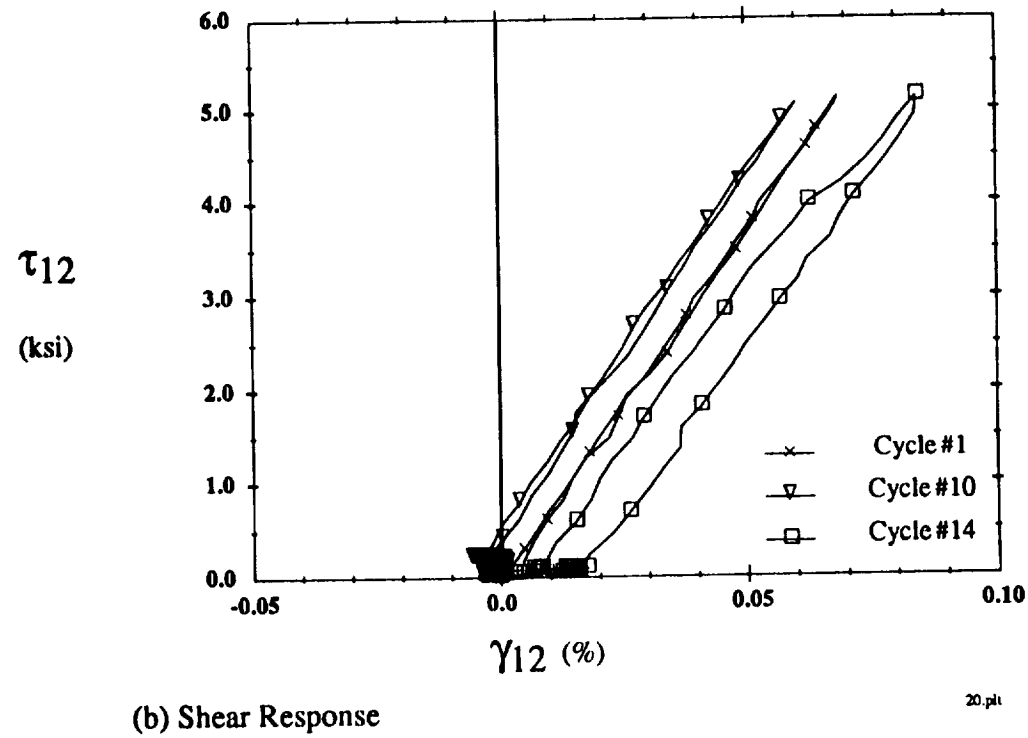

(b) Shear Response

Figure 6.24: [0_4] Type III Loading - Axial and Shear Responses

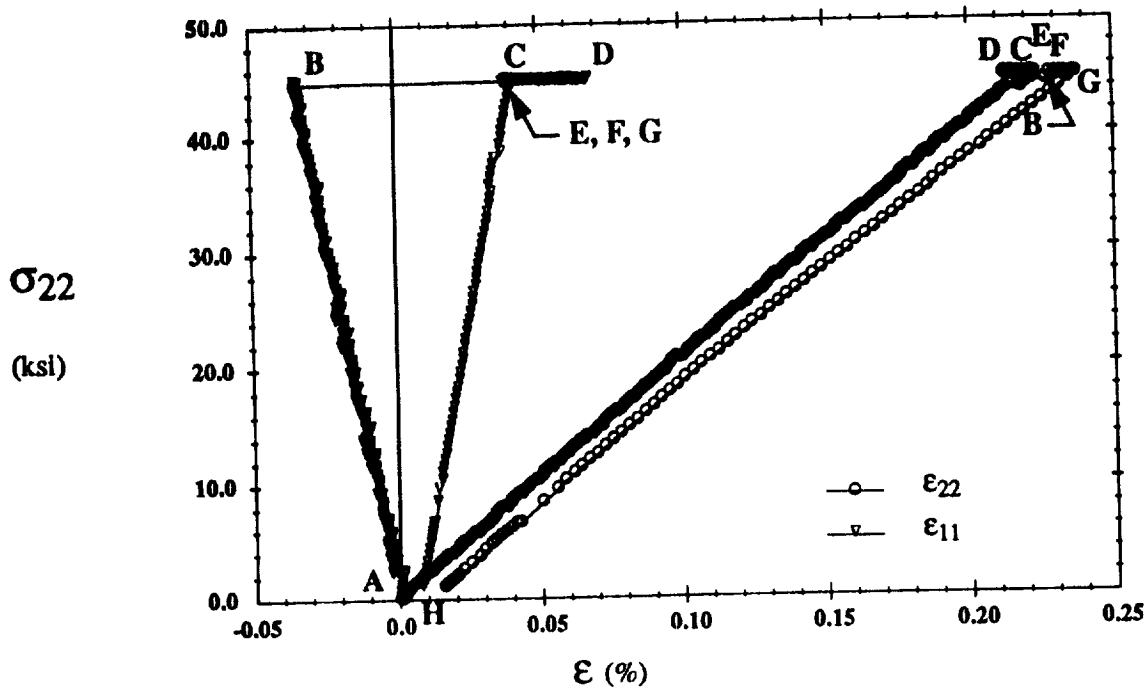

Figure 6.25: $[0_4]$ Type III Loading Cycle #14

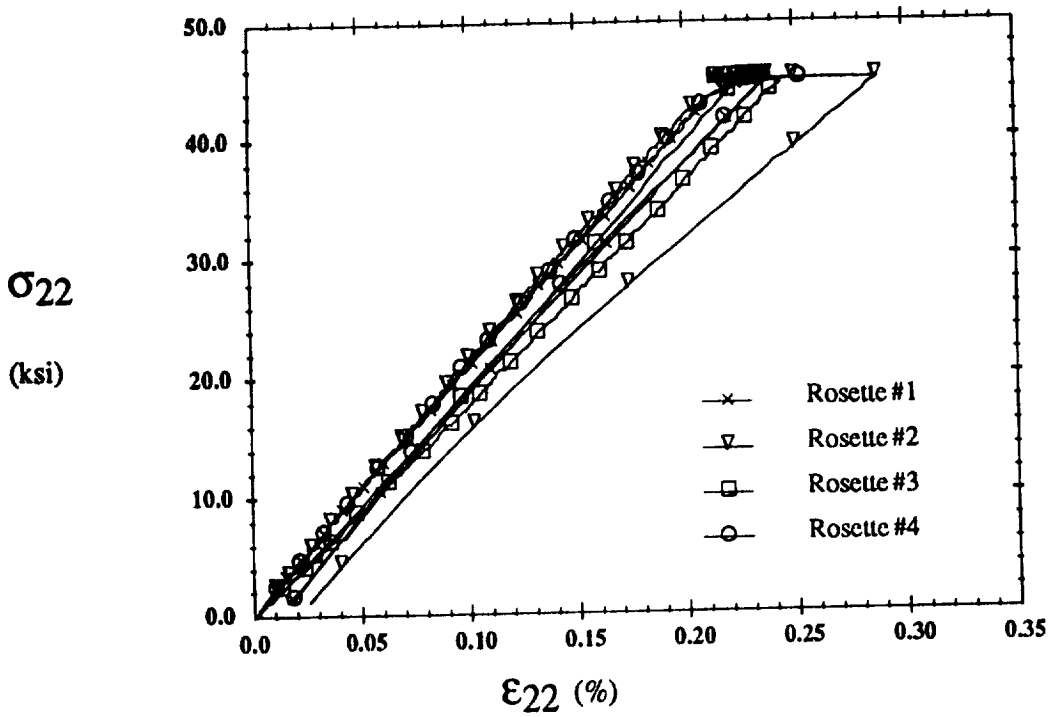

Figure 6.26: $[0_4]$ Type III Loading Cycle #14 Transverse Response

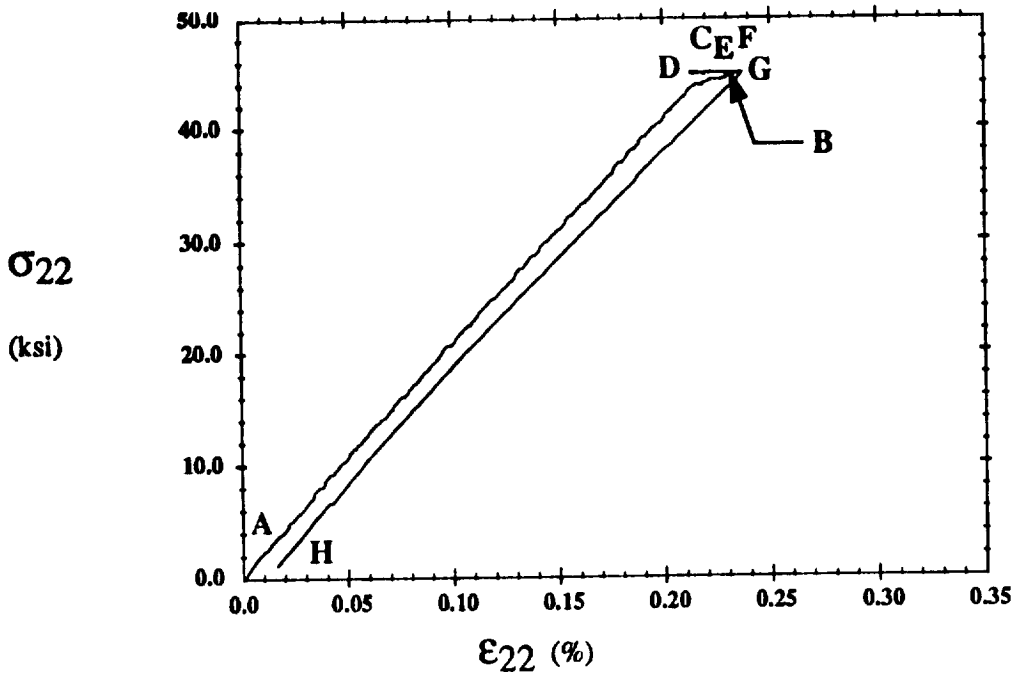

(a) Cycle #14, Rosette #1

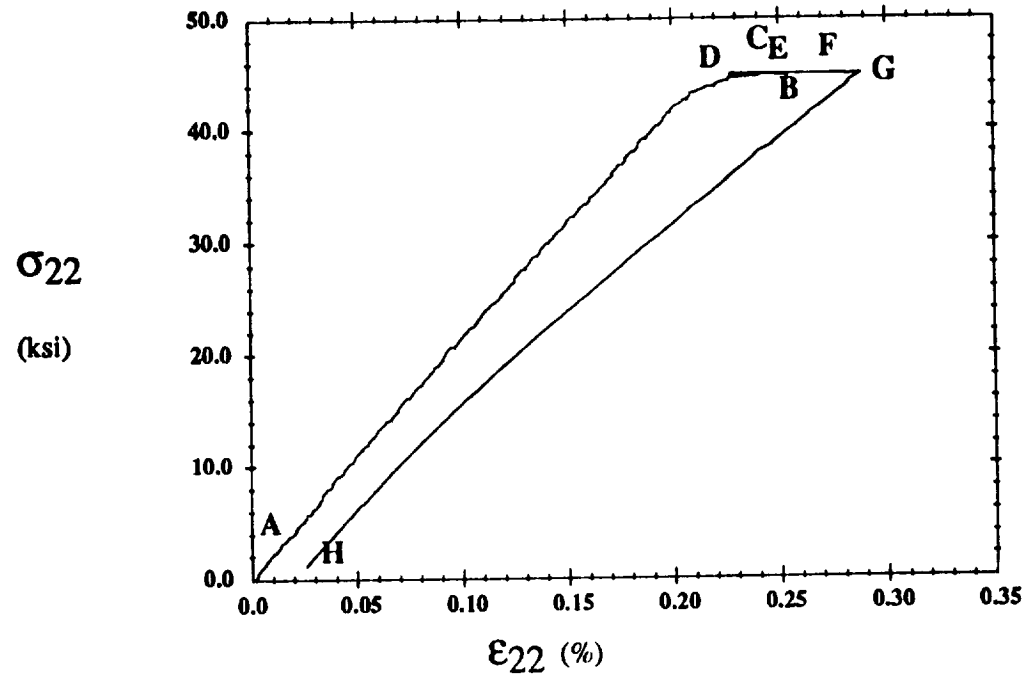

(b) Cycle #14, Rosette #2

Figure 6.27: [0_4] Type III Loading Transverse Response

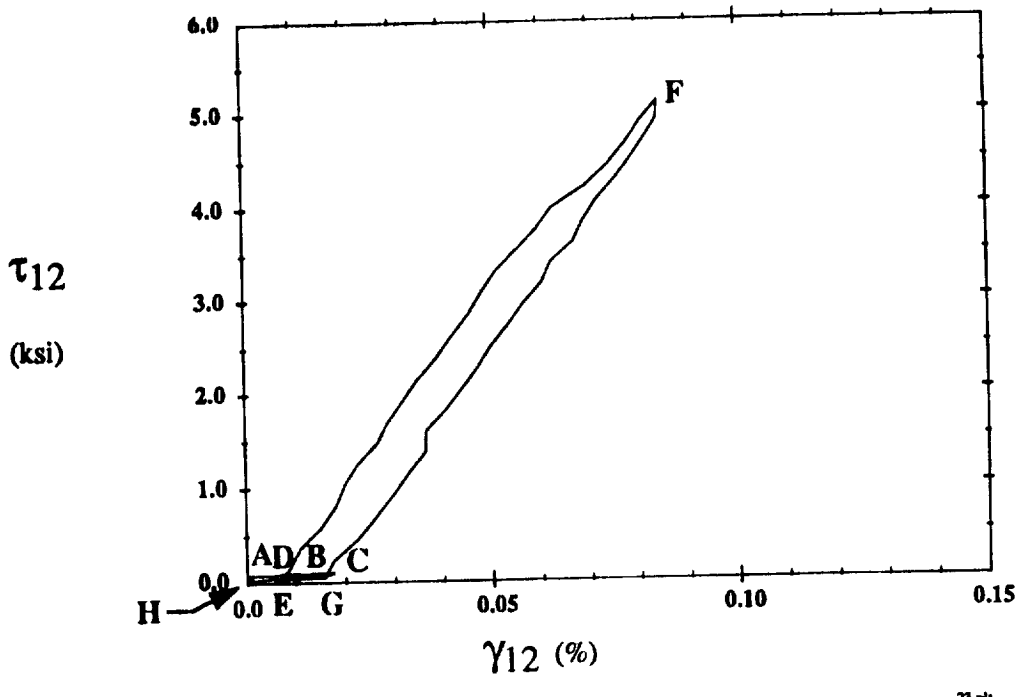

(a) Cycle #14, Rosette #1

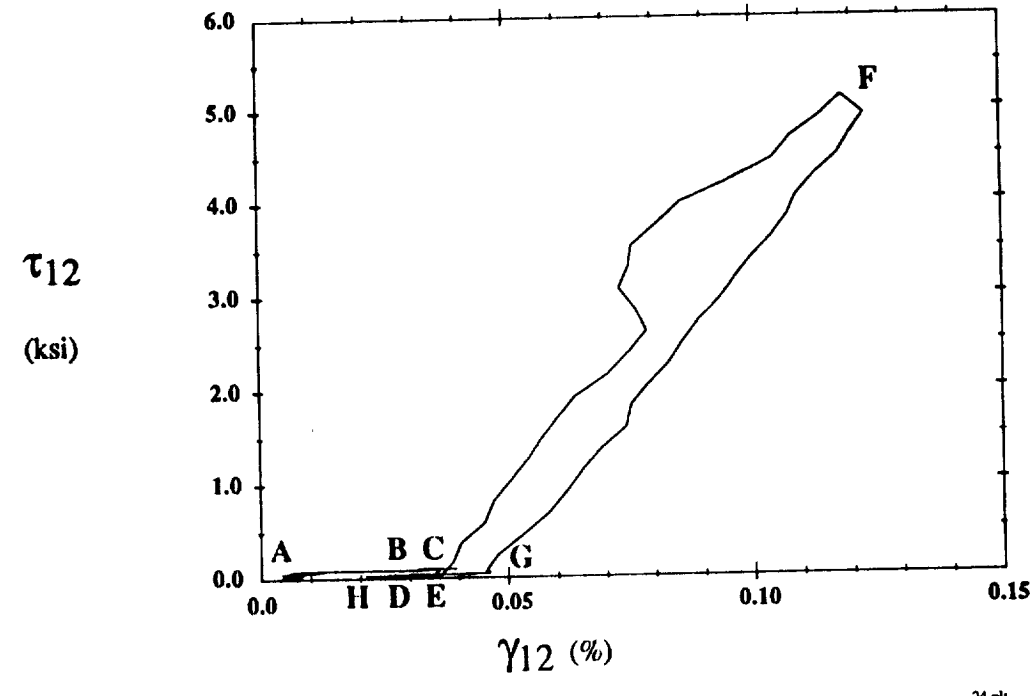

(b) Cycle #14, Rosette #2

Figure 6.28: [0_4] Type III Loading Shear Response

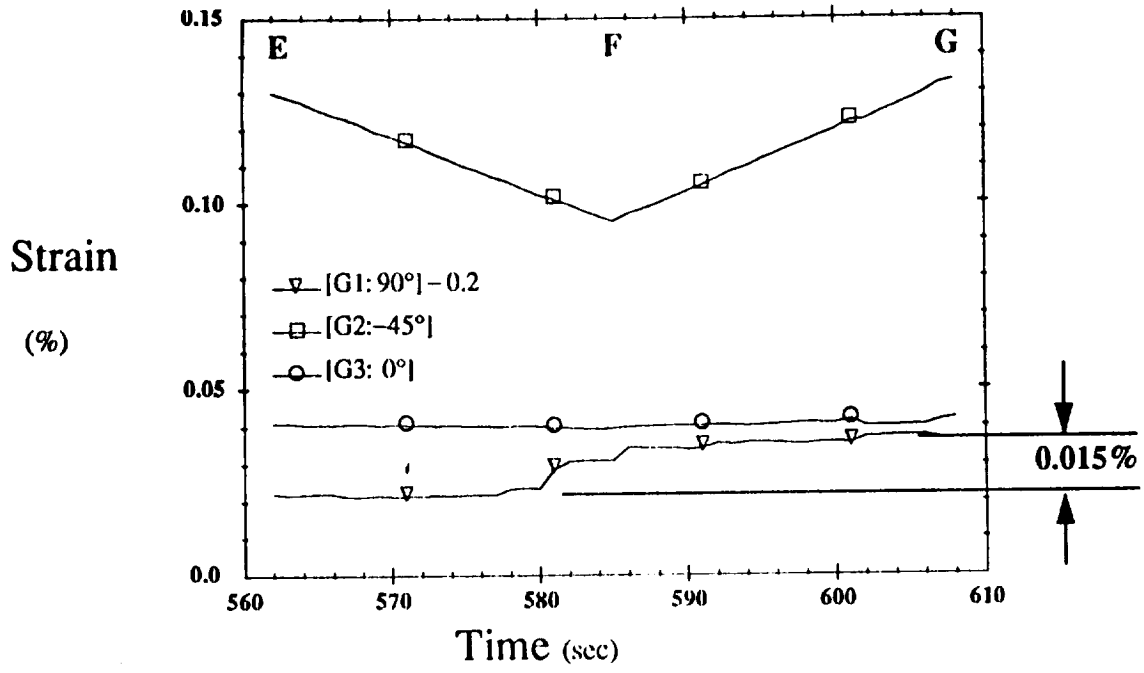

(a) Cycle #14, Rosette #1

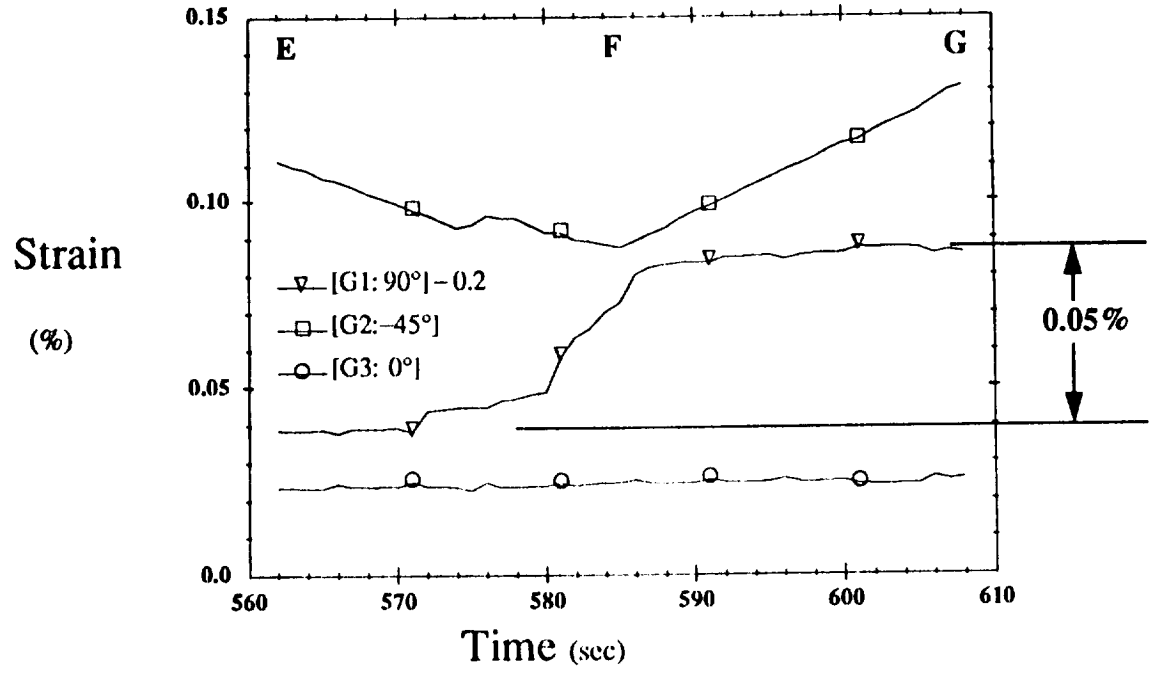

(b) Cycle #14, Rosette #2

Figure 6.29: [0_4] Type III Loading Raw Strain Data

inelastic deformation present in the tube. Again, the letters A-H represent points in the load history shown in Fig. 5.6c. It is very evident that the transverse unloading response (G-H) is nonlinear. In fact it appears to be bilinear, with the initial unloading stiffness being much less than the final unloading stiffness. This phenomenon suggests that separation occurs at fiber/matrix interfaces at high stress levels, these separations then close upon unloading, leading to a higher stiffness in the final unloaded state. As observed in Fig. 6.25, there is a substantial accumulation of transverse strain during shear loading (E-G), this will be discussed in conjunction with Fig. 6.29.

The shear response (Fig. 6.28) indicates once again that shear strains are coupled elastically (A-E and G-H) with transverse and axial strains. More interesting are the permanent shear strains present upon complete unloading, and the large anomaly in the Rosette #2 data that occurs around a shear stress of 3 ksi. The permanent shear strains seem to indicate the presence of plasticity, but could also be caused by damage.

In order to determine the cause of the anomaly in the shear strain data it is necessary to look at the strain readings from the individual strain gages in Rosette #2. This is done in Fig. 6.29b. A strain of 0.2% has been subtracted from the 90° strain gage (G1) in order to fit all the data on the figure at a reasonable scale. Also notice that because gage #2 is oriented at -45°, a positive applied shear stress results in a negative strain (relative to the initial value). The most outstanding feature of the figure is the large increase (0.05%) in strain measured by the transverse 90° strain gage during shear loading. This transverse strain occurs while the transverse stress is being held at a high, constant value, and shear stresses are being applied. The largest rate of increased transverse strain corresponds with the largest applied shear stresses. No further transverse strains are accumulated once the maximum shear stress is reached (point F) and shear unloading begins. This behavior

strongly suggests that the titanium matrix has yielded, and coupling associated with loading on the current yield surface and the normality criterion for the plastic strain rate vector is occurring.

The absolute increase (or relative decrease) in the strain measured by the -45° gage appears to be due to the increase in transverse strain, leading to the anomaly noted in Fig. 6.28b. Rosette #1 also displays coupling between shear and transverse strains, although to a much less degree (Fig. 6.29a). For both Rosettes #1 and 2 no axial strain accumulation occurred during shear loading.

Failure occurred during internal pressure loading at the transverse stress of 46.2 ksi in cycle #15 prior to tensile and shear loading. The failure occurred in the form of a longitudinal crack running the length of the tube as shown in Fig. 6.30. The crack is fairly wide, in that a relatively large amount of hydraulic oil sprayed out into the shield and containment pan.

6.2.2 $[\pm 45]_s$ Tubes

Section 6.1 showed that the $[\pm 45]_s$ tubes display a rather nonuniform response due to material nonuniformity manifested in the form of fiber-rich and fiber-depleted regions. The current section presents results from one strain gage rosette located at the mid-length of a tube. While one rosette does not represent the range of stiffnesses, or even the average, it does serve to describe the general behavior of a tube.

6.2.2.1 Type I Loading

The axial response of a $[\pm 45]_s$ tube under Type I loading is shown in Fig. 6.31a and the shear response in Fig. 6.31b. The cyclic response illustrated in Fig. 6.31a can be

divided into three categories based on the phenomena observed in cycles #1-4, cycles #5-6, and cycles #7-15. The axial response observed in cycles #1-4 was elastic and bilinear. A slight knee was observed at approximately 8 ksi. Upon unloading, the initial stress-strain path was retraced with no apparent strain accumulation in the unloaded state. During the shear loading portion of the load cycle, no axial strain increase was observed.

When the axial stress reached 20 ksi during cycle #5, the response clearly became nonlinear and was characterized by degradation in the axial stiffness and dissipation of energy upon unloading. However, no axial strain growth was observed during the torsional portion of the loading cycle. A small amount of permanent axial strain, likely

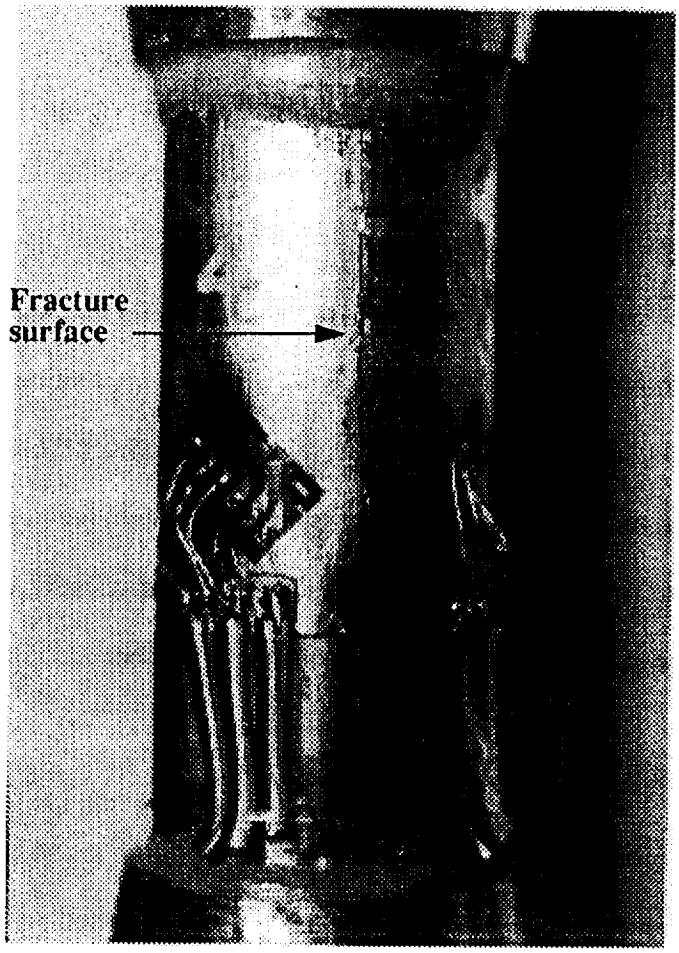

Figure 6.30: $[0_4]$ Type III loading fracture

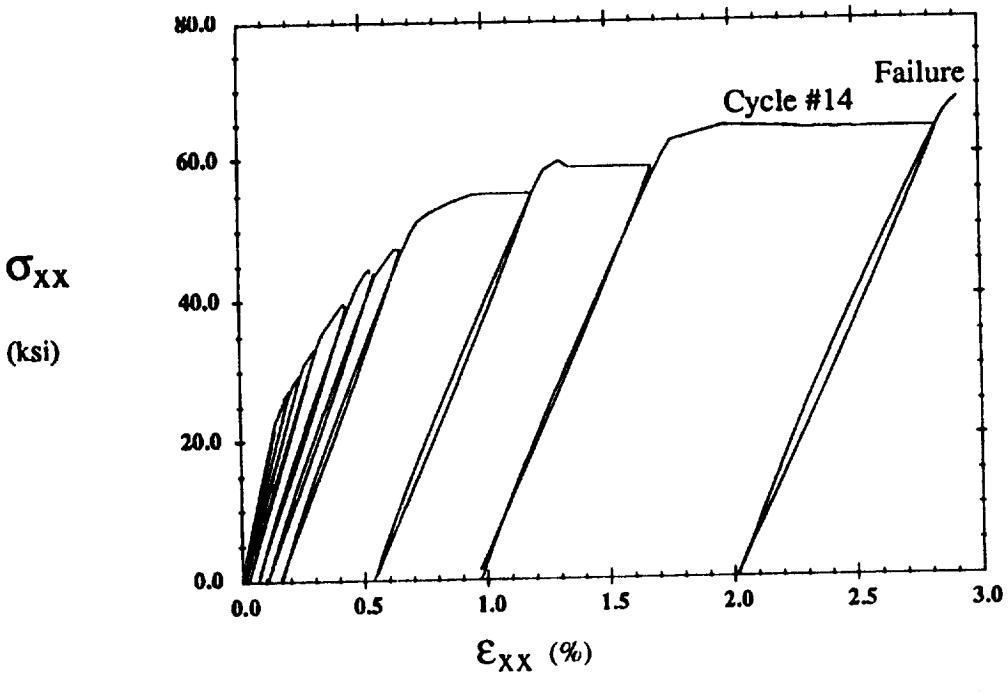

(a) Axial Response

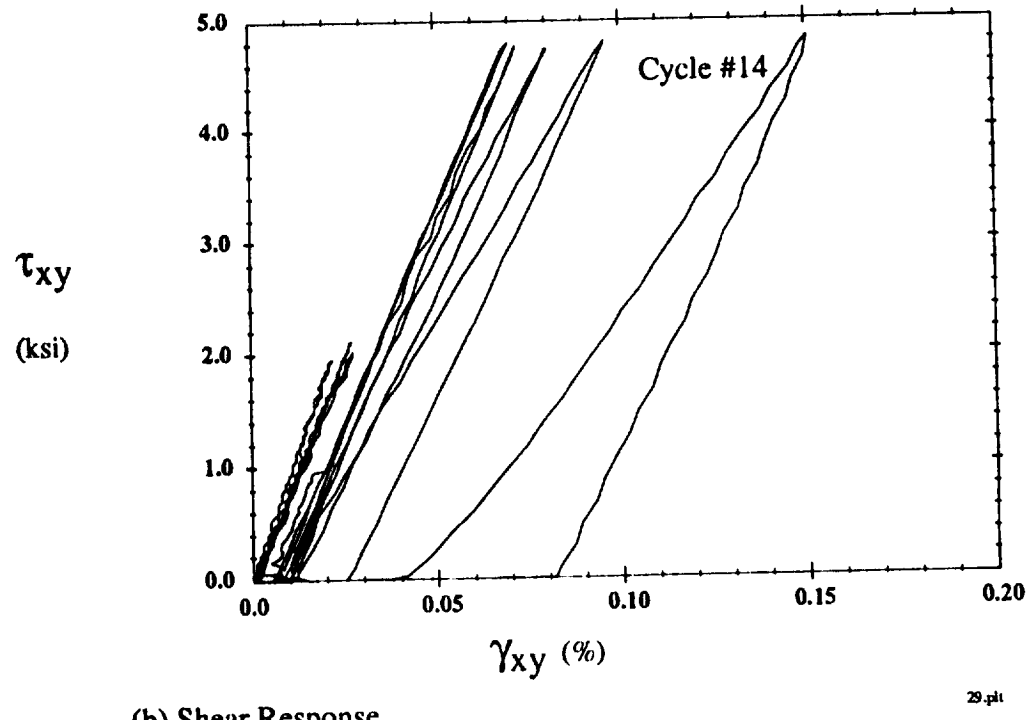

(b) Shear Response

Figure 6.31: $[\pm 45]_s$ Type I Loading

associated with interfacial slippage, was evident when the material was completely unloaded. Cycle #6 was similar to #5 except the amount of permanent strain in the unloaded state was higher.

Cycles #7-15, in addition to further degradation in the axial stiffness, exhibited axial strain accumulation during the torsional portion of the load cycle when the axial stress was kept constant. This axial strain response is characteristic of the perfectly plastic type behavior of the titanium matrix in the plastic region and suggests that the load vector is on the current yield surface when the shear loading is applied. The axial strain accumulation during shear loading increases with increasing axial stress. The plastic axial strain accumulation initiates during cycle #7 at the axial stress of 30 ksi. Figure 6.31a indicates that hysteresis takes place during unloading and reloading. This could be due to dissipation of energy through frictional sliding during opening and closing of the separated fiber/matrix interface, or possibly kinematic hardening effects after the matrix has yielded.

Permanent shear strains began to be accumulated in cycle #9, as shown in Fig. 6.31b, the amount of permanent strain present in the unloaded state increased with increasing axial stress. The final cycle (#14) displays a shear stiffening behavior.

Low level AE was heard during all cycles above the axial stress of approximately 12 ksi. The intensity of the acoustic activity increased with increasing axial stress and again followed the Kaiser effect.

The stiffness degradation data from Type I testing of a $[\pm 45]_s$ tube are summarized in Fig. 6.32. Both the initial loading and initial unloading stiffnesses are shown. At first, the loading and unloading shear stiffnesses were the same, due to the linear elastic shear

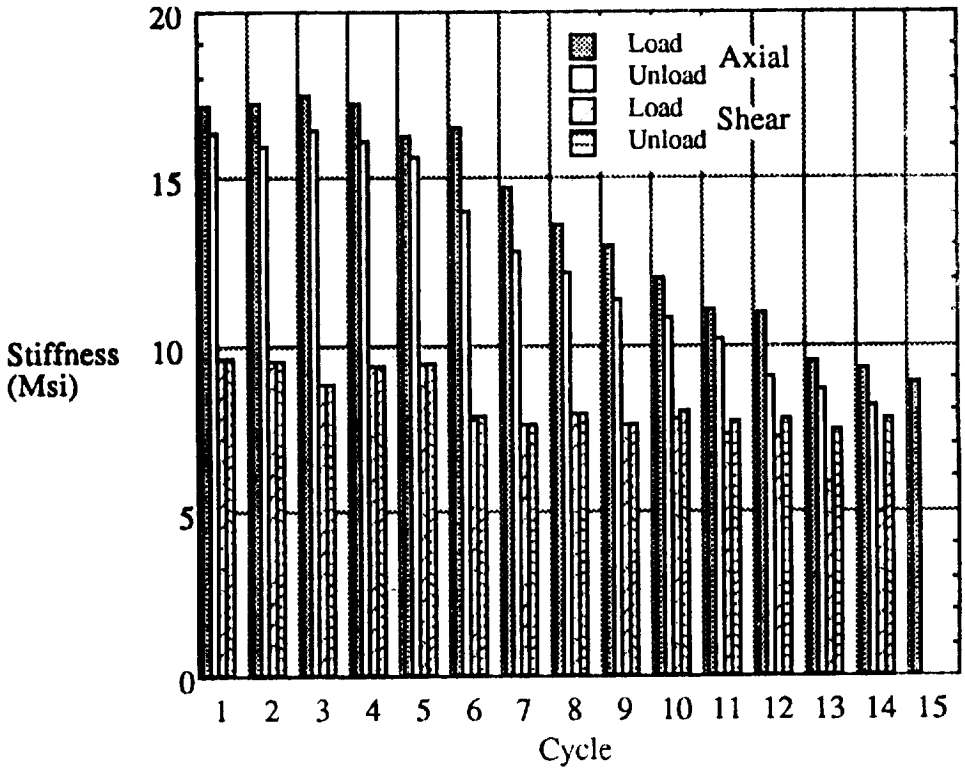

Figure 6.32: $[\pm 45]_S$ Type I Loading

response. To the contrary, the initial loading and unloading axial stiffnesses were never the same, because of the nonlinear axial response that occurred even at low stress levels. Degradation of the loading and unloading axial stiffnesses initiated after cycle #5 and coincided with the onset of nonlinear behavior observed at an axial stress of 20 ksi. This degradation appears to proceed in a roughly linear fashion with increasing axial stress. Degradation of both shear stiffnesses is observed in cycle #6. The degraded shear unloading stiffness then remains essentially constant. In contrast, the shear loading stiffness is further degraded when large permanent axial strains are accumulated during shear loading (cycles #12-14). This further decrease in stiffness occurs in a linear fashion with increasing axial stress.

A sudden failure occurred in cycle #15 at the applied axial stress of 68.2 ksi. The fracture surface is seen to follow straight line segments oriented ±45° from the axis of the

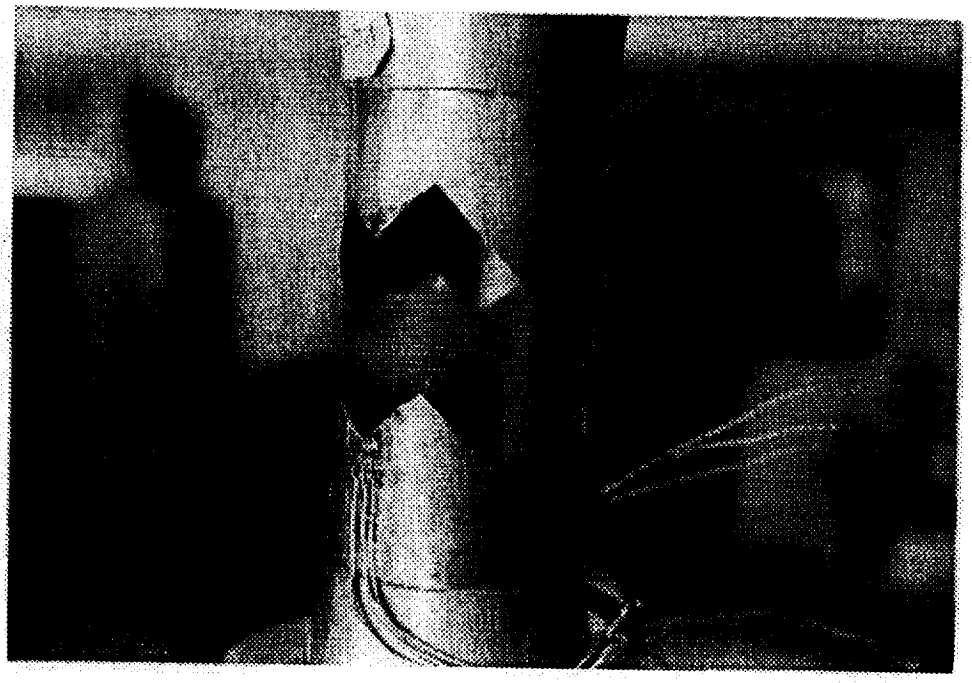

Figure 6.33: $[\pm 45]_s$ Type I loading failure

tube in Fig. 6.33. These segments corresponded with the location of a moly wire in at least one of the plies, thus suggesting that the presence of moly wires decreases the strength of the composite.

6.2.2.2 Type IA Loading

Type I loading was modified by the addition of two time periods when all applied loads were held constant. The first hold period was immediately after the maximum tensile stress had been applied and the second hold period was immediately after the maximum shear stress had been applied. The purpose in conducting these Type IA tests was to determine the contribution of time dependent components of the inelastic response to axial and combined axial/shear loading. Specifically, the goal was to determine what portion of the large axial strain accumulated during the torsional loading portion of the Type I tests was due to time dependency rather than coupling with shear stresses.

The history of cyclic axial response to Type IA loading is presented in Fig. 6.34a.

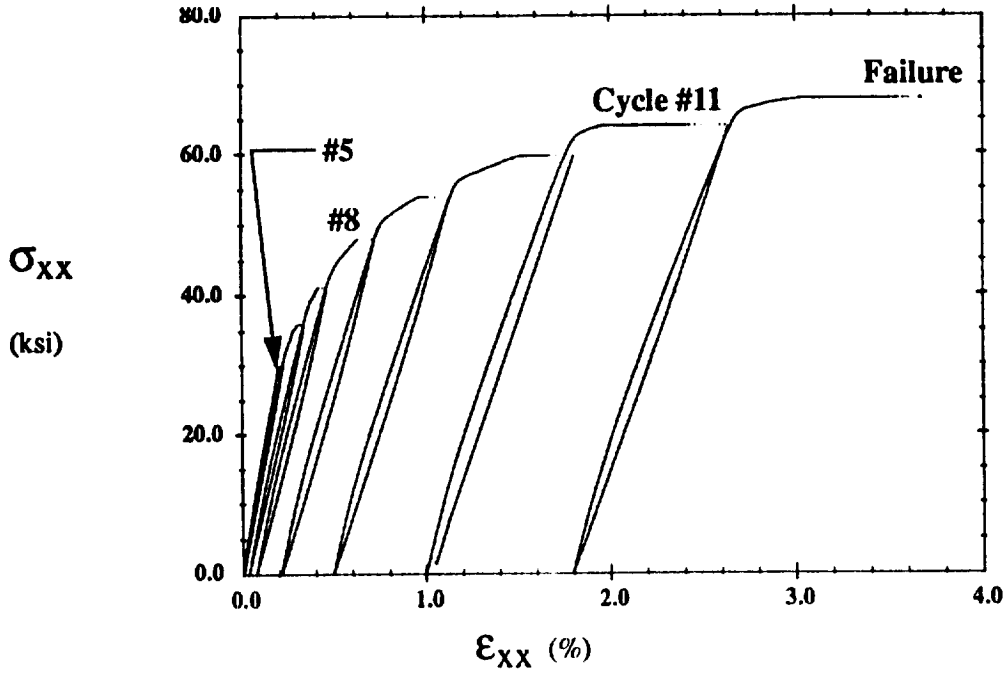

(a) Axial Response

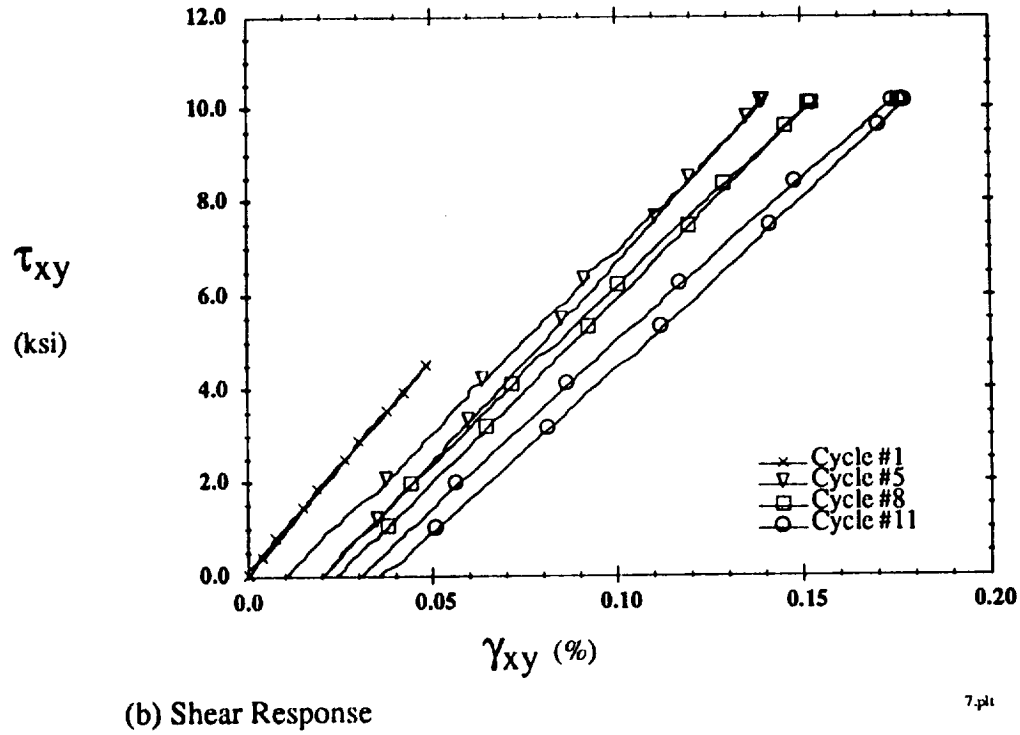

(b) Shear Response

Figure 6.34: $[\pm 45]_s$ Type IA Loading

The response of cycles #1-4 is not visible at the scale of the figure, because it is overshadowed by cycle #5. The initial axial stiffness is degraded with each cycle after cycle #3, where the maximum axial stress was 24 ksi (see also Fig. 6.42). The unloading/ reloading cycles display a hysteresis type behavior characteristic of slippage or cracks opening and closing. As for Type I loading, axial strains were accumulated in certain cycles after the applied axial stress was held constant. This accumulation increased as the maximum applied stress in each cycle increased, and was permanent. The shear response from selected cycles is shown in Fig. 6.34b, where the cycles have been offset for clarity. Beginning with cycle #5 the shear response was mildly nonlinear with a small amount of permanent shear strain present in the unloaded state. A very small amount of shear strain was accumulated during the second hold period in cycle #11.

To facilitate the separation of time dependent axial strain components from axial strains associated with shear coupling, accumulated axial strain has been plotted (Fig. 6.35) versus elapsed time from the point at which the axial stress was held constant. While the horizontal scale is the same in each Fig. 6.35a and 6.35b, the vertical scale of Fig. 6.35a has been magnified eight times to amplify the strains in cycles #1-6. Torsional loading and unloading is darkened to emphasize shear coupling effects. In Fig. 6.35a, that is, cycles #1-6 where the maximum axial stress is 36 ksi, the accumulated strains are primarily due to shear coupling. Positive axial strains are induced by both shear loading and unloading. Conversely, the axial strains accrued in cycles #7-12 are principally due to time dependent components, or creep. These creep strains increase dramatically as the maximum applied axial stress increases.

Figure 6.36 presents the temporal history of the axial Poisson's ratio for Type IA loading. Overall, Poisson's ratio is greatly increased as the axial stress level is increased.

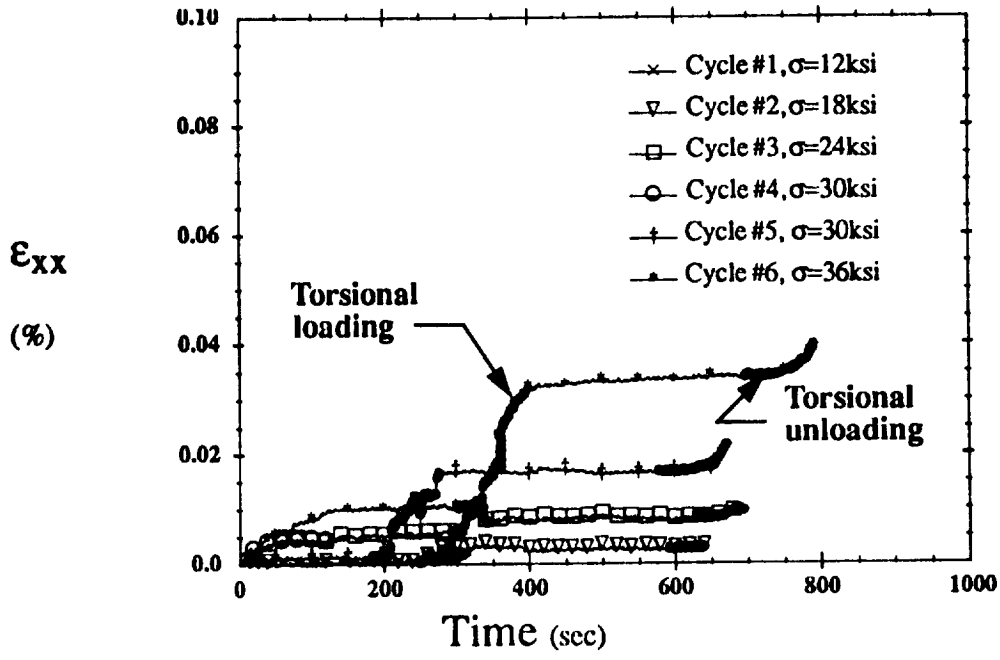

(a) Cycles #1-6

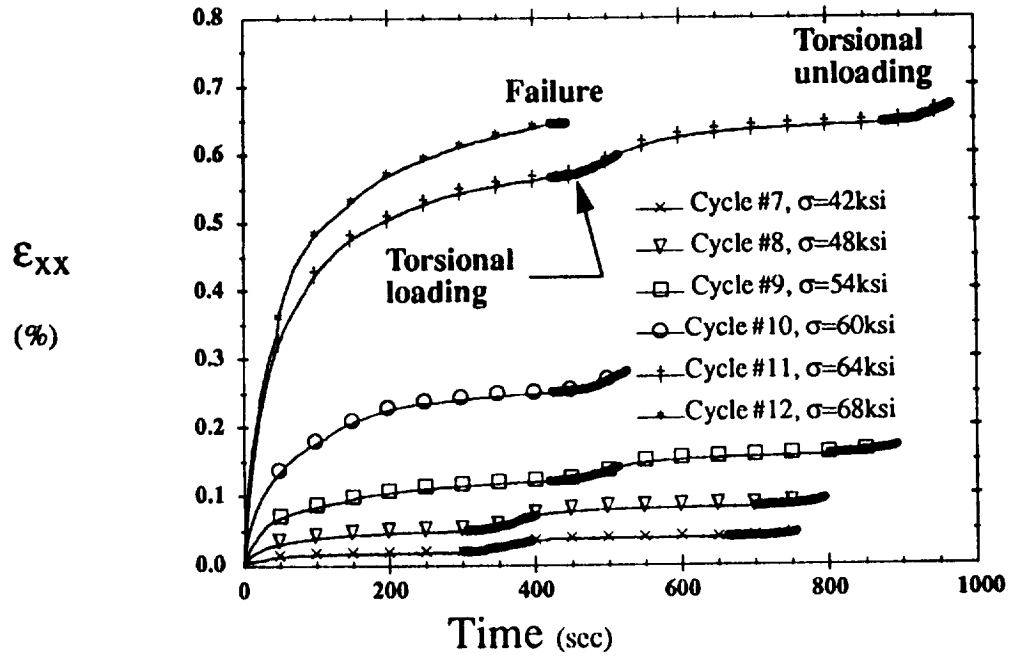

(b) Cycles #7-12

Figure 6.35: $[\pm 45]_s$ Type IA Loading Creep Response

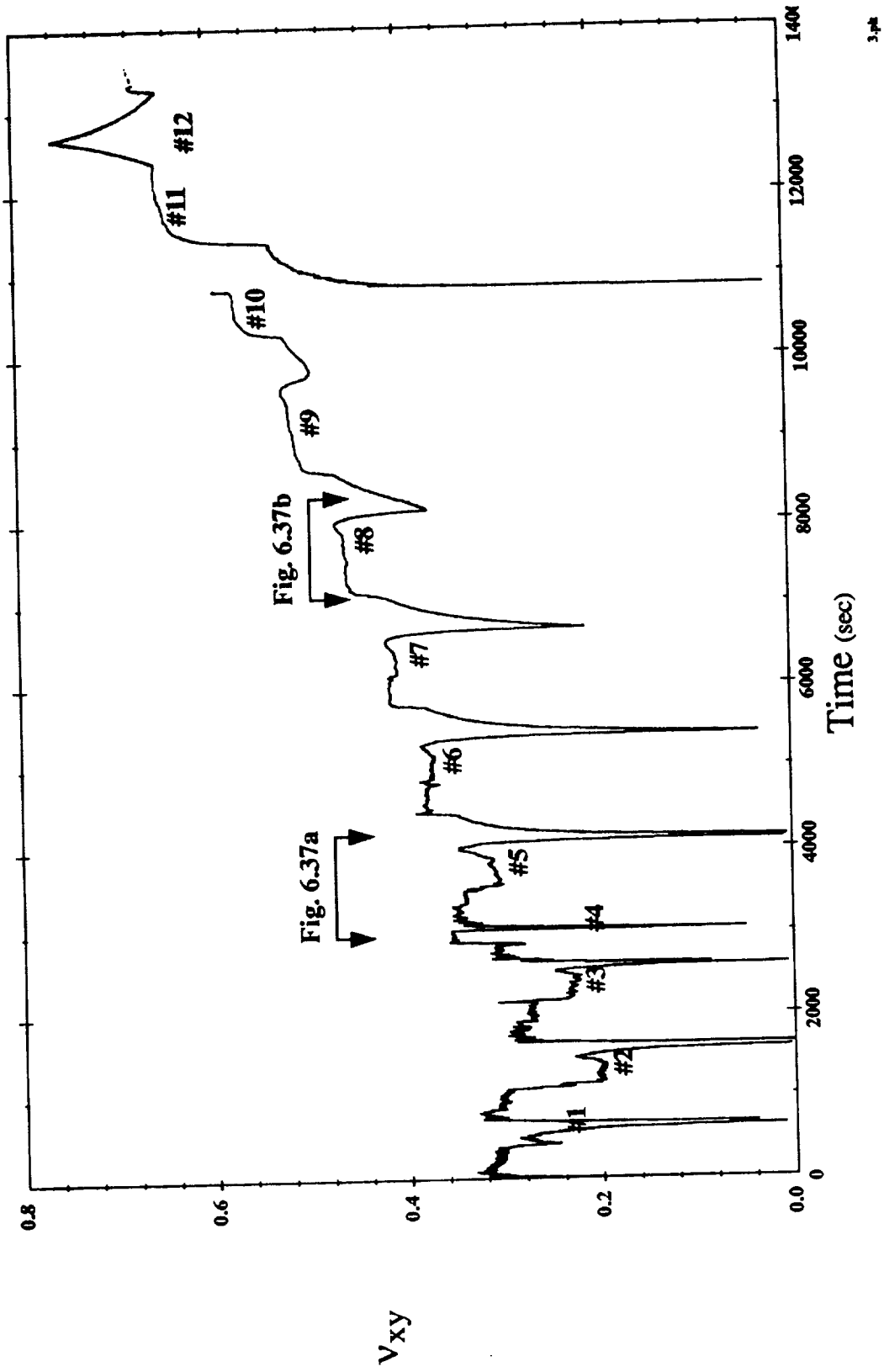

Figure 6.36: Type IA Loading Poisson Ratio

The history of Poisson's ratio in each cycle can loosely be classified into two general categories, that of cycles #1-6, and that of cycles #7-12. Figure 6.37 shows an enlarged view of cycles #5 and 8. Poisson's ratio in cycle #5 (Fig. 6.37a) remains constant during tensile loading and the first hold period. It is then reduced during shear loading, remains constant during the second hold period, and then increased back to the original value during unloading. In contrast, Poisson's ratio in cycle #8 (Fig. 6.37b) increased significantly during tensile loading, then remained relatively constant through the balance of the load cycle.

The sequence of figures 6.38-6.41 present normalized stress, strain, and AE data as a function of elapsed time beginning at the start of each of cycles #1, 2, 8, 11, and 12. The AE data shown was collected using the piezoelectric sensor system described in Section 5.2. Comparison of AE data between the piezoelectric sensor system and the VCR system indicated that the VCR system was more completely capturing the essence of the acoustic activity. The sensor system could sample AE data approximately every two seconds, while the VCR system provided a continuous record. Acoustic events often occurred at a rate much faster than the sensor system could record them. The onset of AE data collected from both systems coincided very well. The AE data shown in the figures is the RMS voltage of the waveform sensed by the transducer. The sequence of figures 6.38-6.41 shows that the intensity of AE increases with increasing axial stress. Also of major significance is that AE continue at a high intensity after applied stresses have been held at a constant level. Acoustic activity is also recorded at the end of the torsional unloading portion of the load cycle. The acoustic activity appears to be associated with fiber/matrix interfacial debonding.

Preliminary findings from metallography conducted by Lerch (1993) revealed that

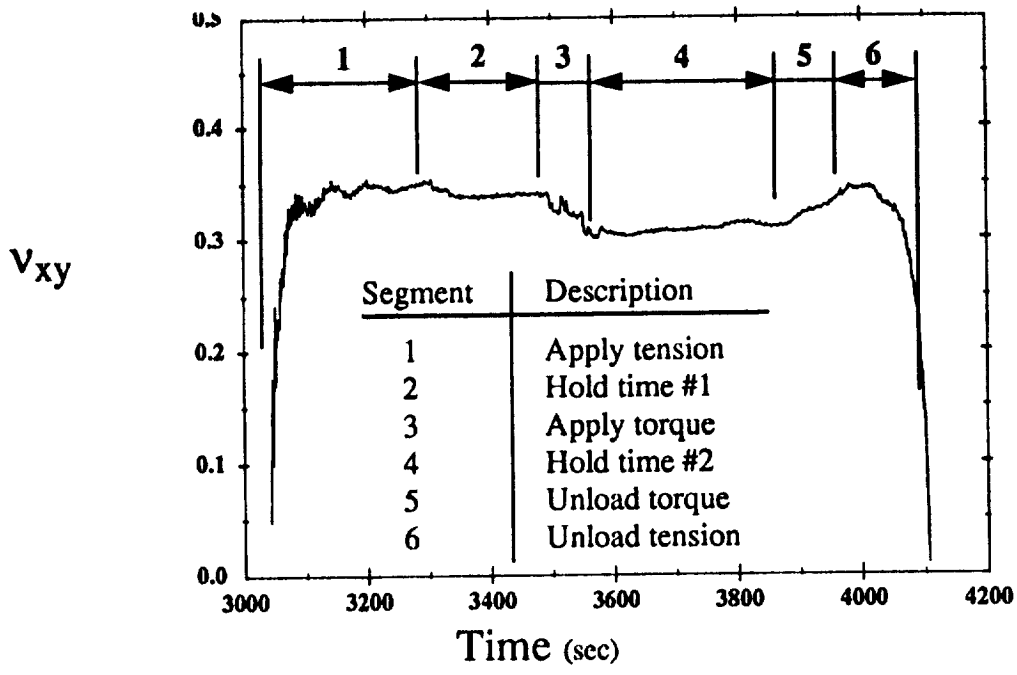

(a) Cycle 5

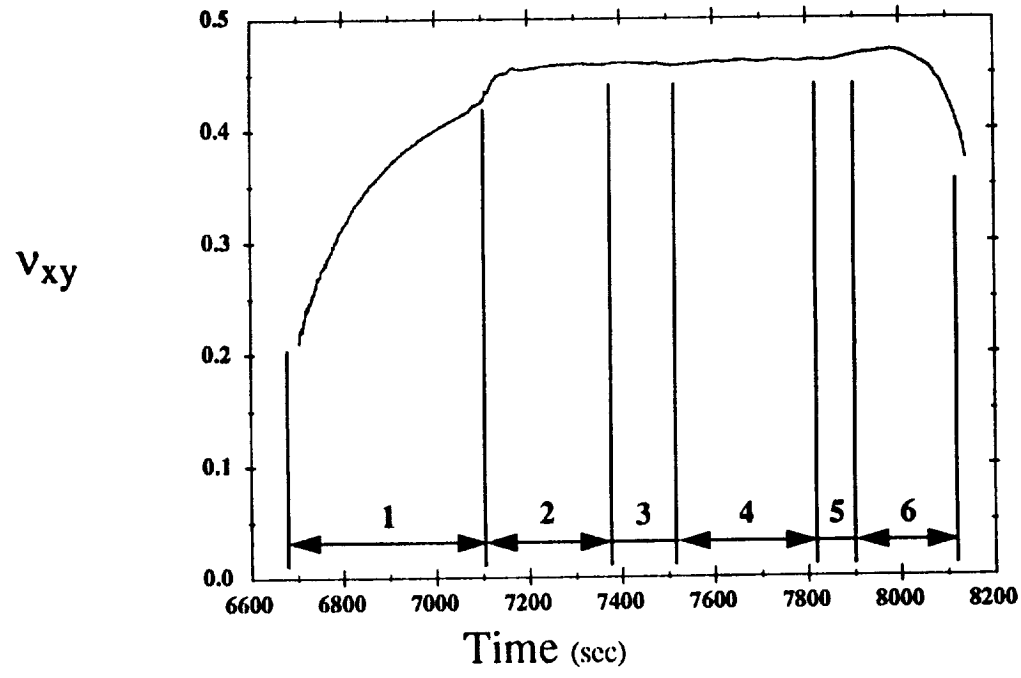

(b) Cycle 8

Figure 6.37: $[\pm 45]_s$ Type IA Loading Poisson Ratio

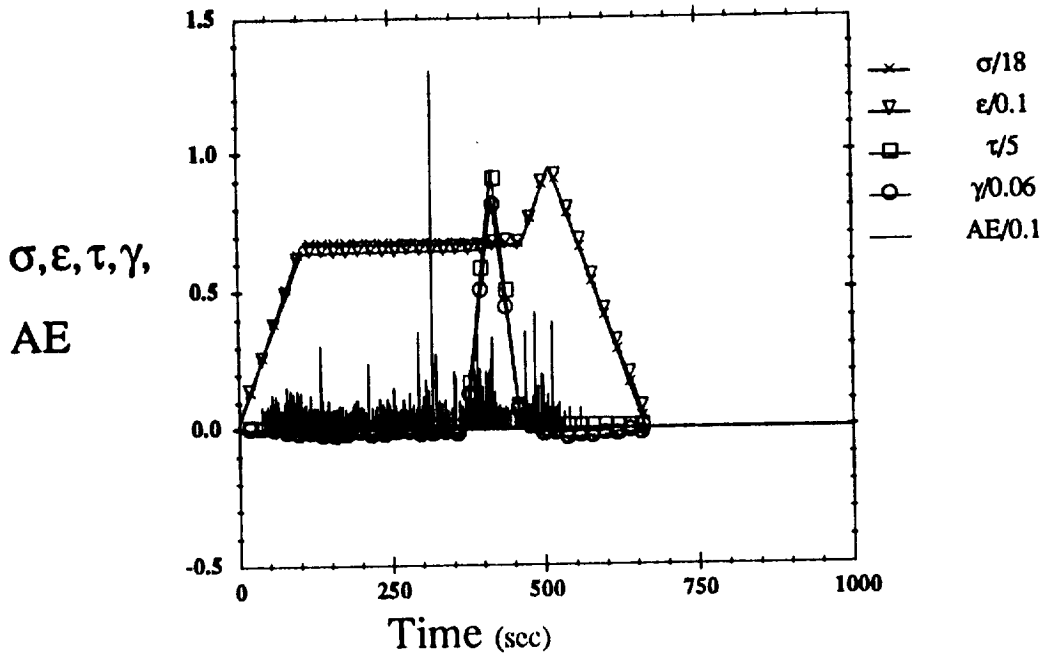

(a) Cycle #1

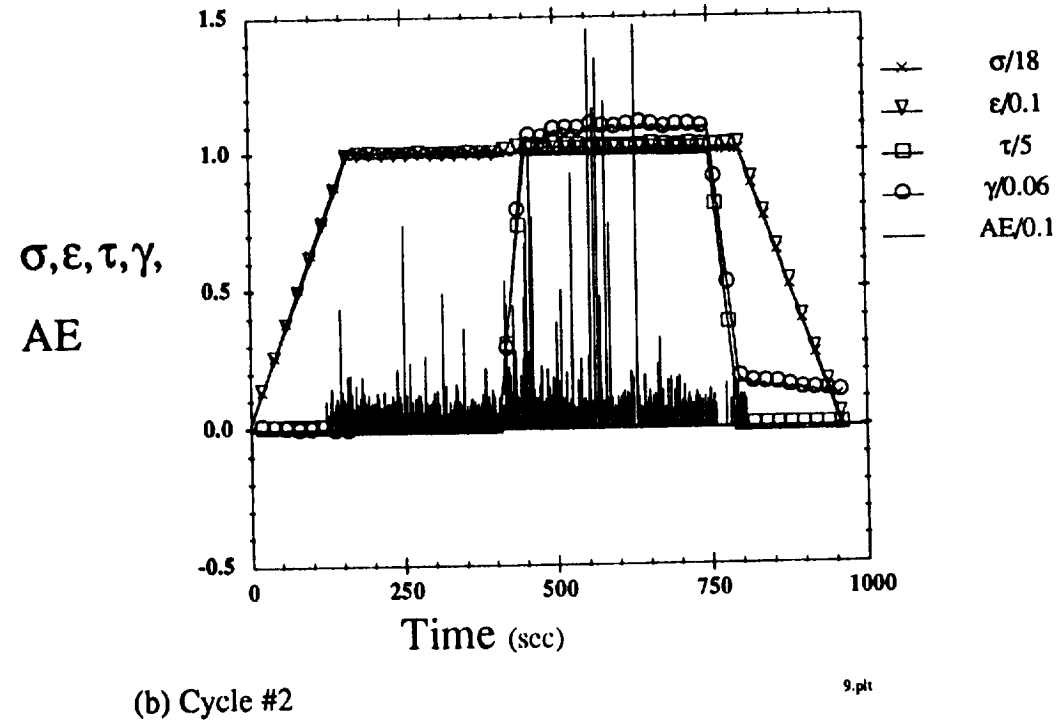

(b) Cycle #2

Figure 6.38: $[\pm 45]_S$ Type IA Loading

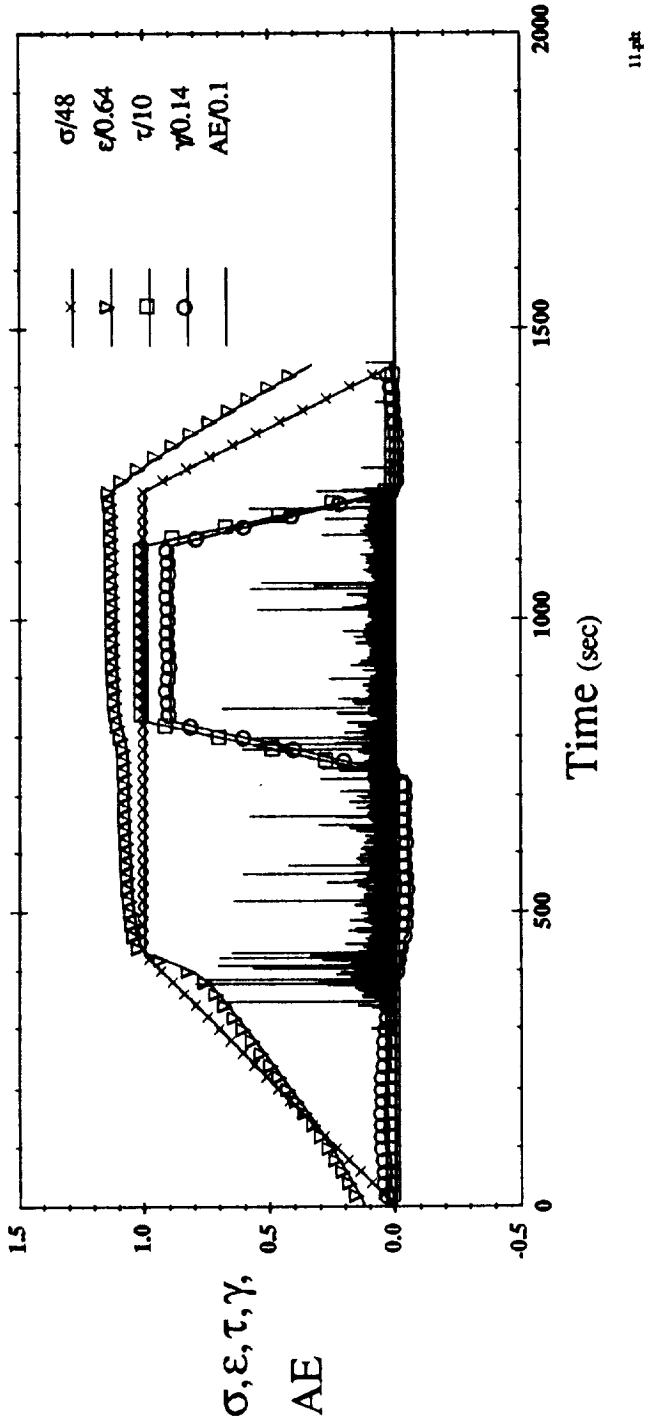

Figure 6.39: $[\pm 45]_s$ Type IA Loading - Cycle #8

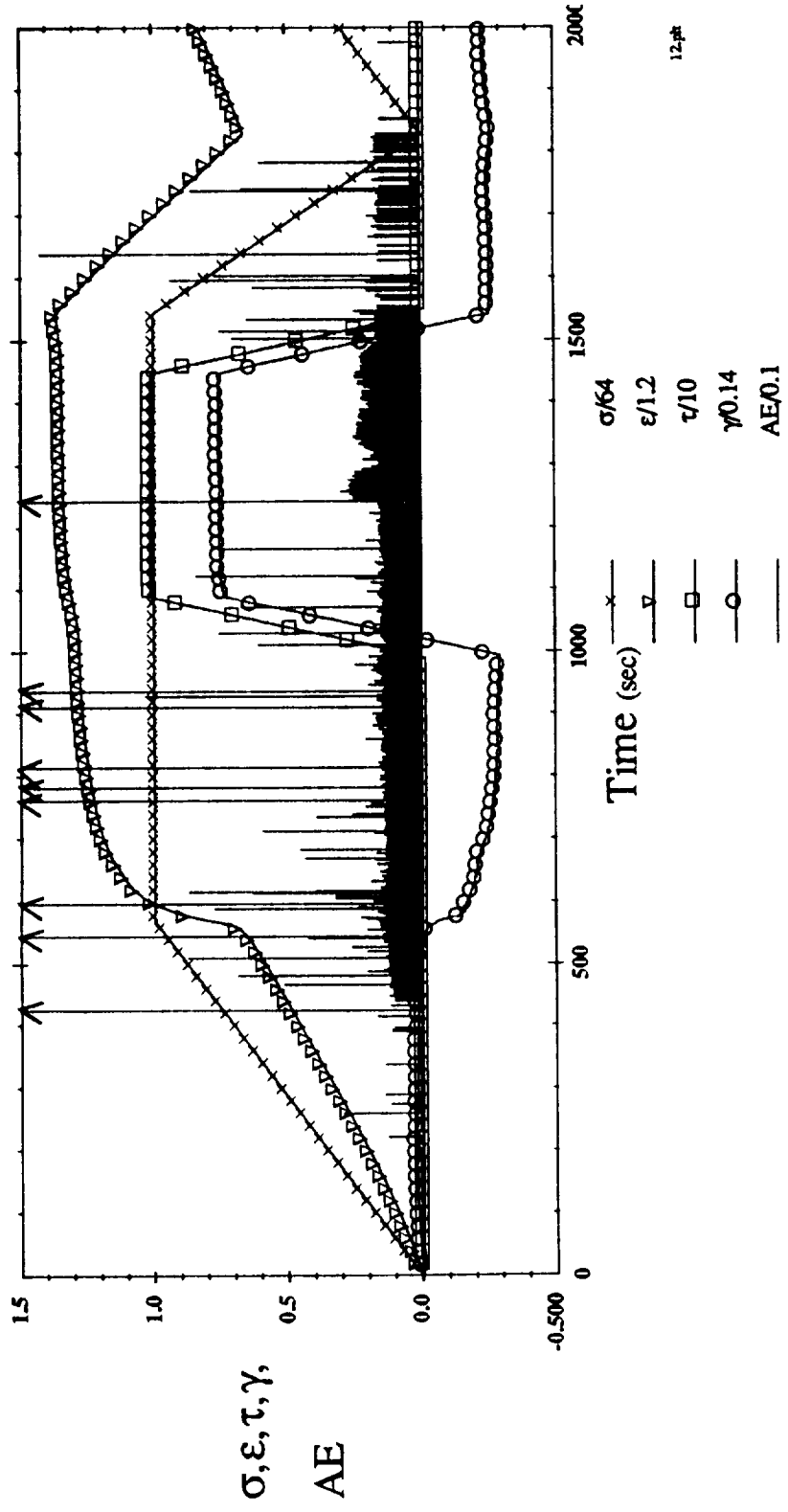

Figure 6.40: $[\pm 45]_s$ Type IA Loading - Cycle #11

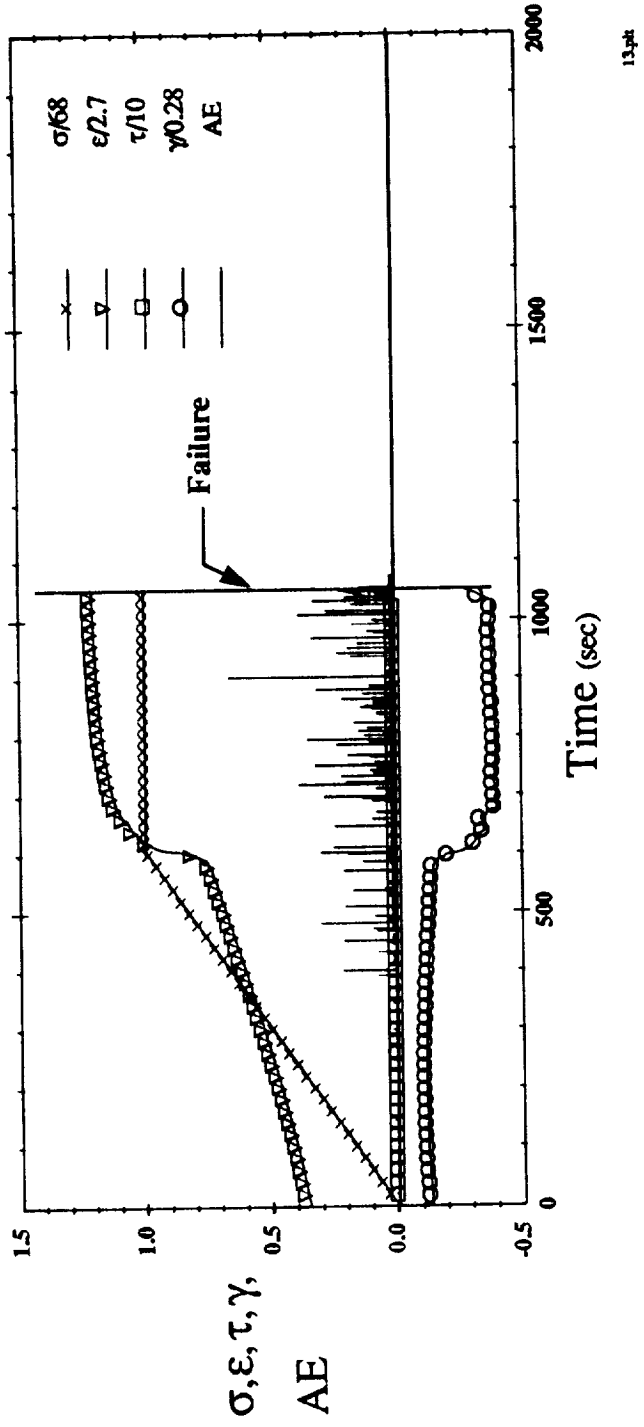

Figure 6.41: $[\pm 45]_s$ Type IA Loading - Cycle #12

the most prevalent damage mechanism in the $[\pm 45]_S$ tubes was fiber/matrix debonding. This reinforces the premise that the AE monitored were primarily due the fiber/matrix interfacial debonding.

A summary of the degradation of both axial and shear stiffnesses is shown in Fig. 6.42. As for Type I loading, a nearly linear degradation in the axial stiffness is present after a threshold value of axial stress (24 ksi) has been surpassed. The shear stiffness is also degraded in a roughly linear fashion, which is different from the shear stiffness degradation observed in Type I tests.

6.2.2.3 Type II Loading

The maximum shear stress that could be applied to a $[\pm 45]_S$ tube was limited by the capacity of the load stand. In fact, failure of a $[\pm 45]_S$ tube by torsional loading was not

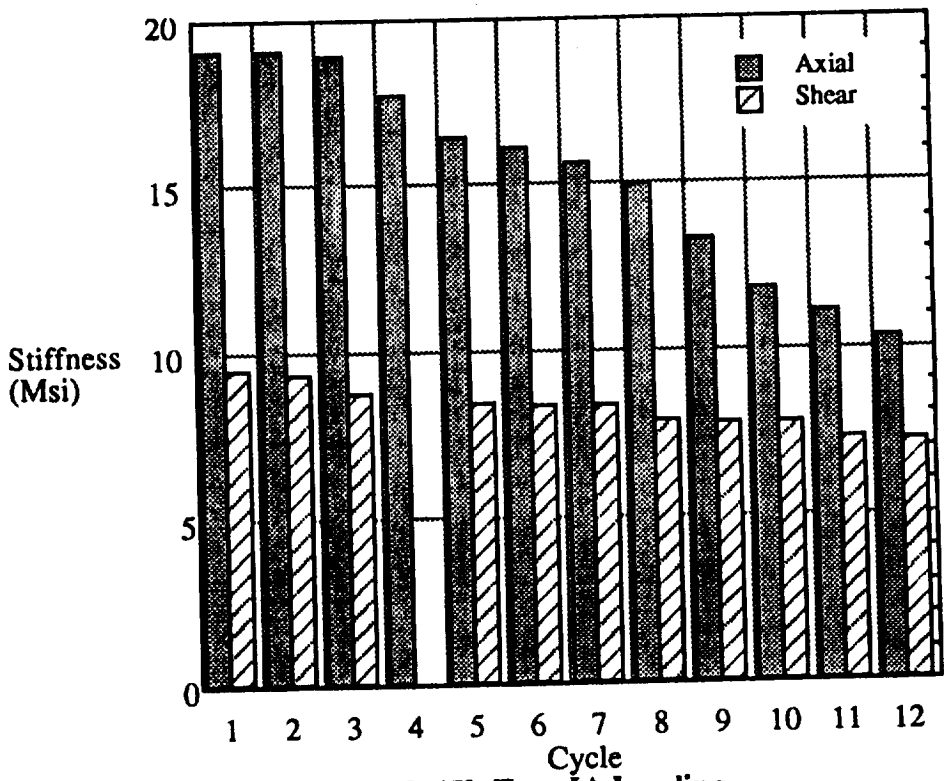

Figure 6.42: $[\pm 45]_S$ Type IA Loading

possible. Because the $[\pm 45]_s$ tubes have such a large diameter (4 inches), the torsional rigidity is very large, thus requiring a very large torque to produce a moderate level shear stress. The shear and axial responses of a $[\pm 45]_s$ tube subjected to Type II loading are shown in Fig. 6.43. The cyclic shear responses have been offset to enhance the clarity of Fig. 6.43a, while the axial responses in Fig. 6.43b were not. Both shear and axial responses are seen to be linear elastic. AE was initially heard at the shear stress of approximately 6.5 ksi and followed the Kaiser effect. The shear and axial stiffnesses are displayed graphically in Fig. 6.44. The shear stiffness was degraded by only 6% and the axial stiffness degraded 14%. Relative to the axial tests (Type I and IA), the decrease in stiffness for torsional loading (Type II) is minimal for the range of loads applied.

6.3 Ti-15-3 Creep Tests

Short term creep tests were conducted on bulk Ti-15-3 to gain a better understanding of the creep response of SiC/Ti composites. It is necessary to know the response of the constituents in order to understand the composite response. The fibers are elastic, but the matrix is elastic-viscoplastic. The creep response of the matrix is then crucial in determining the composite creep response. It is acknowledged that it would have been more beneficial to conduct experiments on as-fabricated Ti-15-3 (a fiberless composite) because the fabrication process changes the material properties. However, only bulk Ti-15-3 was available at the time. All tests were conducted at room temperature on dog-bone tensile specimens.

Three specimens approximately 0.11 in. thick by 0.20 in. wide were tested in load control to failure. The specimens were 6 in. long with a gage length of 3 in. A single longitudinal strain gage was used to measure axial strains. The axial modulus was found to be 11.9 Msi from low level tests. Loading rates of 20 lb/sec and 50 lb/sec were used.

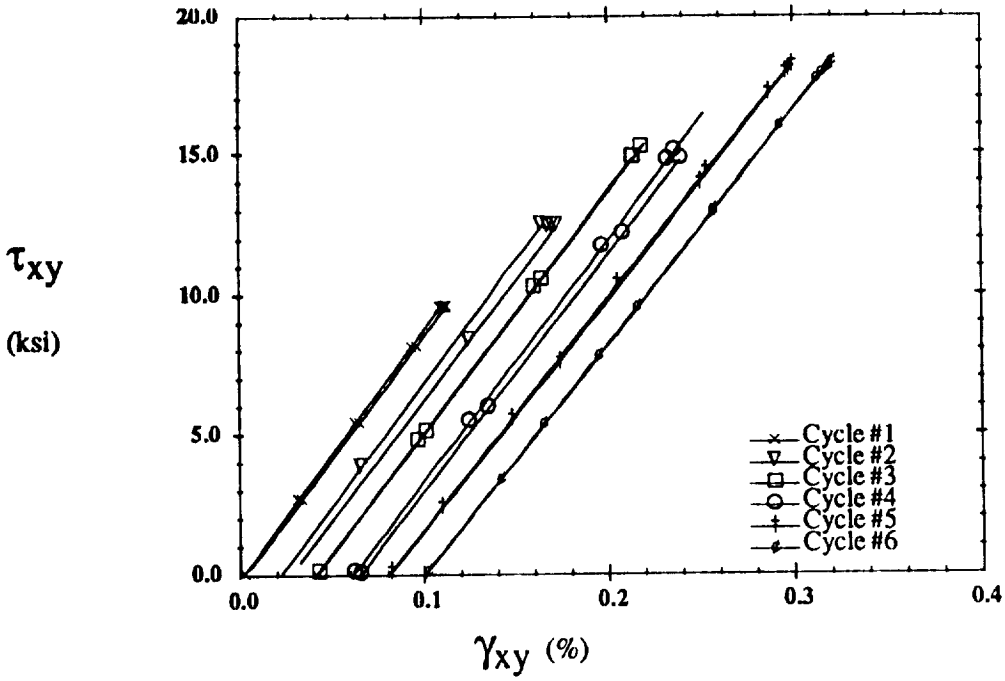

(a) Shear Response

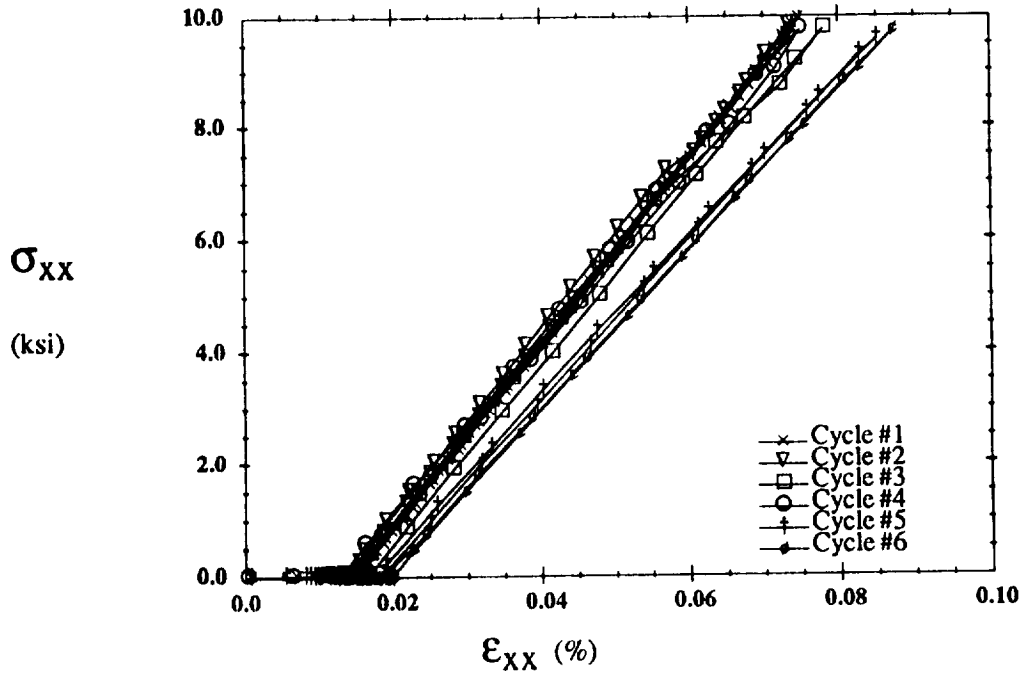

(b) Axial Response

Figure 6.43: $[\pm 45]_s$ Type II Loading

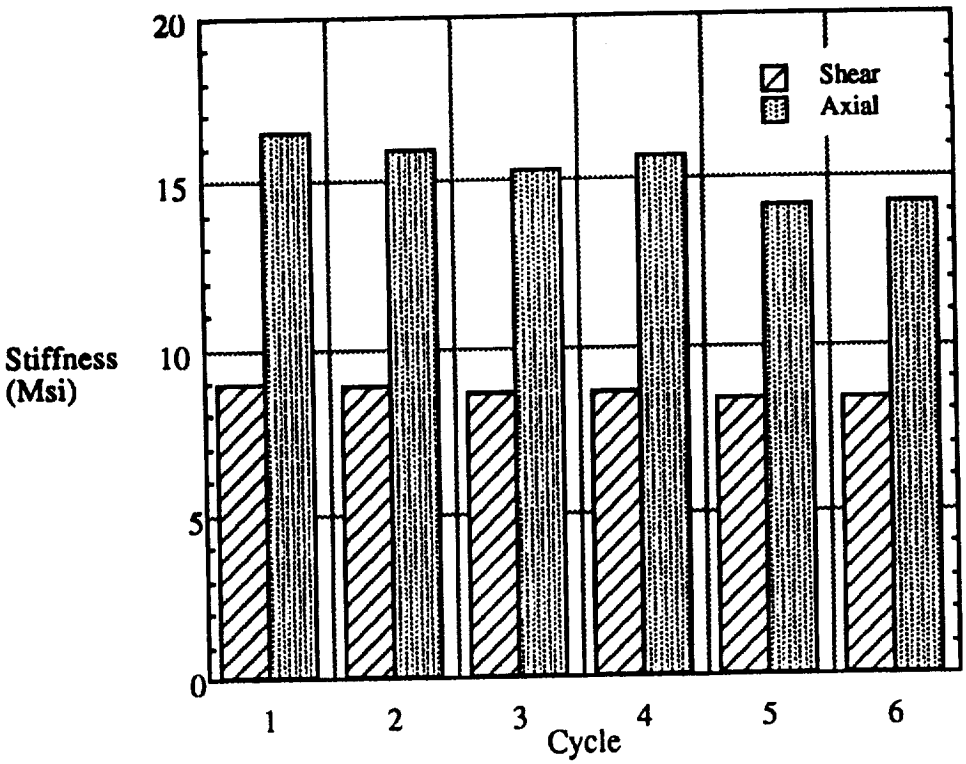

Figure 6.44: $[\pm 45]_s$ Type II Loading

Table 6.3: Ti-15-3 Loadings

Specimen #1		Specimen #2	
σ	Time	σ	Time
ksi	sec	ksi	sec
60.6	226	79.5	266
80.3	278	91.2	269
90.6	272	96.4	265
100.1	577	102.2	607
110.2	26[a]	109.6	41[b]

a. Failure
b. Failure

The load histories for specimens #1 and 2 are presented in Table 6.3. As shown in the stress-strain diagram of Fig. 6.45a specimen #1 exhibited no creep until the stress of

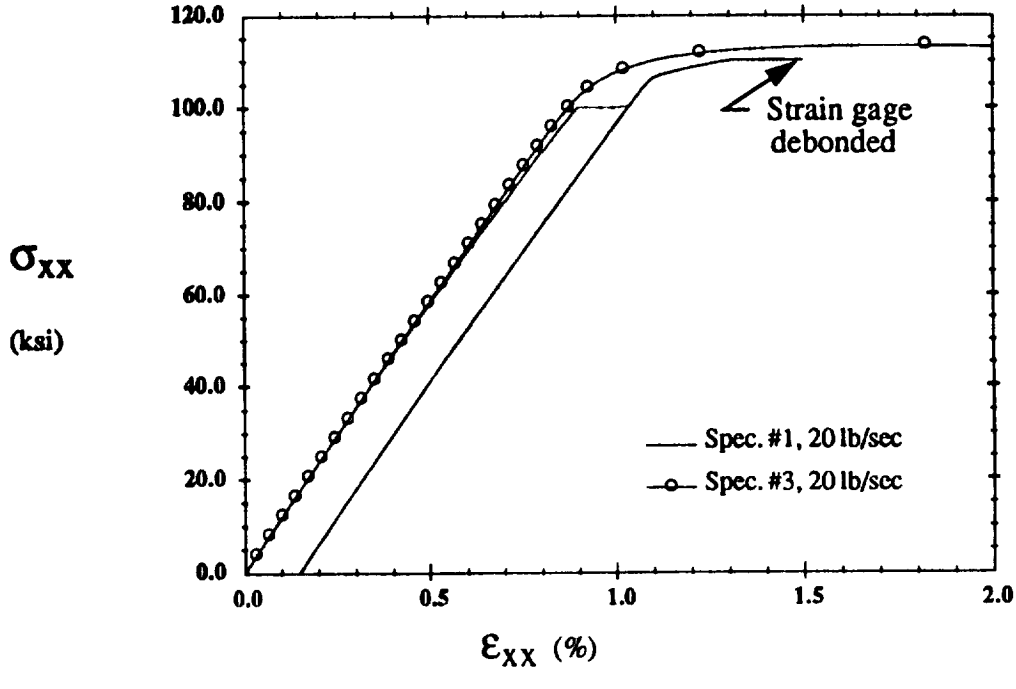

(a) Specimen #1

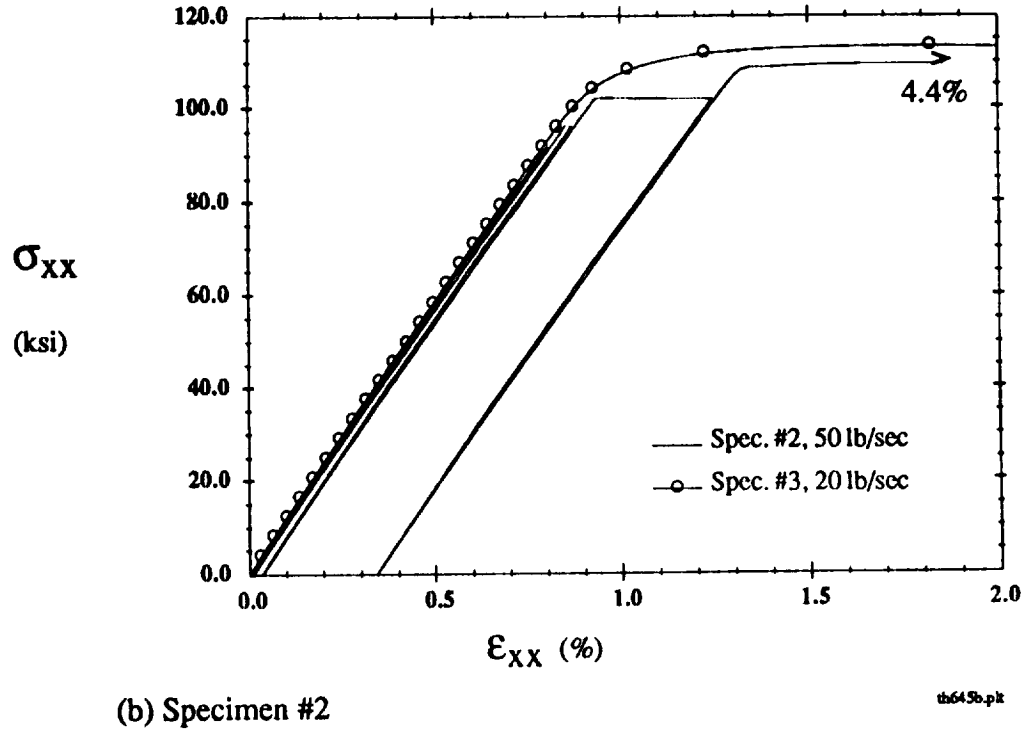

(b) Specimen #2

Figure 6.45: Ti-15-3 Cyclic Creep Tests

100 ksi was applied. Creep began in specimen #2 at the stress of 96 ksi (Fig. 6.45b). The creep strains for specimen #2 at 102 ksi were much higher than those for specimen #1 at 100 ksi, as shown in Fig. 6.46. This can be attributed to the faster loading rate for specimen #2, 50 lb/sec versus 20 lb/sec, as well as the higher stress level (102 ksi to 100 ksi). The other difference between loadings on specimens #1 and 2 was that specimen #2 was completely unloaded after each cycle, while specimen #1 was only unloaded after the applied stress of 100 ksi. Both specimens crept to failure at the stress of 110 ksi.

It is important to know the response of the material to monotonically increasing loads to compare and contrast the creep response with the time independent component of plastic response. Specimen #3 was tested to failure at a load rate of 20 lb/sec. The response shown in Fig. 6.45 indicates that creep does not occur until the transition region between the elastic and perfectly plastic regions is reached. It is noted that the elastic response from all three specimens was slightly nonlinear. Also, significant necking

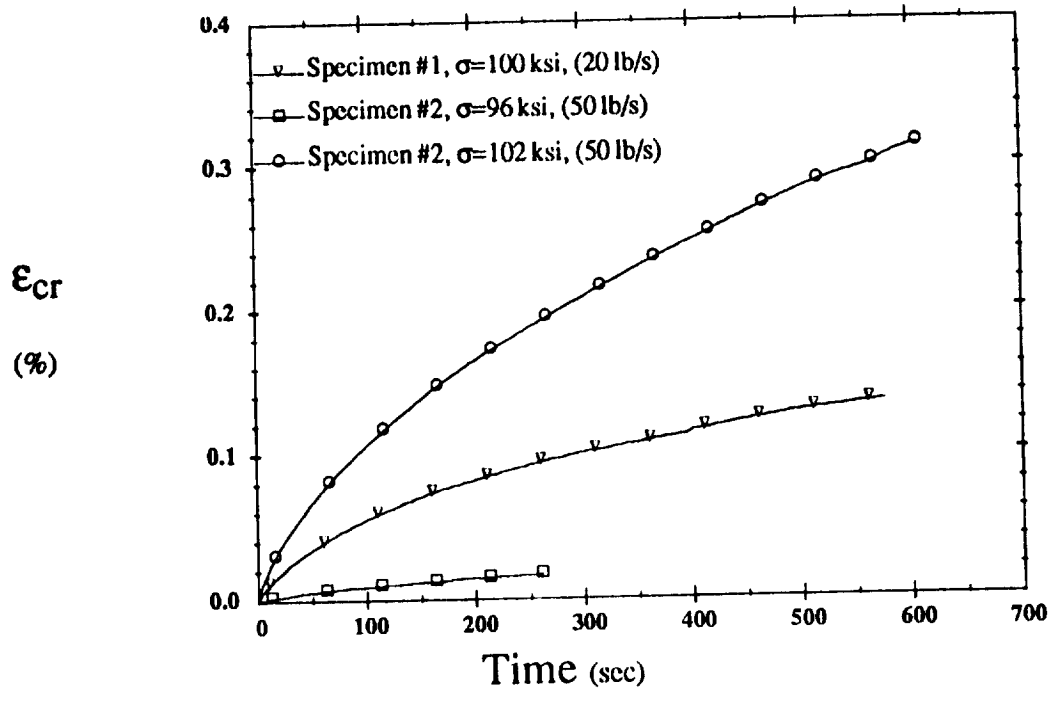

Figure 6.46: Ti-15-3 Creep Response

resulting in a cross section approximately 50% of its original area occurred at the failure surface of all three specimens.

CHAPTER 7

COMPARISON OF THEORY AND EXPERIMENT

The validity of the theoretical model presented in Chapters 2 and 3, henceforth known as the debonding unit cell model (DUCM) to distinguish it from other models that consider imperfect bonding, must be verified through comparison with experimental data. In the following, DUCM predictions are compared with experimental data from multiaxial tests conducted on unidirectional $[0_4]$ and angle-ply $[\pm 45]_s$ tubular SiC/Ti specimens.

For transverse tensile loading theoretical predictions obtained from the method of cells (Aboudi, 1991) will also be presented to illustrate the differences in the treatments of the fiber/matrix interface. The method of cells predictions are made using the flexible interface model (Jones and Whittier, 1967). The traction-displacement interfacial constitutive relations are linear, thus the interfacial model represents a predetermined amount of imperfect bonding and not the debonding process. In DUCM the interfacial tractions are determined by a function that increases, reaches a maximum, then decreases to zero as interfacial displacements increase. The model is intended to represent the debonding process rather than a predetermined state of imperfect bonding. Both models use the elastic-viscoplastic model of Bodner and Partom (Bodner, 1987) for the matrix constitutive relations.

There is however an unresolved issue. What are the interfacial properties? DUCM requires values for the normal interfacial separation strength, shear strength ratio, normal and tangential characteristic lengths, and the coefficient of kinetic friction between the two sides of the interface after failure. In theory at least, these interfacial properties can be

measured experimentally as discussed in Chapter 4. If the interfacial properties were determined from such a set of experiments then the response of a composite composed of a doubly periodic array of fibers could be predicted provided the model is correct. However, real composites, particularly the ones used in this experimental program, are not truly doubly periodic (Fig. 5.1) but are more random in nature due to fiber misalignment. For perfectly bonded fiber/matrix interfaces this deviation from the assumed packing sequence is insignificant, as shown in Section 4.1. Conversely, for imperfect bonding the response of a unit cell is quite sensitive to its aspect ratio; the random nature of the actual material causes the response to be nonuniform. The debonding process begins sooner at locations where high local stress and strain fields exist than it does elsewhere.

The fiber/matrix interface in SiC/Ti composites with coated fibers, as discussed in Section 5.1, is generally considered to be brittle and weak. However, if a unit cell is to be considered an RVE it must represent the average behavior of the composite at large. In some cases experimental results indicate that the overall composite response is that of a composite with a ductile interface. The conclusion to be drawn here is that if the loading on all interfaces is uniform then the interfacial properties may be experimentally measured at any representative interface. Otherwise, the interfacial properties must be determined from a statistical analysis of all interfaces in the composite, because by definition of a RVE the unit cell must represent the composite at-large to be a valid micromechanical model. At present it is unclear how to perform the necessary statistical analysis to determine the effective interfacial properties for a nonuniform composite. Therefore, interfacial properties must be treated as parameters and a curve fitting technique used to match predicted effective response with experimentally determined response.

Sometimes it is useful to be able to predict yield surfaces so that it is not necessary

to conduct a large quantity of experiments to determine the yield surfaces for a material. Comparison of a predicted yield surface with a limited number of experimentally determined yield points can be very helpful in understanding material behavior. However, many viscoplastic theories do not include a yield criterion, thus no yield surface exists. DUCM uses the unified viscoplastic theory of Bodner and Partom (Bodner, 1987) which does not use a yield criterion. Hence, in its current form, DUCM can not predict yield surfaces. However, Pindera and Aboudi (1988) included the Mises yield criterion in the method of cells to enable the prediction of initial yield surfaces. Yield surfaces predicted by the method of cells, including the effects of an imperfect fiber/matrix interface, are presented in this chapter to aid in understanding the experimentally observed material response.

7.1 Unidirectional Composites

Theoretical predictions are compared with experimental results from Type I, Type II, and Type III tests on $[0_4]$ SiC/Ti tubes. In the following, perfect bonding will be denoted PB, a debonding or imperfect interface will be denoted DB, and an interface with no bond between the fiber and matrix will be denoted NB.

7.1.1 Initial Elastic Properties

A comparison between the predicted and experimentally determined initial elastic properties was displayed in Table 6.1. The comparison is shown graphically in Fig. 7.1 as well. Predictions from DUCM for both perfect and no bond conditions are presented to establish a range where the experimentally determined values are expected to lie. Thermal residual stresses are not considered for these predicted properties.

The histograms in Fig. 7.1 are for initial modulus, Poisson's ratio, and axial shear

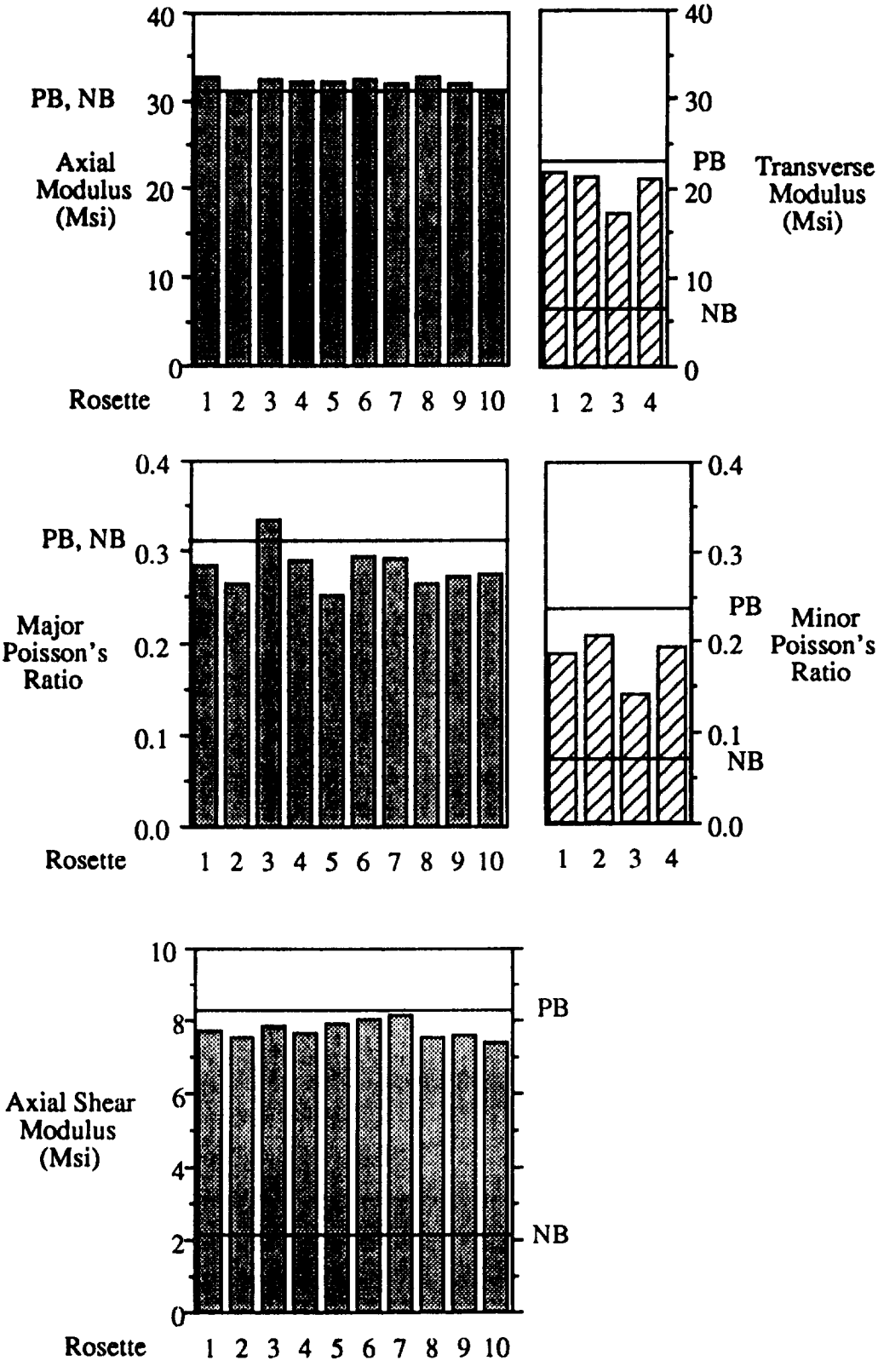

Figure 7.1: [0_4] SiC/Ti Initial Elastic Properties

modulus. Experimental data from strain gages located at the mid-length of all $[0_4]$ tubes tested are presented along the horizontal axis of each graph. Only data from the initial, low load level tests are presented. Axial and transverse moduli, E_{11} and E_{22}, respectively, are compared to accent the differences between axial and transverse moduli. Likewise for the major and minor Poisson's ratios, ν_{12} and ν_{21}. Data from only four strain gages was available for the transverse modulus and minor Poisson's ratio because just one tube was subjected to internal pressure.

The model predicts that the condition of the fiber/matrix bond has no effect on either the axial modulus or the major Poisson's ratio. However, for transverse modulus, minor Poisson's ratio, and axial shear modulus, G_{12}, a wide range of values are predicted as the condition of the bond varies from PB to NB.

The experimental data for axial modulus is very uniform and agrees extremely well with the prediction. As observed in Section 6.1 three of the four experimentally determined values for transverse modulus are very uniform, while the fourth value is much lower. The three uniform values are approximately 10% below the PB prediction. Experimental data for major Poisson's ratio is slightly more scattered, but agrees reasonably well with the predicted value. The three uniform experimental values for minor Poisson's ratio are approximately 18% below the prediction for perfect bonding. The experimentally determined values for the axial shear modulus are quite uniform and on average are just 7% below the prediction for perfect bonding.

These comparisons reveal that the experimentally determined properties are at least bracketed by the PB and NB predictions. Reasonably good agreement is observed between experimental initial elastic properties and model predictions for perfect bonding. There are two possible explanations for why the model predicts a slightly higher

transverse modulus, minor Poisson's ratio, and axial shear modulus. It is possible that the specimens in the as-fabricated state do not have perfectly bonded interfaces. Second, the representation of the composite with a repeating unit cell model, while making the analysis possible, may simply overestimate the actual elastic properties.

7.1.2 Type I Loading

The response of a $[0_4]$ tube subjected to Type I loading was linear elastic to failure. No appreciable acoustic emissions were heard prior to failure. Comparisons between DUCM and the experimental data are shown for loading cycles #11 and 12 in Fig. 7.2. Excellent agreement is observed in Fig. 7.2a for the axial stress-axial strain response. DUCM predicts a linear elastic axial response for PB and NB. No stiffness degradation is predicted for axial loading and none was observed experimentally. As mentioned above for initial axial modulus (Fig. 7.1), the predicted axial stiffness agrees well with that observed experimentally. Figure 7.2b compares the predicted transverse strain-axial strain response with that determined experimentally. DUCM predicts no change in the slope of the transverse-axial strain response (Poisson's ratio) regardless of the condition of the fiber/matrix bond. Once again the predicted response is observed to agree well with the experimental data. It is interesting to note that the experimental transverse strain-axial strain data is slightly nonlinear and that cycle #11 displays a hysteresis type behavior. At present this phenomenon is unexplained.

No inelastic deformation was observed in Type I tests because the tube failed outside the gage section due to stress concentrations associated with the grips. Fractography conducted by Lerch (1993) indicated that failure initiated at the bolt hole where the pin transmitted applied loads to the tube. The failure can be summarized as follows. In the cycle prior to failure (#12) the adhesive bonding the tube to the top grip

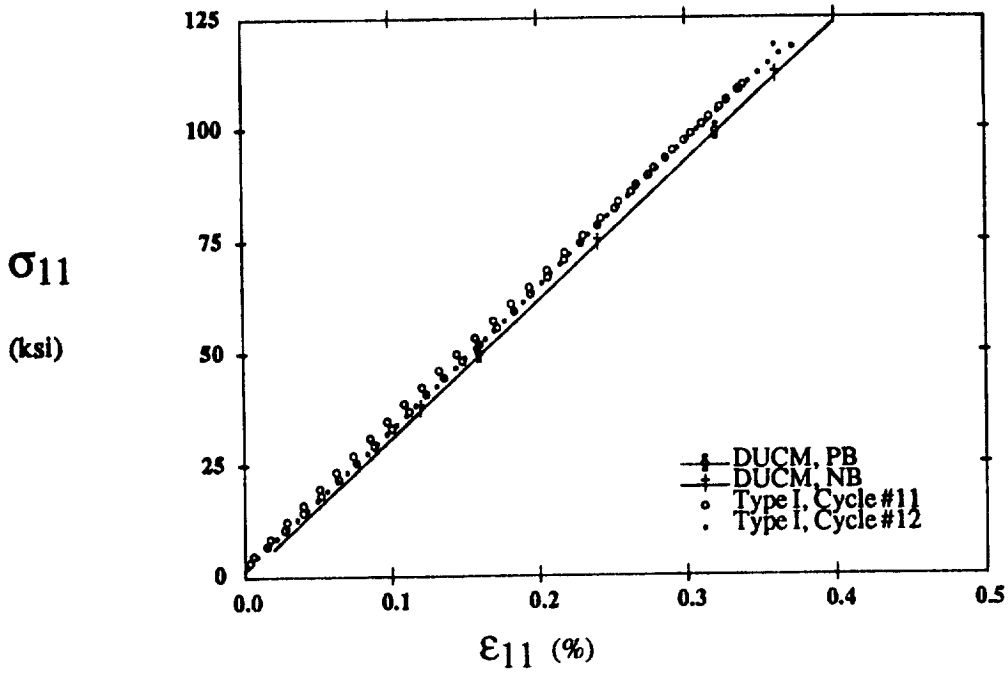

(a) Axial Response

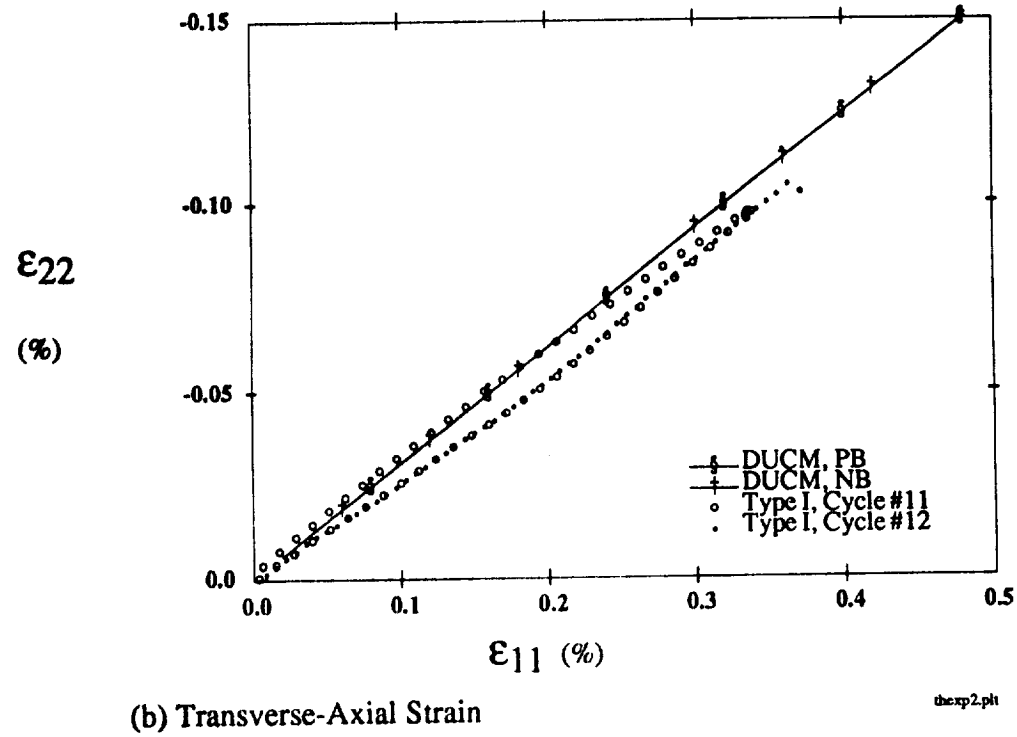

(b) Transverse-Axial Strain

Figure 7.2: [0_4] SiC/Ti Type I Loading Comparison

failed at a gage section stress of 119 ksi. Failure initiated at the bolt holes in the top grip during cycle #13 at a gage section stress of 108 ksi. The fracture surface propagated to the bottom of the steel plug bonded to the inside of the tube where it continued transverse to the fibers until complete failure occurred (Fig. 6.16). Visual microscopy revealed that the portion of the fracture surface transverse to the fibers occurred where a moly wire existed in one of the plies.

A linear elastic finite element analysis was performed on the tube and fixture assemblage using ABAQUS (Hibbitt, Karlsson, and Sorensen, Inc., 1989). Axisymmetric elements were used to model one half of the assemblage (using longitudinal symmetry) in the longitudinal, radial plane. The results showed that not only was the longitudinal stress concentration factor approximately 1.65, but that significant bending stresses developed in the tube at the bottom of the steel plug due to the restraint it provided against radial contraction associated with longitudinal tension. These bending stresses are the reason for the clean, straight failure transverse to the fiber direction (Fig. 6.16).

Initial yield surfaces in axial-shear stress space and axial-transverse stress space predicted by the method of cells are shown in Fig. 7.3. Stresses are normalized with respect to the matrix yield stress in uniaxial tension, Y=110 ksi. The effects of thermal residual stresses associated with an effective fabrication cool-down of 1500°F are included in all predictions. Predictions are shown for perfect bonding as well as for two stages of imperfect bonding. Imperfect bonding is observed to reduce the size of the initial yield locus.

Experimentally determined points are also plotted with the predicted initial yield surfaces. The apparent failure stress of 119 ksi for Type I loading is plotted on the horizontal axis. Due to the stress concentrations from the grips (discussed above) the

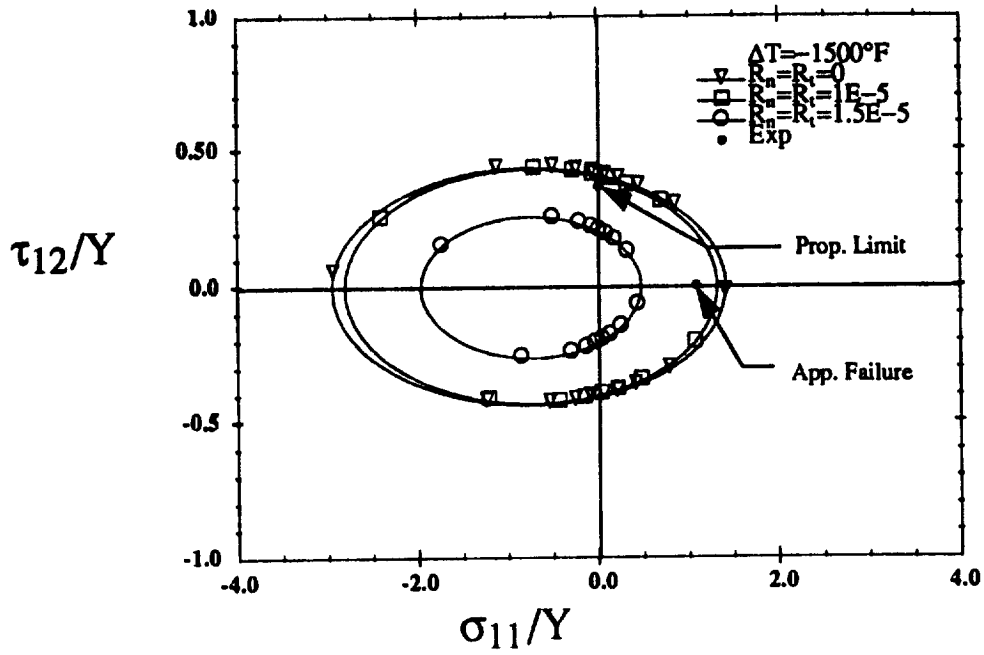

(a)Axial-Shear Space

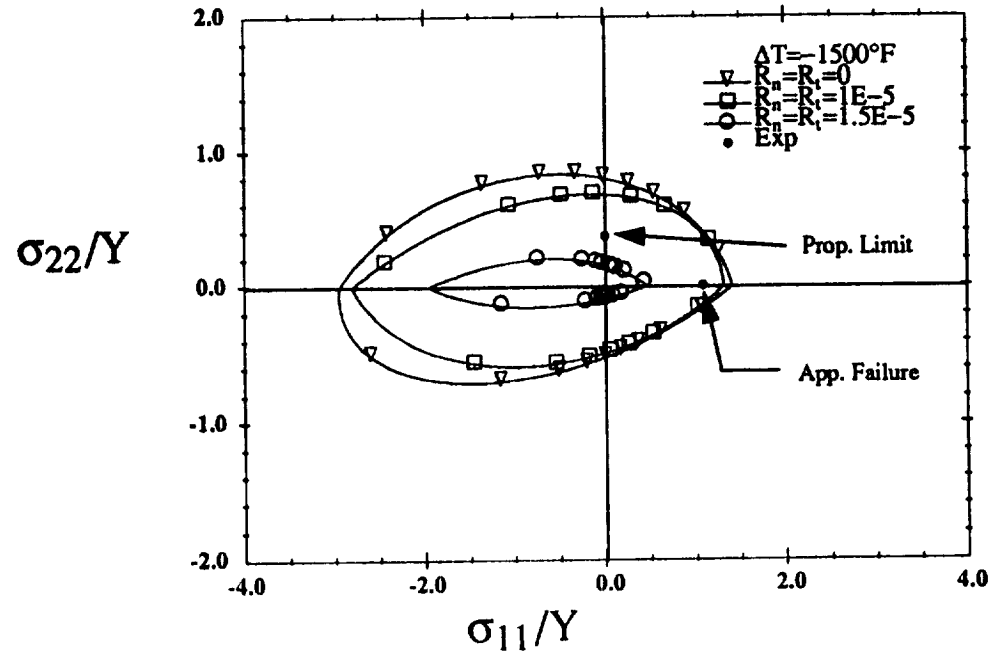

(b)Axial-Transverse Space

Figure 7.3: [0_4] SiC/Ti Predicted Initial Yield Surfaces

stress in the grip region was much higher than the apparent failure stress in the gage section.

7.1.3 Type II Loading

The inelastic shear deformation of a $[0_4]$ tube subjected to Type II loading was clearly nonuniform around the circumference of the tube at the mid-length, as shown in Fig. 6.20. In cycle #13 the response from rosette #2 was linear, while there was a very abrupt knee and a perfectly plastic type response from rosette #3. The reader is reminded that Type II tests were conducted in rotation control. Thus, if the material response was uniform there would have been equal shear strains measured by all the rosettes at the mid-length of the tube. The large uneven horizontal spacing between experimental data points in the response of rosette #3 to loading cycle #13 shown in Fig. 7.4b suggests that not only is the inelastic deformation nonuniform but also sudden. The sudden increase in acoustic activity that corresponds with the observed knee is further evidence of the abrupt nature of the phenomenon.

Unlike the abrupt knee observed experimentally (Fig. 7.4) the predicted response of the titanium matrix has a relatively large, smooth transition region between the elastic and perfectly plastic region as shown in Fig. 7.5. Plotting the proportional limit stress of 40 ksi obtained from rosette #3 in cycle #13 of the Type II tests on the predicted initial yield surfaces (Fig. 7.3a) shows that the nonlinearity occurred prior to predicted initial yielding for a perfectly bonded composite. Thus, the knee in the shear response can only be associated with yielding if there is imperfect bonding between the fiber and the matrix.

DUCM was used to predict the shear response of a unidirectional [0] composite. First the fabrication cool-down cycle was simulated by a uniform temperature change

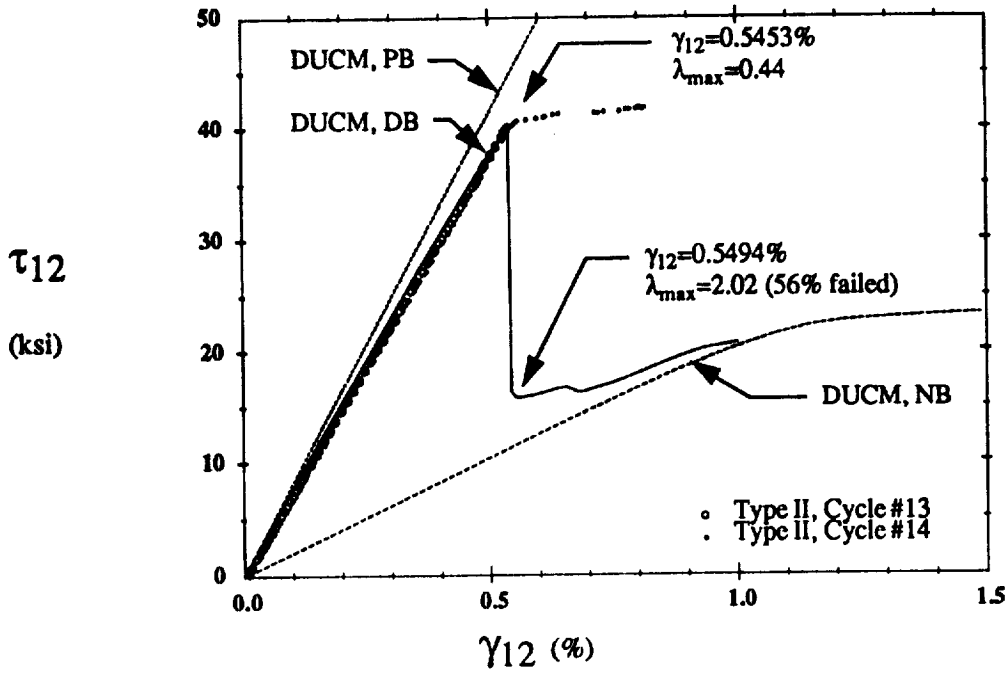

(a)Axial Shear Response, Rosette #2

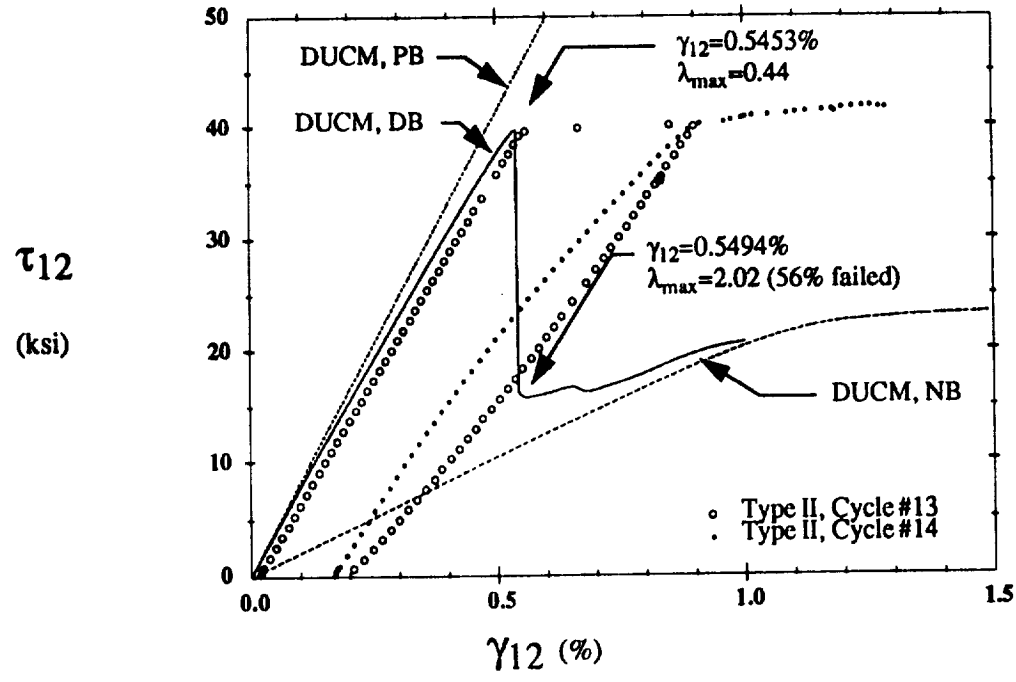

(b)Axial Shear Response, Rosette #3

Figure 7.4: [0_4] Type II Loading Comparison

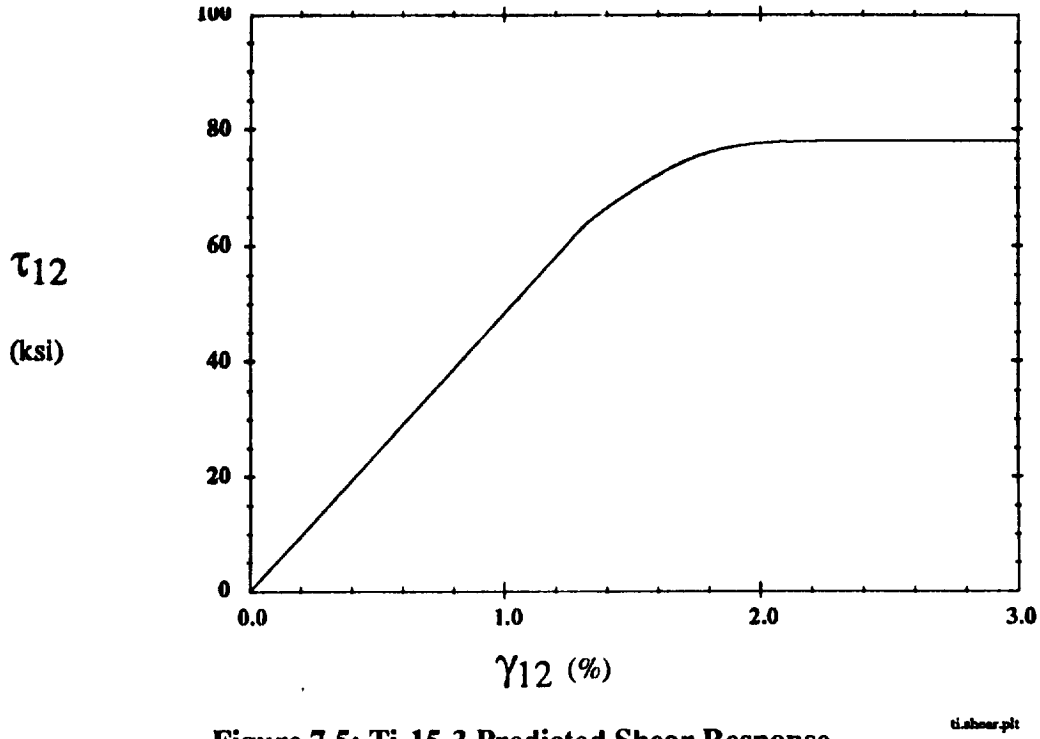

Figure 7.5: Ti-15-3 Predicted Shear Response

(ΔT=-1500°F), then an axial shear strain of 1.0% was applied. All attempts to predict the unloading response resulted in a system of equations that could not be solved within the appropriate equilibrium tolerances prior to completing the unloading cycle. The properties for the interface model were chosen from a trial and error curve fitting procedure to be: σ_0=15 ksi, α=3.3, $\delta=10\times10^{-6}$ in., μ=0. Both axial shear and transverse tensile loading on a [0] lamina were considered in the curve fitting procedure. The interface properties chosen represent the best fit to both loadings considered and will be used throughout the remainder of this work for [0] lamina. The DUCM prediction is compared with experimental results from rosettes #2 and 3 in Fig. 7.4. DUCM predictions for PB and NB are also shown in the figure to provide extreme conditions.

Figure 7.4 shows excellent agreement between the DUCM prediction and experimental results up to the shear stress of 40 ksi at which point the predicted response displays an instability while the observed experimental response exhibits a large

instantaneous reduction in stiffness. The model predicts sudden debonding to occur at the shear stress of 40 ksi. Due to the sudden nature of the debonding event the solution is very difficult to obtain and it is necessary to substantially reduce the size of the applied displacement increment. The parameter λ describes the condition of the bond at a point along the fiber/matrix interface. For perfect bonding λ=0. Bond failure occurs when λ=1. For the shear strain of 0.5453% the maximum value of λ along the interface was 0.44. But for the next displacement increment (γ_{12}=0.5494%) the maximum value of λ was 2.02 and bond failure has occurred over more than 50% of the interface. The model indicates that matrix plasticity has not yet occurred, in fact the predicted maximum effective stress in the matrix is reduced from 101 ksi to 89 ksi by the sudden debonding. Here effective stress is defined to be

$$\bar{\sigma}_e = \sqrt{\frac{3}{2} s_{ij} s_{ij}} \tag{7.1}$$

where s_{ij} are the stress deviators defined by eqn. (2.4). The maximum effective stress of 101 ksi is very near the yield stress (110 ksi) of the matrix.

The model considers debonding to be macroscopically uniform, but experimentally debonding occurred in a nonuniform manner. The predicted instability is due to the sudden brittle nature of the debonding event. The interfacial debonding model dictates that the effective response approaches that predicted for no interfacial bond after debonding begins. The predicted instability was not observed experimentally because, in the experiments, debonding was a local event and only global stresses (τ_{12}=Tc/J) were measured. Because the debonding process was nonuniform in the tube, the global stresses measured (actually torque was measured and shear stress was calculated) are not representative of the local stresses present during and after debonding. Therefore, on the local level it is not possible to determine whether the predicted instability does or does not

occur experimentally. In the presence of nonuniform debonding it is possible that the local response is governed by local stresses even though the global response is governed by displacements, or in this case rotations. If this were the case, no significant instability would be observed on the global level. Notice that if the predicted response obtained after the instability were shifted vertically in Fig. 7.4, the comparison between theory and experiment would be very good.

It is difficult to compare predictions from DUCM with the experimental results from Type II tests due to the nonuniform abrupt debonding present. Strain gages provided local response while the torsional load cell provided global, or average, response. Thus, experimentally it was only possible to plot global stresses versus local strains, which provided neither the global nor the local response. Conversely, macroscopically uniform debonding is assumed in DUCM.

Another possible contributing factor in the difference between the predicted response and the experimental response is the frictional forces at the interface. The presence of frictional forces at the interface allows tractions to be transmitted to the fiber after debonding has occurred. DUCM has the capability to account for frictional forces after bond failure by making the coefficient of friction greater than zero. This was attempted but the finite element program was unable to converge on a solution that satisfied equilibrium within the given tolerances, therefore the coefficient of friction was taken to be zero.

7.1.4 Type III Loading

The axisymmetric finite element model discussed for Type I loading was also used to study the stress distributions in the test specimen assemblage under internal pressure

and combined internal pressure and axial compression. The resulting axial stress, σ_{11}, and circumferential stress (or transverse stress for a $[0_4]$ tube), σ_{22}, distributions are shown in Fig. 7.6. The figure illustrates the stress concentrations caused by the fixture. The simple equations for internal pressure loading of a thin walled cylinder

$$\sigma_{22} = \frac{pr}{t} \qquad \text{and} \qquad \sigma_{11} = \frac{pr}{2t} \tag{7.2}$$

are satisfied at the mid-length of the tube (Fig. 7.6a). Application of an axial compressive stress equal in magnitude to the tensile axial stress $\sigma_{11}=pr/2t$ creates a zero net axial stress at the mid-length of the tube (Fig. 7.6b).

The proportional limit transverse stress of 40 ksi is plotted on the predicted initial yield surface (Fig. 7.3b). This point lies well within the predicted initial yield surface for perfect bonding. Therefore, the knee (proportional limit) appears to be associated with damage rather than yielding. This is in agreement with virtually all other work in the literature for transversely loaded unidirectional composites.

DUCM predictions are compared with the final two cycles (#14 and 15) of Type III loading in Fig. 7.7. The same interfacial properties were used for DUCM as discussed for Type II loading. The loading sequence for the predictions was as follows:

1. thermal loading (ΔT=-1500°F) associated with fabrication cool-down
2. apply a transverse strain of 0.25%
3. apply and unload an axial strain of 0.10%
4. apply and unload a shear strain of 0.10%
5. unload the transverse strain
6. apply a transverse strain of 0.5%.

Predictions from DUCM for PB and NB are also shown to indicate extreme conditions. The predicted transverse response for no bond (DUCM, NB in Fig. 7.7) illustrates the effects of the thermal residual stresses. A distinct knee associated with overcoming the

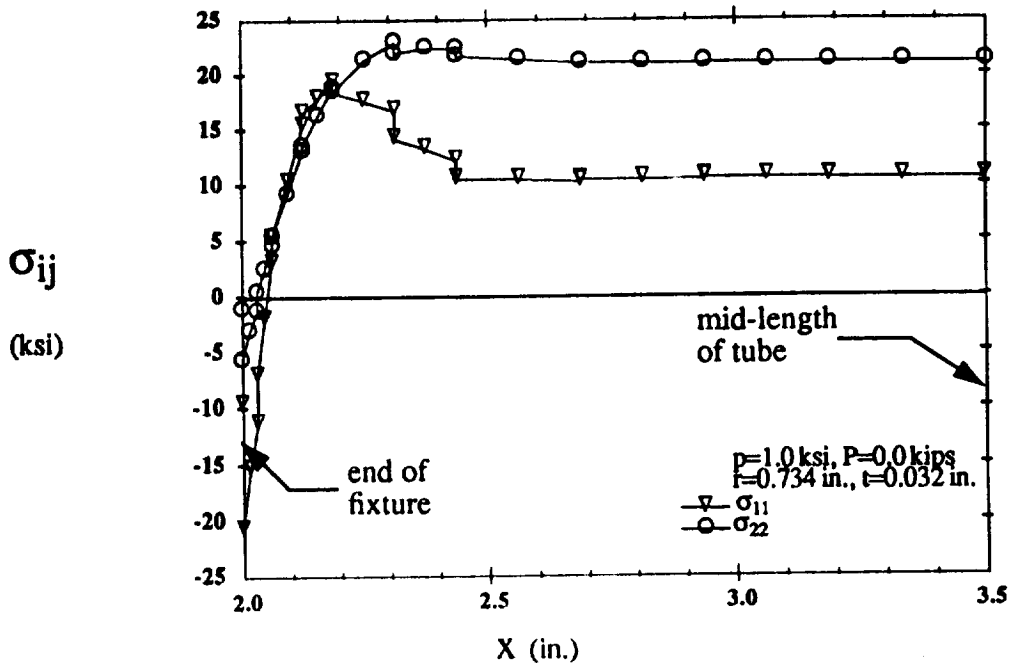

(a)Internal Pressure

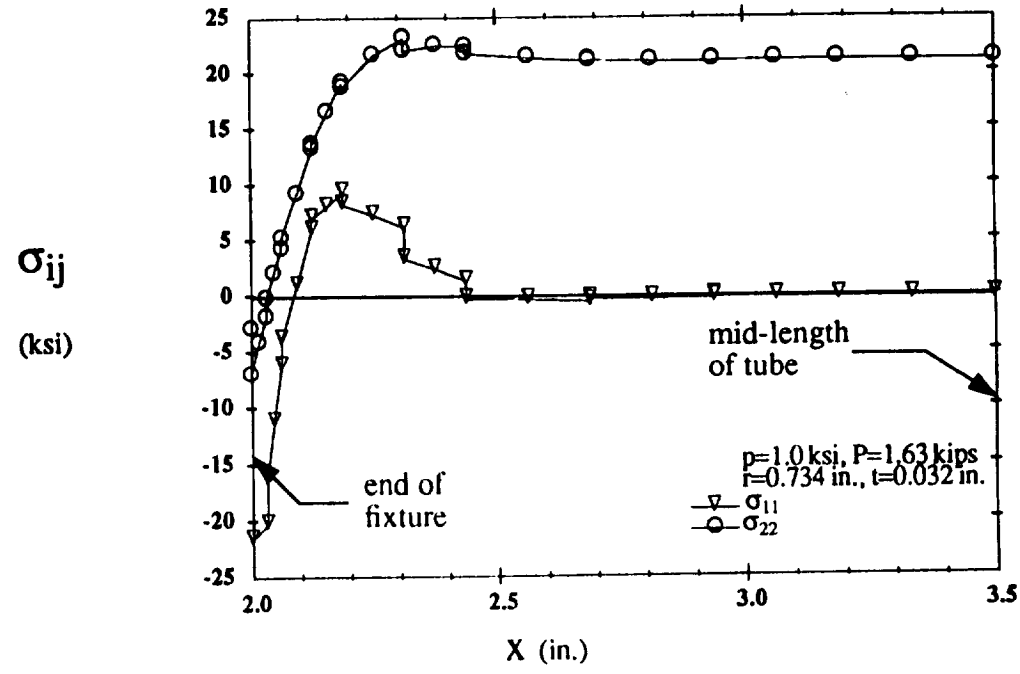

(b)Internal Pressure and Axial Compression

Figure 7.6: [0_4] SiC/Ti Predicted Stress Distributions

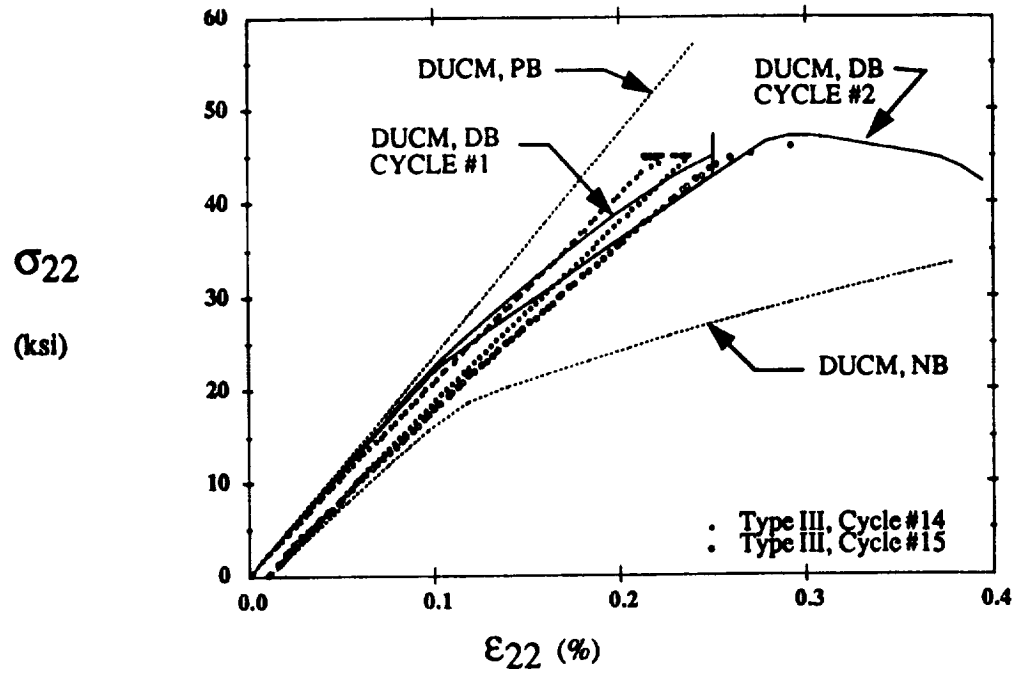

(a)DUCM and Experiment (Rosette #1)

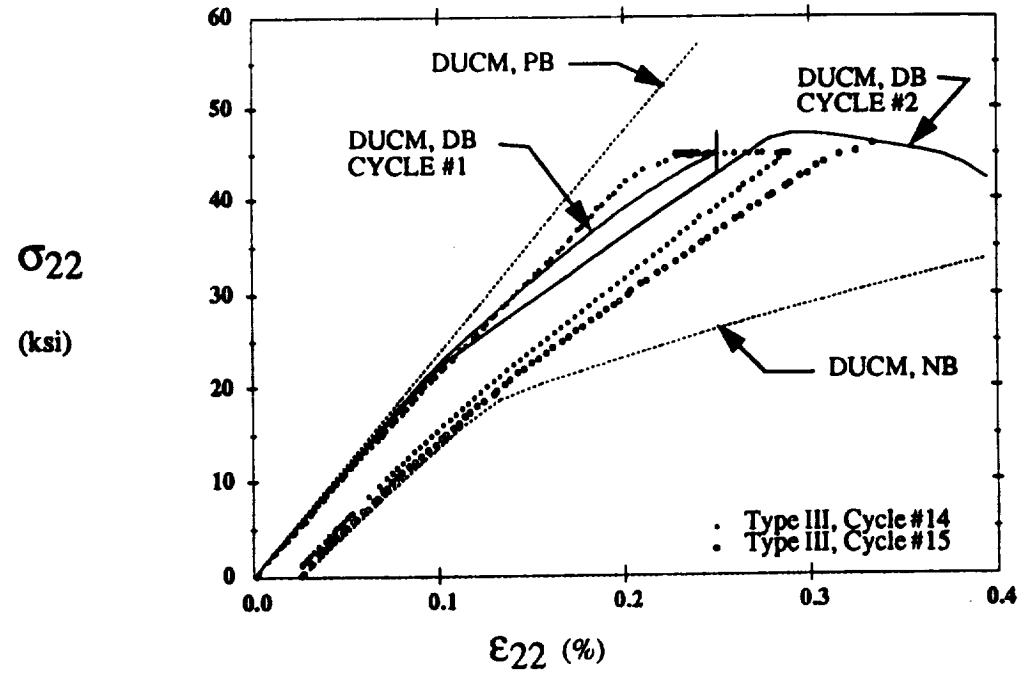

(a)DUCM and Experiment (Rosette #2)

Figure 7.7: [0_4] SiC/Ti Type III Loading Comparison

compressive residual stresses at the interface occurs at approximately 18 ksi. For clarity the no bond prediction has been offset such that it starts at the same point as data from cycle #15.

Comparisons are made between the theoretical model and the response from both rosettes #1 and 2 in Fig. 7.7 because of the differences in the experimental data at different locations on the tube. The model (DUCM, DB) predicts a knee at the transverse stress of approximately 23 ksi that is associated with overcoming the thermal residual stresses. This knee was not observed in the Type III tests possibly because of the additional restraint to circumferential deformation provided by the fixtures. The Type III tests displayed a larger elastic region than results presented in the literature for transverse tension tests conducted on flat specimens. It is surmised that the additional constraint provided by the fixtures served to retard the debonding process. The vertical spike present in the predicted response (DUCM, DB) at the transverse strain of 0.25% is created by an increase and then a decrease in the effective transverse stress during axial and shear loading and unloading, while the transverse strain is held constant. This is probably caused by changes in the local stress fields in the fiber and matrix. Transverse unloading began at a lower stress (σ_{22}=43 ksi) than had been present prior to the biaxial loading (σ_{22}=45 ksi). The predicted unloading response is bilinear due to the compressive radial residual stresses that clamp the matrix around the fiber.

Permanent axial strains were observed experimentally from both strain gage rosettes but were not predicted by DUCM. Prior to transverse unloading the maximum effective stress predicted in the matrix was 116 ksi which is greater than the yield stress (110 ksi) of the matrix for uniaxial tension. Thus, the model predicts local plastic strains, but they are insufficient to cause significant plastic strains in the composite (overall) stress

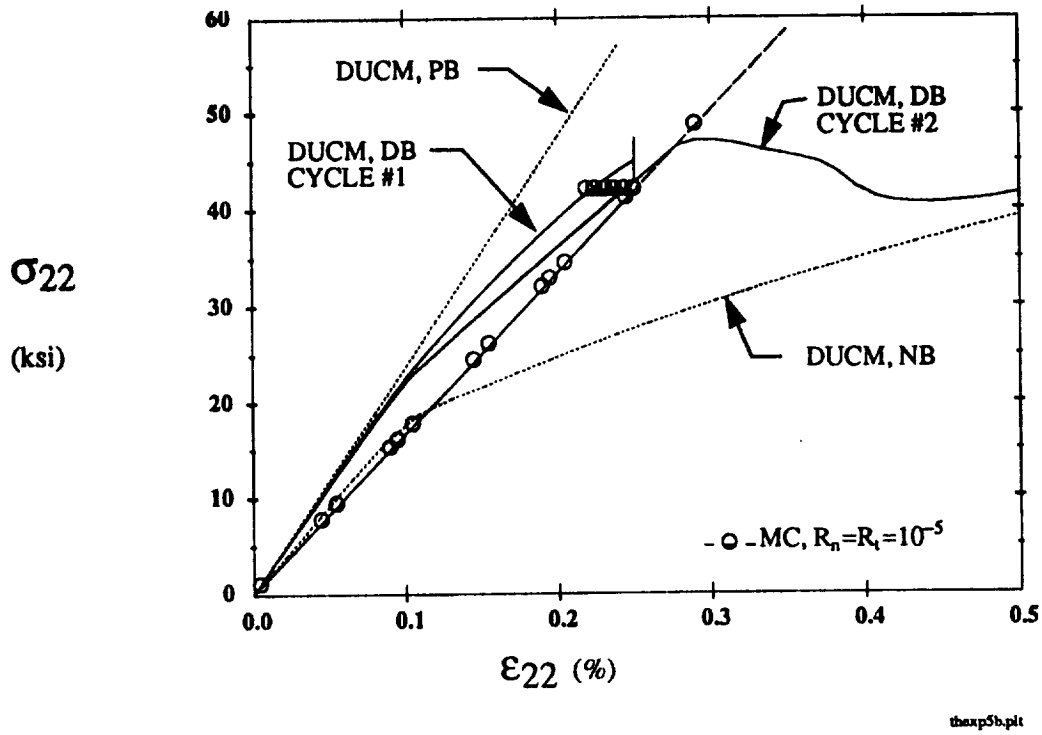

Figure 7.8: [0_4] SiC/Ti DUCM and Method of Cells Comparison

field. The fact that DUCM under-predicted the transverse plastic strains for this loading cycle is significant in that it shows that the model does not accurately represent all the deformation mechanisms for this loading cycle.

The flexible interface model used in the method of cells (MC) is compared with DUCM in Fig. 7.8. The same loading sequence was applied using the method of cells as discussed above in conjunction with Fig. 7.7. The normal and tangential bonding parameters for the flexible interface model were taken to be $R_n = R_t = 10 \times 10^{-6}$in./ksi. The linear interfacial constitutive equations cause the response predicted by the method of cells to be degraded but linear in the range shown in the figure. Again it is observed that the flexible interface model does not provide a representation of the debonding process but rather it models a predetermined amount of imperfect bonding.

The predicted and experimental axial strain-transverse strain response for Type III

loading is shown in Fig. 7.9a. The DUCM prediction is based upon the loading cycle discussed above in conjunction with Fig. 7.7, but for clarity only data from the two transverse loading cycles is presented. The agreement between theory and experiment is very good except, as discussed above, DUCM did not predict permanent strains after loading to the transverse strain of 0.25% and then unloading.

Predicted and experimental axial shear responses are compared in Fig. 7.9b. DUCM accurately predicted the axial shear stiffness but did not predict the permanent shear strain observed experimentally. It is noted that residual stresses do not significantly affect the response in the range shown in the figure.

7.2 Angle-Ply Composites

Theoretical predictions are compared with experimental results from Type I, Type IA, and Type II tests on $[\pm 45]_s$ SiC/Ti tubes. As for the discussion regarding unidirectional tubes perfect bonding will be denoted PB, a debonding or imperfect interface will be denoted DB, and an interface with no bond between the fiber and matrix will be denoted NB.

7.2.1 Initial Elastic Properties

The predicted and experimentally determined initial elastic properties for a $[\pm 45]_s$ tube were presented in Table 6.2. The comparison is repeated graphically in Fig. 7.10. The three histograms show the initial axial modulus, E_{xx}, Poisson's ratio, ν_{xy}, and shear modulus, G_{xy}. Predictions from DUCM for the perfect and no bond conditions are presented to establish a range where the experimentally determined values are expected to lie. Thermal residual stresses are not considered in the predictions. Experimentally determined data from strain gages located at the mid-lengths of three $[\pm 45]_s$ tubes are

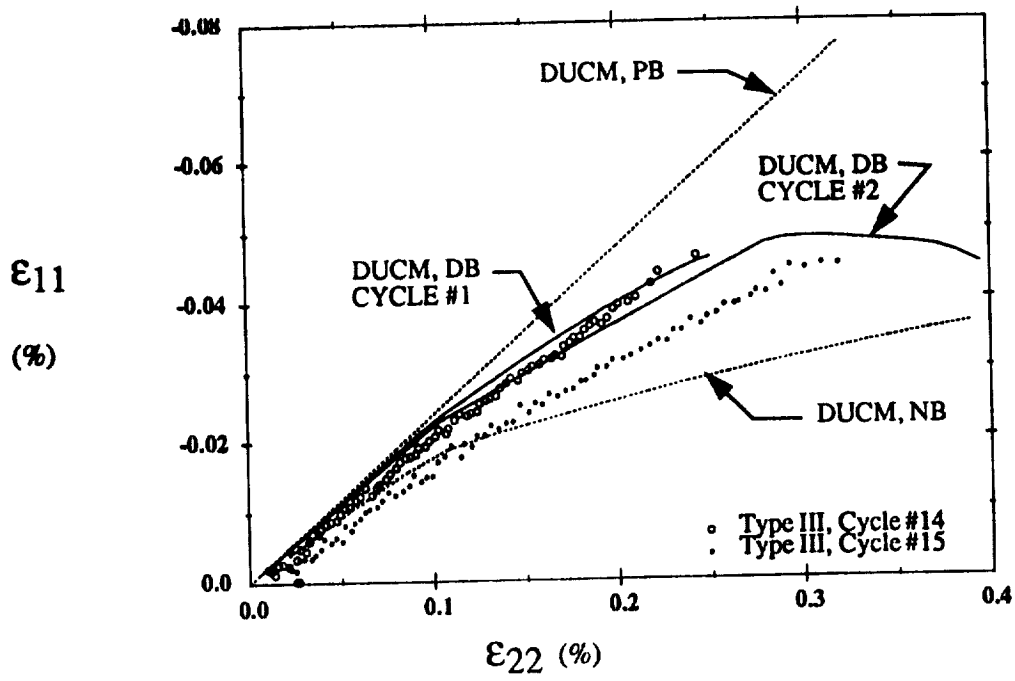

(a)Axial Strain-Transverse Strain

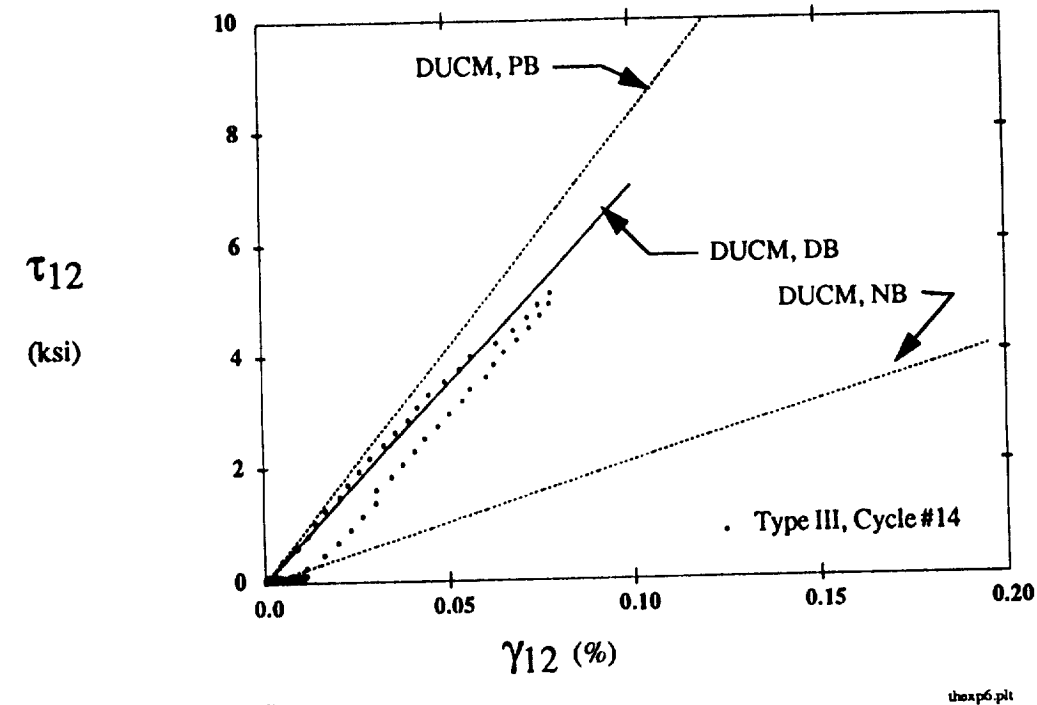

(b)Shear Response

Figure 7.9: [0_4] SiC/Ti Type III Loading Comparison

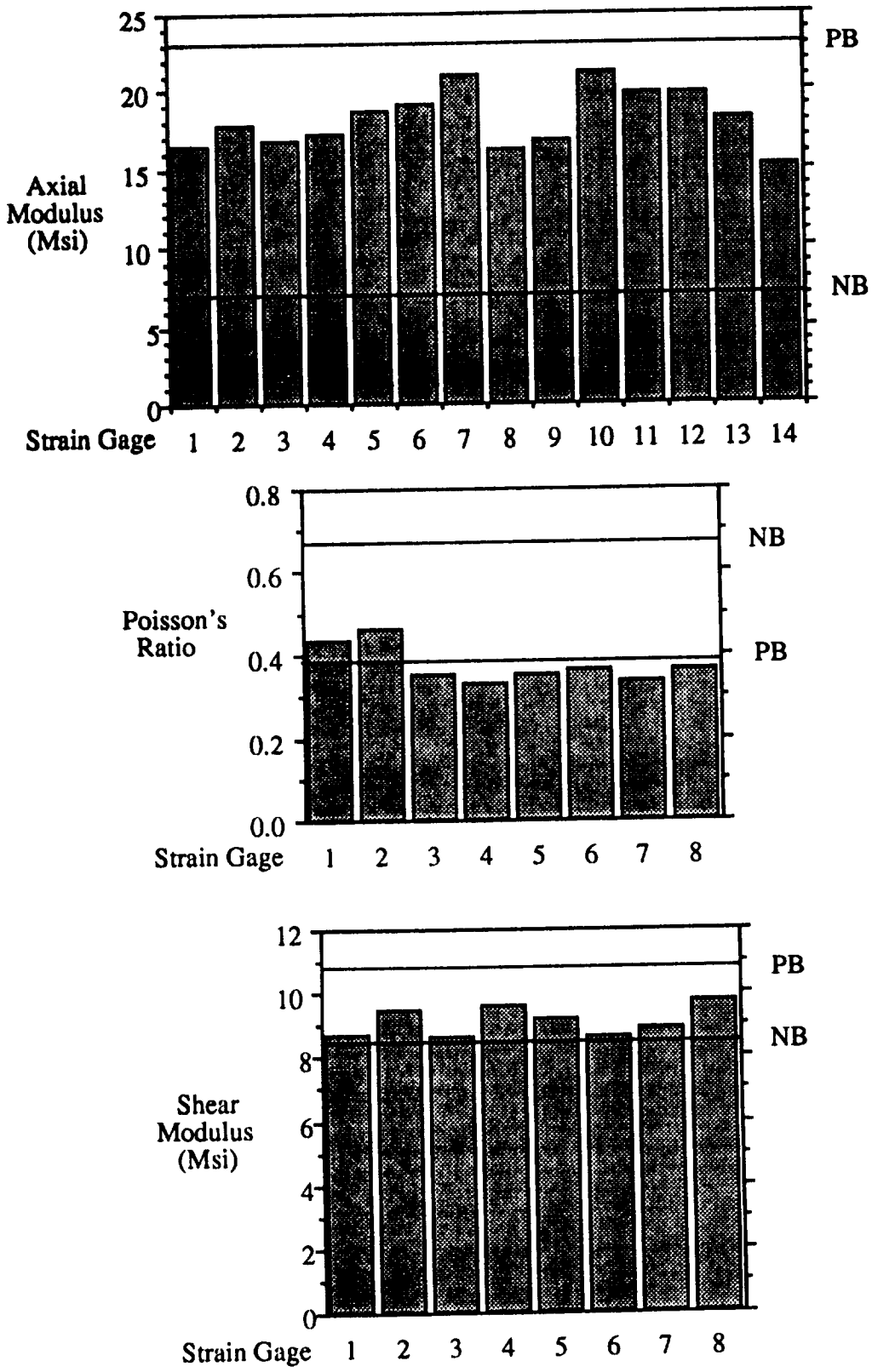

Figure 7.10: $[\pm 45]_s$ SiC/Ti Initial Elastic Properties

presented along the horizontal axis of each graph.

The experimentally determined axial moduli range from 15.1-21.0 Msi, with the average being 18.1 Msi. The wide range of experimental values is the result of material nonuniformity, or more specifically, local variations in the fiber volume fraction. The highest experimental axial modulus (21.1 Msi) is 8% below the predicted value for perfect bonding. In order to explain this discrepancy a study using the method of cells model was conducted to determine the sensitivity of the predicted axial modulus to fiber modulus, matrix modulus, fiber orientation, and fiber volume fraction. The method of cells is an analytical model that allows elastic properties to be predicted very quickly. Because no debonding was being considered it was not necessary to use DUCM. Only one of the above mentioned variables was changed at a time. For the fiber modulus of 58 Msi, matrix modulus of 13.2 Msi, fiber volume fraction of 0.40, and fiber angles of ±45°, the predicted axial modulus was 22.29 Msi while DUCM predicted it to be 23.0 Msi. The results of the sensitivity study are summarized in Table 7.1. The variations required to produce the

Table 7.1: Sensitivity Study

	E_{xx} (Msi)		E_{xx} (Msi)
Fiber modulus, E_f=40 Msi	19.92	Fiber vol. fraction, c_f=0.30	19.37
E_f=50 Msi	21.35	c_f=0.35	20.77
Matrix modulus, E_m=10 Msi	18.20	Fiber angle, θ=±40°	23.05
E_m=12 Msi	20.81	θ=±50°	21.87

discrepancy between experimental and predicted initial axial modulus for perfect bonding were much larger than could be expected in the specimens. The most likely explanation for the low measured modulus is that imperfect fiber/matrix bonding exists after fabrication. Figure 7.11 shows the global and material principal stresses predicted by a

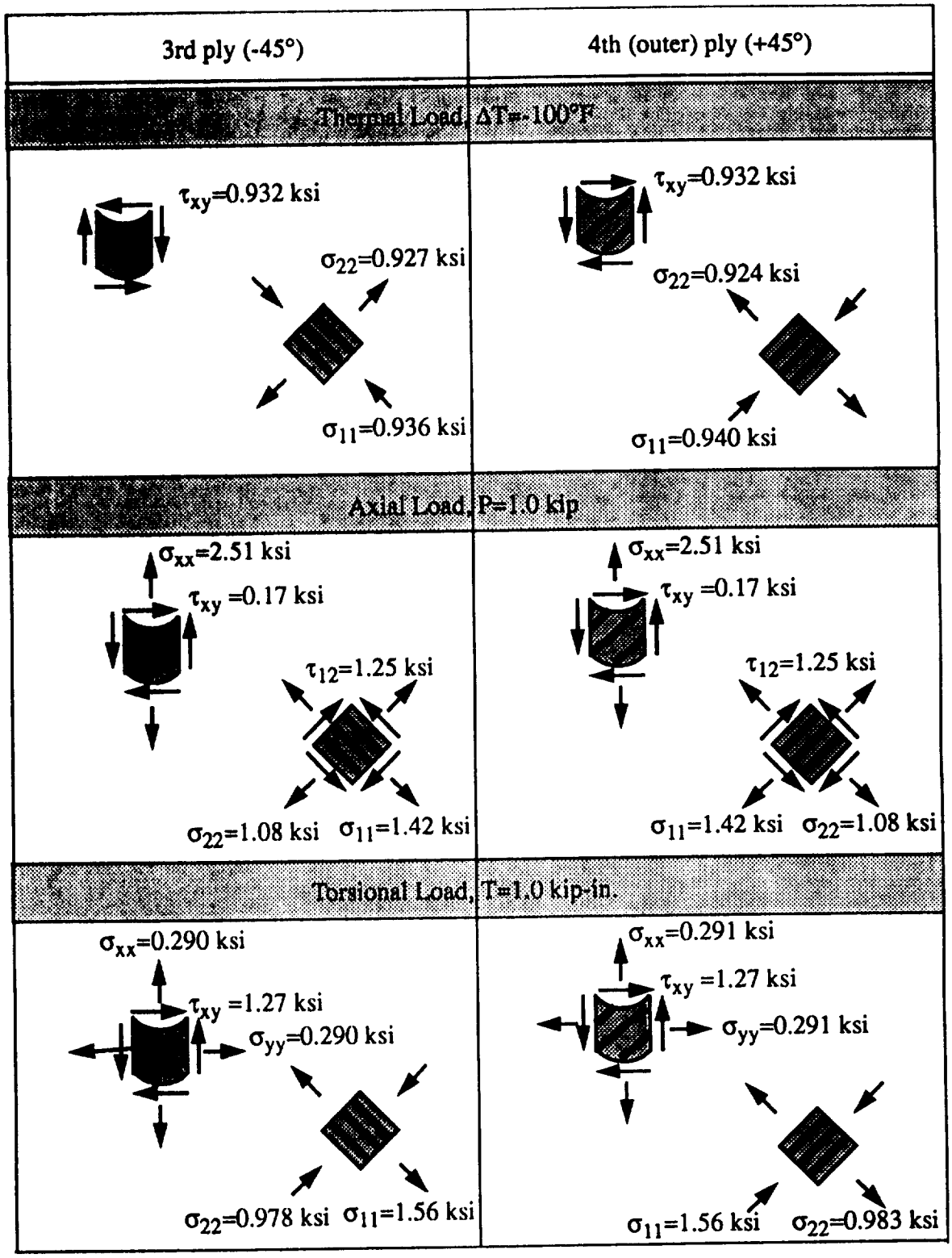

Figure 7.11: $[\pm 45]_s$ SiC/Ti Tube Global and Material Principal Stresses

laminated tube analysis program, developed by Derstine and Pindera (1989), for a $[\pm 45]_s$ tube subjected to thermal, axial, and torsional loads applied independently. While the program is capable of nonlinear analysis, only a linear elastic analysis was performed. Thus, the values presented in the figure may be scaled provided the stresses remain in the linear elastic range. The figure shows that cooling the composite tube down during fabrication creates transverse tensile, σ_{22}, stresses in all plies. Because transverse tension causes debonding, the thermal stresses associated with fabrication cool-down initiate the debonding process.

The range of shear moduli predicted for PB and NB is relatively small (Fig. 7.10) and the measured values all fall within the predicted range, but the average of the measured values (9.08 Msi) is 16% below the predicted value for perfect bonding. This provides further evidence that the as-fabricated $[\pm 45]_s$ tubes do not contain perfectly bonded interfaces.

Poisson's ratio is predicted to increase as the fiber/matrix bond is degraded (Fig. 7.10). However, the average measured Poisson's ratio is 4% below the prediction for perfect bonding. This data is in conflict with the explanation presented above; that the low measured initial axial and shear moduli are due to imperfect fiber/matrix bonding. No logical explanation can be given for this inconsistency at this time.

7.2.2 Type I Loading

Figure 7.11 indicates that applying axial load to a $[\pm 45]_s$ tube creates axial shear stresses, τ_{12}, as well as transverse tensile stresses, σ_{22}, in all plies. Both axial shear and transverse tensile stresses cause the fiber/matrix interfaces to debond. Due to the material nonuniformity debonding occurs at different applied stress levels at different locations.

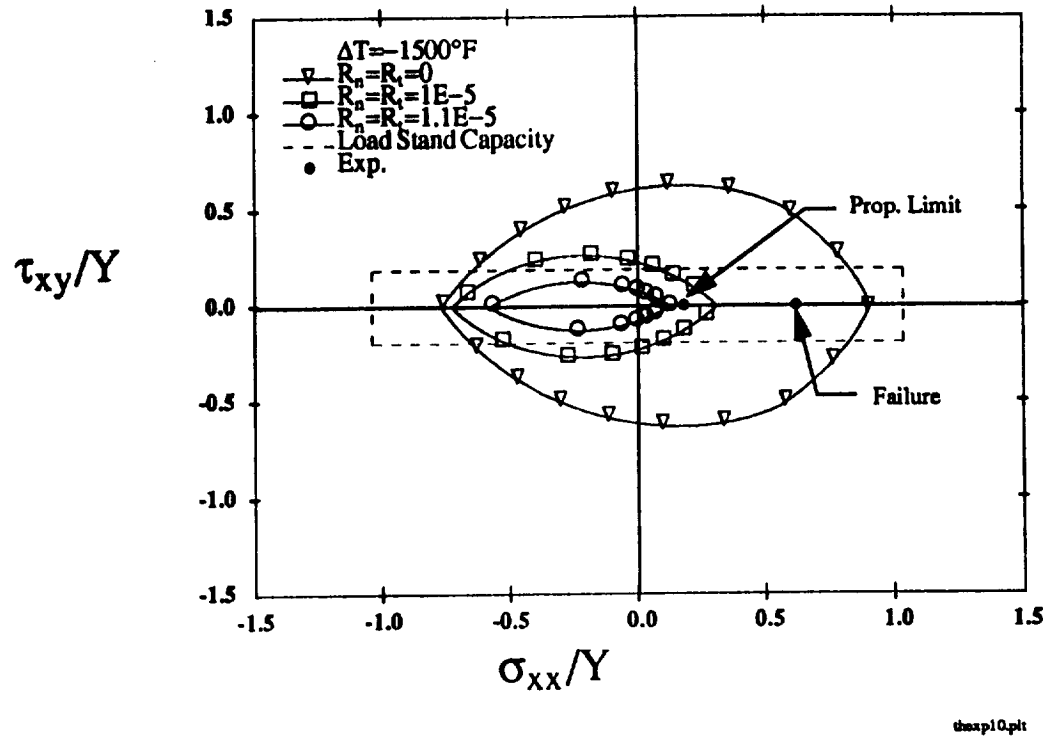

Figure 7.12: $[\pm 45]_s$ SiC/Ti Predicted Initial Yield Surfaces

This is evident from the observed continuous stiffness degradation, in contrast to the sudden degradation observed for Type II loading on a $[0_4]$ tube, as well as from the gradual increase in acoustic activity.

Predicted initial yield surfaces in the axial-shear stress space are plotted in Fig. 7.12. As for the $[0_4]$ predictions stresses are normalized with respect to the matrix yield stress in simple tension, Y=110 ksi. Thermal residual stresses associated with cooling the composite from the fabrication temperature are included. Different normal and tangential bonding parameters were considered to illustrate the effects of imperfect bonding. Figure 7.12 shows that as the interfacial bond is degraded the initial yield surface translates along the horizontal axis in addition to decreasing in size. The proportional limit and failure stress from Type I tests are also shown in the figure. The location of these points (well within the predicted yield surface for perfect bonding) indicates that interfacial damage

precedes and accelerates matrix yielding.

A comparison between the predicted and experimentally observed responses for a $[\pm 45]_s$ tube is shown in Fig 7.13. Residual stresses associated with fabrication cool-down are included and the interfacial properties were taken to be σ_0=15 ksi, α=2.0, $\delta_n=10\times10^{-6}$ in., $\delta_t=\delta_b=10\delta_n$, and μ=0. While both $[0_4]$ and $[\pm 45]_s$ tubes were fabricated from the same materials using the same process they exhibited different types of nonuniform response. The initial elastic properties were uniform for $[0_4]$ tubes but not for $[\pm 45]_s$ tubes. The individual interfaces in each type of tube are the same but are loaded differently. Because the interfacial properties used for a RVE must be representative of the statistical average rather than the properties of an individual interface the use of different properties for $[\pm 45]_s$ tubes is justified. Previously, for simplicity the characteristic length, δ, had been assumed to be the same in the normal and tangential directions. This is not necessarily the case and for $[\pm 45]_s$ laminates the characteristic length in tangential directions was taken to be an order of magnitude larger than in the normal direction.

The experimental data lies within the range predicted by DUCM for the perfect (PB) and no bond (NB) conditions. The stiffness was degraded with each load cycle and approached the NB prediction as the maximum applied stress level in each cycle increased, thus indicating that bonding between the fiber and matrix was initially present. At the higher applied stress levels creep response was observed experimentally, as indicated by the data points that lie on a horizontal line and are spaced closer and closer together for increasing axial strain in Fig. 7.13a. For clarity the unloading response is not shown for the loading cycles when large creep strains were measured. The stiffness degradation and nonlinear response is of primary importance in Fig. 7.13a. The predicted response (DUCM, DB) somewhat resembles the experimental data but agreement could

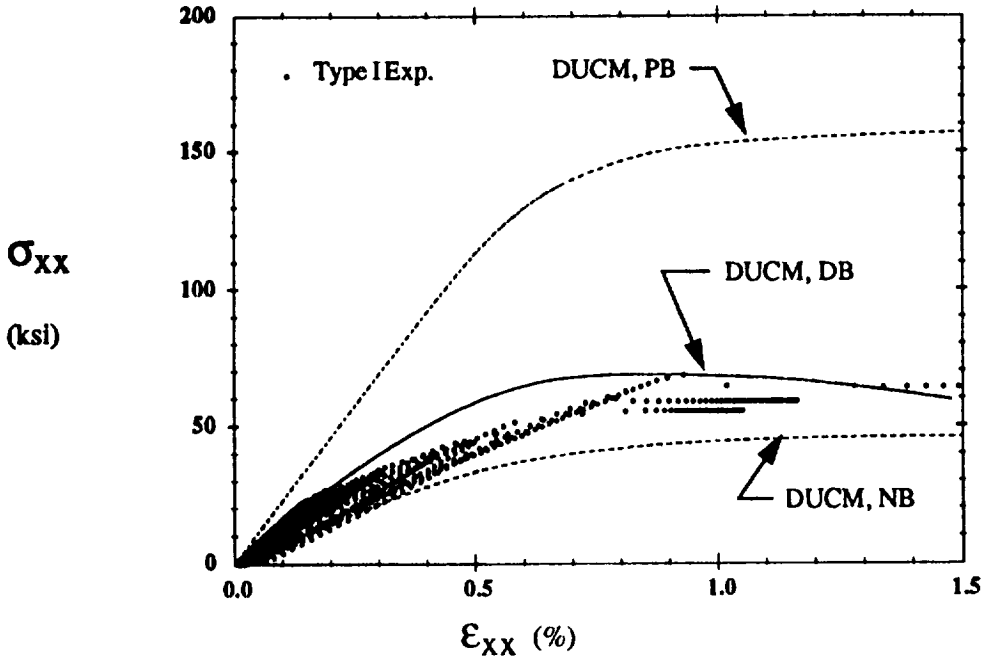

(a)Axial Response

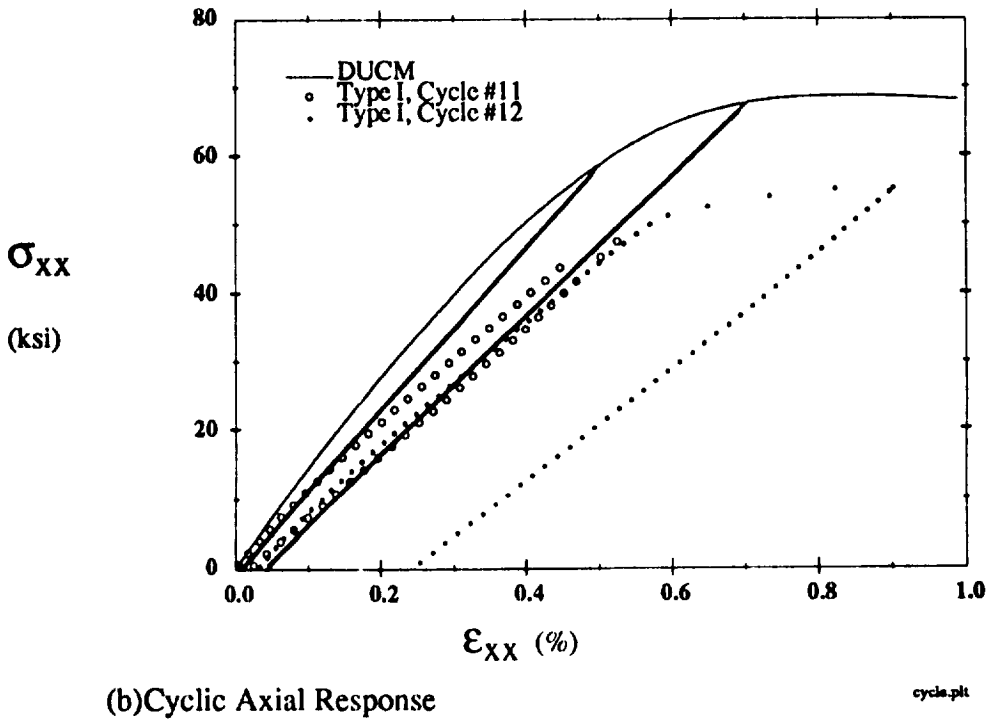

(b)Cyclic Axial Response

Figure 7.13: $[\pm 45]_s$ SiC/Ti Type I Loading Comparison

be better. Initially the predicted response was slightly more compliant than the experimental response. However, the nonlinear response observed experimentally was more abrupt than DUCM predicted. Although not evident from the figure the model predicted local plastic strains to occur in conjunction with nonlinear strains associated with debonding. This will be discussed in more detail in the subsequent section.

The predicted cyclic axial response is compared with two Type I loading cycles of experimental data in Fig. 7.13b. Accumulated axial strains associated with shear coupling and creep have not been included in the experimental data so that only cyclic axial loading is compared in the figure. DUCM predicts a continuously degraded axial stiffness as well as permanent axial strains. The experimental initial axial stiffness was less than that predicted by DUCM due to debonding that occurred in previous loading cycles. Experimentally, more permanent strain was present after each cycle than was predicted, however, the maximum axial strain in each cycle was not the same for theory and experiment.

Transverse strain-axial strain response is plotted in Fig. 7.14. The transverse strain-axial strain response lies within the predicted range for perfect bond (DUCM, PB) and no bond (DUCM, NB) except when large creep strains have been accumulated. The experimental data lies closer to the perfect bond prediction than to the debonding interface prediction (DUCM, DB) suggesting that Poisson's ratio (defined by the slope of the transverse strain-axial strain response) is not as sensitive to interfacial debonding as the model predicts.

7.2.3 Type IA Loading

Type IA experiments were conducted to determine how much of the permanent

strain accumulated during Type I tests was time-dependent and how much was time-independent. Figure 6.35 summarizes the results quite well. At low applied stress levels (below 42 ksi) the strain accumulation is due primarily to time independent coupling between shear and axial strains. But at higher applied stress levels (above 42 ksi) the strain accumulation is due primarily to creep. Creep strains increase dramatically at very high applied stress levels. Clearly, room temperature creep is a significant design consideration.

Short term creep tests conducted on bulk Ti-15-3 at room temperature indicated that creep behavior does not begin until the yield point has been reached (Fig. 6.45). Since the theoretical model uses a unified viscoplastic theory to describe the material behavior of the constituents it is possible to predict the creep response. The predicted creep response of as-fabricated Ti-15-3 is shown in Fig. 7.15b for applied stresses of 100, 110, 120 and 130 ksi. The yield point of as-fabricated Ti-15-3 is 110 ksi (Fig. 7.15a). No creep is predicted for the applied stress of 100 ksi, but creep response is observed for the other

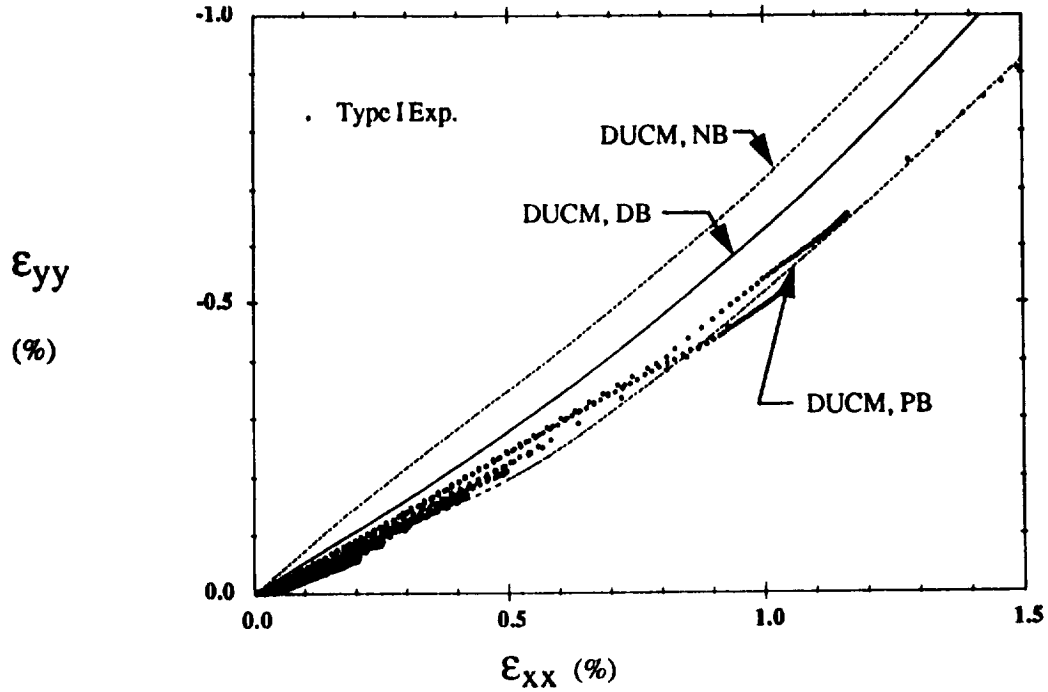

Figure 7.14 $[\pm 45]_s$ SiC/Ti Transverse Strain-Axial Strain Comparison

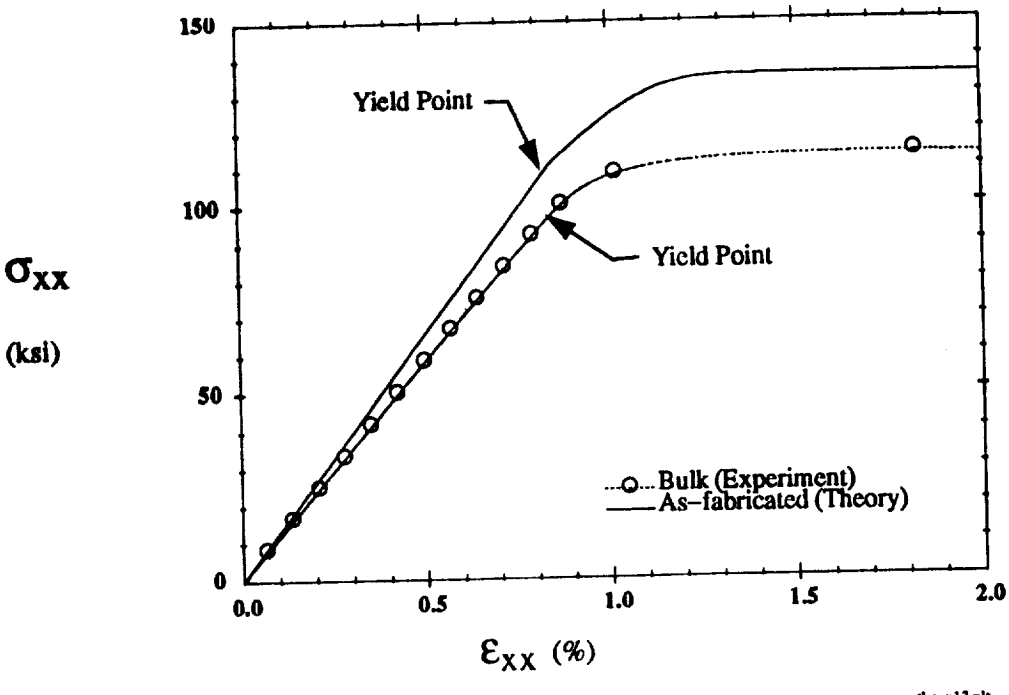

(a) Tensile Response

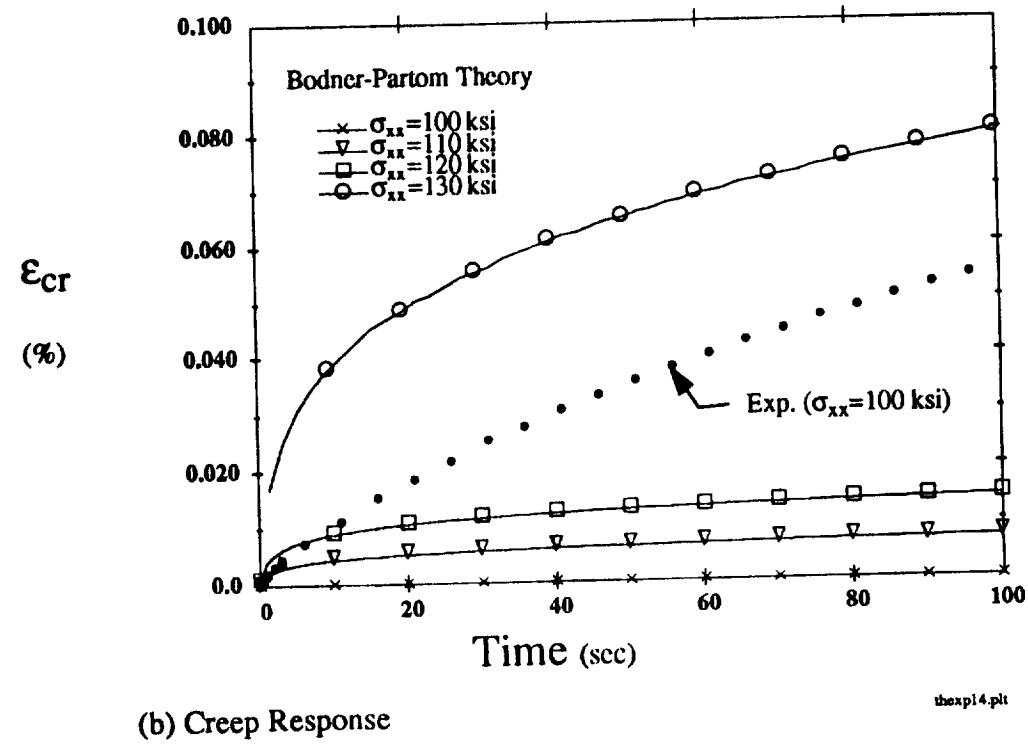

(b) Creep Response

Figure 7.15: Ti-15-3 Theory-Experiment Comparison

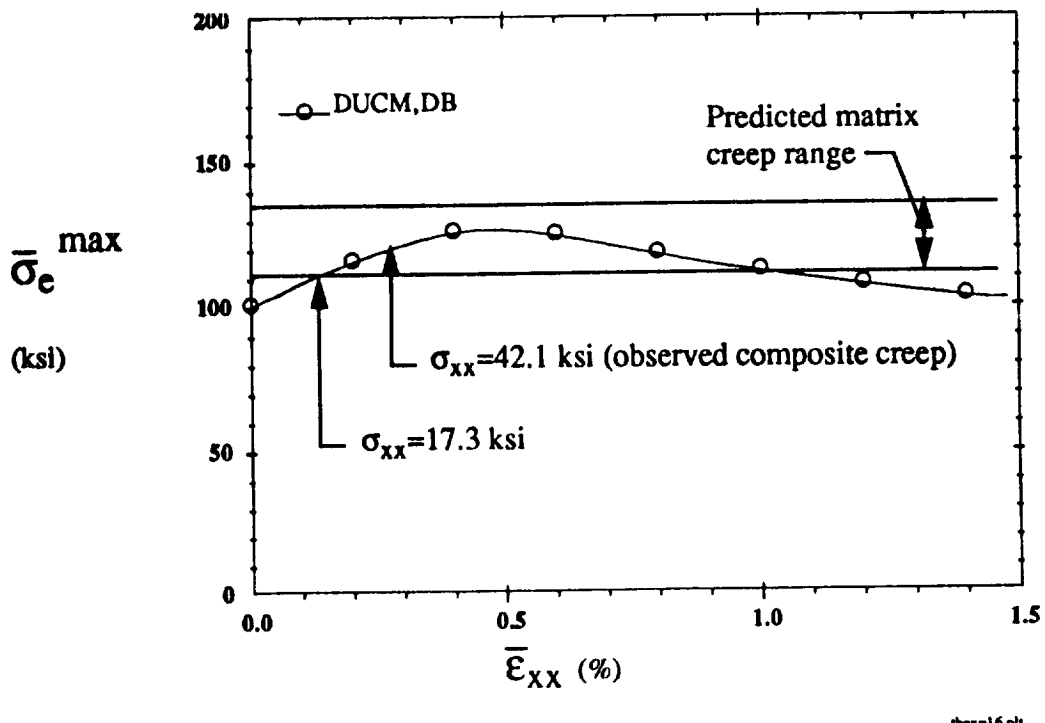

Figure 7.16: SiC/Ti Matrix Maximum Effective Stress

three higher applied stress levels. These predictions are consistent with the experimentally obtained creep response of bulk Ti-15-3 in that creep does not occur until after the yield stress has been surpassed.

In principle DUCM is therefore capable of predicting creep response in laminated MMC. However, the current laminate analysis program can only apply thermal and strain loadings to a laminate. In order to be able to predict creep response it is necessary to apply stress loadings. This is not possible at the present time but should be considered in future work. In light of the observation that creep response is initiated once the yield point has been reached it is instructive to consider the maximum effective stress in the matrix. Creep in the matrix is expected to occur once the maximum effective stress in the matrix exceeds 110 ksi. The maximum effective stress in the matrix is plotted against the applied axial strain in Fig. 7.16 for a $[\pm 45]_s$ laminate with a debonding interface. As before, residual stresses due to an effective cool-down of 1500°F were considered. These residual stresses

cause the maximum effective stress in the matrix to be approximately 100 ksi initially. The interface properties used were the same as discussed for Type I loading: σ_o=15 ksi, α=2, δ_n=10×10^{-6} in., δ_t=δ_b=10δ_n, and μ=0. Effective stress (eqn. (7.1)) is calculated for each matrix element in the finite element mesh (Fig. 3.1). The effective stress in one element reaches 110 ksi at a composite stress of 17.3 ksi. The first significant creep was observed experimentally for an applied stress of 42 ksi which corresponds with a maximum effective stress of 123 ksi. This demonstrates consistency between DUCM and the experimental data because the initiation of measurable composite creep is expected to be caused by high effective stress in a somewhat larger portion of the matrix than just one finite element.

7.2.4 Type II Loading

Type II loading was limited by the capacity of the load stand as shown in Fig. 7.12. The experimental response appeared to be linear elastic in each loading cycle but was degraded slightly with each cycle (Fig. 6.44). Figure 7.11 shows that torsion of a $[\pm 45]_s$ tube causes tensile transverse stresses, σ_{22}, in the third (and second) ply and compressive transverse stresses in the fourth (and first) ply. No shear stresses, τ_{12}, are present in any ply. Torsional loading is expected to have a fairly minimal effect on stiffness degradation because only two plies experience stresses, in this case tensile transverse stresses, that cause debonding. The shear stiffness of the tubes varied with location, thus results from two strain gages are compared with theoretical predictions. The shear response is plotted at two different scales in Fig. 7.17. The larger scale (Fig. 7.17a) shows the predicted shear response to be slightly nonlinear for high shear stresses. The smaller scale (Fig. 7.17b) provides a better view of the comparison between theory and experiment. Perfect bond and no bond predictions are shown to indicate extreme conditions. The residual stresses

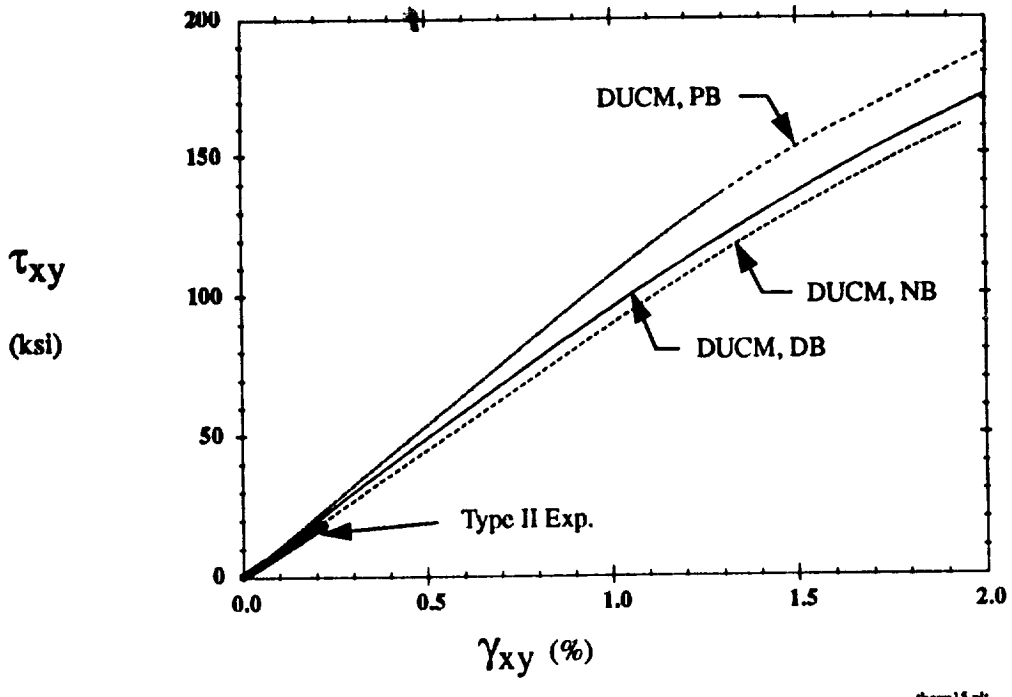

(a)Shear Response

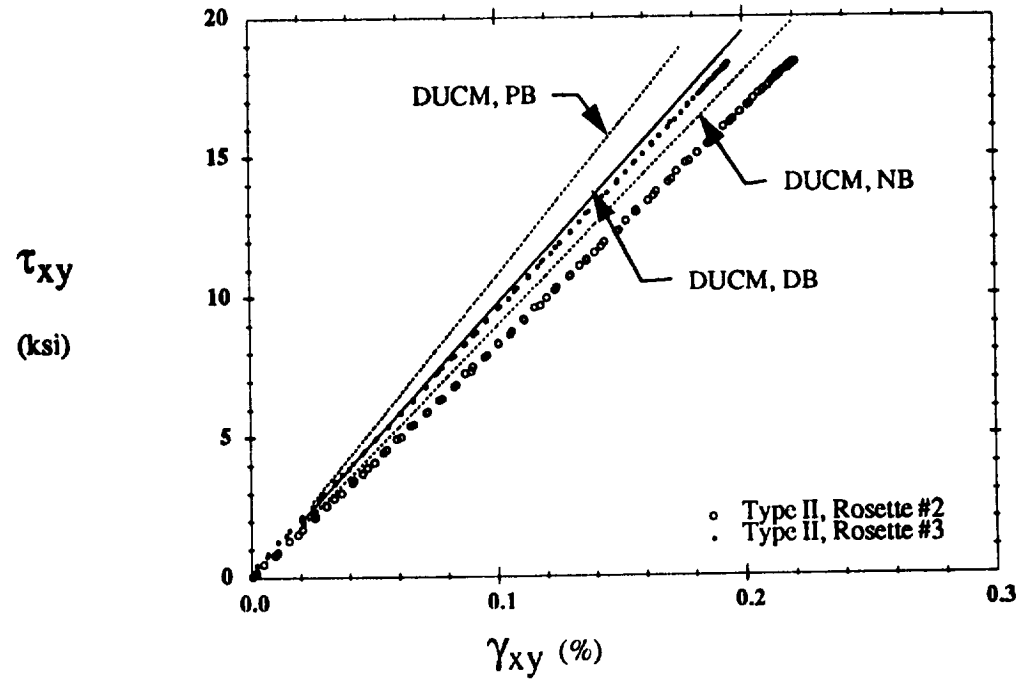

(b)Shear Response (Enlarged View)

Figure 7.17: $[\pm 45]_s$ SiC/Ti Type II Loading Comparison

and interface properties used for the debonding interface prediction are the same as used previously for $[\pm 45]_s$ tubes. The data from rosette #2 falls outside the predicted range, indicating that this strain gage could have been located where there were fewer than average fibers. To reiterate, both axial and shear stiffnesses measured at different points on the tube varied significantly due to material nonuniformity. The data from rosette #3 is in very good agreement with the debonding interface prediction (DUCM, DB).

7.3 Discussion

The elastic-viscoplastic model of Bodner and Partom (1987) and an extension of the interfacial debonding model of Tvergaard (1990) are incorporated in the current theoretical model (DUCM) to predict the inelastic response of metal matrix composites with debonding fiber/matrix interfaces. Results from DUCM have been compared with experimental results from a limited number of different types of multiaxial tests. DUCM was seen to predict the inelastic response of metal matrix composites with debonding fiber/matrix interfaces reasonably well.

The framework of the model is such that virtually any constitutive theory may be used. The viscoplastic theory of Bodner and Partom was chosen for this work because of its simplicity. Any viscoplastic theory could be used in its place. The debonding model of Tvergaard was chosen because it provided a rational approach to combined normal and tangential fiber/matrix debonding. For purely normal separation the interfacial constitutive relations resemble the dependence of interatomic forces on interatomic separation. However, there is no physical evidence that on an atomistic scale a fiber/matrix interface behaves as described by the model. Thus, the model is viewed as phenomenological in nature. Any such model that describes interfacial tractions in terms of interfacial displacements could be implemented using DUCM. This is one of the outstanding features

of the model. It can be used to study how well different interfacial constitutive models predict the local and overall stress and strain fields in composites with debonding interfaces.

The occurrence of nonuniform debonding in a composite dictates that a statistical average of the interfacial properties be used to describe an effective interface for a repeating unit cell analysis. Currently, the properties of such an effective interface must be treated as parameters and determined by curve fitting experimental data. The usefulness of a model that requires parameters to be determined from comparisons with precisely the response to be predicted is limited. Thus, unless composites can be manufactured such that debonding occurs in a uniform manner, it may be more useful to develop stochastic models that are better suited for nonuniform processes.

CHAPTER 8

CONCLUSIONS

A micromechanical model has been developed to predict the inelastic deformation of laminated metal matrix composites in the presence of interfacial debonding. The representative cell of the model was considered to be in a state of generalized plane strain, enabling a quasi two-dimensional analysis to be performed while retaining the capability to apply loads in all three coordinate directions. Residual stresses and matrix viscoplasticity were explicitly included in the model. Interfacial tractions were related to interfacial displacements by a function that increases to a maximum, decreases, then vanishes for monotonically increasing interfacial displacements. The model was compared with experimental data from multiaxial tests conducted on SiC/Ti tubular specimens.

Several technologically important conclusions can be reached based upon the results of the experimental program. Following are key conclusions presented in the order of their perceived importance.

[0] SiC/Ti lamina

- Fiber/matrix interfacial damage is nonuniform and a major factor in the transverse and shear responses.
- The axial shear response exhibits a sudden loss of stiffness.
- Axial shear loading results in brittle fiber/matrix debonding prior to initial yielding.
- Fiber/matrix debonding introduced during shear loading degrades the shear stiffness.

•Transverse tensile loading results in fiber/matrix interfacial debonding prior to initial yielding.

•Inelastic coupling between transverse and shear strains occurs for shear loading in the presence of constant transverse stress.

•The uniaxial tensile response is independent of the condition of the fiber/matrix interface.

$[\pm 45]_s$ SiC/Ti laminates

•Fiber/matrix interfacial damage is a major factor in the tensile response.

•Interfacial damage precedes and accelerates matrix yielding for tensile loading.

•The axial modulus exhibits a damage induced degradation of as much as 50% in cyclic tensile tests to sequentially higher stress levels.

•At room temperature longitudinal creep strains occur at applied stresses less than 50% of the stress level required to initiate creep response in bulk Ti-15-3.

•Inelastic coupling between axial and shear strains occurs for shear loading in the presence of constant axial stress.

•Imperfect bonding exists in the as-fabricated material as a result of thermal cool-down during processing.

General

•The aspect ratio in a rectangular repeating cell micromechanical model is insignificant for perfectly bonded composites but is a major factor in determining the effective response of imperfectly bonded composites.

•Titanium (Ti-15-3) exhibits creep behavior at room temperature.

•Acoustic emissions in SiC/Ti follow the Kaiser effect and provide a good qualitative indication of when damage is occurring.

•Current fabrication techniques for SiC/Ti tubes need to be improved to obtain a more uniform distribution of fibers throughout the tube.

•The molybdenum wire weave was observed in most fracture surfaces and reduces the composite strength.

REFERENCES

Aboudi, J., 1987a, "Closed form constitutive equations for metal matrix composites," *Int. J. Engng. Sci.*,Vol. 25, No. 9, pp. 1229-1240.

Aboudi, J., 1987b, "Constitutive relations for cracked metal matrix composites," *Mech. of Materials*, Vol. 6, pp. 303-315.

Aboudi, J., 1988, "Constitutive equations for elastoplastic composites with imperfect bonding," *Int. J. Plasticity*,Vol. 4, pp. 103-125.

Aboudi, J., 1989, "Micromechanical analysis of fibrous composites with coulomb frictional slippage between the phases," *Mech. of Materials*, Vol. 8, pp. 103-115.

Aboudi, J., 1991, *Mechanics of Composite Materials: A Unified Micromechanical Approach*, Elsevier, Amsterdam, The Netherlands.

Achenbach, J.D. and Zhu, H., 1990, "Effect of Interphases on Micro and Macromechanical Behavior of Hexagonal-Array Fiber Composites," *ASME Trans. J. Appl. Mech.*, Vol. 57, pp. 956-963.

Adams, D.F., 1974, "A Micromechanical Analysis of Crack Propogation in an Elastoplastic Composite Material," *Fibre Science and Technology*, Vol. 7, pp. 237-256.

Adams, D.F. and Crane, D.A., 1984, "Combined loading micromechanical analysis of a unidirectional composite," *Composites*, Vol. 15, No. 3, pp. 181-191.

Arnold, S.M., Robinson, D.N., and Bartolotta, P.A., 1992, "Unified Viscoplastic Behavior of Metal Matrix Composites," *NASA Technical Memorandum* 105819.

Bahei-El-Din, Y.A. and Dvorak, G.J., 1982, "Plasticity Analysis of Laminated Composite Plates," *ASME Trans. J. Appl. Mech.*, Vol. 49, pp. 740-746.

Becker, R.C., 1988, "Interface Constitutive Relations for use with the Finite Element Code ABAQUS," ALCOA Memorandum, unpublished.

Benveniste, Y., 1985, "The effective mechanical behavior of composite materials with imperfect contact between the constituents," *Mech. of Materials*, Vol. 4, pp. 197-208.

Benveniste, Y., 1987, "A new approach to the application of Mori-Tanaka's theory in composite materials," *Mech. of Materials*, Vol. 6, pp. 147-157.

Benveniste, Y., Dvorak, G.J., and Chen, T., 1989, "Stress fields in composites with coated inclusions," *Mech. of Materials*, Vol. 7, pp. 305-317.

Benveniste, Y., Dvorak, G.J., and Chen, T., 1991, "On effective properties of composites with coated cylindrically orthotropic fibers," *Mech. of Materials*, Vol. 12, pp. 289-297.

Bodner, S.R. and Partom, Y., 1975, "Constitutive Equations for Elastic-Viscoplastic Strain-Hardening Materials," *ASME Trans. J. Appl. Mech.*, Vol. 42, pp. 385-389.

Bodner, S.R., 1987, "Review of a Unified Elastic-Viscoplastic Theory," *Unified Constitutive Equations for Creep and Plasticity*, A.K. Miller, Ed., Elsevier, London, pp. 273-301.

Chen, T., Dvorak, G.J., and Benveniste, Y., 1990, "Stress fields in composites reinforced by coated cylindrically orthotropic fibers," *Mech. of Materials*, Vol. 9, pp. 17-32.

Christensen, R.M. and Lo, K.H., 1979, "Solutions for Effective Shear Properties in Three Phase Sphere and Cylinder Models," *J. Mech. Phys. Solids*, Vol. 27, pp. 315-330.

Derstine, M.S. and Pindera, M-J., 1989, "Nonlinear response of composite tubes under combined thermomechanical loading," *Composites and Other New Materials for PVP: Design and Analysis Considerations*, ASME PVP-Vol. 174, D. Hui, T.J. Kozik, G.E.O. Widera, and M. Shiratori, Eds., ASME, New York, pp. 19-28.

Dvorak, G.J., 1991, "Plasticity Theories for Fibrous Composite Materials," *Metal Matrix Composites: Mechanisms and Properties*, R.K. Everett and R.J. Arsenault, Eds., Academic Press, Boston, pp. 1-77.

Dvorak, G.J. and Bahei-El-Din, Y.A., 1982, "Plasticity Analysis of Fibrous Composites," *ASME Trans. J. Appl. Mech.*, Vol. 49, pp. 327-335.

Dvorak, G.J. and Teply, J.L., 1985, "Periodic Hexagonal Array Models for Plasticity Analysis of Composite Materials," *Plasticity Today: Modelling, Methods and Applications, W. Olszak Memorial Volume*, A. Sawczuck, and V. Bianchi, Eds., Elsevier, London, pp 623-642.

Dvorak, G.J., Bahei-El-Din, Y.A., Macheret, Y., and Liu, C.H., 1988, "An experimental study of elastic-plastic behavior of a fibrous boron-aluminum composite," *J. Mech. Phys. Solids*, Vol. 36, No. 6, pp. 655-687.

Dvorak, G.J., Bahei-El-Din, Y.A., Shah, R.S., and Nigam, H., 1990, "Experiments and Modeling in Plasticity of Fibrous Composites," *Inelastic Deformation of Composite Materials*, G.J. Dvorak, Ed., Springer-Verlag, New York, pp. 283-306.

Eggleston, M.R. and Krempl, E., 1992, "Modeling the transverse creep of titanium-based metal matrix composites," *Damage Mechanics in Composites*, D.H. Allen and D.M. Lagoudas, Eds., ASME-AMD-Vol. 150, pp. 313-326.

Freed, A.D. and Walker, K.P., 1991, "A viscoplastic theory with thermodynamic considerations," *Acta Mechanica*, Vol. 90, pp. 155-174.

Freed, A.D., Walker, K.P., and Verrilli, M.J., 1993, "Extending creep to viscoplasticity," submitted to the *ASME Journal of Pressure Vessel Technology*.

Hashin, Z., 1972, "Theory of Fiber-Reinforced Materials," Final Report, Contract NAS1-8818, Nov. 1970, NASA CR 1974.

Hashin, Z., 1990, "Thermoelastic properties of fiber composites with imperfect interface," *Mech. of Materials*, Vol. 8, pp. 333-348.

Hashin, Z. and Rosen, B.W., 1964, "The Elastic Moduli of Fiber-Reinforced Materials," *ASME Trans. J. Appl. Mech.*, Vol. 31, pp. 223-232.

Herakovich, C.T. and Hidde, J.S., 1992, "Response of metal matrix composites with imperfect bonding," *Ultramicroscopy*, Vol. 40, pp. 215-228.

Hibbitt, Karlsson, and Sorensen, Inc., 1989, ABAQUS Ver. 4-8 Users Manual.

Hidde, J.S., Beuth, J.L., and Herakovich, C.T., 1988, "MATPAC v2.0, A PC-based Software Package for Materials Testing," Virginia Tech/University of Virginia unpublished report.

Hidde, J.S. and Herakovich, C.T., 1992, "Inelastic Response of Hybrid Composite Laminates," *J. Composite Materials*, Vol. 26, pp. 2-19.

Highsmith, A.L., Shin, D., and Naik, R.A., 1990, "Local Stresses in Metal Matrix Composites Subjected to Thermal and Mechanical Loading," *Thermal and Mechanical Behavior of Metal Matrix and Ceramic Matrix Composites, ASTM STP 1080*, J.M. Kennedy, H.H. Moeller, and W.S. Johnson, Eds., American Society for Testing and Materials, Philadelphia, pp. 3-19.

Johnson, W.S., Lubowinski, S.J., and Highsmith, A.L., 1990, "Mechanical Characterization of Unnotched SCS_6/Ti-15-3 Metal Matrix Composites at Room Temperature," *Thermal and Mechanical Behavior of Metal Matrix and Ceramic Matrix Composites, ASTM STP 1080*, J.M. Kennedy, H.H. Moeller, and W.S. Johnson, Eds., American Society for Testing and Materials, Philadelphia, pp. 193-218.

Jones, R.M., 1975, *Mechanics of Composite Materials*, McGraw-Hill, New York.

Jones, J.P. and Whittier, J.S., 1967, "Waves at a Flexibly Bonded Interface," *ASME Trans. J. Appl. Mech.*, Vol. 34, pp. 905-909.

Kaiser, J., 1950, "Untersuchungen uber das Auftreten Gerauschen Biem Zugversuch," PhD thesis, Technisch Hochschule, Munich.

Lekhnitskii, S.G., 1981, *Theory of Elasticity of an Anisotropic Body*, Mir Publishers, Moscow, (translated from the revised 1977 Russian edition).

Lerch, B.A., 1993, private communication.

Lerch, B.A., Hull, R., and Leonhardt, T.A., 1990, "Microstructure of a SiC/Ti-15-3 composite," *Composites*, Vol. 21, No. 3, pp. 216-224.

Lerch, B.A. and Saltsman, J.F., 1991, "Tensile Deformation Damage in SiC Reinforced Ti-15V-3Cr-3Al-3Sn," *NASA Technical Memorandum 103620.*

MacKay, R.A., 1990, "Effect of fiber spacing on interfacial damage in a metal matrix composite," *Scripta Metallugica et Materialia*, Vol. 24, pp. 167-172.

Majors, P.S. and Krempl, E., 1991, "A Recovery of State Formulation for the Viscoplasticity Theory Based on Overstress," *High Temperature Constitutive Modeling - Theory and Application*, MD-Vol. 26/AMD-Vol. 121, The American Society of Mechanical Engineers, New York, pp. 235-250.

Majumdar, B.S. and Newaz, G.M., 1991, "Inelastic deformation of metal matrix composites," NASA Conference Publication 10082, HITEMP Review.

Majumdar, B.S. and Newaz, G.M., 1992a, "Inelastic Deformation of Metal Matrix Composites: Part I--Plasticity and Damage Mechanisms," NASA Contractor Report 189095.

Majumdar, B.S. and Newaz, G.M., 1992b, "Inelastic Deformation of Metal Matrix Composites: Plasticity and Damage Mechanisms--Part II," NASA Contractor Report 189096.

Majumdar, B.S., Newaz, G.M., and Brust, F.W., 1992, "Constitutive behavior of metal matrix composites," *Constitutive behavior of high-temperature composites*, B.S. Majumdar, G.M. Newaz, and S. Mall, Eds., ASME-MD-Vol. 40, pp. 77-90.

McGee, J.D. and Herakovich, C.T., 1992, "Micromechanics of Fiber/Matrix Debonding," University of Virginia Report AM-92-01.

Mori, T. and Tanaka, K., 1973, "Average stress in matrix and average elastic energy of materials with misfitting inclusions," *Acta Metal.*, Vol. 21, pp. 571-574.

Needleman, A., 1987a, "A Continuum Model for Void Nucleation by Inclusion Debonding," *ASME Trans. J. Appl. Mech.*, Vol. 54, pp. 525-531.

Needleman, A., 1987b, "Void nucleation at fiber ends in Al-SiC composites," *Scripta Metallurgical*, Vol. 21, pp. 705-710.

Needleman, A., 1990a, "An analysis of decohesion along an imperfect interface," *Int. J. Fracture*, Vol. 42, pp. 21-40.

Needleman, A., 1990b, "An analysis of tensile decohesion along an interface," *J. Mech. Phys. Solids*, Vol. 38, No. 3, pp. 289-324.

Needleman, A., 1992, "Micromechanical modelling of interfacial decohesion," *Ultramicroscopy*, Vol. 40, pp. 203-214.

Nimmer, R.P., 1990, "Fiber-Matrix Interface Effects in the Presence of Thermally Induced

Residual Stresses," *J. Comp. Tech. Res.*, Vol. 12, No. 2, pp. 65-75.

Nimmer, R.P., Bankert, R.J., Russel, E.S., Smith, G.A., and Wright, P.K., 1991, "Micromechanical Modeling of Fiber/Matrix Interface Effects in Transversely Loaded SiC/Ti-6-4 Metal Matrix Composites," *J. Comp. Tech. Res.*, Vol. 13, No. 1, pp. 3-13.

Nutt, S.R. and Wawner, F.E., 1985, "Silicon Carbide Filaments: Microstructure," *J. Mater. Sci.*, Vol. 20, No. 6, pp 1953-1960.

Pindera, M-J. and Aboudi, J., 1988, "Micromechanical analysis of yielding of metal matrix composites," *Int. J. Plasticity*, Vol. 4, pp. 195-214.

Renieri, G.D. and Herakovich, C.T., 1976, "Nonlinear Analysis of Laminated Fibrous Composites," Virginia Polytechnic Institute and State University Report VPI-E-76-10.

Rose, J.H., Ferrante, J., and Smith, J.R., 1981, "Universal binding energy curves for metals and bimetallic interfaces," *Phys. Rev. Lett.*, Vol. 47, pp. 675-678.

Rose, J.H., Smith, J.R., and Ferrante, J., 1983, "Universal features of bonding in metals," *Phys. Rev.*, B28, pp. 1835-1845.

Smelser, R.E. and Becker, R., 1989, "ABAQUS User Subroutines for Material Modeling," *ABAQUS User's Conference Proceedings*, Stressa, Italy, Hibbitt, Karlsson, and Sorensen, Inc., May 24-26, pp. 207-226.

Teng, H., 1992, "On stiffness reduction of a fiber-reinforced composite containing interfacial cracks under longitudinal shear," *Mech. of Mechanics*, Vol. 13, pp. 175-183.

Teply, J.L., 1984, "Periodic hexagonal array models for plasticity analysis of composite materials," PhD Dissertation, The University of Utah.

Teply, J.L. and Dvorak, G.J., 1988, "Bounds on overall instantaneous properties of elastic-plastic composites," *J. Mech. Phys. Solids*, Vol. 36, pp. 29-58.

Tvergaard, V., 1990, "Effect of Fibre Debonding in a Whisker-reinforced Metal," *Mat. Sci. Eng.*, Vol. A125, pp. 203-213.

Tvergaard, V., 1991, "Micromechanical Modelling of Fibre Debonding in a Metal Reinforced by Short Fibres," *Inelastic Deformation of Composite Materials*, (G. J. Dvorak, Ed.), Springer-Verlag, New York, pp. 98-111.

Tvergaard, V., 1993, "Model studies of fibre breakage and debonding in a metal reinforced by short fibres," *J. Mech. Phys. Solids*, Vol. 41, No. 8, pp. 1309-1326.

Wisnom, M.R., 1990, "Factors Affecting the Transverse Tensile Strength of Unidirectional Continuous Silicon Carbide Fibre Reinforced 6061 Aluminum," *J. Composite Materials*, Vol. 24, pp. 707-726.

Zhu, H. and Achenbach, J.D., 1991, "Radial matrix cracking and interphase failure in transversely loaded fiber composites," *Mech. of Materials*, Vol. 11, pp. 347-356.

APPENDIX A

SOLID ELEMENTS

In the present analysis the effective response of the representative volume element (RVE) is found by averaging the stress and strain fields. This process is simplified by the use of constant strain elements. Thus, a linear displacement field is employed for each element.

$$u(x, y, z) = u_i + C_1 y + C_2 z \tag{A.1}$$

$$v(x, y, z) = v_i + C_3 y + C_4 z \tag{A.2}$$

$$w(x, y, z) = w_i + C_5 y + C_6 z \tag{A.3}$$

Here (u_i, v_i, w_i) represents the displacement of node i and C_1 through C_6 are unknown constants to be determined. Figure A.1 shows the geometry of an element. The formulation of the generalized plane strain finite elements proceeds as follows. The four nodes are designated i, j, k, and l, where node l is common to all elements in the mesh. By

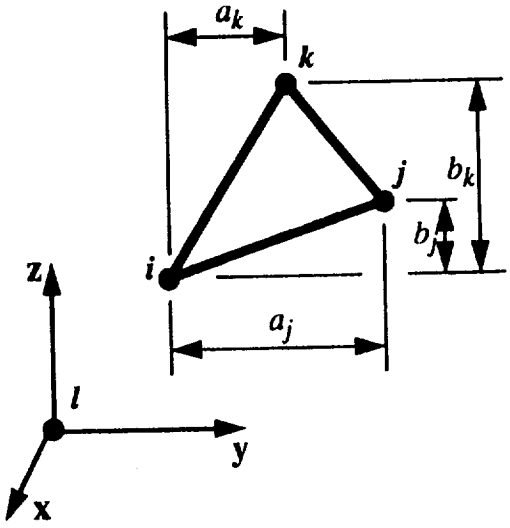

Figure A.1: Solid Element Geometry

writing eqns. (A.1-A.3) at nodes j and k the constants C_1 through C_6 can be expressed in terms of nodal displacements and element dimensions a_i, a_j, a_k, b_i, b_j, and b_k (Fig. A.1) as

$$C_1 = [(b_j - b_k)u_i + b_k u_j - b_j u_k]/\Delta \tag{A.4}$$

$$C_2 = [-(a_j - a_k)u_i - a_k u_j + a_j u_k]/\Delta \tag{A.5}$$

$$C_3 = [(b_j - b_k)v_i + b_k v_j - b_j v_k]/\Delta \tag{A.6}$$

$$C_4 = [(a_k - a_j)v_i - a_k v_j + a_j v_k]/\Delta \tag{A.7}$$

$$C_5 = [(b_j - b_k)w_i + b_k w_j - b_j w_k]/\Delta \tag{A.8}$$

$$C_6 = [(a_k - a_j)w_i - a_k w_j + a_j w_k]/\Delta \tag{A.9}$$

where $\Delta = a_j b_k - a_k b_j$ is twice the area of the element.

The infinitesimal strains are defined by $\{\varepsilon\} = [D]\{u\}$, or

$$\begin{bmatrix} \varepsilon_{xx} \\ \varepsilon_{yy} \\ \varepsilon_{zz} \\ \gamma_{yz} \\ \gamma_{xz} \\ \gamma_{xy} \end{bmatrix} = \begin{bmatrix} \partial/\partial x & 0 & 0 \\ 0 & \partial/\partial y & 0 \\ 0 & 0 & \partial/\partial z \\ 0 & \partial/\partial z & \partial/\partial y \\ \partial/\partial z & 0 & \partial/\partial x \\ \partial/\partial y & \partial/\partial x & 0 \end{bmatrix} \begin{bmatrix} u \\ v \\ w \end{bmatrix} = \begin{bmatrix} 0 \\ C_3 \\ C_6 \\ C_4 + C_5 \\ C_2 \\ C_1 \end{bmatrix} \tag{A.10}$$

For generalized plane strain, set $\varepsilon_x = u_l/(1.0\ \mathrm{L})$, where L is the curent length units, to ensure a constant strain in the x-direction. This, and substituting eqns. (A.4-A.9) into eqn. (A.10) yields

$$\begin{bmatrix} \varepsilon_{xx} \\ \varepsilon_{yy} \\ \varepsilon_{zz} \\ \gamma_{yz} \\ \gamma_{xz} \\ \gamma_{xy} \end{bmatrix} = \frac{1}{\Delta} \begin{bmatrix} 0 & 0 & 0 & 0 & 0 & 0 & 0 & 0 & 0 & \Delta \\ 0 & b_j - b_k & 0 & 0 & b_k & 0 & 0 & -b_j & 0 & 0 \\ 0 & 0 & a_k - a_j & 0 & 0 & -a_k & 0 & 0 & a_j & 0 \\ 0 & a_k - a_j & b_j - b_k & 0 & -a_k & b_k & 0 & a_j & -b_j & 0 \\ -(a_j - a_k) & 0 & 0 & -a_k & 0 & 0 & a_j & 0 & 0 & 0 \\ b_j - b_k & 0 & 0 & b_k & 0 & 0 & -b_j & 0 & 0 & 0 \end{bmatrix} \begin{bmatrix} u_i \\ v_i \\ w_i \\ u_j \\ v_j \\ w_j \\ u_k \\ v_k \\ w_k \\ u_l \end{bmatrix} \tag{A.11}$$

or $\{\varepsilon\} = [B]\{q\}$, where [B] is the strain-nodal displacement relationship defined by the matrix on the right hand side of eqn. (A.11) and $\{q\}$ contains the nodal displacements.

Hooke's law may be written

$$\{\sigma\} = [C]\left(\{\varepsilon\} - \{\varepsilon^T\} - \{\varepsilon^{PL}\}\right) \tag{A.12}$$

where $\{\varepsilon\}$ is the total strain, $\{\varepsilon^T\}$ is the free thermal strain, and $\{\varepsilon^{PL}\}$ is the plastic strain. For isotropic materials the stiffness tensor $[C]$ is

$$[C] = \begin{bmatrix} \frac{(1-\nu^2)E}{\Sigma} & \frac{(\nu+\nu^2)E}{\Sigma} & \frac{(\nu+\nu^2)E}{\Sigma} & 0 & 0 & 0 \\ & \frac{(1-\nu^2)E}{\Sigma} & \frac{(\nu+\nu^2)E}{\Sigma} & 0 & 0 & 0 \\ & & \frac{(1-\nu^2)E}{\Sigma} & 0 & 0 & 0 \\ & & & \frac{E}{2(1+\nu)} & 0 & 0 \\ & & & & \frac{E}{2(1+\nu)} & 0 \\ \text{sym} & & & & & \frac{E}{2(1+\nu)} \end{bmatrix} \tag{A.13}$$

where E is Young's modulus, ν is Poisson's ratio, and $\Sigma = 1 - 3\nu + 2\nu^2$.

The strain energy, U, of an element is

$$U = \frac{1}{2}\int_V \{\varepsilon\}^T \{\sigma\}\, dV \tag{A.14}$$

Rewriting eqn (A.14) in terms of the nodal displacements and applying the principle of virtual work in the usual fashion leads to

$$[K]\,\{q\} = \{F\} + \{F^T\} + \{F^{PL}\} \tag{A.15}$$

where

$$\begin{aligned}
[K] &= \int_V [B]^T [C]\, [B]\, dV && \text{is the element stiffness matrix} \\
\{F^T\} &= \int_V [B]^T [C]\, \{\varepsilon^T\}\, dV && \text{is the thermal force vector} \\
\{F^{PL}\} &= \int_V [B]^T [C]\, \{\varepsilon^{PL}\}\, dV && \text{is the plastic force vector}
\end{aligned} \tag{A.16}$$

and {F} is the applied mechanical force vector. The thermal strains are determined from $\{\varepsilon^T\} = \{\alpha\}\Delta T$, where $\{\alpha\}$ contains the coefficients of thermal expansion and ΔT is a uniform temperature change. The plastic strains are found by the Bodner-Partom model.

APPENDIX B

INTERFACE ELEMENTS

Interface finite elements are derived in the following manner (Becker, 1988 and Smelser and Becker, 1989). The current nodal coordinates are first determined

$$\left.\begin{aligned} x_i &= x'_i + u_i \\ y_i &= y'_i + v_i \\ z_i &= z'_i + w_i \end{aligned}\right\} \qquad i = m, n, p, q \tag{B.1}$$

where the primed coordinates refer to the original coordinate locations; u_i, v_i, and w_i (i = m, n, p, q) are nodal displacements, and m, n, p, and q are the node numbers as shown in Fig. B.1. In the figure α, β represent the element end points and A, B represent integration points. Interfacial tractions for the current load increment are determined by the increments of interfacial displacement discontinuities, which will subsequently be referred to as displacements, in the n, t, b coordinate system.

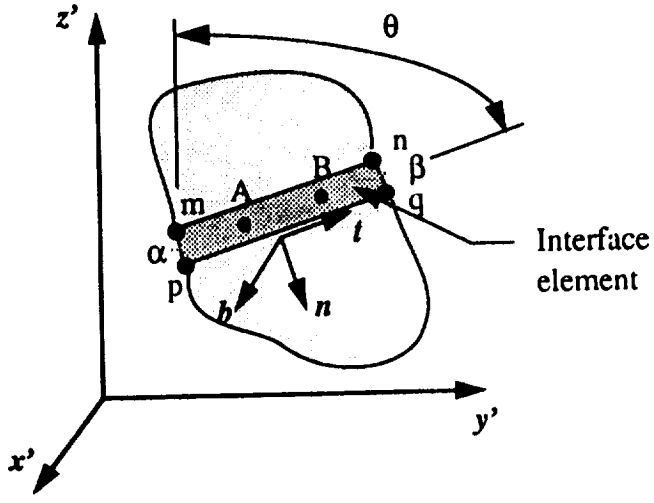

Figure B.1: Interface Element Geometry

$$
\begin{aligned}
u_n^{\alpha} &= (x_m - x_p)\, s - (y_m - y_p)\, c \\
u_n^{\beta} &= (x_n - x_q)\, s - (y_n - y_q)\, c \\
u_t^{\alpha} &= (x_m - x_p)\, c + (y_m - y_p)\, s \\
u_t^{\beta} &= (x_n - x_q)\, c + (y_n - y_q)\, s \\
u_b^{\alpha} &= z_m - z_p \\
u_b^{\beta} &= z_n - z_q
\end{aligned}
\tag{B.2}
$$

Here $c = \cos\theta$ and $s = \sin\theta$ and α, β superscripts designate the end points of the element. Displacements are determined at the integration points A, B

$$
\begin{aligned}
u_i^A &= \xi u_i^{\alpha} + \eta u_i^{\beta} \\
u_i^B &= \eta u_i^{\alpha} + \xi u_i^{\beta}
\end{aligned}
\qquad i = n, t, b \tag{B.3}
$$

where

$$\xi = \frac{1}{2}(1 + 1/\sqrt{3}) \tag{B.4}$$

$$\eta = \frac{1}{2}(1 - 1/\sqrt{3}) \tag{B.5}$$

The tractions obtained in eqns. (2.20-2.25) are differentiated with respect to displacements. For monotonic loading prior to bond failure, $\lambda = \lambda_{max} < 1$,

$$
\frac{dT_n}{du_n} = \begin{cases} 10^6 \dfrac{1}{\delta_n} & \text{for } u_n \le 0 \\ \dfrac{dF}{d\lambda}\dfrac{d\lambda}{du_n}\dfrac{u_n}{\delta_n} + F\dfrac{1}{\delta_n} & \text{for } u_n > 0 \end{cases} \tag{B.6}
$$

$$
\frac{dT_n}{du_t} = \begin{cases} 0 & \text{for } u_n \le 0 \\ \dfrac{dF}{d\lambda}\dfrac{d\lambda}{du_t}\dfrac{u_n}{\delta_n} & \text{for } u_n > 0 \end{cases} \tag{B.7}
$$

$$\frac{dT_n}{du_b} = \begin{cases} 0 & \text{for } u_n \le 0 \\ \dfrac{dF}{d\lambda}\dfrac{d\lambda}{du_b}\dfrac{u_n}{\delta_n} & \text{for } u_n > 0 \end{cases} \tag{B.8}$$

$$\frac{dT_t}{du_n} = \alpha\frac{dF}{d\lambda}\frac{d\lambda}{du_n}\frac{u_t}{\delta_t} \tag{B.9}$$

$$\frac{dT_t}{du_t} = \alpha\frac{dF}{d\lambda}\frac{d\lambda}{du_t}\frac{u_t}{\delta_t} + \alpha F\frac{1}{\delta_t} \tag{B.10}$$

$$\frac{dT_t}{du_b} = \alpha\frac{dF}{d\lambda}\frac{d\lambda}{du_b}\frac{u_t}{\delta_t} \tag{B.11}$$

$$\frac{dT_b}{du_n} = \alpha\frac{dF}{d\lambda}\frac{d\lambda}{du_n}\frac{u_b}{\delta_b} \tag{B.12}$$

$$\frac{dT_b}{du_t} = \alpha\frac{dF}{d\lambda}\frac{d\lambda}{du_t}\frac{u_b}{\delta_b} \tag{B.13}$$

$$\frac{dT_b}{du_b} = \alpha\frac{dF}{d\lambda}\frac{d\lambda}{du_b}\frac{u_b}{\delta_b} + \alpha F\frac{1}{\delta_b} \tag{B.14}$$

where

$$\frac{d\lambda}{du_n} = \frac{1}{\lambda\delta_n}\frac{u_n}{\delta_n} \tag{B.15}$$

$$\frac{d\lambda}{du_t} = \frac{1}{\lambda\delta_t}\frac{u_t}{\delta_t} \tag{B.16}$$

$$\frac{d\lambda}{du_b} = \frac{1}{\lambda\delta_b}\frac{u_b}{\delta_b} \tag{B.17}$$

$$\frac{dF}{d\lambda} = \frac{27}{4}\sigma_o(\lambda - 1)\,(2) \tag{B.18}$$

For unloading and reloading below the previous maximum load

$$\frac{dT_n}{du_n} = \begin{cases} 10^6\dfrac{1}{\delta_n} & u_n \le 0 \\ F\dfrac{1}{\delta_n} & u_n > 0 \end{cases} \tag{B.19}$$

$$\frac{dT_t}{du_t} = \alpha F\frac{1}{\delta_t} \tag{B.20}$$

$$\frac{dT_b}{du_b} = \alpha F\frac{1}{\delta_b} \tag{B.21}$$

$$\frac{dT_n}{du_t} = \frac{dT_n}{du_b} = \frac{dT_t}{du_n} = \frac{dT_t}{du_b} = \frac{dT_b}{du_n} = \frac{dT_b}{du_t} = 0 \tag{B.22}$$

For loading and unloading after bond failure, $\lambda \geq 1$, and when a compressive normal force is present, $u_n \leq 0$

$$\frac{dT_n}{du_n} = 10^6 \frac{1}{\delta_n} \tag{B.23}$$

$$\frac{dT_n}{du_t} = \frac{dT_n}{du_b} = 0 \tag{B.24}$$

$$\frac{dT_t}{du_u} = \begin{cases} -\text{sgn}\,(du_t)\,\mu\,(10^6)\,\dfrac{1}{\delta_n} & |T_t| \geq \mu|T_n| \quad \text{(sliding)} \\ 0 & |T_t| < \mu|T_n| \quad \text{(no sliding)} \end{cases} \tag{B.25}$$

$$\frac{dT_t}{du_t} = \begin{cases} 0 & |T_t| \geq \mu|T_n| \\ -4\mu\,(10^6)\,\dfrac{u_n}{\delta_n}\dfrac{1}{\delta_t} & |T_t| < \mu|T_n| \end{cases} \tag{B.26}$$

$$\frac{dT_t}{du_b} = 0 \tag{B.27}$$

$$\frac{dT_b}{du_u} = \begin{cases} -\text{sgn}\,(du_b)\,\mu\,(10^6)\,\dfrac{1}{\delta_n} & |T_b| \geq \mu|T_n| \quad \text{(sliding)} \\ 0 & |T_b| < \mu|T_n| \quad \text{(no sliding)} \end{cases} \tag{B.28}$$

$$\frac{dT_b}{du_t} = 0 \tag{B.29}$$

$$\frac{dT_b}{du_b} = \begin{cases} 0 & |T_b| \geq \mu|T_n| \\ -4\mu\,(10^6)\,\dfrac{u_n}{\delta_n}\dfrac{1}{\delta_b} & |T_b| < \mu|T_n| \end{cases} \tag{B.30}$$

If there is no normal compressive force, $u_n > 0$, separation occurs and

$$\frac{dT_n}{du_n} = \frac{dT_n}{du_t} = \frac{dT_n}{du_b} = 0 \tag{B.31}$$

$$\frac{dT_t}{du_n} = \frac{dT_t}{du_t} = \frac{dT_t}{du_b} = 0 \tag{B.32}$$

$$\frac{dT_b}{du_n} = \frac{dT_b}{du_t} = \frac{dT_b}{du_b} = 0 \tag{B.33}$$

In order to form the interface element stiffness matrix,

$$K^{NM} = \frac{\partial F^N}{\partial u^M} \tag{B.34}$$

where F^N is the force contributed by the element to degree of freedom N and u^M is the displacement at degree of freedom M, it is necessary to multiply the traction derivatives by the area associated with the integration point to determine the force derivatives. The force derivatives are projected to the nodes to obtain the element stiffness matrix in the n, t, b coordinate system.

$$[k] = \begin{bmatrix} k^I & k^{II} \\ k^{II} & k^I \end{bmatrix} \tag{B.35}$$

The submatrices k^I and k^{II} are related 6x6 matrices. The terms in the k^I submatrix are

$$k^I_{11} = \left[a\left(\frac{dT_n}{du_n}\right)^A + b\left(\frac{dT_n}{du_n}\right)^B \right] \text{AREA} \tag{B.36}$$

$$k^I_{12} = \left[a\left(\frac{dT_n}{du_t}\right)^A + b\left(\frac{dT_n}{du_t}\right)^B \right] \text{AREA} \tag{B.37}$$

$$k^I_{13} = \left[a\left(\frac{dT_n}{du_b}\right)^A + b\left(\frac{dT_n}{du_b}\right)^B \right] \text{AREA} \tag{B.38}$$

$$k^I_{14} = \left[d\left(\frac{dT_n}{du_n}\right)^A + d\left(\frac{dT_n}{du_n}\right)^B \right] \text{AREA} \tag{B.39}$$

$$k^I_{15} = \left[d\left(\frac{dT_n}{du_t}\right)^A + d\left(\frac{dT_n}{du_t}\right)^B \right] \text{AREA} \tag{B.40}$$

$$k^I_{16} = \left[d\left(\frac{dT_n}{du_b}\right)^A + d\left(\frac{dT_n}{du_b}\right)^B \right] \text{AREA} \tag{B.41}$$

$$k^I_{21} = \left[a\left(\frac{dT_t}{du_n}\right)^A + b\left(\frac{dT_t}{du_n}\right)^B \right] \text{AREA} \tag{B.42}$$

$$k^I_{22} = \left[a\left(\frac{dT_t}{du_t}\right)^A + b\left(\frac{dT_t}{du_t}\right)^B \right] \text{AREA} \tag{B.43}$$

$$k^I_{23} = \left[a\left(\frac{dT_t}{du_b}\right)^A + b\left(\frac{dT_t}{du_b}\right)^B \right] \text{AREA} \tag{B.44}$$

$$k^I_{24} = \left[d\left(\frac{dT_t}{du_n}\right)^A + d\left(\frac{dT_t}{du_n}\right)^B \right] \text{AREA} \tag{B.45}$$

$$k^I_{25} = \left[d\left(\frac{dT_t}{du_t}\right)^A + d\left(\frac{dT_t}{du_t}\right)^B \right] \text{AREA} \tag{B.46}$$

$$k^I_{26} = \left[d\left(\frac{dT_t}{du_b}\right)^A + d\left(\frac{dT_t}{du_b}\right)^B \right] \text{AREA} \tag{B.47}$$

$$k^I_{31} = \left[a\left(\frac{dT_b}{du_n}\right)^A + b\left(\frac{dT_b}{du_n}\right)^B \right] \text{AREA} \tag{B.48}$$

$$k^I_{32} = \left[a\left(\frac{dT_b}{du_t}\right)^A + b\left(\frac{dT_b}{du_t}\right)^B \right] \text{AREA} \tag{B.49}$$

$$k^I_{33} = \left[a\left(\frac{dT_b}{du_b}\right)^A + b\left(\frac{dT_b}{du_b}\right)^B \right] \text{AREA} \tag{B.50}$$

$$k^I_{34} = \left[d\left(\frac{dT_b}{du_n}\right)^A + d\left(\frac{dT_b}{du_n}\right)^B \right] \text{AREA} \tag{B.51}$$

$$k^I_{35} = \left[d\left(\frac{dT_b}{du_t}\right)^A + d\left(\frac{dT_b}{du_t}\right)^B \right] \text{AREA} \tag{B.52}$$

$$k^I_{36} = \left[d\left(\frac{dT_b}{du_b}\right)^A + d\left(\frac{dT_b}{du_b}\right)^B \right] \text{AREA} \tag{B.53}$$

$$k^I_{41} = k^I_{14} \tag{B.54}$$

$$k^I_{42} = k^I_{15} \tag{B.55}$$

$$k^I_{43} = k^I_{16} \tag{B.56}$$

$$k^I_{44} = \left[b\left(\frac{dT_n}{du_n}\right)^A + a\left(\frac{dT_n}{du_n}\right)^B \right] \text{AREA} \tag{B.57}$$

$$k^I_{45} = \left[b\left(\frac{dT_n}{du_t}\right)^A + a\left(\frac{dT_n}{du_t}\right)^B \right] \text{AREA} \tag{B.58}$$

$$k^I_{46} = \left[b\left(\frac{dT_n}{du_b}\right)^A + a\left(\frac{dT_n}{du_b}\right)^B \right] \text{AREA} \tag{B.59}$$

$$k^I_{51} = k^I_{24} \tag{B.60}$$

$$k^I_{52} = k^I_{25} \tag{B.61}$$

$$k^I_{53} = k^I_{26} \tag{B.62}$$

$$k^I_{54} = \left[b\left(\frac{dT_t}{du_n}\right)^A + a\left(\frac{dT_t}{du_n}\right)^B \right] \text{AREA} \tag{B.63}$$

$$k^I_{55} = \left[b\left(\frac{dT_t}{du_t}\right)^A + a\left(\frac{dT_t}{du_t}\right)^B \right] \text{AREA} \tag{B.64}$$

$$k^I_{56} = \left[b\left(\frac{dT_t}{du_b}\right)^A + a\left(\frac{dT_t}{du_b}\right)^B \right] \text{AREA} \tag{B.65}$$

$$k^I_{61} = k^I_{34} \tag{B.66}$$

$$k^I_{62} = k^I_{35} \tag{B.67}$$

$$k^I_{63} = k^I_{36} \tag{B.68}$$

$$k^I_{64} = \left[b\left(\frac{dT_b}{du_n}\right)^A + a\left(\frac{dT_b}{du_n}\right)^B \right] \text{AREA} \tag{B.69}$$

$$k^I_{65} = \left[b\left(\frac{dT_b}{du_t}\right)^A + a\left(\frac{dT_b}{du_t}\right)^B \right] \text{AREA} \tag{B.70}$$

$$k^I_{66} = \left[b\left(\frac{dT_b}{du_b}\right)^A + a\left(\frac{dT_b}{du_b}\right)^B \right] \text{AREA} \tag{B.71}$$

Here,

$$a = \frac{1}{3} + \frac{1}{2\sqrt{3}} \qquad b = \frac{1}{3} - \frac{1}{2\sqrt{3}} \qquad d = \frac{1}{3} \tag{B.72}$$

Also, $k^{II}_{ij} = - k^I_{ij}$. The stiffness terms must now be translated to the global coordinate system.

$$K^I_{11} = s\,(sk^I_{11} + ck^I_{12}) + c\,(sk^I_{21} + ck^I_{22}) \tag{B.73}$$

$$K^I_{12} = s\,(-ck^I_{11} + sk^I_{12}) + c\,(-ck^I_{21} + sk^I_{22}) \tag{B.74}$$

$$K^I_{14} = s\,(sk^I_{14} + ck^I_{15}) + c\,(sk^I_{24} + ck^I_{25}) \tag{B.75}$$

$$K^I_{15} = s\,(-ck^I_{14} + sk^I_{15}) + c\,(-ck^I_{24} + sk^I_{25}) \tag{B.76}$$

$$K^I_{21} = -c\,(sk^I_{11} + ck^I_{12}) + s\,(sk^I_{21} + ck^I_{22}) \tag{B.77}$$

$$K'_{22} = -c\,(-ck'_{11} + sk'_{12}) + s\,(-ck'_{21} + sk'_{22}) \tag{B.78}$$

$$K'_{24} = -c\,(sk'_{14} + ck'_{15}) + s\,(sk'_{24} + ck'_{25}) \tag{B.79}$$

$$K'_{25} = -c\,(-ck'_{14} + sk'_{15}) + s\,(-ck'_{24} + sk'_{25}) \tag{B.80}$$

$$K'_{41} = K'_{14} \tag{B.81}$$

$$K'_{42} = K'_{15} \tag{B.82}$$

$$K'_{44} = s\,(sk'_{44} + ck'_{45}) + c\,(sk'_{54} + ck'_{55}) \tag{B.83}$$

$$K'_{45} = s\,(-ck'_{44} + sk'_{45}) + c\,(-ck'_{54} + sk'_{55}) \tag{B.84}$$

$$K'_{51} = K'_{24} \tag{B.85}$$

$$K'_{52} = K'_{25} \tag{B.86}$$

$$K'_{54} = -c\,(sk'_{44} + ck'_{45}) + s\,(sk'_{54} + ck'_{55}) \tag{B.87}$$

$$K'_{55} = -c\,(-ck'_{44} + sk'_{45}) + s\,(-ck'_{54} + sk'_{55}) \tag{B.88}$$

$$K'_{ij} = k'_{ij} \qquad \text{all others} \tag{B.89}$$

And finally,

$$[K] = \begin{bmatrix} K' & K'' \\ K'' & K' \end{bmatrix} \tag{B.90}$$

where $K''_{ij} = -K'_{ij}$.

APPENDIX C

EXPERIMENTAL DATA

Material

•Ti-15V-3Cr-3Sn-3Al matrix foil

•SCS-6 Continuous fibers spaced at 128 per inch

•0.002 inch diameter molybdenum wires spaced at 5 per inch woven with fibers

•0.008 inch nominal ply thickness

•0.4 nominal fiber volume fraction

Tube Geometry

Tube #	I.D. #	Layup	I.D. (in.)	O.D.(in.)	t (in.)	L (in.)
1	N880162	$[0_4]$	1.429	1.491	0.0310	6.9
2	N880160	$[0_4]$	1.4249	1.4893	0.0322	7.0
4	N880159	$[0_4]$	1.4256	1.4910	0.0327	7.0
5	P880019	$[\pm 45]_s$	3.9048	3.9824	0.0388	12
9	P880022	$[\pm 45]_s$	3.908	3.980	0.0360	11.9
10	P880023	$[\pm 45]_s$	3.9068	3.9808	0.0370	12

$[0_4]$ Tube Elastic Properties

Tube #1

Rosette	R1	R2	R3	R4
E_{11} (Msi)	32.4	30.7	32.3	32.1
ν_{12}	0.282	0.263	0.333	0.289
E_{22} (Msi)	21.6	21.2	17.1	21.0
ν_{21}	0.187	0.207	0.140	0.193
G_{12} (Msi)	7.69	7.49	7.84	7.63

Tube #2

Rosette	R1	R2	R3	R4*	R5*
E_{11} (Msi)	31.9	32.2	31.7	33.6	37.6
ν_{12}	0.251	0.293	0.290	0.98	0.275
G_{12} (Msi)	7.85	8.00	8.11	7.69	8.20

Tube #4

Rosette	R1	R2	R3	R4*	R5*
E_{11} (Msi)	32.4	31.7	30.8	36.2	38.5
ν_{12}	0.263	0.270	0.274	0.188	0.338
G_{12} (Msi)	7.48	7.56	7.35	8.06	8.82

* Strain gage rosette located at the end of the gage section.

$[\pm 45]_s$ Tube Elastic Properties

Tube #5

Rosette	R1	R2	R3	R4*	R5*
E_{xx} (Msi)	16.4	17.8	16.7	19.8	16.5
ν_{xy}	0.433	0.459	0.351	0.370	0.418
G_{xy} (Msi)	8.69	9.45	8.62	8.60	8.71

Tube #9

Rosette	R1	R2	R3	R4
E_{xx} (Msi)	17.2	18.6	19.1	21.0
ν_{xy}	0.331	0.352	-	-
G_{xy} (Msi)	9.57	9.13	-	-

Tube #10

Rosette	R1	R2	R3	R4*	R5*
E_{xx} (Msi)	16.1	16.7	21.1	18.5	20.3
ν_{xy}	0.360	0.332	0.362	0.360	0.369[1]
G_{xy} (Msi)	8.59	8.85	9.75	8.93	9.70
Strain Gage	G1	G2	G4	G5	
E_{xx} (Msi)	19.8	19.8	18.1	15.1	

* Strain gage rosette located at the end of the gage section.

Failure Data

$[0_4]$ Tubes

Tube #	Ultimate Stress	Comments
1	σ_{11}=119 ksi	Failure occurred in grip section at σ_{11}=108 ksi
2	τ_{12}=42 ksi	Inelastic shear strains were very nonuniform
4	σ_{22}=46 ksi	Nonuniform inelastic transverse strains

$[\pm 45]_s$ Tubes

Tube #	Ultimate Stress	Comments
5	σ_{xx}=68 ksi	Failure occurred during uniaxial tensile loading
9	σ_{xx}=66 ksi	Failure occurred during a hold time after the accumulation of a large amount of creep strain
10	σ_{xx}=68 ksi, τxy=3 ksi	Failure occurred during shear loading with constant axial load

REPORT DOCUMENTATION PAGE

Form Approved
OMB No. 0704-0188

Public reporting burden for this collection of information is estimated to average 1 hour per response, including the time for reviewing instructions, searching existing data sources, gathering and maintaining the data needed, and completing and reviewing the collection of information. Send comments regarding this burden estimate or any other aspect of this collection of information, including suggestions for reducing this burden, to Washington Headquarters Services, Directorate for Information Operations and Reports, 1215 Jefferson Davis Highway, Suite 1204, Arlington, VA 22202-4302, and to the Office of Management and Budget, Paperwork Reduction Project (0704-0188), Washington, DC 20503.

1. AGENCY USE ONLY (Leave blank)	2. REPORT DATE	3. REPORT TYPE AND DATES COVERED
	September 1993	Contractor Report

4. TITLE AND SUBTITLE
Inelastic Deformation of Metal Matrix Composites

5. FUNDING NUMBERS
NAG1-745
WU 506-73-43-03

6. AUTHOR(S)
C. J. Lissenden, C. T. Herakovich, and M-J. Pindera

7. PERFORMING ORGANIZATION NAME(S) AND ADDRESS(ES)
University of Virginia
School of Engineering and Applied Science
Charlottesville, VA 22903-2442

8. PERFORMING ORGANIZATION REPORT NUMBER
AM-93-03

9. SPONSORING/MONITORING AGENCY NAME(S) AND ADDRESS(ES)
National Aeronautics and Space Administration
Langley Research Center
Hampton, VA 23681-0001

10. SPONSORING/MONITORING AGENCY REPORT NUMBER
NASA CR-191522

11. SUPPLEMENTARY NOTES
Langley Technical Monitor: W. Steven Johnson
Final Report

12a. DISTRIBUTION/AVAILABILITY STATEMENT
Unclassified - Unlimited

Subject Category 24

12b. DISTRIBUTION CODE

13. ABSTRACT *(Maximum 200 words)*

A theoretical model capable of predicting the thermomechanical response of continuously reinforced metal matrix composite laminates subjected to multiaxial loading has been developed. A micromechanical model is used in conjunction with nonlinear lamination theory to determine inelastic laminae response. Matrix viscoplasticity, residual stresses, and damage to the fiber/matrix interfacial zone are explicitly included in the model. The representative cell of the micromechanical model is considered to be in a state of generalized plane strain, enabling a quasi two-dimensional analysis to be performed. Constant strain finite elements are formulated with elastic-viscoplastic constitutive equations. Interfacial debonding is incorporated into the model through interface elements based on the interfacial debonding theory originally presented by Needleman (1987), and modified by Tvergaard (1990). Nonlinear interfacial constitutive equations relate interfacial tractions to displacement discontinuities at the interface. Theoretical predictions are compared with the results of an experimental program conducted on silicon carbide/titanium (SiC/Ti) unidirectional, $[0_4]$, and angle-ply, $[\pm 34]_s$, tubular specimens. Multiaxial loading included increments of axial tension, compression, torque, and internal pressure. Loadings were chosen in an effort to distinguish inelastic deformation due to damage from matrix plasticity and separate time-dependent effects from time-independent effects. Results show that fiber/matrix debonding is nonuniform throughout the composite and is a major factor in the effective response. Also, significant creep behavior occurs at relatively low applied stress levels at room temperature.

14. SUBJECT TERMS
Titanium; Plasticity; Fiber/matrix debonding; Multi-axial loading; Composite tubes

15. NUMBER OF PAGES
208

16. PRICE CODE
A10

17. SECURITY CLASSIFICATION OF REPORT	18. SECURITY CLASSIFICATION OF THIS PAGE	19. SECURITY CLASSIFICATION OF ABSTRACT	20. LIMITATION OF ABSTRACT
Unclassified	Unclassified		